Experimental Study of Three-Dimensional Offset Jets and Wall Jets

by

Martin Agelin-Chaab

A Thesis submitted to the Faculty of Graduate Studies of
The University of Manitoba
in partial fulfillment of the requirements of the degree of

DOCTOR OF PHILOSOPHY

Department of Mechanical and Manufacturing Engineering
University of Manitoba
Winnipeg

ABSTRACT

An experimental study was designed to examine and document the development and structures of turbulent 3D offset jets. The generic 3D wall jets at the same Reynolds numbers was used as the basis of comparison. The experiments were performed using a high resolution particle image velocimetry technique to perform velocity measurements at three Reynolds numbers based on the jet exit diameter and velocities of 5000, 10000 and 20000 and four jet offset height ratios of 0.5, 1.0, 2.0 and 4.0. The measurements were performed in the streamwise/wall-normal plane from 0 to 120 jet exit diameters and in the streamwise/lateral plane from 10 to 80 jet exit diameters. The velocity data were analyzed using (i) mean velocities and one-point statistics such as turbulence intensities, Reynolds stresses, triple velocity products and some terms in the transport equations for the turbulence kinetic energy, (ii) two-point velocity correlations to study how the turbulence quantities are correlated as well as the length scale and angle of inclination of the hairpin-like vortex structures, and (iii) proper orthogonal decomposition to examine the energy distribution and the role of the large scale structures in the turbulence intensities and Reynolds shear stresses.

The decay of the maximum mean velocities and spread of the jet half widths became independent of Reynolds number much earlier in the generic wall jet than the offset jets. The flow development is delayed with increasing offset heights. The decay rate and wall-normal spread rate increased with the offset heights, whereas the lateral spread rate decreased with offset heights, which is consistent with previous students.

The two-point auto-correlations and the proper orthogonal decomposition results indicate the presence of more large scale structures in the outer and self-similar regions than in the inner and developing regions. The iso-contours of the streamwise auto-correlations in the inner regions were inclined at similar angles of $\beta = 11.2^{o} \pm 0.6^{o}$, which are in good agreement with reported values in boundary layer studies. The angles decrease with increasing distance from the wall.

ACKNOWLEDGEMENTS

I would like to acknowledge the invaluable guidance and support of my supervisor, Dr. Mark F. Tachie. I am very grateful for the financial support of NSERC, and the University of Manitoba. I salute my colleagues Drs. Samuel S. Paul, Kofi F. K. Adane, and Khalid M. Shah for their co-operation and friendship. I would like to thank the technicians in the Mechanical Engineering department especially, Paul Krueger and John Finken for their diverse technical assistance. Finally but not the least, my thanks go to some of my friends right here in Canada including Dr. and Mrs. Nanang, Mr. and Mrs. Amoah, Ms. Merle Metke, Dr. Wisdom Agorde, Sr. Georgina Brenya, and Mr. Benjamin Amoyaw for their patient friendship in the course of this program.

DEDICATION

I would like to dedicate this thesis to my wife, Glana, and my mom, Apekame, for their constant love and patience.

TABE OF CONTENTS

LIST OF FIGURES

LIST OF TABLES

LIST OF EQUATIONS

NOMENCLATURE

English Symbols

B	breadth of test section
d	jet exit diameter
d_p	diameter of seeding particle
d_{pitch}	pixel pitch
E_λ	fractional energy or energy per divided by the total energy
g	acceleration due to gravity
h	jet offset distance
H	height of test section
l_m	mixing length
L	length of test section
Lx_{uu}	streamwise extent of R_{uu}
Lx_{vv}	streamwise extent of R_{vv}
Ly_{uu}	wall-normal extent of R_{uu}
Ly_{vv}	wall-normal extent of R_{vv}
m	number of modes
M	number of vectors in a snapshot
M_f	magnification factor
n	number of readings
N	number of snapshots
P	thermodynamic pressure
q^2	$u^2 + v^2$
R_{uu}	auto-correlation of the streamwise turbulence intensities
R_{vv}	auto-correlation of the wall-normal turbulence intensities
R_{ww}	auto-correlation of the lateral turbulence intensities
Δt	laser pulse separation time
U	local mean streamwise velocity or time mean streamwise velocity at a point
U_{bulk}	bulk velocity

U'	instantaneous streamwise velocity
U_j	jet exit velocity
U_m	local maximum mean streamwise velocity
U_τ	friction velocity
u	streamwise turbulence intensity
u_m	maximum streamwise turbulence intensity
u^3, u^2v, uv^2, u^2w	triple velocity correlations
uv	Reynolds shear stress
v	wall-normal turbulence intensity
V	local mean wall-normal velocity or time mean wall-normal velocity at a point
V'	instantaneous wall-normal velocity
v_m	maximum wall-normal turbulence intensity
v^3	triple wall-normal velocity correlation
v_s	seeding particle settling velocity
W	local mean lateral velocity or time mean lateral velocity at a point
W'	instantaneous lateral velocity
w^3	triple lateral velocity correlation
x	streamwise direction in the Cartesian coordinates axis
x_r	length of recirculation region
y	wall-normal direction in the Cartesian coordinates axis
y_m	wall-normal location (y) where U_m occurs
$y_{0.5}$	wall-normal location (y) where $0.5U_m$ occurs
$Y_{0.5}$	wall-normal distance from the wall to the outer location where the streamwise mean velocity is half of the local maximum streamwise velocity in the attachment region.
z	spanwise direction in the Cartesian coordinates axis
$z_{0.5}$	lateral location (z) where U_m occurs

Greek Symbols

β	angle of inclination of hairpin vortex
μ_f	dynamic viscosity of the working fluid
ν	kinematic viscosity of the working fluid
ν_t	eddy viscosity
ρ_f	density of working fluid
ρ_p	seeding particle density
ρ_{pp}	correlation coefficient of the fluctuating wall pressure
ρ_{pu}	correlation coefficient of the fluctuating wall pressure and streamwise fluctuating velocity
ρ_{pv}	correlation coefficient of the fluctuating wall pressure and wall-normal fluctuating velocity
ρ_{uv}	correlation coefficient of the streamwise and wall-normal fluctuating velocity
ρ_{uw}	correlation coefficient of the streamwise and lateral fluctuating velocity
τ_r	seeding particle response time
τ_w	wall shear stress
Ω_x	streamwise mean vorticity

Acronyms & Other Notations

2D	two-dimensional
3D	three-dimensional
Re_j	Reynolds number based on the jet exit velocity, U_j and exit diameter, d
Re_j^*	Re_j divided by 1000
Re_θ	Reynolds number based on momentum thickness, θ
Re_τ	Reynolds number based on the friction velocity, U_τ
PIV	Particle Image Velocimetry
POD	proper orthogonal decomposition
DNS	Direct Numerical Simulation
LES	Large Eddy Simulation
RANS	Reynolds Averaged Navier Stokes

CHAPTER 1

INTRODUCTION

1.1 Overview

A generic wall jet is formed when a jet of fluid is directed tangentially along a wall. As the ambient fluid is entrained and the flow evolves downstream, the maximum local mean velocity decays and the jet spreads in both the wall-normal and lateral directions. The flow field of a wall jet consists of an inner layer, which extends from the wall to the point of maximum streamwise mean velocity, and an outer layer, which stretches from the point of maximum streamwise mean velocity to the outer edge of the flow. The inner layer possesses some of the characteristics of a boundary layer while the structure of the outer layer is similar to that of a free shear flow. The wall jet is, therefore, a composite flow consisting of a boundary layer and a free shear flow.

An offset jet is formed when a jet discharges into a medium above a wall parallel to the axis of the jet exit but offset by a certain distance. Entrainment of the fluid in this region creates a low pressure zone causing the jet to deflect towards the wall and eventually attaches to the wall. After reattachment, the flow remains attached to the wall and evolves downstream to form a generic wall jet. The flow field of offset jets is complex with intriguing features. In the attachment region, the flow has features qualitatively akin to other reattaching shear layer flows such as flow over a backward facing step (BFS). However, an offset jet represents a more complex flow configuration because there are two shear layers developing in an offset jet as opposed to only one in a BFS flow. It should be noted that in both the offset and wall jets, the driving force is the jet exit momentum.

Offset jets and generic wall jets have attracted extensive research attention mainly due to their important and diverse practical and theoretical applications. Some of these applications include: (i) flow separation control, where wall jets are mixed with the ambient flow to provide additional momentum to a boundary layer at the verge of separation; (ii) film-cooling technology in which wall jets are used to improve the thermal performances of gas turbines; (iii) evaporation enhancement such as in automobile defrosters; (iv) air distribution in enclosed environments; (v) thrust-augmenting ejectors for vertical/short takeoff and landing aircrafts; (vi) effluent disposal into water bodies such as in marine tailings; and (vi) predicting the nature of aircraft exhausts and the loading effects of aircraft exhausts on ground structures. In view of their interesting characteristics, offset and wall jets have also attracted considerable fundamental research interests. For example, they are used as prototypical flows for investigating the physics of complex near-wall and free shear flows. In addition, the complexity of offset and wall jets makes them more severe test cases for assessing the performance of various turbulence models.

As with other fluid flows, offset and wall jets can either be two-dimensional (2D) or three-dimensional (3D). They can also be either laminar or turbulent. When the jet exit is finite, the jet is said to be 3D. Three-dimensional jets are more complex than when the widths of the jet exits are infinite (i.e., 2D jets). The jet can discharge into either a quiescent medium or a moving stream. In the latter case, the stream can either be in the same direction as the jet (i.e., co-flowing) or against it (i.e., counter-flowing). Most turbulent offset and wall jet experimental studies were performed in quiescent media. Even in those cases there are some discrepancies among the experimental results. This

study presents a comprehensive experimental study of incompressible 3D turbulent offset jets in a quiescent medium. Detailed measurements are also made in generic 3D turbulent wall jets to facilitate the interpretation and discussion of the results from the relatively more complex offset jets.

In this chapter, general remarks about turbulence including the equations of motion are presented. Also presented in this chapter are the definitions of offset and wall jets, the research methodology and measuring devices, and some of the one- and multi-point turbulence statistics that are used to interpret the experimental results. The chapter concludes with a statement of the research objective and structure of the thesis.

1.2 General Remarks

1.2.1 Fluid turbulence

Fluid turbulence is everywhere: in industrial and environmental flows, aerodynamics, hydrodynamics, meteorology, and oceanography, etc. Sreenivasan (1999) painted the most compelling picture of the practical importance and ubiquity of fluid turbulence:

"*Few would dispute the importance of turbulence. Without it, the mixing of air and fuel in an automobile engine would not occur on useful time scales; the transport and dispersion of heat, pollutants, and momentum in the atmosphere and the oceans would be far weaker; in short, life as we know it would not be possible on the earth. Unfortunately, turbulence also has undesirable consequences: it enhances energy consumption of pipe lines, aircraft and ships, and automobiles; it is an element to be reckoned with in air-travel safety; it distorts the propagation of electromagnetic signals;*

and so forth. A major goal of a turbulence practitioner is the prediction of the effects of turbulence and control them - suppress or enhance them, as circumstances dictate - in various applications such as industrial mixers and burners, nuclear reactors, aircraft and ships, and rocket nozzles."

In spite of the practical importance of fluid turbulence and the extensive research on turbulence, fundamental understanding of the physics of fluid turbulence is still lacking due its complex characteristics. For example, turbulent flows are characterized by disorderly fluctuations in time and three-dimensional in space with rich and varied time and spatial scales. Many leading researchers have acknowledged the challenges that turbulence presents. Turbulence is also, in the words of the late Nobel Prize physicist Richard Feynman, "*the last great unsolved problem of classical physics*."

1.2.2 Equations of motion and notation

Although analytical solution for a turbulent flow is not yet possible, on the basis of the continuum fluid assumption, the dynamics of turbulence is adequately described by the continuity and Navier-Stokes equations. Using tensor notation, the continuity and the Reynolds-averaged Navier-Stokes equations for incompressible fluid are, respectively, given by:

$$\frac{\partial U_i}{\partial x_i} = 0 \tag{1.1}$$

$$\frac{\partial U_i}{\partial t} + U_j \frac{\partial U_i}{\partial x_j} = -\frac{1}{\rho}\frac{\partial P}{\partial x_i} + \frac{\partial}{\partial x_j}\left(\nu \frac{\partial U_i}{\partial x_j} - u_i u_j\right), \tag{1.2}$$

where P is the thermodynamic pressure, ρ is the fluid density, ν is the kinematic viscosity

and $u_i u_j$ denotes the Reynolds stresses. In the Cartesian coordinate system, x, y and z denote the streamwise, wall-normal and lateral directions, respectively. The corresponding components of the mean velocities are represented by U, V and W, respectively. Also the corresponding turbulence intensities are u, v and w, respectively.

1.3 Description of Wall and Offset Jets

1.3.1 Wall jet

Launder & Rodi (1981) provided the following definition for a wall jet:

"*A wall jet may be defined as a shear flow directed along a wall where, by virtue of the initially supplied momentum, at any downstream station, the streamwise velocity over some region within the shear flow exceeds that in the external stream.*"

Figure 1.1 shows a sketch of the mean velocity profiles in the self-similar region of a generic 3D wall jet. The symbol U_m represents the local maximum mean velocity and y_m and $y_{0.5}$ denote the wall-normal locations of U_m and $0.5U_m$, respectively, while $z_{0.5}$ represents the lateral location from the jet symmetry plane where $0.5U_m$ occurs. Note that

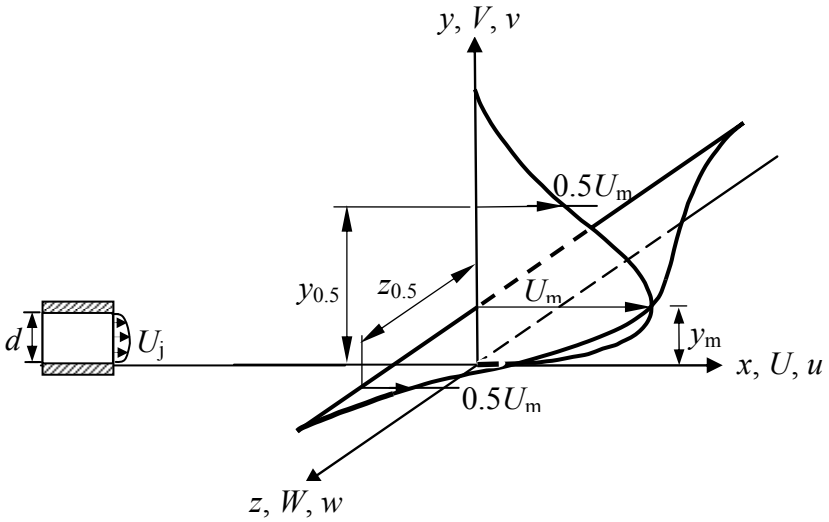

Figure 1.1: Schematic of a 3D generic wall jet

$y_{0.5}$ and $z_{0.5}$ are also referred to as the jet half-widths in the wall-normal and lateral directions, respectively. As the jet discharges from an exit into a quiescent medium and evolves downstream, it entrains the ambient fluid. As a result, U_m decays and the jet spreads in both the y and z directions. As noted earlier, the flow field of a wall jet is traditionally divided into two regions: an inner layer, which extends from the wall to the point of maximum velocity (i.e., $y \leq y_m$) and an outer layer, which stretches from the point of maximum velocity to the outer edge of the flow (i.e., $y > y_m$). At the outer edges of the jet, the mean velocities are low and the local turbulence levels become high.

1.3.2 Offset jet

The general flow field of an offset jet is schematically depicted in Fig. 1.2. Note that the figure is a sectional view through the jet symmetry plane of a jet that discharges into a quiescent medium from an exit. In the sketch U_j is the jet exit maximum mean velocity, and d and h are the jet exit diameter and offset height, respectively. There are three regions in the flow field: (I) the reverse flow region, which extends from the jet exit, $x/d = 0$ to the reattachment point (x_{rp}) and denoted by x_r; (II) the attachment region, which stretches from x_{rp} to the beginning of the wall jet region; and (III) the wall jet region, where the jet develops the characteristics of a generic wall jet. The symbols have the same meaning as defined in Section 1.3.1. The wall-normal location of $0.5U_m$ in the outer shear layer of the attachment region is denoted by $Y_{0.5}$. There is also a shear layer dividing line, which splits the shear layer into the inner and outer layers. Entrainment of the fluid bounded by the jet and the wall creates a sub-atmospheric pressure zone causing the jet to deflect towards the wall and eventually attaches to the wall. In the attachment

region, the flow has features qualitatively similar to other reattaching shear layer flows, such as flow over a backward facing step (BFS). Some of these similarities include flow reversal, low velocities and high local turbulence levels in the recirculation region, and unsteady reattachment points. However, an offset jet represents a more complex flow configuration because there are two shear layers developing in an offset jet as opposed to only one in a BFS flow. Far downstream from the jet exit, the flow develops characteristics that resemble a generic wall jet flow. The transition from the attachment region to the wall jet region is characterized by a linear increase of $Y_{0.5}$ with downstream distance (x).

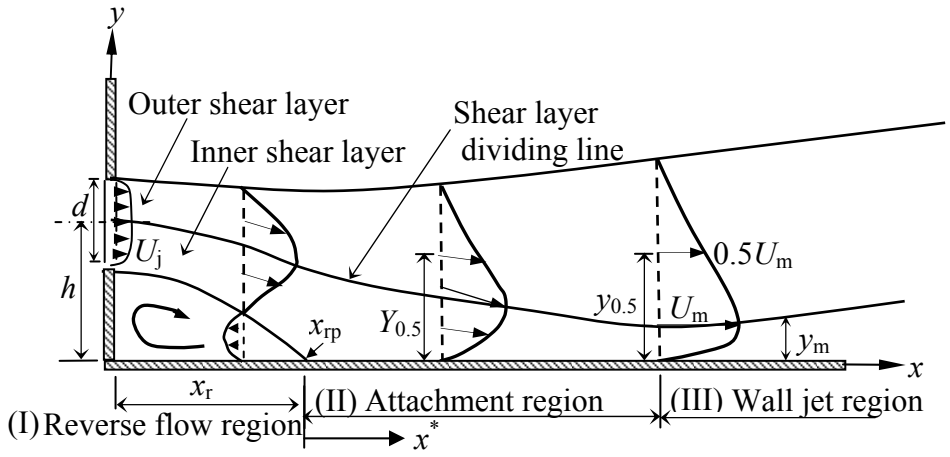

Figure 1.2: Schematic of an offset jet through the jet symmetry plane

1.4 Research Methodologies and Measuring Devices

Analytical, numerical and experimental techniques are traditionally employed in the study of fluid flows. As mentioned earlier, analytical techniques are not possible for turbulent flows. It is also evident that experimental techniques are more time consuming and are getting increasingly more expensive compared with numerical techniques.

Numerical techniques provide opportunity to study many more flow variables and complex geometries than would be possible in experimental studies. However, like the other techniques, numerical techniques have some limitations.

The different types of numerical techniques include Direct Numerical Simulation (DNS), Reynolds Averaged Navier Stokes (RANS) modeling, and Large Eddy Simulation (LES). In DNS of turbulent flows, the exact governing equations are solved. This provides precise results but requires huge computational resources. The cost of DNS increases with both Reynolds number and complexity of the flow. The technique has been used to study fully developed channel flow and two-dimensional separated and reattached flows at relatively low Reynolds numbers. It cannot be used for complex and high Reynolds number turbulent flows of engineering and industrial importance due to the wide range of scales to be resolved and the limits of computational resources. To date, there is no DNS of 3D turbulent offset jets or wall jets.

A far less expensive alternative to DNS is the RANS modeling, which involves techniques developed for predicting average flow quantities. The quantities to be modeled have to be identified and model constants calibrated. This requires an understanding of the physics of the terms that are modeled and accurate benchmark data for validation. Models of varying sophistication have been developed. Examples include eddy viscosity models such as the two-equation models and also the second moment closures.

Another computational technique is the LES, which seeks to directly compute the large spatial scales (as in DNS), while modeling the smaller scales (as in RANS models). This hybrid technique involves the filtering of the Navier-Stokes equations to

separate the scales which are modeled from those which are computed directly. The computational cost of LES is in-between those of DNS and RANS.

Based on the above discussion, experimental studies will continue to play a vital role in turbulence research. With respect to experimental investigation, one- and multi-point measurement techniques, as well as flow visualisation are the common approaches. Measuring instruments such as conventional thermal anemometers and Pitot-tubes are one-point measurement devices and are most extensively employed in experimental studies of turbulent flows. While these techniques have been used to obtain information that provided insight into turbulent flows, they are not reliable for velocity measurements in certain flow regions. For example, they exhibit directional ambiguity, which makes it difficult to reliably measure velocities in reversed flow regions. Furthermore, it is difficult to obtain reliable velocity measurement in regions with high local turbulence levels such as in reverse flow regions and outer edges of the jets. These techniques are also intrusive and exert some interference on the flow field. The development of optical techniques such as laser Doppler anemometry (LDA) and particle image velocimetry (PIV), which do not interfere with the flow and overcome directional ambiguity, has advanced experimental techniques. Like the conventional thermal anemometers, LDA is a point-wise measurement technique; whereas PIV is a multipoint technique. Since turbulent flows are spatially heterogeneous, simultaneous multi-point measurement techniques are more appropriate. The PIV technique has the advantage of providing simultaneous whole field instantaneous velocity measurements. From such measurements, the various terms in the transport equations and the spatial structures can be evaluated and studied. The downside of PIV is that it produces huge data with high

cost of data storage. In addition, the spatial and temporal resolutions of the standard PIV are relatively low compared to those of hotwire and LDA.

1.5 One- and Multi-point Statistics

Statistical averaging can be used to study average flow quantities involving a number of points in space and time. One-point statistics generally simplify flow information into quantities such as mean velocities, turbulence kinetic energy, Reynolds shear stresses and triple velocity products. Although one-point statistics include many of the important physical measures of turbulent flows, and provide useful information about the flow field, they do not constitute the full statistics of the flow. For example, spatial flow information cannot be deduced from one-point data and flow information essential to the understanding of some aspects of the flow may be lost (Mathieu & Scott, 2000). As noted earlier, one of the difficulties with turbulence is its rich and varied scales that are characterized by interacting vortical motions. These vortical motions are difficult to account for using one-point statistics alone (Bernard & Wallace, 2002). It is, therefore, useful to apply multi-point statistics such as two-point velocity correlations and proper orthogonal decomposition (POD) in addition to the one-point statistics in analyzing turbulence data.

Two-point velocity correlation is used to reveal the distances and times over which the turbulence field is correlated across the flow. It can be used to estimate the integral length and time scales. Two-point correlation can also be used to quantify the average extent and inclination of the hairpin-like vortex packets. For instance the angle of inclination of the spatial autocorrelation in the streamwise direction is related to the

average inclination of the hairpin packets (Volino et al., 2007).

Proper orthogonal decomposition is a multi-point statistical technique for extracting energetically dominant modes in a flow. It decomposes a series of measurements into an optimal set of basis functions (Holmes et al., 1996). Proper orthogonal decomposition captures the most energetic and hence the largest structures of the flow in the first few modes. This means that if the dynamics of the flow are dominated by large flow structures, the data can be represented satisfactorily using only the few first modes. More importantly, the contribution of the extracted structures to turbulence stresses and their importance to turbulence production can be determined and reconstructed (Holmes et al., 1996).

1.6 Objective and Thesis Structure

1.6.1 Objective

As noted in Section 1.4, analytical techniques are not possible for turbulent flows. Direct numerical simulation is limited by high Reynolds numbers and complexity of flows. Reynolds Averaged Navier Stokes modeling is the future of turbulence flow of engineering importance. However, it requires understanding of the physics of terms modeled and accurate benchmark data for validation. In view of this, the overall goal of this experimental study is to advance physical understanding of 3D turbulent offset jets, provide detailed and comprehensive experimental data sets that will be useful for validating future turbulence models or developing new advanced models.

The specific objective is to study the evolution and structures of 3D turbulent offset jets and compare the 3D wall jets formed downstream of the offset jets with the

generic 3D turbulent wall jets at identical Reynolds numbers. This is achieved by using PIV to perform detailed velocity measurements from which the following one-point and multi-point statistics are used to interpret the data:

i. Mean velocities, turbulence intensities, Reynolds shear stresses, stress ratios, triple products, and some of the terms in the turbulence kinetic energy budget.
ii. Two-point velocity correlations
iii. Proper orthogonal decomposition

1.6.2 Thesis structure

In this study, an experimental investigation of 3D turbulent offset jets is presented. In Chapter 2, pertinent studies on 3D turbulent wall and offset jets are reviewed. Chapter 3 provides an overview of the experimental setup and measurement procedure. The results and discussions are presented in Chapter 4. Finally, the conclusions from the study as well as recommendations for future works are presented in Chapter 5.

CHAPTER 2

LITERATURE REVIEW

2.1 Overview

In this chapter, a review of previous studies of turbulent offset and wall jets is presented. It will be seen subsequently that the vast majority of these studies reported only the mean velocities and one-point turbulence statistics. As mentioned in Chapter 1, one of the salient features of turbulence is its rich and varied scales that are characterized by interacting vortical motions. These make it impossible to completely describe the vortical motions using one-point statistics alone. Therefore multi-point techniques such as two-point velocity correlations and proper orthogonal decomposition, which are used to analyze the experimental data, are also briefly reviewed in this chapter.

2.2 Scaling Considerations

As indicated in the Chapter 1, the offset jet has three major regions: reverse flow, attachment and wall jet regions. The flow structures of these regions resemble those of free jets, backward facing step flow, and wall jets, respectively. Different length and velocity scales have been used in the literature in studying the mean velocities and some of the turbulence statistics. Because the inner layer possesses the characteristics of a boundary layer, a number of researchers used the friction velocity, U_τ (i.e., $U_\tau = (\tau_w/\rho)^{0.5}$, where τ_w is wall shear stress and ρ is fluid density), as the velocity scales and the fluid viscosity and the friction velocity (i.e., ν/U_τ) as the length scale (Eriksson et al., 1998; Fujisawa & Sharai, 1989; Abrahamsson et al., 1997). In the outer region, there is consensus in the literature that the appropriate velocity scale for turbulent jets

is the local maximum mean velocity, U_m. However, several parameters have been used as the appropriate length scale. For the generic turbulent wall jets and free jets, the length scale commonly employed is the jet half widths (i.e., $y_{0.5}$ or $z_{0.5}$ as shown in Fig. 1.1). However, the jet exit diameter or height has been employed as the appropriate length scales in some offset jet studies (Nasr & Lai, 1997, 1998; Pelfrey & Liburdy, 1986a, b). In addition, the jet exit diameters or heights as well as a combination of $y_{0.5}$ and y_m have been used as the appropriate length scale (Davis & Winarto, 1980). Similar to wall jets, the jet half width is the appropriate length scale for free jets. The jet exit diameter is traditionally employed as the length scale for the downstream distance. However, for studies involving different jet exit geometries, the area equivalent diameter, defined as the square root of the cross sectional area of the jet exit has been used as the length scale (Rajaratnam & Pani, 1974; Padmanabham & Gowda, 1991a, b; Abrahamsson et al., 1997).

2.3 Previous Studies

Attention is now turned to the previous studies of both turbulent wall jets and offset jets. This review focuses on the maximum velocity decay rates and the spread of the jet half widths of these flows and the turbulent quantities. Although the focus of this work is on turbulent offset jets, the relevant experimental studies on generic wall jets are reviewed first. The rationale is to provide the essential background information to better understand the relatively more complex offset jets.

2.3.1 Turbulent wall jets

Extensive research has been performed on turbulent wall jets. These include wall jets over curved surfaces (Guitton & Newman, 1977), around a cylinder (Neuendorf & Wygnanski, 1999), and radial wall jets (Codazzi et al., 1981). Forthman (1934) is one of the pioneers to report measurements in 2D turbulent wall jets. An extensive review of the wall jet literature prior to 1981 was done by Launder & Rodi (1981, 1983). Wall jet studies conducted subsequent to those reviews are summarized in Padmanabham & Gowda (1991a, b), Tachie (2000) and Law & Herlina (2002).

A summary of the most relevant 3D turbulent wall jets is presented in Table 2.1. A few 2D turbulent wall jet experiments are also included for comparison. In Table 2.1, Re_j (= $U_j d/\nu$) is the Reynolds number based on the jet exit velocity and exit diameter, $dy_{0.5}/dx$ is the wall-normal spread rate, and $dz_{0.5}/dx$ is the lateral spread rate. The decay rate (n) in the table is explained in Section 2.3.1.2.1. As the table shows, the majority of the studies were carried out using hotwire anemometry (HWA) and Pitot tubes (PT). The jet exit geometries include circular, square, rectangular, triangular and segments of a circle. The experiments were conducted at a wide range of Reynolds numbers ($5.5\times 10^3 \leq Re_j \leq 170 \times 10^3$), and over an extended streamwise distance ($0 \leq x/d \leq 350$).

2.3.1.1 General characteristics of wall jets

There is agreement among previous 2D and 3D turbulent generic wall jet studies on some general characteristics of the turbulent wall jet. For example, there is a consensus that the mean streamwise velocities exhibit self-similarity in the region $x/d >$ 20 when the wall-normal jet half width and local maximum mean velocity are used as the

Table 2.1: Summary of relevant turbulent wall jet literature

Authors	**Technique**	**Orifice Type/Shape**	**Re_j (10^3)**	**Data range *x/d***	**$dy_{0.5}/dx$**	**$dz_{0.5}/dx$**	**Decay rate (*n*)**
Hall & Ewing (2007a, b)	HWA	LP/rectangular	89.6	3 - 60	0.051	0.28	
Sun & Ewing (2002a, b)	HWA	LP,CN/round	65, 108	35 - 90	0.053 - 0.060	0.27 - 0.28	
Law & Herlina (2002)	PIV	round	5.5 - 13.7	0 - 50	0.042	0.21	1.07
Venas et al. (1999)	HWA	CN/round	53	80			
Abrahamsson et al. (1997)	HWA	CN /round	79	50 - 90	0.065	0.32	1.29
Padmanabham & Gowda (1991a,b)	HWA &PT	OP/segments	95.4	0 - 100	0.040 - 0.045	0.22 - 0.25	1.12-1.16
Matsuda et al. (1990)	HWA	CN/round	160	0 - 4			
Fujisawa & Shirai (1989)	PT & HWA	LP/square	60	50 - 150	0.052 - 0.059	0.25 - 0.32	1.20
Davis & Winarto (1980)	HWA	OP/round	170	0 - 65	0.037	0.32	1.15
Swamy & Bandyopadhyay (1975)	HWA	round	71.7	0 - 40	0.046	0.17	1.10
Rajaratnam & Pani (1974)	PT	CN/various	59.5 - 97.5	3 - 70	0.040 - 0.045	0.20 - 0.27	1.00
Newman et al. (1972)	HWA	LP/round	2.8-16.4	20 - 200	0.042	0.28	1.00
Sforza & Herbst (1970)	HWA & PT	OP/rectangular		1 - 350			1.14
Eriksson et al. (1998)	LDA	2D	9.6	5-200	0.078	N/A	1.08
Abrahamsson et al. (1994)	HWA	2D	10-20	70-175	0.075-0.081	N/A	
Karlsson et al. (1992)	LDA	2D	10	5-200	0.075	N/A	

HWA = hotwire anemometry; PIV = particle image velocimetry, LP = long pipe.

CN = contoured nozzle, OP = orifice plate, various = round, rectangular, triangular and elliptic nozzles.

length and velocity scales, respectively. In addition, there is no significant difference in the normalized streamwise mean velocity profiles of 2D and 3D generic turbulent wall jets. Also the wall-normal location of the maximum mean velocity (i.e., y_m) is about 0.16 ~ 0.18$y_{0.5}$ (Abrahamsson et al., 1997; Padmanabham & Gowda, 1991a, b; Fujisawa & Shirai, 1989; Rajaratnam & Pani, 1974). The wall-normal mean velocities in the 3D turbulent wall jet are negative across the jet and have negative gradients. In contrast, the wall-normal mean velocities in the 2D wall jet are positive up to at least the jet half width and then become negative (Abrahamsson et al., 1997; Karlsson et al., 1992).

2.3.1.2 Development of turbulent wall jets

The flow development is usually divided into three fields: the near field, which is associated with the flow before the collapse of the potential core; the intermediate field, which is after the collapse of the potential core but before the jet becomes self-similar; and the far field, where the jet becomes self-similar (Sforza & Herbst, 1970). The potential core is the central portion of the flow in which the velocity remains constant and nearly equal to the jet exit velocity (Ashforth-Frost & Jambunathan, 1996). In the self-similar region, the mean velocities in the streamwise direction, the turbulence intensities and Reynolds shear stresses collapse reasonably well when normalized by the appropriate length and velocity scales. The development of turbulent wall jets is usually examined by studying the decay and spread rates of the jets in the self-similar region.

2.3.1.2.1 Decay rates

The rate at which the maximum velocity (U_m in Fig. 1.1) decays in the streamwise

direction in the self-similar region determines the decay rate of the jet. In the far field, U_m decays according to the following power law: $U_m = ax^{-n}$, where a and n are constants and n is known as the decay rate. Reported values of n vary considerably from n = 1.0 to 1.29 as shown in Table 2.1. For example, Newman et al. (1972) and Law & Herlina (2002), respectively, reported n = 1.00 and 1.07 while Abrahamsson et al. (1997) reported n = 1.29. The reasons for the inconsistencies are not well understood but are often attributed to exit geometry and Reynolds number. Sun & Ewing (2002a, b) investigated the effects of exit geometry and Reynolds number on the decay rate. It was observed that the type of velocity profiles at the exit (i.e., a top-hat profile from a contoured exit or a turbulent profile from a long pipe) affects the development of the 3D turbulent wall jet. More specifically, they observed that the local maximum streamwise velocity from the contoured exit decays faster. However they concluded that there are no Reynolds number effects on the decay rates in the self-similar region. Law & Herlina (2002) also conducted experiments for $5500 \leq Re_j \leq 13700$ but found no Reynolds number effects on the decay rates.

2.3.1.2.2 Spread rates

The spread rate of the jet is determined by the spread of the jet half widths ($y_{0.5}$ and $z_{0.5}$) in the wall-normal and lateral directions. Launder & Rodi (1981, 1983) reviewed earlier turbulent wall jet literature and determined that the wall-normal spread rates in the far-field can be represented by Eqns. 2.1 and 2.2, respectively, for 2D and 3D turbulent wall jets.

$$\frac{dy_{1/2}}{dx} = 0.073 \pm 0.002 \tag{2.1}$$

$$\frac{dy_{1/2}}{dx} = 0.048 \pm 0.003 \tag{2.2}$$

It is evident from the equations that the 3D turbulent wall jet spreads much slower (about 52%) in the wall-normal direction than its 2D counterpart. The smaller spread rate is associated with a large lateral spread rate (Eqn. 2.3). Launder & Rodi (1981, 1983) also determined that the lateral spread rate of a 3D turbulent wall jet can be represented by the following equation:

$$\frac{dz_{1/2}}{dx} = 0.26 \pm 0.002 \tag{2.3}$$

Equations 2.2 and 2.3 clearly demonstrate that the spread in the lateral direction is about 5.4 times as large as it is in the wall-normal direction. This anisotropic spread rate is an intriguing characteristic of the 3D turbulent wall jet.

As shown in Table 2.1, there is considerable scatter among the reported 3D turbulent wall jet spread rates. It has been suggested that the spread rates may also depend on the exit geometries and Reynolds numbers. A number of studies have been conducted to verify this. Rajaratnam & Pani (1974) found that the lateral spread rate from a square geometry was about 30% higher than that from a circular geometry, while the wall-normal spread rates were the same. Similarly, Padmanabham & Gowda (1991a, b) found that the lateral and wall-normal spread rates of jets from segments of a circle were about 8% and 12%, respectively, larger than those from the circular jet exit. In a later study, Abrahamsson et al. (1997) observed that the spread rates from top-hat profiles

were approximately 15% to 20% larger than those from fully developed pipe flows. Sun & Ewing (2002a, b) also found that beyond x/d = 10, the wall-normal and lateral spread rates from a top-hat profile are approximately 0.05d and 0.24d larger than those from a fully developed pipe flow. The effect of Reynolds number on the spread rates has also been studied. Newman (1972) reported no significant change in the lateral spread rate when the jet exit Reynolds number (Re_j) was increased from 2800 to 16400. Sun & Ewing (2002a, b) investigated Reynolds number effects for Re_j = 65000 and 108000 while Law & Herlina (2002) conducted studies in the range $5500 \leq Re_j \leq 13700$ and both found no Reynolds number effects on the spread rates.

The ratio of the lateral to wall-normal spread rates of the studies summarized in Table 2.1 range widely from 3.7 (Swamy & Bandyopadhyay, 1975) to 8.6 (Davis & Winarto, 1980). The mechanism responsible for the large lateral spread rate of 3D turbulent wall jets is not fully understood. Launder & Rodi (1983) argued that the large lateral spread is caused by mean secondary flow in the 3D turbulent wall jet and examined the transport equation for the mean streamwise vorticity, Ω_x, for an incompressible flow (Eqn. 2.4). They proposed that the vorticity production by vortex-line bending term (term C) is the source of the streamwise vorticity in 3D turbulent wall jet.

$$\underbrace{\frac{D\Omega_x}{Dt}}_{A} = \underbrace{\Omega_x \frac{\partial U}{\partial x}}_{B} + \underbrace{\Omega_y \frac{\partial U}{\partial y} + \Omega_z \frac{\partial U}{\partial z}}_{C} + \underbrace{\frac{\partial^2}{\partial y \partial z}\left(u^2 - w^2\right)}_{D} + \underbrace{\left(\frac{\partial^2}{\partial z^2} - \frac{\partial^2}{\partial y^2}\right)uw}_{E} + \underbrace{\nu\left(\frac{\partial^2 \Omega_x}{\partial x^2} + \frac{\partial^2 \Omega_x}{\partial y^2} + \frac{\partial^2 \Omega_x}{\partial z^2}\right)}_{F} \tag{2.4}$$

where $\Omega_x = \frac{\partial V}{\partial z} - \frac{\partial W}{\partial y}; \quad \Omega_y = \frac{\partial W}{\partial x} - \frac{\partial U}{\partial z}; \quad \Omega_z = \frac{\partial U}{\partial y} - \frac{\partial V}{\partial x}$ (2.5)

and $\frac{D}{Dt} = \frac{\partial}{\partial t} + U\frac{\partial}{\partial x} + V\frac{\partial}{\partial y} + W\frac{\partial}{\partial z}$ (2.6)

For a steady flow the time derivative ($\partial/\partial t$) is zero and the meaning of each term in the equation represented by letters A to F is as follows:

A: Transport of streamwise vorticity by the mean flow

B: Streamwise amplification of mean vorticity by vortex stretching

C: Vorticity production by vortex-line bending

D: Vorticity production by gradients in Reynolds normal stresses

E: Vorticity production due to gradients in Reynolds shear stresses

F: Vorticity destruction by viscous diffusion

Term C can further be expanded as

$$\Omega_y \frac{\partial U}{\partial y} + \Omega_z \frac{\partial U}{\partial z} = \frac{\partial W}{\partial x}\frac{\partial U}{\partial y} - \frac{\partial V}{\partial x}\frac{\partial U}{\partial z} \quad (2.7)$$

Using scaling argument, Launder & Rodi (1983) concluded that in the far field the first term on the right of Eqn. 2.7 is dominant. The term $\partial W/\partial x$ is always negative since the mean velocity decreases with distance from jet exit. In the inner layer, $\partial U/\partial y$ is positive resulting in a net negative streamwise vorticity source; however, $\partial U/\partial y$ is negative in the outer layer. Thus the vorticity source is a net positive. Based on this argument they depicted the source of the streamwise vorticity as shown in Fig. 2.1. This arrangement induces a laterally outward secondary motion which causes the larger lateral spread of 3D turbulent wall jet (Launder & Rodi, 1983).

Launder & Rodi (1983) also recognized that the source of streamwise

vorticity could be the gradients in the Reynolds stresses (Terms D and E in Eqn. 2.4) akin to the secondary flows in turbulent flows in straight square ducts. However, they concluded that the production of streamwise vorticity due to gradients in the normal stresses (Term D in Eqn. 2.4) would serve to reinforce the secondary flow due to vortex-tilting in the far-field. To further explore the spreading mechanism in 3D wall jets, Craft & Launder (2001) studied the 3D turbulent wall jet computationally and confirmed that the additional source driving the mean streamwise vorticity in the 3D turbulent wall jet is due to gradients in the Reynolds normal stresses (Term D in Eqn. 2.4). There are neither reported experimental data nor DNS/LES on the complete Reynolds stresses to quantify the contribution of the gradients in the Reynolds shear stress (Term E in Eqn. 2.4) to the generation of streamwise vorticity in 3D wall jets.

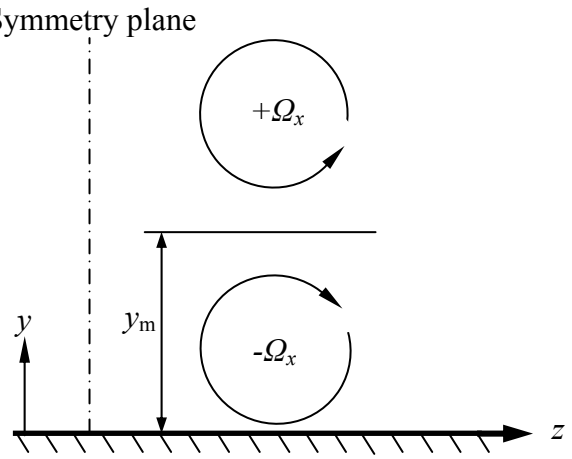

Figure 2.1: Streamwise mean vorticity generation proposed by Launder & Rodi (1983) for the far field of the 3D turbulent wall jet

Lida & Matsuda (1988) obtained both components of the mean streamwise

vorticity in the near-field and observed two regions of counter-rotating mean streamwise vorticity on each side of the jet symmetry. In addition, they observed that two regions that were initially by each other diverged from the jet symmetry as the jet evolved downstream and the outer regions appeared to deflect from the wall. Ewing & Pollard (1997) later proposed that the source of the inner regions of streamwise vorticity obtained by Lida & Matsuda (1988) was the quasi-periodic passage of smaller horseshoe structures created when the bottom of the ring structures formed at the nozzle exit lifted from the wall. This is depicted in Fig. 2.2. In a more recent experimental study, Hall (2005) examined large scale structures in the three-dimensional wall jet using concurrent measurements of the fluctuating wall pressure, and the streamwise and lateral components of the turbulent velocity at a point. His results also revealed two pairs of streamwise mean vorticity (i.e., $\Omega_x \approx \partial W/\partial y$) on either side of the jet symmetry.

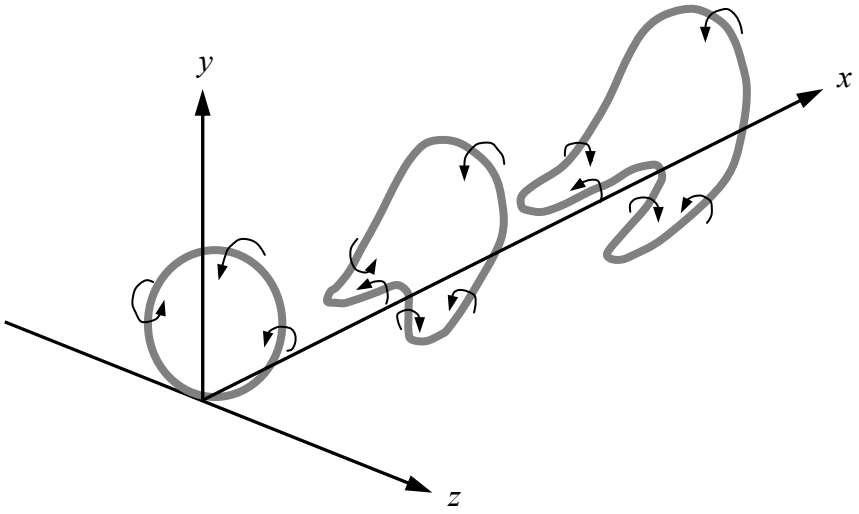

Figure 2.2: The structure of vortices in the near to intermediate fields proposed by Ewing & Pollard (1997).

2.3.1.3 Turbulence statistics

2.3.1.3.1 Turbulence intensities and Reynolds stresses

The turbulence intensities of turbulent wall jets exhibit similarity when U_m and $y_{0.5}$ or $z_{0.5}$ are used as velocity and length scales, respectively. The streamwise turbulence intensities in the x-y plane at $z = 0$ have double peaks, one each in the inner and outer layers compared to a single peak for canonical boundary layers. The peak values of the turbulence intensity of wall jets are generally higher than values reported for boundary layers. For example, the peak values of the streamwise turbulence intensities in 2D wall jets (Karlsson et al., 1992; Venas et al., 1999) and a 3D wall jet (Venas et al., 1999) are typically 20% and 27%, respectively, compared with 16% for boundary layers. Unlike boundary layers, the streamwise and wall-normal turbulence intensities are positively correlated; and as a result, the Reynolds shear stress in the x-y plane, uv, is positive compared with the negative values reported in boundary layers. Another important observation is that in the 2D and 3D turbulent wall jets, uv, is negative close to the wall ($y < 0.10y_{0.5}$) and positive in the region $y > 0.10y_{0.5}$ (Swamy & Bandyopadhayay, 1981; Padmanabham & Gowda, 1991a, b; Abrahamsson et al., 1997; Karlsson et al., 1992). This change of sign closer to the wall than the location of maximum mean velocity is attributed to the strong interaction between the outer and inner layers of the turbulent wall jet, and poses a challenge to turbulence models that are based on the eddy viscosity concept such as k-epsilon and k-omega models. For example, since $\partial U/\partial y$ is positive in the inner region ($y \leq 0.18y_{0.5}$), there exists a region ($0.10y_{0.5} \leq y \leq 0.18y_{0.5}$) where the eddy viscosity, $\nu_t = -uv/(\partial U/\partial y)$, is negative.

2.3.1.3.2 Energy budget terms and triple velocity products

For a steady turbulent flow, the transport equation for the turbulent kinetic energy is:

$$U_j \frac{\partial k}{\partial x_j} = -u_i u_j \frac{\partial U_i}{\partial x_j} - \nu \frac{\partial u_i}{\partial x_j}\frac{\partial u_i}{\partial x_j} + \frac{\partial}{\partial x_i}\left(-\frac{1}{\rho} p u_i - k u_i\right), \qquad (2.8)$$

where the term on the left hand side is the convection by the mean flow, and the first, second and third terms on the right hand side are, respectively, the production, dissipation rate and diffusion terms. The individual terms in the transport equation for the turbulence kinetic energy are also hardly reported for 3D turbulent wall jets. Padmanabham & Gowda (1991a, b) and Swamy & Bandyopadhyay (1981) reported an approximate production term $\{P_k = -(uu - vv)\partial U/\partial x - uv\partial U/\partial y\}$ in the x-y plane at $z = 0$. They observed that the major contributor is $uv\partial U/\partial y$ which is negative in the inner layer where the shear stress changes sign ($y \leq 0.10y_{0.5}$). Abrahamsson et al. (1997) reported the most comprehensive analysis of the turbulence kinetic energy budget. Their results include the production, advection, dissipation and diffusion terms. Consistent with previous studies, they concluded that the term $uv\partial U/\partial y$ is the major contributor to the production term in the turbulence kinetic energy transport equation. They also observed that the distribution of the turbulence kinetic energy budget in 3D wall jets is similar to that in 2D. However, there is larger advection by mean flow in the 3D wall jet. It was also observed that the streamwise component of the advection is much larger than the wall-normal component. This was attributed to the rapid mean flow decay and the small wall-normal mean velocity.

The triple velocity products are important quantities in turbulent flows and more

especially to turbulence modeling. This is because the gradients of the triple velocity products constitute the turbulence diffusion terms in the transport equations for the turbulence kinetic energy (Eqn. 2.8). For example, $\partial(u^3 + uv^2 + uw^2)/\partial x$ is associated with the transport of the turbulence kinetic energy ($u^2 + v^2 + w^2$) in the streamwise direction. Similarly, $\partial(u^2v + v^3 + vw^2)/\partial y$ is associated with the transport of the turbulence kinetic energy ($u^2 + v^2 + w^2$) in the wall-normal direction. In spite of their significance to the turbulence modeling community, the triple velocity products and other higher order moments are rarely reported in turbulent wall jets studies. In their 2D wall jets study, Irwin (1973) reported six velocity products (u^3, u^2v, uv^2, v^3, uw^2 and vw^2). The profiles are nearly anti-symmetric and change sign at $0.7 < y/y_{0.5} < 0.8$, which is closer to the wall than the position of the maximum Reynolds shear stress, uv ($y/y_{0.5} \approx 0.8$). For the 3D turbulent wall jets, Abrahamsson et al. (1997) reported profiles of some triple velocity products (u^2v and v^3 in the x-y plane at $z = 0$; and u^2w and w^3 in the x-z plane at $y = y_{max}$) and diffusion terms {$\partial(u^3)\partial x$, $\partial(u^2v)\partial y$, $\partial(v^3)\partial y$, and $\partial(u^2w)\partial y$ in the x-y plane at $z = 0$}. They concluded that the diffusion term redistributes energy from the central part of the flow towards the wall and the outer-most flow region.

This thesis reports the turbulence energy budget terms and triple velocity products in the symmetry plane only. This is because there is a lot of scatter in these quantities in the lateral (x-z) plane measured at $y = y_m$ and it was decided not to report them here. More specifically, the production (P_k), dissipation (ε_k), and advection (C_k) terms of the turbulence kinetic energy transport equation are reported. The terms are estimated directly from the 2D PIV data using the following expressions:

$$P_k = -u^2\partial U/\partial x - uv\partial V/\partial x - uv\partial U/\partial y - v^2\partial V/\partial y \qquad (2.9)$$

$$C_k = U\partial(u^2 + v^2)/\partial x + V\partial(u^2 + v^2)/\partial y \qquad (2.10)$$

$$\varepsilon_k = \nu[2(\partial U'/\partial y \cdot \partial V'/\partial x) + (\partial U'/\partial y)^2 + (\partial V'/\partial x)^2$$
$$\cdots + 2(\partial U'/\partial x)^2 + 2(\partial V'/\partial y)^2 + 2(\partial W'/\partial z)^2] \qquad (2.11)$$

Because the lateral velocity was not measured simultaneously with streamwise and normal velocities, the last term in the expression for ε_k was estimated from the continuity equation for the fluctuating velocity components as follows: $(\partial W'/\partial z)^2 = (\partial U'/\partial x + \partial V'/\partial y)^2$. The diffusion term was also estimated, however, it is not reported because the data showed considerable scatter. In addition to the quantities from the above equations, the triple velocity products including u^3, u^2v, uv^2, v^3 are presented.

2.3.2 Turbulent offset jets

Before discussing offset jets, it is worthwhile to briefly consider the general case of separated flows in order to provide background knowledge necessary to interpret the characteristics of the offset jets. The most comprehensive review of separated flows is provided by Simpson (1976) covering separation due to a variety of conditions including separation from sharp-edge bluff bodies as in backward facing steps (BFS). As mentioned earlier, flows over BFS are akin to the offset jet and therefore of interest to this study. A detailed review of turbulent flows over BFS was performed by Eaton & Johnson (1981). The following is a summary of the general pattern of flows over BFS.

The dividing streamline in flow over BFS is slightly curved in the first half of the separated region but curves more sharply close to the reattachment point. At reattachment, some of the fluid in the shear layer is deflected upstream by strong adverse

pressure gradient into the reverse flow. Etheridge & Kemp (1978) determined that roughly 17% of the mass flow was deflected upstream. Also a new shear layer begins to develop after reattachment. For the turbulence quantities, Etheridge & Kemp (1978) showed that the wall-normal turbulence intensities are at least the same as the streamwise turbulence intensities in the reverse flow region. Based on their results, Aung (1983) argued that the Reynolds shear stress distribution has maximum values close to the dividing streamline, which increase with downstream location to a peak at the reattachment point. The peak can be up to 20 times the value at the step but sharply decrease downstream of reattachment. The separation zone fluctuates so that the reattachment point of the shear layer is unstable and moves upstream and downstream. The maximum backflow velocity is usually more than 20% of the freestream velocity (Eaton & Johnson, 1981). A primary characteristic of BFS flows is the reattachment length (x_r). Aung (1983) stated that the following flow conditions influence x_r: (i) adverse pressure gradients appear to increase x_r; (ii) sufficiently high Reynolds number makes the entire boundary layer turbulent and x_r becomes independent of Reynolds number; and (iii) increase in the initial boundary layer thickness or freestream turbulence appear to decrease x_r.

Having summarised the pertinent characteristics of flows over BFS, attention is now turned to offset jets. Compared to the generic turbulent wall jets, turbulent offset jets have not been studied in great detail. Most of the previous investigations were performed for 2D and primarily focused on the reverse flow region (Fig. 1.2). A summary of the relevant previous experimental studies is provided in Table 2.2. In the table, $(x/d)_m$ is the maximum downstream measurement range. The other symbols are

Table 2.2: Summary of relevant turbulent offset jet literature

Authors	Technique		h/d	$Re_j/1000$	$(x/d)_m$	x_r/d	Quantities reported
Gao & Ewing (2007, 2008)	HWA, Ptap	2D	0.7 – 1.5	44	18	0.60-5.04	*sp*, *U*, *V*, *u*, *v*, *uv*, ρ_{pp}, ρ_{pu} ρ_{pv}
Tsunoda et al. (2006)	PIV		7.5 - 30	2.5	30	15 - 45	*U*, *u*, *v*
Nasr & Lai (1997, 1998)	LDA, Pprobe		2.13	11	20	4.65	*sp*, *U*, *V*, *u*, *v*, *uv*
Pelfrey & Liburdy (1984,1986a,b)	LDA		7.00	15	19	13	*U*, *V*, *u*, *v*, q^2
Lund (1986)	Ptap		0.69-21.80	20*		0.97-35.8	*sp*
Hoch & Jiji (1981)	HWA, Ptap		3.00-8.70	2.7-18.2	60		*sp*, *U*
Rajaratnam & Subramanya (1968)	PT, Ptap		1.0-6.5	50.4-99.2	78	3.7-14.5	*sp*, *U*
Sawyer (1960, 1963)	PT, Ptap		4.15-24.40	95	51	9.34-35.6	*sp*, *U*
Bourque & Newman (1960)	Ptap		4.0-48.5	1.65-10.5*	137	10-60.5	*sp*
Nozaki et al. (1979, 1981, 1983)	HWA, Ptap	3D	0.8-10	10-70	35	1.2-25	*sp*, *U*
Davis & Winarto (1980)	HWA		1.0-4.0	170	64		*U*, *V*, *u*, *v*, *uv*, l_m, spectra
McRee & Moses (1967)	Ptap		2-10	2-12*	22	6-32	*sp*

sp = static pressure
Ptap = pressure taps
Pprobe = pressure probe
$q^2 = (u^2 + v^2)$
l_m = mixing length
ρ_{pp}, = correlation coefficient of the fluctuating wall pressure
ρ_{pu} = correlation coefficient of the fluctuating wall pressure and the streamwise fluctuating velocity
ρ_{pv} = correlation coefficient of the fluctuating wall pressure and the wall-normal fluctuating velocity
* $Re_j = (2\Delta P/\rho)^{1/2}/(d/\nu)$, ΔP is pressure across jet exit
$(x/d)_m$ is the maximum downstream measurement location

either defined earlier or below the table. As the table shows, most of the studies were performed with HWA and Pitot tubes. The majority of these studies involved jets with large offset heights ($h/d > 5$). The few studies with small offset heights ($h/d < 5$) include Lund (1986), and Gao & Ewing (2007, 2008).

The 3D turbulent offset jet studies are rare as shown in the table. Of these, only the study by Davis & Winarto (1980) has a circular jet exit, while the rest have rectangular jet exits. This review will categorize information from the various studies into the three main regions of the offset jets namely the reverse flow, attachment and wall jet regions. The reported turbulent quantities will also be briefly reviewed.

2.3.2.1 Reverse flow region

As mentioned earlier, the reverse flow region extends from the jet exit to the point of reattachment (x_{rp}). Pelfrey (1984) defined x_{rp} as the location at which the mean velocity gradient at the wall was zero when averaged over a sufficiently long time period. Other researchers defined the x_{rp} as the point of maximum wall static pressure (Sawyer, 1960; Kumada et al., 1973; Nasr & Lai, 1998). The reattachment point is defined in this thesis as the location where the mean streamlines reattach to the wall.

One important characteristic of the shear layer in the reverse flow region is the reattachment length, x_r. One of the primary objectives of most of the offset jet studies is to determine x_r. There is a general agreement in most of the studies that x_r increases with the offset height, h. Bourque & Newman (1960) observed that x_r approached a constant value for large h and obtained the limiting values of $h/d \approx 35$. Nasr & Lai (1997) obtained $x_r/d \approx 4.7$ for $h/d \approx 2.13$. In addition, they used their own data and the data of other

researchers (Perry, 1967; Nozaki et al., 1979, 1981; Pelfrey & Liburdy, 1986a, b) to develop the following power law relation: $x_r/d = 2.63(h/d)^{0.855}$, which is valid for $h/d <$ 20. More recently, Gao & Ewing (2007) determined $x_r/d \approx 0.6$ to 5 for jets with $h/d = 0.7$ to 1.5 which is not consistent with the power law expression developed by Nasr & Lai (1997). In fact, the later values are approximately 15% larger than those reported by Lund (1986).

For the 3D offset jets only Nozaki et al. (1979, 1981) reported x_r values. They observed that x_r depends on the nozzle geometry and showed that for a nozzle aspect ratio (AR) of AR < 3, x_r increases with decreasing AR and more so at high h/d. However, for AR $\geq$ 3, x_r does not change with AR irrespective of h/d. For the 3D offset jet from a square nozzle, Nozaki (1983) reported $x_r/d \approx 3.8$, 6.7, and 9.9 for $h/d = 1.5$, 2.5, and 3.5, respectively, which are in agreement with the power law approximation developed by Nasr & Lai (1997).

2.3.2.2 Attachment region

The attachment region stretches from the attachment point to the beginning of the wall jet region (Fig. 1.2). In this region, the flow has features qualitatively akin to other reattaching shear layer flows. Rajaratnam & Subramanya (1968) described this region as the characteristic decay region, where the rate of decay of the maximum mean velocity is a function of the offset height. The development of the jets after reattachment is usually studied by examining the changes in U_m, and the outer jet half width, $Y_{0.5}$ (Fig. 1.2) with x/d. Gao & Ewing (2007) concluded that the attachment region is characterized by a rapid decrease in U_m and an increase in $Y_{0.5}$, which suggest transition of the flow from an offset

jet to a wall jet. Furthermore, the structures in both the attaching shear layer and the wall jet regions are three-dimensional in nature (Gao & Ewing, 2007). Nasr & Lai (1998) also reported that downstream of the reattachment point, the velocity decay rate is much slower than a free jet but higher than that of the wall jet. However, for h/d = 7 the velocity decay increases downstream of the reattachment point because of stronger collision of the jet centreline with the wall and conversion of the static pressure into velocity momentum (Pelfrey & Liburdy, 1986a, b).

2.3.2.3 Wall jet region

Far downstream of the jet exit, the offset jet ultimately develops into a generic wall jet. This region is described as the classical wall jet decay region, where the decay rate is the same as that of the classical wall jet (Rajaratnam & Subramanya, 1968). Kumada et al. (1973) stated that in the wall jet region the gradient of the velocity decay is equal to that of the generic wall jet regardless of h/d. Hoch & Jiji (1981) reported measurements of the maximum velocity decay, which is in good agreement with results reported by Rajaratnam & Subramanya (1968).

As shown in Table 2.2, Davis & Winarto (1980) reported the most detailed results in the wall jet region of the 3D offset jet. Their results revealed that the wall-normal spread rate does not vary significantly with offset height if $h/d \leq 2$. For example, for h/d = 1.0 and 2.0, $dy_{0.5}/dx$ = 0.036 and 0.039. For these relatively small offset heights, the spread rate is not significantly different from a value of $dy_{0.5}/dx$ = 0.037 reported for their generic wall jet. For a larger offset height of h/d = 4.0, $dy_{0.5}/dx$ increased to 0.046. For the lateral spread rate, values of $dz_{0.5}/dx$ = 0.33, 0.29 and 0.23 were reported, respectively, for

h/d = 1.0, 2.0 and 4.0. The corresponding values of $(dz_{0.5}/dx)/(dy_{0.5}/dx)$ for h/d = 1.0, 2.0 and 4.0 are, respectively, 9.2, 7.4 and 5.0. The value of 9.2 obtained for h/d = 1.0 is not significantly different from 8.6 for their generic wall jet. However, it is important to note from Table 2.1 that $dy_{0.5}/dx$ values reported by Davis & Winarto (1980) are much lower than those reported in other 3D wall jets while their $dz_{0.5}/dx$ is larger than in most of the other previous studies. Thus, although the value of $(dz_{0.5}/dx)/(dy_{0.5}/dx)$ = 9.2 for h/d = 1.0 is not significantly different from 8.6 for their generic wall jet, it is almost twice as large as reported in the other generic 3D wall jet experiments.

2.3.2.4 Turbulent quantities

Thus far only the mean quantities have been reviewed. As can be seen in Table 2.2, the majority of the studies focussed on the mean flow quantities. However, the more recent works reported turbulent quantities (e.g., Gao & Ewing, 2007, 2008; Nasr & Lai, 1997, 1998; Pelfrey & Liburdy, 1986a, b; and Davis & Winarto, 1980). For the 2D offset jet studies, the turbulent quantities were reported for only a limited downstream distance (up to 20 nozzle heights). Meanwhile, the 3D offset studies (Davis & Winarto, 1980) reported turbulent quantities up to 32 nozzle diameters. The turbulence intensities and Reynolds shear stresses are the most commonly reported but the triple products or the terms in the transport equation of the turbulence kinetic energy are not reported. The focus of this section is to summarize the previous results of the turbulence intensities and Reynolds shear stresses.

The results of Pelfrey (1984) showed that there are significant differences in the turbulence intensities along the upper and lower sides of the dividing streamline. They

reported that unstable characteristics due to entrainment in the outer region of the jet increased the turbulence intensities along the upper and lower sides of the dividing streamline. Furthermore, the turbulence intensities within the reverse flow region are relatively uniform with slightly larger values below the center of recirculation (or reverse flow) where the mean velocity is negative. According to Nasr & Lai (1997,1998), the streamwise evolution of the profiles of turbulence intensities and Reynolds shear stress indicate that the offset wall jet has significant retarding and suppression effects on the turbulence field in the reverse flow and reattachment regions. In addition, the locations of maximum turbulence intensities and Reynolds shear stress in the inner shear layer occur in the vicinity of the dividing streamline and immediately upstream of the reattachment point. This indicates strong interactions between the flow in the reverse flow zone and the inner shear layer flow in the vicinity of the reattachment point. These characteristics are similar to those found in separated and reattached flows (Eaton & Johnson, 1981). Gao & Ewing (2007) reported that the magnitude of the turbulent fluctuations in the inner shear layer increased downstream to the reattachment point and then decreased due to the interaction with the wall. The fluctuations in the inner shear layer near the reattachment location increased as the initial offset height of the jet increased.

Nozaki et al. (1981) examined the effects of exit turbulence levels on the flow dynamics and found that for levels greater than 6%, the flow is independent of exit turbulence levels. The turbulence intensities reported by Davis & Winarto (1980) have peak values that increase monotonically with x/d to peak values of 20% and 24% at $x = 32d$ for $h/d = 2$ and 4, respectively. The turbulence intensities in the region $x/d < 32$ also do not collapse.

2.4 Multi-point Statistics

Turbulence is characterized by disorderly fluctuations in time and three-dimensionality in space. However, it is generally accepted that there are repeating patterns of motion or organised motions (also known as coherent structures) embedded in turbulent flows. These coherent structures possess a substantial portion of the total turbulence kinetic energy (Hammad & Milanovic, 2009). Identifying these coherent structures is a challenge in part because they are buried in massive and chaotic data. In this thesis the proper orthogonal decomposition (POD) is employed to study the energy distribution and the role of the large structures in the 3D turbulent offset flows. In addition, the two-point velocity correlations are employed to examine the distances over which the turbulence field is correlated across the shear layer. It is, therefore, imperative to provide a brief overview of the two-point velocity correlation and POD techniques. Detailed implementation of the POD technique is described in Appendix A.

2.4.1 Two-point velocity correlations

Following Volino et al. (2007), the two-point correlation functions are defined for two arbitrary quantities A and B in a plane at reference points separated by Δr_1 and Δr_2 as follows:

$$R_{AB} = \langle A(r_1, r_2)\, B\,(r_1+\Delta r_1, r_2+\Delta r_2)\rangle / \sigma_A\, \sigma_B, \qquad (2.12)$$

where σ_A and σ_B are the standard deviations of A and B , respectively, at (r_1, r_2) and $\langle\cdots\rangle$ denotes the average. In this study, σ_A and σ_B represent the turbulence intensities, while A and B are the fluctuating velocities. In the x-y plane, for example, σ_A and σ_B are,

respectively, the streamwise (u) and wall-normal (v) turbulence intensities while A and B are the streamwise (u') and wall-normal (v') fluctuating velocities, respectively. It should be noted that Eqn. 2.12 can also apply to the autocorrelations. These are denoted by R_{AA} or R_{BB}.

As mentioned earlier, two-point correlation can be used to determine the distances and times over which the turbulence field is correlated across the flow. It can also be used to estimate the integral as well as the Taylor micro length and time scales. For example, the area under the two-point velocity correlation curve is often interpreted as the integral length scale. Two-point correlations have been used to study offset and wall jets previously.

Hall (2005) applied the two-point, two-time correlation of fluctuating wall pressure as well as fluctuating wall pressure and velocity to wall jets in rectangular channels. The results revealed that the pressure fluctuations are well correlated laterally across only one side of the jets suggesting lack of symmetry in the coherent structures. The results also showed that the correlations are larger for the jet from square channel than rectangular channel suggesting that there are more spatial and temporal variability in the passage of coherent structures in the jet from a square channel.

In a more recent study, Gao & Ewing (2007) used pressure-velocity correlations to reveal that large scale structures in the attaching shear layers are convected along the the wall after the jet attaches to the wall. Further examination revealed larger structures in the outer jet region, and smaller structures near the wall. The results show that the smaller structures from the attaching shear layer are convected downstream faster than the larger outer structures causing the inner structure to approach the slower moving outer structure.

The correlations suggest that the large and small scale structures merge and travel downstream together in the wall jet region similar to those observed in planar wall jet.

The two-point correlation has been used more extensively in boundary layer studies to quantify the average extent and shape of the hairpin-like vortex packets. For example, the angle of inclination of the spatial autocorrelation in the streamwise direction, $R_{uu}(x)$, can be interpreted as the average inclination of the hairpin packets (Volino et al., 2007). Based on DNS data, Moin & Kim (1985) concluded that the two-point correlations strongly support a flow model with hairpin-like vortices inclined at 45^o to the wall in a channel flow. They also found that the size of vortices increased with wall-normal location. The angles of inclination of R_{uu} can be estimated by fitting least-squares through points farthest away from the self-correlation peak at different contour levels. Christensen & Wu (2005) determined that, for turbulent channel flow, the hairpin-like vortex packets are inclined at an angle of 11^o to the channel wall. Their results are in good agreement with values of 12^o to 13^o reported by Christensen & Adrian (2001) for turbulent boundary layers at Reynolds numbers based on friction velocity of $Re_\tau = 547$ to 1734. In an earlier study, Head & Bandyopadhyay (1981) reported inclination angles between 15^o and 20^o for $500 < Re_\theta < 17500$, where Re_θ is the Reynolds numbers based on momentum thickness. More recently, Tomkins & Adrian (2003) reported angles between 10^o and 20^o at $Re_\theta = 1015$ and 7705, respectively. The results from the experimental studies show that, for canonical turbulent flows, the inclination of the hairpin-like vortex packets is approximately $15^o \pm 5^o$.

2.4.2 Proper orthogonal decomposition

As mentioned in Chapter 1, proper orthogonal decomposition (POD) is a statistical technique for extracting energetically dominant modes in a flow. It decomposes a series of data into an optimal set of basis functions, which is also called an eigenfunction or orthogonal function (Holmes et al., 1996). It has been argued that POD is the most efficient technique for extracting the most energetic components of an infinite dimensional process with only a few modes (Adrian et al., 2000 and Holmes et al., 1996). Proper orthogonal decomposition requires multi-points measurements such as data from PIV or hotwire rakes.

Proper orthogonal decomposition has been used in various disciplines that include fluid mechanics, oceanography, and image processing (Cizmas et al., 2003). Comprehensive reviews of the application of POD to turbulent flows can be found in Holmes et al. (1996), and Gordeyev (1999). Depending on the discipline, the same procedure for implementing POD goes by different names such as Karhunen-Loeve decomposition, principal components analysis, singular systems analysis, and singular value decomposition (Holmes et al., 1996). Proper orthogonal decomposition was first introduced to the field of fluid turbulence by Lumley (1967) as an unbiased method for extracting structures in a turbulent flow (Holmes et al., 1996). Lumley (1967) defined coherent structures in terms of the eigenfunctions with the associated turbulent kinetic energy (Hammad & Milanovic, 2009) and frame it as a maximization problem that results in an integral equation with fixed limits. This equation is also known as the Fredholm type integral equation with the correlation tensor as the kernel. The direct method of POD involves solving this equation (Shinneeb, 2006). Detailed presentation of the direct

method was reported by Shinneeb (2006) and Kostas (2002).

Sirovich (1987) argued that when the resolution of the spatial domain (M) is higher than the number of observations (N), computation by the direct method becomes inefficient. This is because the direct method requires $O(M^3 + M^2N)$ operations for completion. This is the case for PIV data where a large number of vectors can be obtained in each velocity field. A more computationally efficient technique called the snapshot method was introduced by Sirovich (1987). The snapshot method requires $O(N^3 + N^2M)$ for convergence. This method is simply a numerical technique which can compute the empirical eigenfunctions efficiently and give an equivalent solution to the direct method (Sirovich, 1987). Graftieaux et al. (2001) compared the direct and snapshot methods for unsteady turbulent swirling flows and found no significant differences in their results. The snapshot method is the technique employed in this study and its implementation is described in detailed in Appendix A. Breuer & Sirovich (1991) observed that as the number of snapshots increases, the computed energy spectra approaches the analytical spectra and the fidelity of the snapshot procedure improves. They also demonstrated that if $N > M$, spurious eigenvalues would be generated, however, if $N < M$, all the eigenvalues would provide valid approximation to the analytical spectra.

One of the earliest applications of POD to turbulent flows was by Bakewell & Lumley (1967), who applied POD to a fully developed turbulent pipe flow. Subsequently, POD has been implemented in many types of flows including free jets (Shinneeb, 2006; Bi et al., 2003; Zhou & Hitt, 2004; Gamard et al., 2004; Sakai et al., 2006a, b, Gordeyev & Thomas, 2000; 2002; Meyer et al., 2007; Iqbal & Thomas, 2007), channel flows

(Reichert et al., 1994; Sen et al., 2007; Moin & Moser, 1989), boundary layer flows (Alfonsi & Primavera, 2007; Orrelano & Wengle, 2001), backward facing step flow (Kostas et al., 2002, 2005), and 3D turbulent wall jet (Hall & Ewing, 2005, 2007). Kostas et al. (2002, 2005) used POD to reveal the presence of vortical structures throughout the shear layer. They found more irregular structures at downstream locations than upstream locations which suggested that there is an increase in turbulent interactions with downstream distance. Low order representations of the turbulence intensities and Reynolds shear stresses suggest that large scale structures contribute more to u^2 and $-uv$ than v^2 in the flow downstream of reattachment. For Reynolds numbers (based on the step height and freestream velocity) of 580 and 4660, they found that the structure of the smaller scales depend strongly on Reynolds number whereas the larger scales do not.

Although POD has been extensively employed to study the role of large scale structures in turbulent free jets and near-wall turbulent flows, only a few applications of POD to wall jets are available in the literature. Hall (2005) applied POD of a fluctuating pressure field to 3D turbulent wall jets. The results showed that a substantial portion of energy was contained in structures associated with high frequencies near the centreline of the jet. Reconstructions of the fluctuating pressure field revealed poor correlation of the pressure across the jet. This was attributed to the effect of comparable levels of energy captured by the first symmetric and antisymmetric POD modes.

2.5 Summary of the Literature

In this chapter, the relevant experimental studies on the generic turbulent wall and offset jets are reviewed. It is evident from the literature review that despite the extensive

investigations of the turbulent generic 3D wall jets, discrepancies still exist in the body of knowledge. For example, inconsistencies exist even in the mean flow quantities such as maximum velocity decay and the spread rates. In addition, the mechanism responsible for the larger lateral spread rate of the 3D turbulent wall jet is not well understood. Furthermore, only a few studies reported comprehensive datasets that would provide a useful guide to the development of accurate turbulence models for 3D wall jets.

The literature also shows that there have been a number of experimental investigations on 2D turbulent offset jets. These studies included the measurements of static pressure distributions and mean velocity profiles using Pitot tubes, hotwires, and laser Doppler anemometry as well as investigation of the effect of offset ratio on the reattachment point. However, 3D offset jets have not attracted the attention that their 2D counterparts have. Detailed velocity measurements of 3D offset jets, especially using multi-point measurement techniques is nonexistent in the open literature. The most comprehensive 3D offset jet study to date is that by Davis & Winarto (1980). In that study, hotwires were employed to measure the mean and turbulent quantities at a Reynolds number of 170000. However, the study reported only profiles of the mean velocities up to 64d and the turbulence intensities and Reynolds shear stresses up to 32d. In addition, iso-contours of the mean velocities were reported in the plane perpendicular to the flow direction. The study provided insight into the nature of 3D offset jets.

The overall goal of this study is to advance physical understanding of 3D turbulent wall and offset jets, and provide more comprehensive experimental data sets that will be useful for validating future turbulent models. The specific objective is to examine and document the evolution and structures of 3D turbulent offset jets at more

extended downstream distances using the generic 3D wall jets at the same Reynolds numbers as the basis of comparison. This is achieved by using a high resolution PIV to perform velocity measurements at three Reynolds numbers and four offset heights. The velocity data would then be analyzed using (i) mean velocities and one-point statistics such as turbulence intensities, Reynolds stresses, triple velocity products and some terms in the transport equations for the turbulence kinetic energy, (ii) two-point velocity correlations to study how the turbulence quantities are correlated as well as the length scale and angle of inclination of the hairpin-like vortex structures, and (iii) proper orthogonal decomposition to examine the energy distribution and the role of the large scale structures on the Reynolds stresses and turbulence production.

CHAPTER 3

EXPERIMENTAL SETUP AND MEASUREMENT PROCEDURE

In this chapter, an overview of the offset jet test facility, the PIV system, and measurement procedure is reported. The principles and various components of PIV are discussed in detail in Appendix B. This is followed by a description of the experiments and summary of the tests conditions. The chapter concludes with a summary of estimated measurement uncertainties. Detailed uncertainty analysis in PIV is reported in Appendix C.

3.1 Experimental Setup

Figure 3.1 shows a schematic of the jet test facility used in this study. The length (L), height (H) and breadth (B) are, respectively, L = 1000 mm, H = 300 mm, and B = 500 mm (not shown). The test section was made of clear acrylic plates to facilitate optical access. The acrylic sheets used to fabricate the test facility are 25.4 mm thick. The x coordinate is aligned with the streamwise flow direction, while y and z coordinates are, respectively, in the wall-normal and lateral directions; $x = 0$ is at the jet exit, $y = 0$ is on the floor (bottom wall) of the test section and $z = 0$ is in the jet symmetry plane. The flow is driven by a variable speed centrifugal pump (Model 75211-62) from a reservoir through a 12.7 mm flexible hose (Swagelok PB-8), a paddle wheel flow meter (Blue-White F-1000), all of which were supplied by Cole-Parmer Instruments, and then into a settling chamber through a long circular pipe to the test section as shown schematically in Fig. 3.1a. The jets are formed by water exiting the pipe. The pipe is 1000 mm long and is

made of stainless steel with inside diameter of $d = 7 \pm 0.1$ mm. A schematic of the flow conditioner is shown in Fig. 3.1b. The flow conditioner was made of transparent 40 mm diameter and 435 mm long polyvinyl chloride (PVC) pipes that were connected by PVC Unions. It contains three wire screens arranged in order of decreasing coarseness, at three stages separated by the distances shown in Fig. 3.1b, to break down any large scale turbulence. The screens are made from stainless steel wires. The coarsest screen has 8 squares per inch (or #8), the intermediate coarse screen has 24 squares per inch (or #24), and the least coarse screen has 38 squares per inch (or #38). In-between #8 and #24 screens, 150 mm long drink straws with inside diameters of approximately 5 mm were

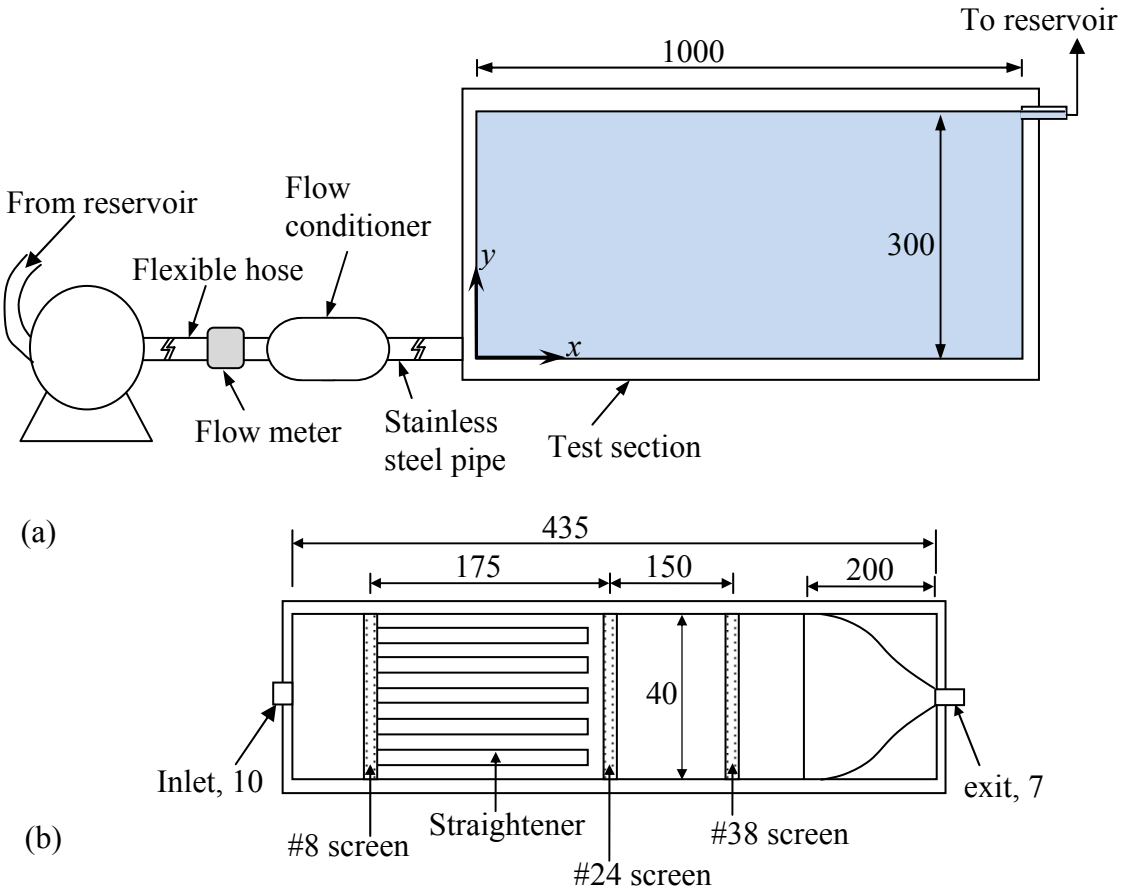

Figure 3.1: Schematic of (a) wall jet facility and (b) flow conditioner. All units are in mm (not to scale). The width is 500 mm (not shown).

inserted to serve as flow straighteners. The exit end of the settling chamber was designed to converge smoothly from the 40 mm diameter to flush off with the 7 mm exit into the long pipe to avoid flow separation. The 1000 mm long pipe (L/d = 143) ensures a fully developed flow at the jet exit. The floor of the section was designed to be adjustable so that the height from the floor to the of the jet exit centreline (i.e., h/d) can be varied. The jet exit can therefore be flush with the floor to produce a generic wall jet (or h/d = 0.5) as shown in Fig. 1.1 or offset from the exit to create an offset jet as shown in Fig. 1.2.

3.2 PIV System and Measurement Procedure

The velocity measurements were performed using a PIV technique. As noted earlier, the basic principles of PIV are described in detail in Appendix B. Therefore, only an overview of the PIV and information pertinent to the system used in this study are presented in this section. Particle image velocimetry is a non-intrusive optical velocity measurement technique. It can perform simultaneous multiple-point instantaneous velocity measurements in a whole-field of a flow. As a result of its attractive features, PIV has been employed in many areas of fluid dynamics research.

A PIV system comprises a laser source used to illuminate the flow field, a camera used to image the flow field, a data acquisition system to acquire and process the images. The basic principle of the PIV involves the following. A flow field is seeded with small light scattering particles that are presumed to faithfully follow the fluid motion. The flow field is then illuminated by two pulses of laser sheet separated by a time delay, Δt. The light scattered by the seeding particles and two successive images are recorded. The images are divided into grids called interrogation areas. For each interrogation area, a

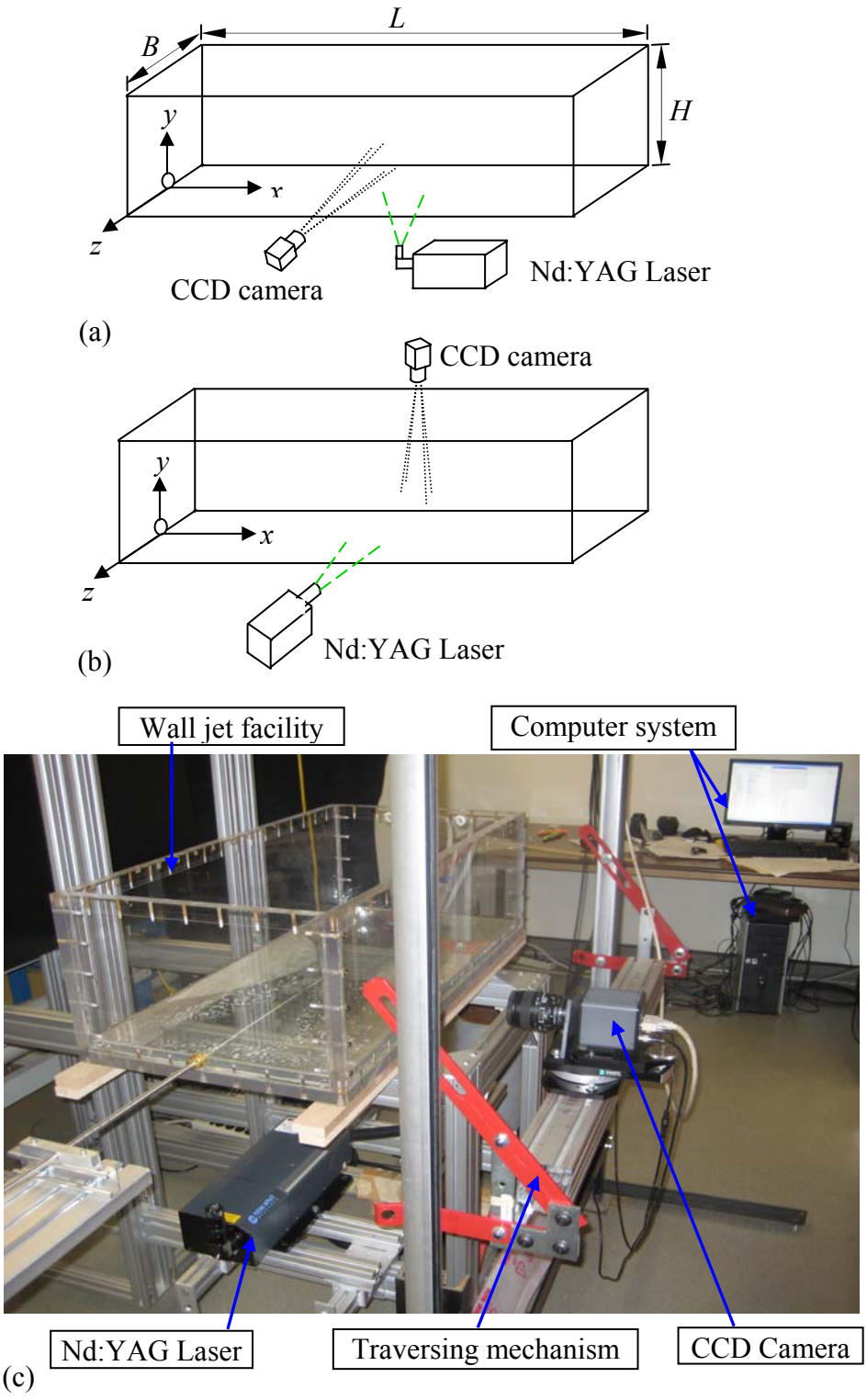

Figure 3.2: Schematic of the experimental setup in the *x*-*y* (a) and *x*-*z* (b) planes as well as a picture of the experimental setup for measurement in *x*-*y* plane (c).

numerical correlation algorithm (auto-correlation or cross-correlation) is applied to statistically determine the local displacement vector (Δs) of particles between the first and the second illuminations. The velocity, V, for a particular interrogation area is then obtained from the expression $V = \Delta s/\Delta t$. A velocity vector map over the whole target area is obtained by repeating the correlation for each interrogation area over the two image frames captured. Since the entire flow field can be analyzed at once, the PIV provides simultaneous whole field measurement. The description of the basic components of a PIV is presented in detail in Appendix C.

In the present experiments, the flow was seeded with 10 μm silver coated hollow glass spheres having a specific gravity of approximately 1.4. These particular seeding particles were chosen because they are large enough to scatter sufficient light to be detected by the digital camera and small enough to follow the flow faithfully. Using Eqn. B.1 in the appendix, the settling velocity and response time of the particles were calculated to be 2.18×10^{-7} m/s and 7.78×10^{-8} s, respectively. This settling velocity is insignificant (up to six orders of magnitude smaller) compared to the streamwise mean velocities measured. Similarly, the response time is very small compared to the sampling times employed in this study. This implies that the particles follow the fluid flow faithfully. An Nd-YAG laser (120 mJ/pulse) of 532 nm wavelength was employed to illuminate the flow field. A 12-bit HiSense 4M camera (2048 pixel × 2048 pixel CCD array size and a 7.4 μm pixel pitch) was coupled to a 60 mm AF Micro Nikkor lens.

Figure 3.2 is a schematic and a picture of the experimental set up showing the arrangement of the CCD camera, the laser head, and the test facility. In particular, the schematic shows the arrangement of the camera, and the laser for measurement in

both the *x*-*y* plane (Fig. 3.2a) and *x*-*z* plane (Fig. 3.2b). However, the picture (Fig. 3.2c) shows only the arrangement for measurements in the *x*-*y* plane.

For a given interrogation window size, the particle displacement of one quarter of the interrogation or less is recommended to ensure a good signal-to-noise ratio. The laser pulse separation time Δt was determined based on the particle displacement of one quarter of the interrogation using the following expression (Dantec Dynamic PIV Manual),

$$\Delta t = \frac{N \times d_{pitch}}{4 M_f U_m}, \tag{3.1}$$

where N is the interrogation window size, d_{pitch} is the pixel pitch, M_{f} is the magnification factor, and U_{m} is the maximum velocity of the flow. In addition to the condition stated above, particle displacements of at least two times the pixel pitch was satisfied in order to ensure high signal-to-noise ratio and minimize peak locking. Before acquiring data at any test location, a small sample was initially acquired and analyzed to ensure that the PIV parameters were correctly chosen to yield high quality velocity vectors. In all the cases examined, the number of substituted velocity vectors in the main flow domain was less than 2%.

The instantaneous digital images were post-processed by the adaptive-correlation option of the commercial software (FlowManager 4.50.17) developed by Dantec Dynamics Inc. The adaptive-correlation algorithm is an advanced type of the standard cross-correlation. It uses a multi-pass FFT cross-correlation algorithm to determine the average particle displacement within the interrogation area (IA). The Gaussian window function and the low-pass Gaussian filter that come with the FlowManager were used as

input and output filters, respectively, to the correlation algorithm. A moving average validation was used during image processing. The technique validates or rejects vectors based on a comparison between neighbouring vectors. The average of the vectors in a rectangular neighbourhood of a vector is calculated and compared with the vector. Continuity of the flow field's behaviour is an implicit assumption in the moving-average validation method. The idea behind this approach is that the velocity field is slowly changing so that there is not too much change from a vector to its neighbour vectors. Thus, if a vector deviates too much from its neighbours, it must be an outlier.

3.3 Experimental Test Conditions

The test conditions consist of four different offset heights, h/d, and three different Reynolds numbers, Re_j (= $U_j d/\nu$). The complete test conditions are shown in Table 3.1, where the superscripts denote the extent (x/d) and plane (x-y or x-z) of measurements. Also included on the table are the jet exit velocity, U_j, and the ratio of U_j to the bulk velocity, U_{bulk}. The experiments were conducted for the following four jet offset heights: h/d = 0.5, 1.0, 2.0, and 4.0; and the following three jet exit Reynolds numbers: Re_j = 5000, 10000, and 20000. The facility was designed to perform measurements as far downstream as $x/d \approx 120$ in order to report quantities at much farther downstream locations than reported in the previous 3D offset jet studies. In this study, measurements were conducted over $0 \leq x/d \leq 120$ in the x-y plane at $z = 0$ and $10 \leq x/d \leq 80$ in the x-z plane at y_m for all h/d values at Re_j = 10000 to study the effect of offset height (h/d) on velocity characteristics in both planes. In order to study the effect of Re_j, measurements were performed over the same range for all Re_j = 5000, 10000, and 20000 for h/d = 0.5,

and 2.0. The Reynolds numbers were chosen to be at the lower end of the values reported in most the previous studies. This low range of Reynolds numbers is chosen because Reynolds number effects are more likely to be most evident at relatively lower Reynolds numbers than at higher Reynolds numbers.

Table 3.1: Summary of test conditions

Tests	***h/d***	***x-y* plane**	***x-z* plane**	U_j (m/s)	Re_j
1	0.5	$0 \le x/d \le 120$	$10 \le x/d \le 80$	0.72	5000
2	0.5			1.43	10000
3	0.5			2.86	20000
4	1.0			1.43	10000
5	1.0	$0 \le x/d \le 24$	none	0.72	5000
6	1.0			2.86	20000
7	2.0	$0 \le x/d \le 120$	$10 \le x/d \le 80$	0.72	5000
8	2.0			1.43	10000
9	2.0			2.86	20000
10	4.0			1.43	10000
11	4.0	$0 \le x/d \le 24$	none	0.72	5000
12	4.0			2.86	20000

3.4 Uncertainty Estimates

Measurement uncertainty analysis was performed following the AIAA standard derived and explained by Coleman & Steele (1995). Analyses of bias and precision errors inherent in the PIV technique are available in Prasad et al. (1992) and Forliti et al. (2000). In general, a complete uncertainty analysis involves identifying and quantifying both the bias and precision errors in each part of the measurement chain.

In PIV technique, the accuracy of velocity measurement is limited by the accuracy of the sub-pixel interpolation of the displacement correlation peak. Particle

response to fluid motion, light sheet positioning, light pulse timing and size of interrogation area are among the other sources of measurement uncertainties. On basis of the size of interrogation area and curve fitting algorithm used to calculate the instantaneous vector maps, and the large number of instantaneous vector maps used to calculate the mean velocity and turbulent quantities, the uncertainty in the streamwise and wall-normal mean velocities at 95% confidence level was estimated to be ±2.8% and ±2.4% of the local mean velocity, respectively. In addition, the measurement uncertainties in turbulence intensities, Reynolds stresses, and triple products are estimated to be ±8%, ±12%, and ±14%, respectively. Detailed uncertainty analyses in this study are presented in Appendix C.

CHAPTER 4

RESULTS AND DISCUSSIONS

The mean flow quantities and one-point statistics of 3D turbulent offset and wall jets as well as two-point correlation and POD analysis are reported in this chapter. For the one-point statistics, the quantities reported include the profiles of the turbulence intensities, Reynolds shear stresses, stress ratios, triple velocity products, and some of the terms in the transport equation for the turbulence kinetic energy. Where previous data are available, they are plotted with the present data for comparison. The chapter is divided into four sections. In the first section (Section 4.1), flow qualification and similarity considerations are discussed. Section 4.2 reports the mean flow and one-point statistics. The two-point correlations and POD are discussed in Sections 4.3 and 4.4, respectively.

4.1 Flow Qualification and Similarity Consideration

4.1.1 Flow qualification

Considering the fact that nozzle geometry affects the jet flow dynamics close to the exit (Nozaki, 1983; Sun & Ewing, 2002)**,** it is necessary to qualify the exit profiles. This qualification will also facilitate comparison with previous experiments as well as making the data more suitable for numerical code validation. To this end, the jet exit profiles are shown in Fig. 4.1. The profiles of the normalized mean velocity and streamwise turbulence intensities at $x/d = 0.6$ are shown in the figure for the three Reynolds numbers. Reflection of the laser light on the upstream wall distorted velocities at the jet exit, (i.e., $x/d = 0$) and as a result profiles could not be extracted in the region x/d

< 0.5. It should be noted that in this section and all subsequent sections, between 4 to 10 data points were skipped to avoid data congestion. The U profiles of Re_j = 5000 are less full than the profiles for Re_j = 10000 and 20000 reflecting its lower Reynolds number. The profiles of the streamwise turbulence intensities are symmetric as expected with the exception of that for Re_j = 5000. The turbulence levels near the jet centreline in the present study are $u/U_m \approx 6\%$ which is about twice the value reported by Sun & Ewing (2002a, b) for a jet emanating a circular pipe. In addition, the peak values of u/U_m are also much higher than the value reported by Sun & Ewing (2002a, b).

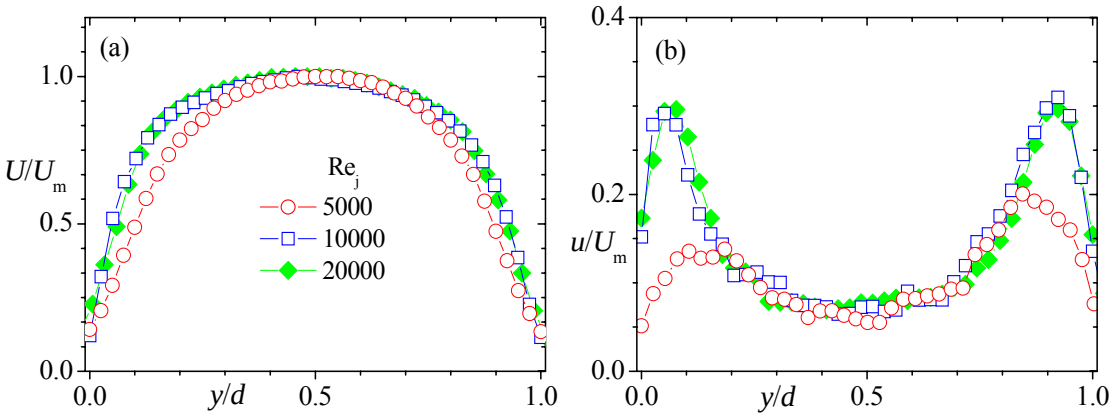

Figure 4.1: Profiles of streamwise (a) mean velocities and (b) turbulence intensitites close to the jet exit, x/d = 0.6 for three Reynolds numbers.

The bulk velocities were calculated from both the flow meter and by integrating the exit velocity profiles using the following relation: $\frac{4}{\pi d^2}\int_0^{d/2} 2U\pi r dr$. The ratio of the exit velocity (U_j) to the bulk velocity (U_{bulk}) for the three Reynolds numbers is presented in Table 4.1. The U_j/U_{bulk} values from the flow meter for Re_j = 10000 and 20000 are

consistent with the value of 1.22 obtained from the $1/7^{th}$ power law approximation for a fully developed turbulent pipe flow. However, the area average values are about 5% higher than 1.22. The high values are attributed to the fact the velocities were obtained at $x/d = 0.6$ instead of $x/d = 0.0$. The bulk velocity for $Re_j = 5000$ in both cases are larger than 1.22 but much smaller than the value of 2.0 for a laminar pipe flow.

Table 4.1: Exit bulk velocity (U_{bulk}) and the ratio U_j/U_{bulk}

Re_j	U_j (m/s)	Area average of exit profiles		Flow meter values		
		U_{bulk} (m/s)	U_j/U_{bulk}	litres/min	U_{bulk} (m/s)	U_j/U_{bulk}
5000	0.72	0.51	1.43	1.11	0.48	1.50
10000	1.43	1.11	1.28	2.75	1.19	1.20
20000	2.86	2.21	1.29	5.45	2.36	1.21

In order to reveal some of the qualitative features of the flow in the near field, the iso-contours of the mean velocities in the symmetry plane from $0.6d$ to about $5d$ jet exit diameters downstream are shown in Fig. 4.2. Because the flow patterns are generally similar, only contours for $Re_j = 20000$ are shown. The iso-contours of $U^* = U/U_j$, and the two-component estimate of the turbulence kinetic energy, $k^* = (u^2 + v^2)/U_j^2$ are plotted in the figure with the velocity vectors superimposed on them. The iso-contours show values of $U^* \geq 0.9$ everywhere along the centerline of the jet exit down to $x/d = 4.0 \pm 0.3$. The direction of the vectors in Fig. 4.2 clearly shows that the jet entrains the stagnant ambient fluid above and below it. As a result, the regions with high U^* decrease in width downstream and the jets spread in all directions. As the figure shows, the direction of some of the vectors in the region $x/d < 2$ (for $h/d = 2.0$ and 4.0) is opposite to that of the jet; but no sustained recirculation is present. The maximum negative velocities are only

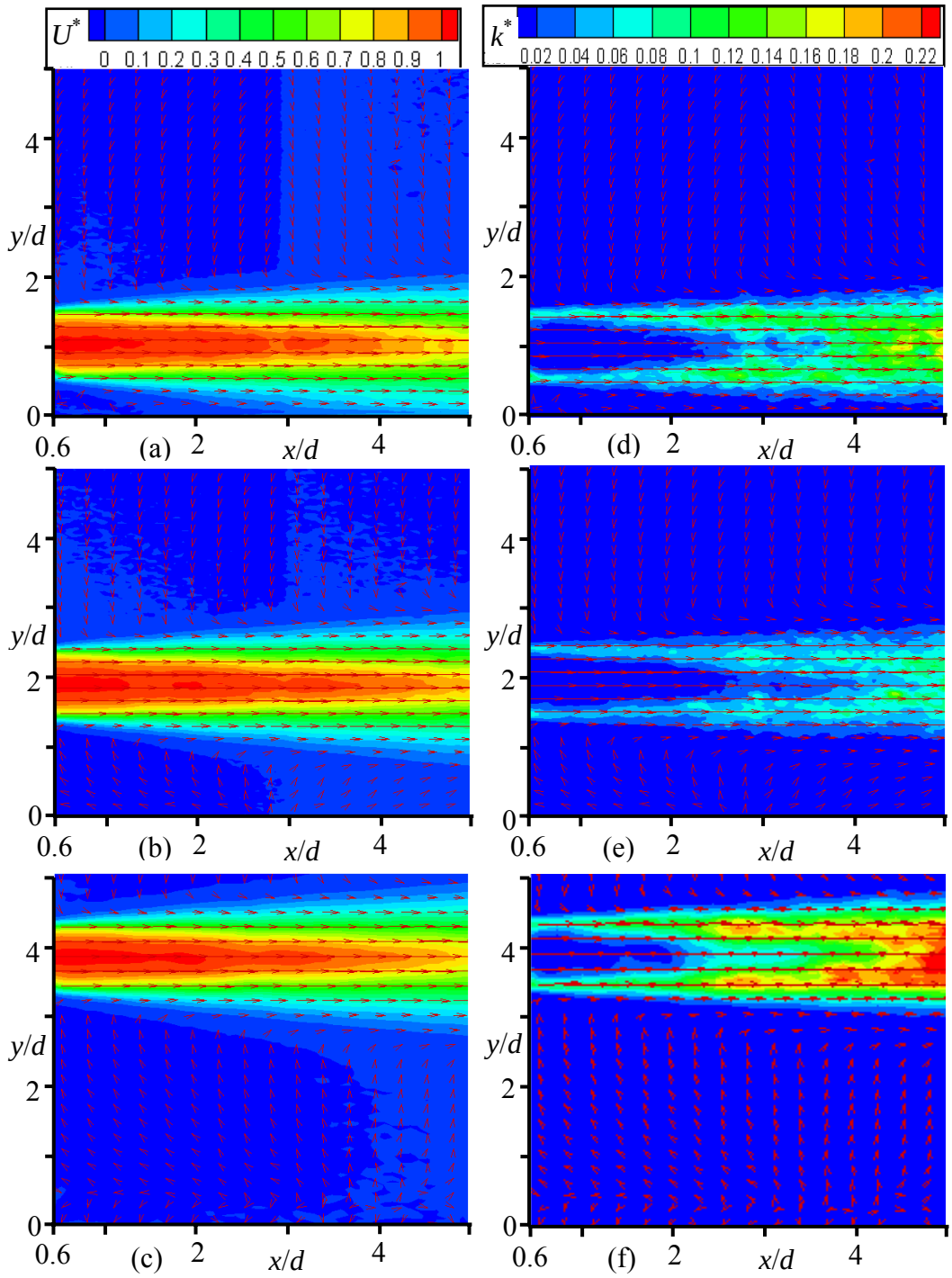

Figure 4.2: Mean velocity vectors and iso-contours of the mean velocities ($U^* = U/U_j$) and turbulence kinetic energy $\{k^* = (u^2 + v^2)/U_j^2\}$ in the near field for $h/d = 1$ in (a) and (d), $h/d = 2$ in (b) and (e), and $h/d = 4$ in (c) and (f).

$(-U/U_j)_{max}$ = 0.17%, 0.59%, and 0.38%, respectively for h/d = 1, 2, and 4 which are negligible compared to values of 41% reported by Pelfrey & Liburdy (1986) for 2D offset jet with h/d = 7 and the range of 10% to 20% reported for BFS (Eaton & Johnston, 1981; Jovic, 1996). Contours of k^* show low values in the regions with high U^* values but the turbulence level increases downstream.

One of the characteristics of the shear layer is the reattachment length, x_r. This was estimated as the distance from the exit to the location where the mean streamlines (not shown) reattached to the wall. The x_r values for the different Re_j and h/d values are presented in Table 4.1. It is observed that the reattachment length is nearly independent of Reynolds number. This is consistent with the observation reported by Nozaki et al. (1979) for a 2D offset jet, however, the Reynolds numbers in that study are much larger (between 20000 and 70000). The reattachment lengths are x_r/d = 1.5 ± 0.1, 3.2 ± 0.1, and 6.4 ± 0.2 for h/d = 1.0, 2.0, and 4.0, respectively, clearly indicating that the reattachment length is nearly doubled when the offset height is doubled. The values of x_r/d = 3.2 ± 0.1 for h/d = 2.0 in the present study are smaller than a value of $x_r/d \approx 5$ reported by Nasr & Lai (1997) for a 2D offset jet with h/d = 2.13. Nasr & Lai (1997) developed the following correlation using their own data and data from previous studies: $x_r/d = 2.63(x/d)^{0.855}$. The x_r values predicted from this correlation are generally much larger than the present values for the 3D offset jets. In addition, the 3D offset jet (from a square nozzle) values reported by Nozaki (1983) are 3.8, 6.7, and 9.5 for h/d = 1.5, 2.5, and 3.5, respectively, which are also much larger than the present values. Considering the fact that nozzle geometry affects the jet flow dynamics in the near field (Nozaki, 1983; Sun & Ewing, 2002), the differences in x_r values may be partly attributed to the effect of the entrainment in the

near field. In addition, the different techniques applied in determining the x_r values may contribute to differences in the x_r values.

Table 4.2: Reattachment lengths (x_r) for various study conditions

	x_r/d		
h/d	Re_j = 5000	Re_j = 10000	Re_j = 20000
1.0	1.5	1.4	1.5
2.0	3.2	3.3	3.1
4.0	6.3	6.6	6.4

4.1.2 Similarity consideration

In order to study how the velocity profiles evolve downstream and the effect of Reynolds numbers (Re_j), profiles of the streamwise (U) and wall-normal (V) mean velocities, streamwise (u), wall-normal (v) and lateral (w) turbulence intensities, and Reynolds shear stress (uv or $-uw$) at selected downstream locations (x/d) are shown in Figs. 4.3 to 4.10. As stated in Chapter 3, comprehensive measurements were performed for the three Reynolds numbers for only generic wall jet (h/d = 0.5) and offset height h/d = 2.0. These are used to study the effect of Reynolds number in this section. In these figures, the horizontal axes are staggered and the various stations are denoted by I, II, III and IV. Stations I, II, and III represent Reynolds numbers of Re_j = 5000, 10000, and 20000, respectively. These three stations are used to study Reynolds number effects but each of these first three stations shows downstream evolution of the jets. The last station, IV, compares the three Reynolds numbers in the region where the profiles collapsed. Note that U_m and d are the velocity and length scales and $x^* = x - x_r$. Also y^* and z^*

represent $y/y_{0.5}$ and $z/z_{0.5}$, respectively, in this section and all subsequent sections.

4.1.2.1 Symmetry (*x*-*y*) plane

Figures 4.3 to 4.6 show the profiles for $h/d = 0.5$ and 2.0 in the symmetry plane in the range $x^*/d = 10$ to 80. The mean streamwise velocity profiles for the generic jet collapsed in the region $x^*/d \geq 20$ (Fig.4.3a). The location of U_m shifts downwards from

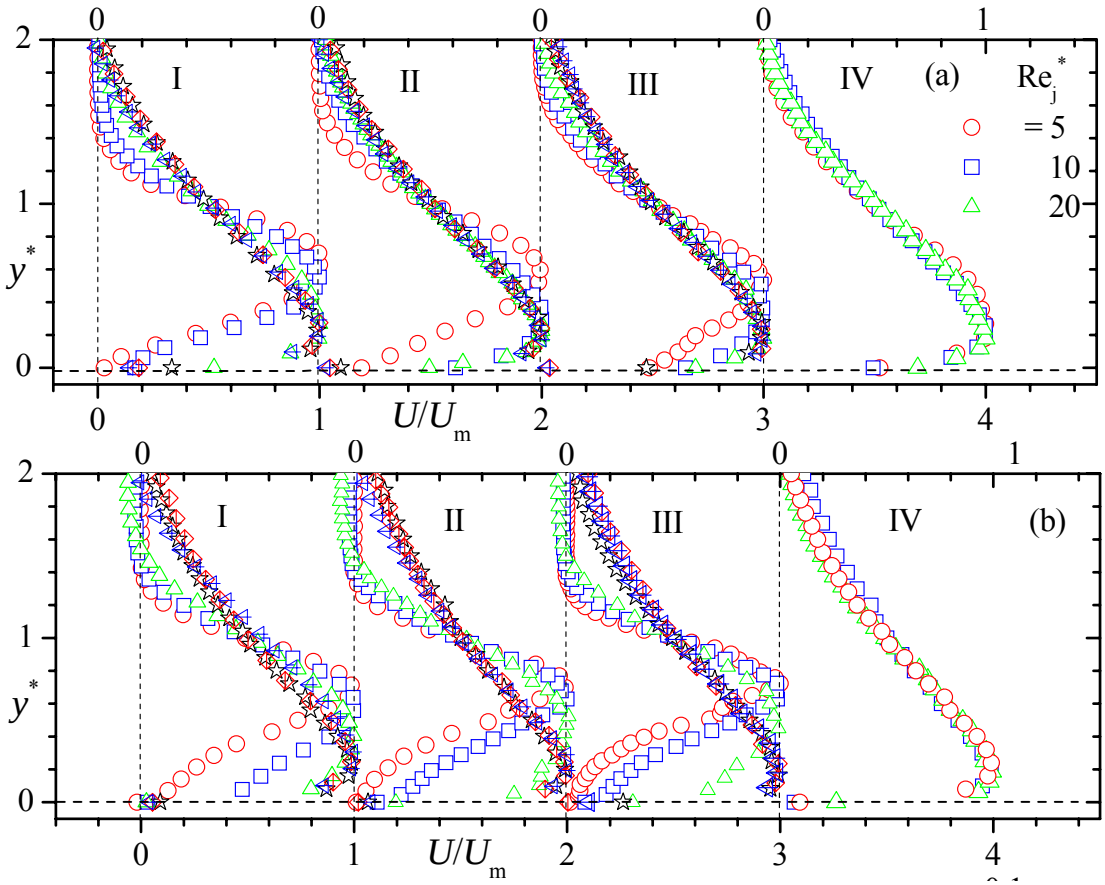

Figure 4.3: Profiles of streamwise mean velocities, U. (a) $h/d = 0.5$ (b) $h/d = 2.0$. $y^* = y/y_{0.5}$. Symbols for Stations I to III: ○: $x^*/d = 4$; □: $x^*/d = 10$; △: $x^*/d = 20$; ☆: $x^*/d = 40$; ◇: $x^*/d = 60$; ◁: $x^*/d = 80$. Symbols for Station IV are shown in (a). $Re_j^* = Re_j/1000$.

$y_m \approx 0.6y_{0.5}$ at $x^*/d = 4$ to a constant value of $y_m \approx 0.19y_{0.5}$ in the region $x^*/d \geq 20$ for h/d = 0.5. This value is consistent with a value of $y_m \approx 0.18y_{0.5}$ by Abrahammson et al. (1997). The mean streamwise velocity profiles for h/d = 2.0 in Fig. 4.3b collapsed in the region $x^*/d \geq 40$, indicating that the high h/d required larger distance to collapse. As expected the peak values for h/d = 2.0 at $x^*/d = 4$ occurred at $y_m \approx 0.7y_{0.5}$ which is 17% higher than the value for the generic wall jet. However by $x^*/d = 40$, the location of U_m shifted to $y_m \approx 0.19y_{0.5}$. The profiles at the various Reynolds numbers (i.e., Station IV) also collapsed indicating the absence of significant Reynolds number effects collaborating previous observations for generic wall jets (Sun & Ewing, 2002; Law & Herlina, 2002). Thus the present study demonstrates that even at the Reynolds number as low as 5000, there is no significant Reynolds number effects in the velocity distribution.

The profiles of wall-normal mean (V) velocities (Fig. 4.4) are hardly reported in previous studies. The profiles are all predominantly negative indicating that the entrained fluid from the ambient medium flows towards the solid surface. In the region $x^*/d \leq 10$, the profiles are more negative with increasing Reynolds number and offset height, h/d. Beyond x^*/d = 10, there is no consistent trends associated with Reynolds number and offset heights. The magnitudes of the V values are generally less than 5% of U_m. It should be noted that the profiles of h/d = 1.0 (not shown), have trends almost identical to that of h/d = 0.5.

The profiles of u, v, and uv are shown in Figs. 4.5 and 4.6 for h/d = 0.5 and 2.0, respectively. Similarity is observed in the u and v profiles as each profile collapsed well in the region $x^*/d \geq 40$, although the collapse of profiles at Re_j = 5000 is not as good as the higher Reynolds number data sets. The profiles of uv collapsed in the region $x^*/d \geq$

40 for both Re_j = 10000 and 20000 but in the region $x^*/d \geq 60$ for Re_j = 5000. This implies the flow development depends on the Reynolds number. Overall, there is no Reynolds number effect beyond x^*/d = 60 which is consistent with the results of Sun & Ewing (2002a, b).

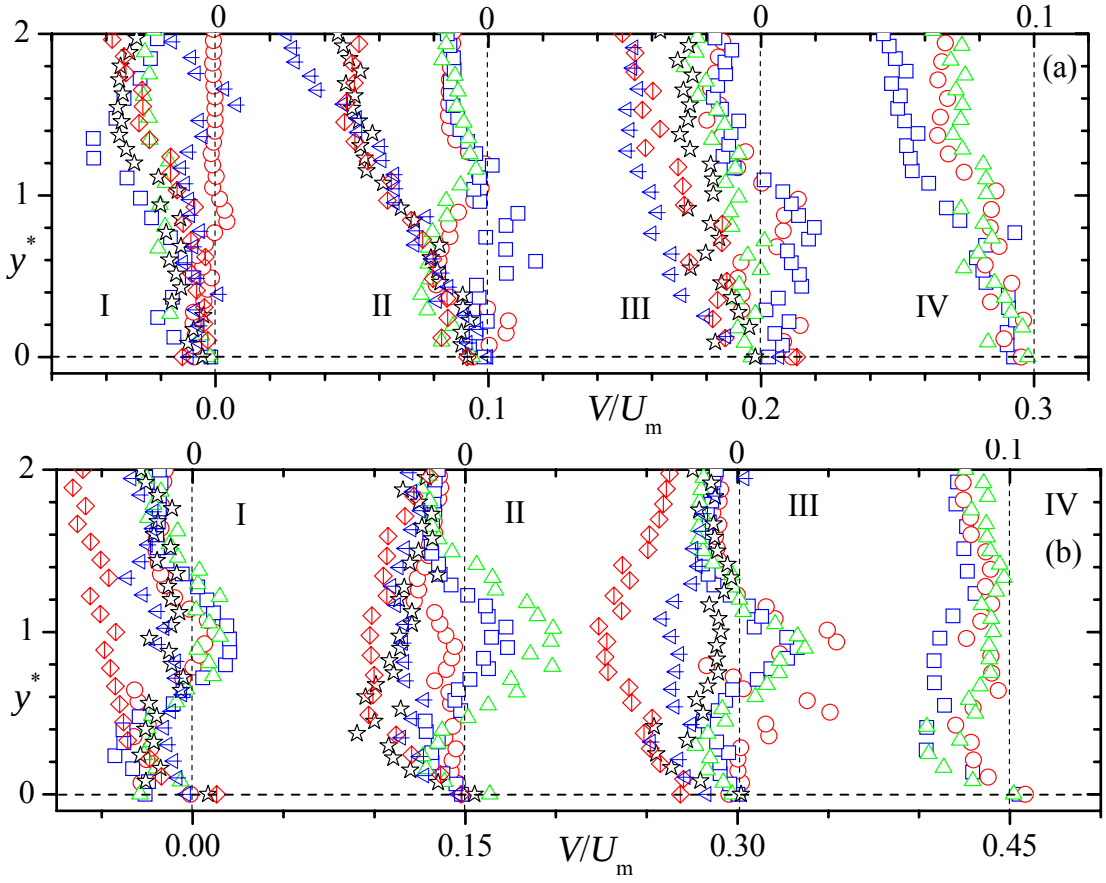

Figure 4.4: Profiles of wall-normal mean velocities, V. (a) h/d = 0.5 (b) h/d = 2.0. y^* = $y/y_{0.5}$. Symbols are as in Fig. 4.3.

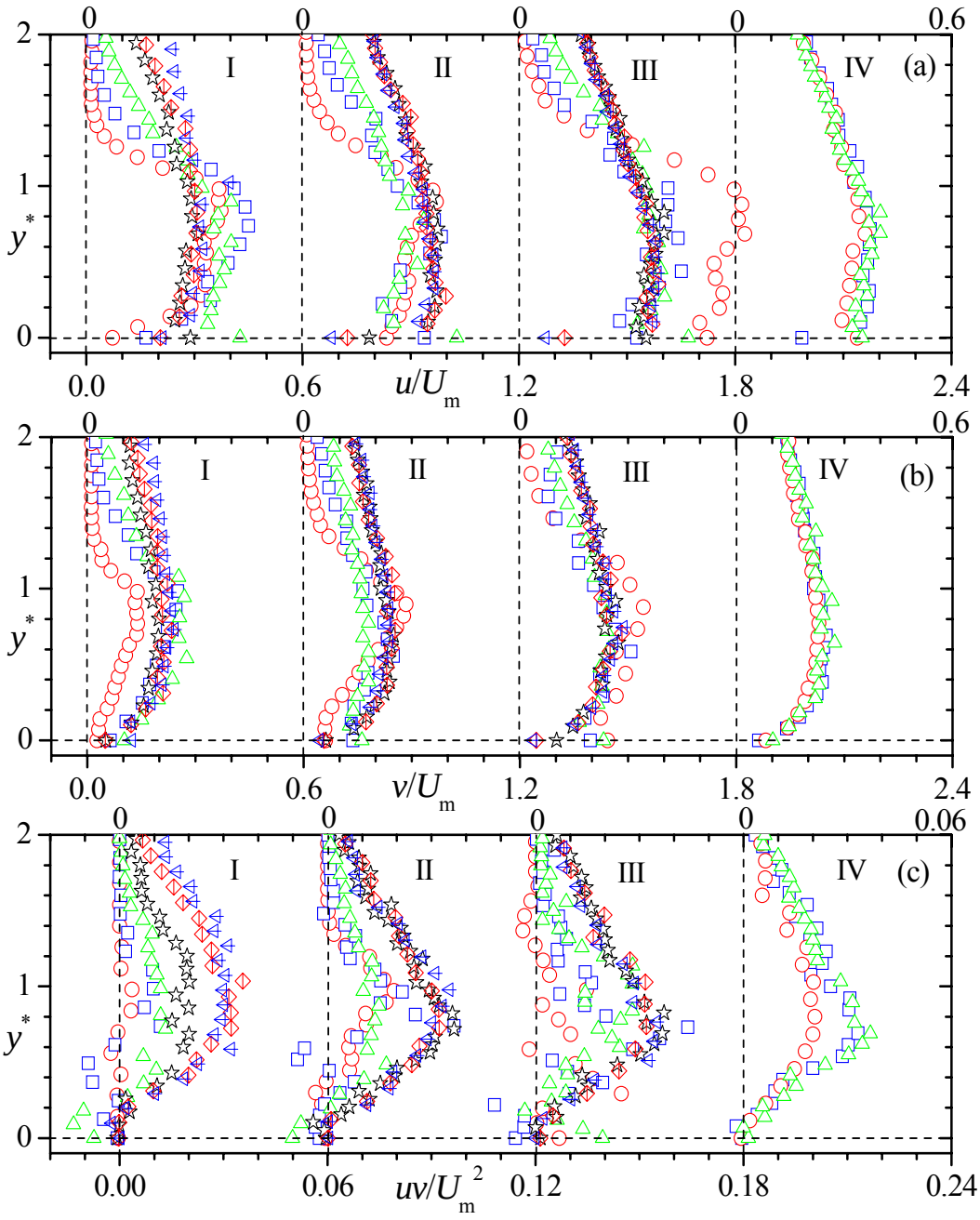

Figure 4.5: Profiles of (a) streamwise turbulence intensities, u, (b) wall-normal turbulence intensities, v, and (c) Reynolds shear stresses, uv, in the symmetry plane for $h/d = 0.5$. $y^* = y/y_{0.5}$. Symbols are as in Fig. 4.3.

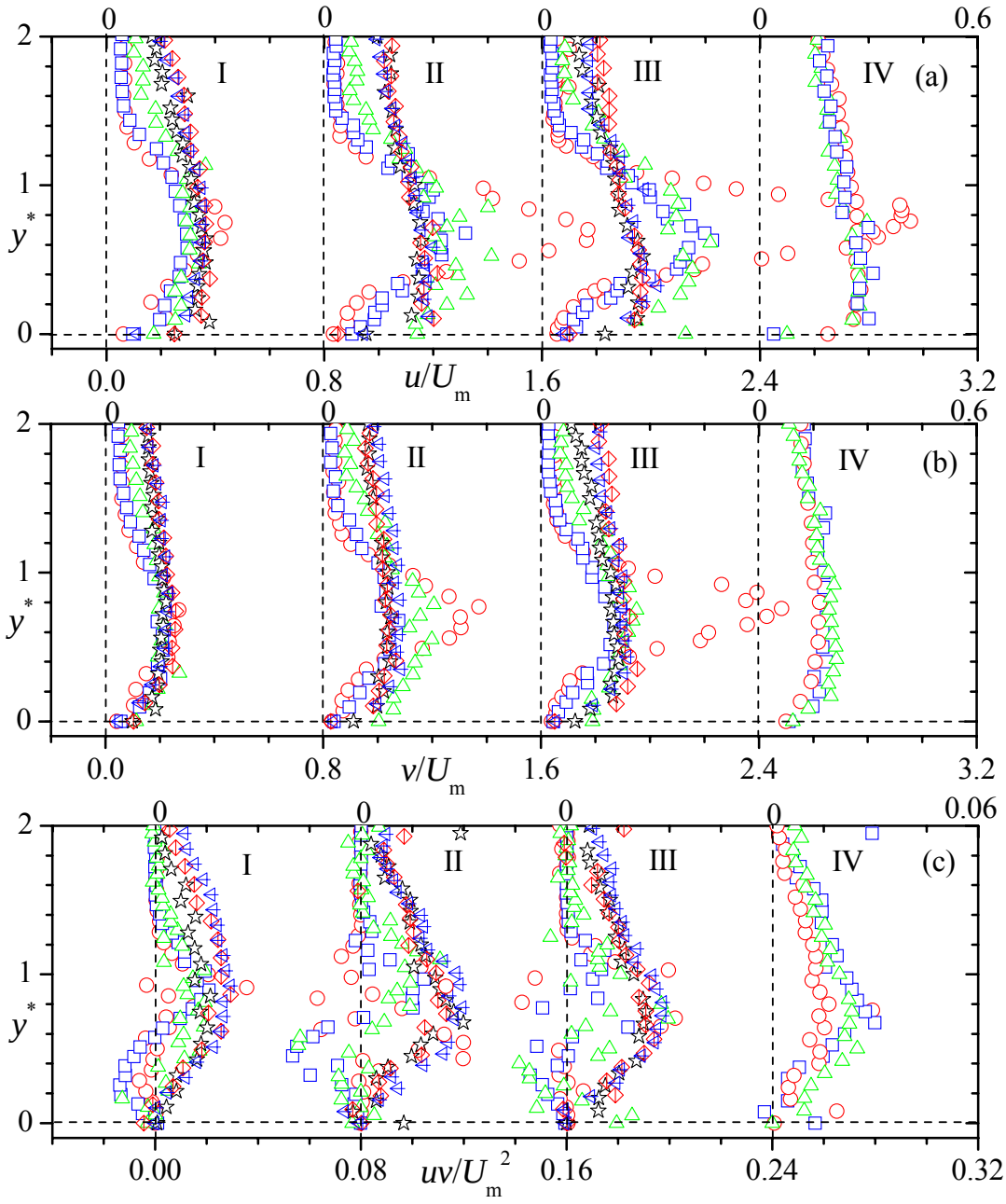

Figure 4.6: Profiles of (a) streamwise turbulence intensities, u, (b) wall-normal turbulence intensities, v, and (c) Reynolds shear stresses, uv, in the symmetry plane for $h/d = 2.0$. $y^* = y/y_{0.5}$. Symbols are as in Fig. 4.3.

As indicated in Chapter 2, other length scales have been used in the past to analyze the mean velocity profiles. Following Davis & Winarto (1980), the following normalization was also used for the offset jets: $y^{**} = (y - y_m)/(y_{0.5} - y_m)$. Figure 4.7a shows U profiles using the above normalization for $Re_j = 10000$. The profiles collapsed at all locations in the region $0 \leq y^{**} \leq 2$. This indicates that this particular scaling is a more appropriate choice for the offset jets in this region. In the inner region ($-2 \leq y^{**} \leq 0$), however, the profiles collapsed in the region $x^*/d \geq 40$ in a similar fashion as using $y_{0.5}$.

The V profiles from the normalization $y^{**} = (y - y_m)/ (y_{0.5} - y_m)$ are shown in Fig. 4.7b. The figure shows positive values close to the wall ($y^{**} < -2$) indicating that fluid is entrained from the wall region upward to the jet. In the core flow region, no consistent trend is observed. The normalization does not improve the trends in the profiles better than $y_{0.5}$ does.

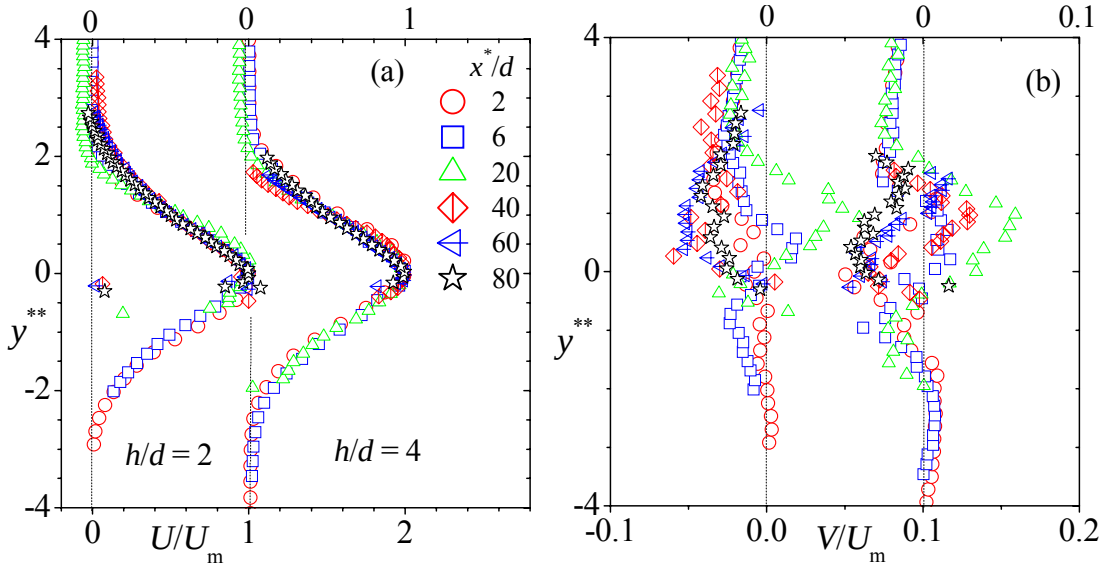

Figure 4.7: Profiles of mean (a) streamwise velocities, U, and (b) wall-normal velocities, V. $y^{**} = (y - y_m)/ (y_{0.5} - y_m)$.

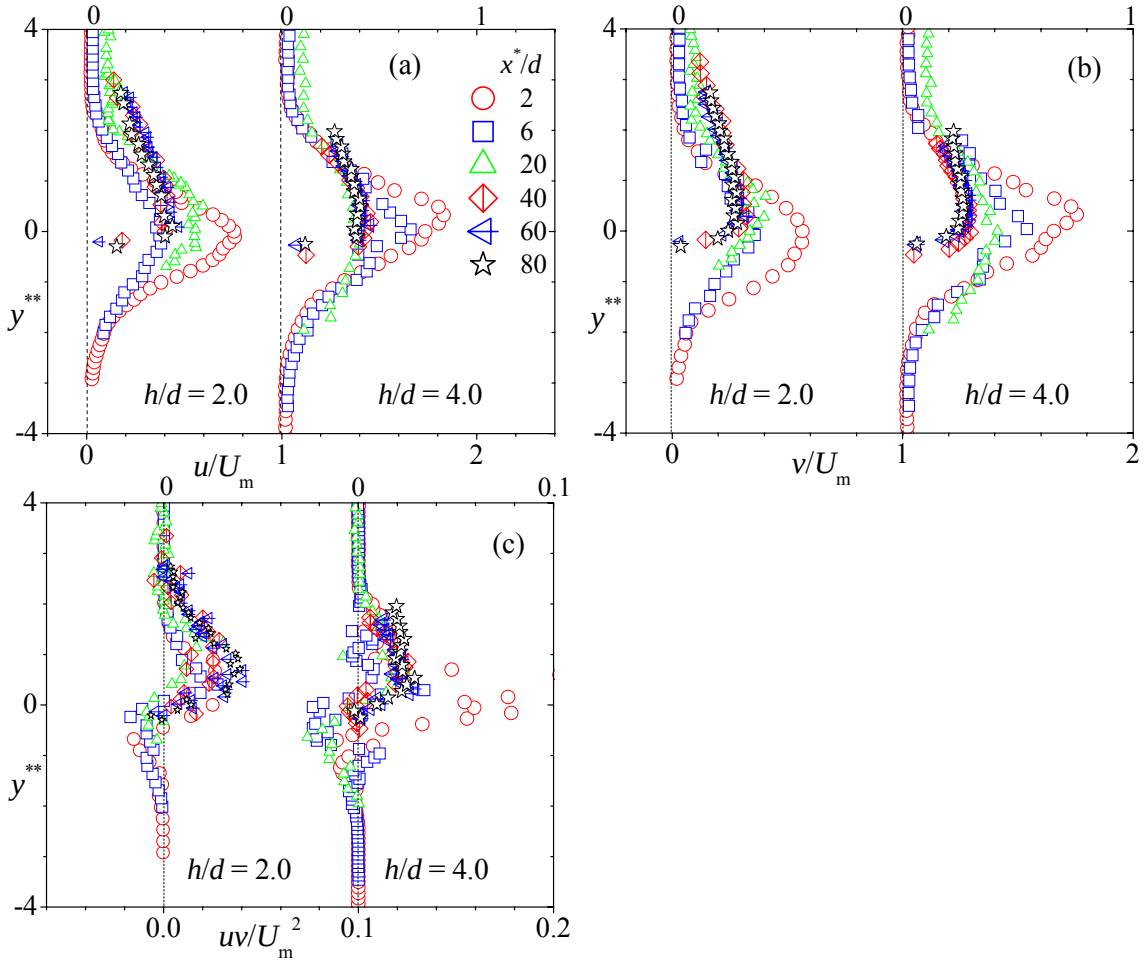

Figure 4.8: Profiles of (a) streamwise turbulence intensities, u, (b) wall-normal turbulence intensities, v, and (c) Reynolds shear stresses, uv, in the symmetry plane. $y^{**} = (y - y_m)/(y_{0.5} - y_m)$.

Using the length scale $y^{**} = (y - y_m)/(y_{0.5} - y_m)$, the profiles of the streamiwse turbulence intensities (Fig. 4.8a) are self-similar in the region $x^*/d \geq 40$ and $x^*/d \geq 60$, respectively, for $h/d = 2$ and 4. The trends of the v profiles (Fig. 4.8b) and their convergence for all h/d are similar to the corresponding u profiles. The uv profiles (Fig. 4.8c) are anti-symmetric in the region $x^*/d \leq 20$ but further downstream the profiles increased and collapsed in the

region $x^*/d \geq 60$. Unlike the mean velocities, this type of normalization does not improve the collapse of the turbulence statistics better than $y_{0.5}$. Figure D.1 in Appendix D also indicates that using jet exit diameter as the length scale does a worse job of collapsing the data.

Measurements were also performed in different offset planes (i.e., x-y planes located at $z/d = 0$, 1, 2, and 4) to examine the flow development in these planes relative to the symmetry plane, $z/d = 0$. The profiles of U, u, v, and uv at $x^*/d = 52$ for different z/d and h/d values are shown in Figure D.2 in Appendix D. The profiles collapsed fairly well indicating that the development of the flow even at $z/d = 4$ is similar to the symmetry plane, $z/d = 0$. It should be pointed out, however, that different U_m and $y_{0.5}$ values at these locations enhanced the collapse of the profiles. These values are contained in Table D.1. These values decrease with increasing z/d as expected, though the decrease is very gradual. For example, even at $z/d = 4$, the decrease in U_m and $y_{0.5}$ values is not more than 20%.

4.1.2.2 Lateral (x-z) plane

In the lateral plane, the mean velocity (U), turbulence intensities (u, w), and Reynolds shear stresses ($-uw$) are shown in Figs. 4.9 and 4.10. The mean velocity profiles also collapsed in the region $x^*/d \geq 20$ for both $h/d = 0.5$ and 2.0. The region of collapse for $h/d = 2.0$ is much earlier than in the symmetry plane. The turbulence quantities, however, collapsed in the region $x^*/d \geq 40$. The different Reynolds numbers shown at Station IV collapsed reasonable well but not as well as in the symmetry plane.

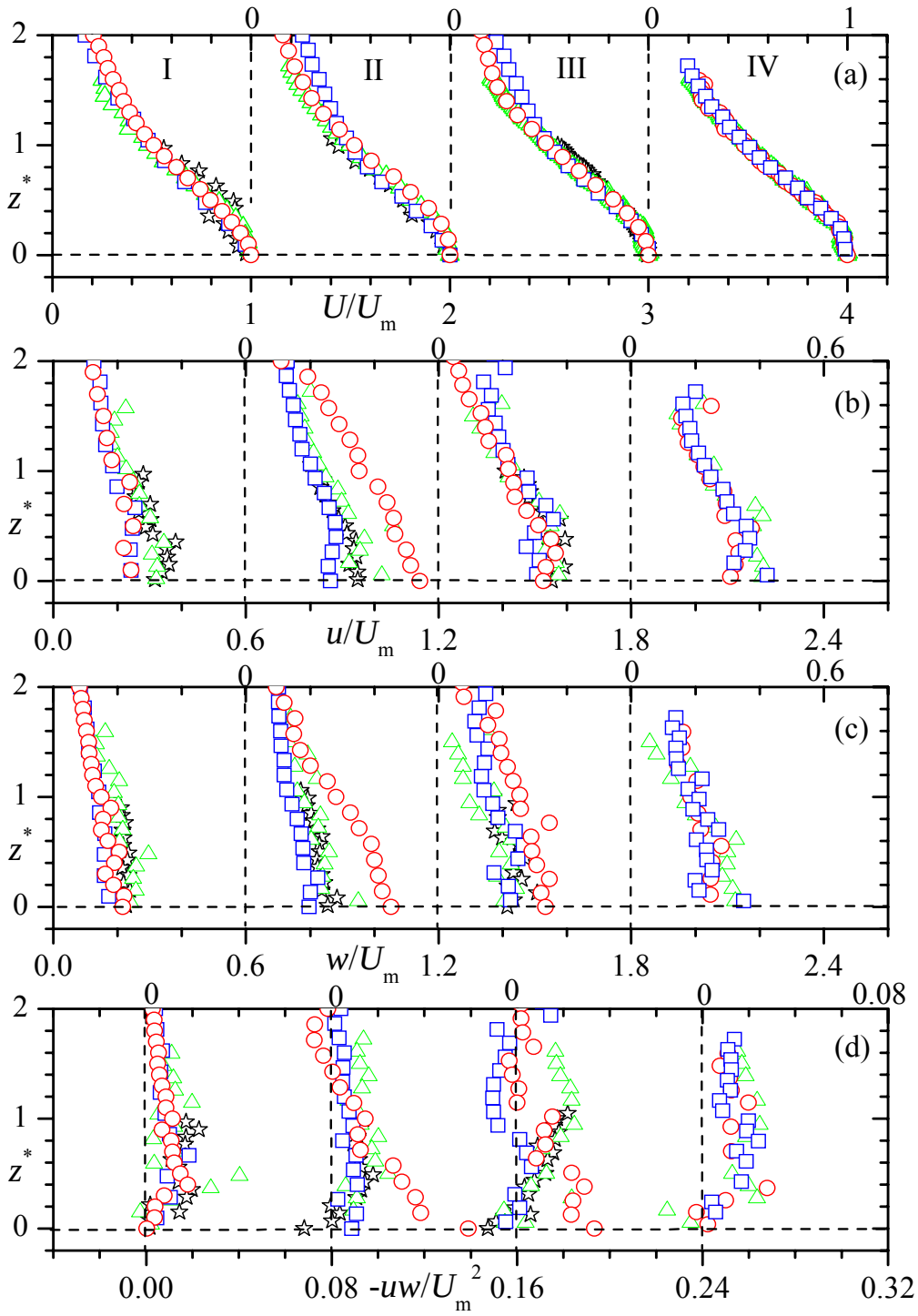

Figure 4.9: Profiles of (a) streamwise mean velocities, U, (b) streamwise turbulence intensities, u, (c) lateral turbulence intensities, w, and (d) Reynolds shear stresses, $-uw$ for $h/d = 0.5$. $z^* = z/z_{0.5}$. Symbols: ○: $x^*/d = 10$; □: $x^*/d = 20$; △: $x^*/d = 40$; ☆: $x^*/d = 60$.

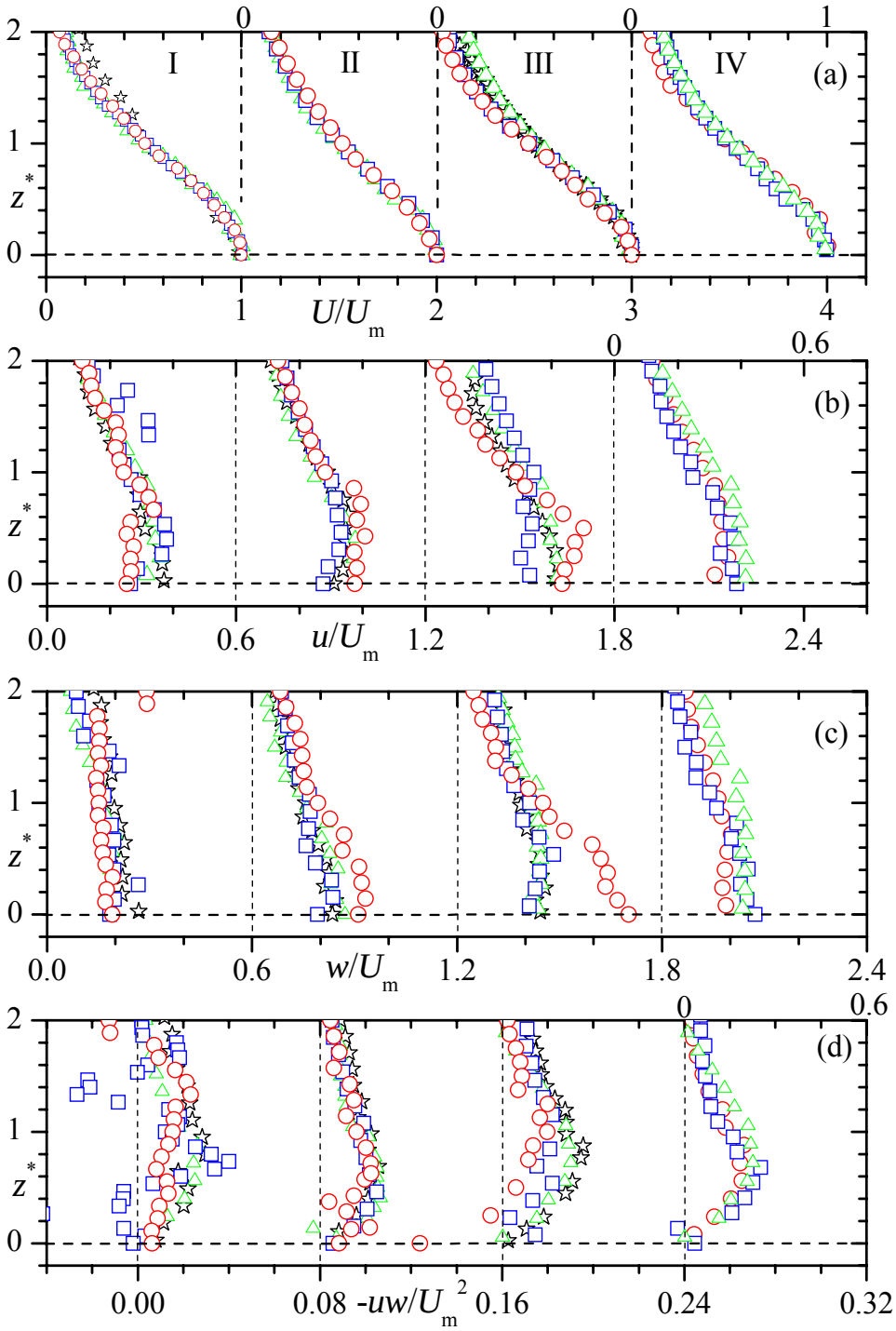

Figure 4.10: Profiles of (a) streamwise mean velocities, U, (b) streamwise turbulence intensities, u, (c) lateral turbulence intensities, w, and (d) Reynolds shear stresses, $-uw$ for $h/d = 2.0$. $z^* = z/z_{0.5}$. Symbols are as in Fig. 4.9.

4.2 Mean Flow and One-Point Statistics

4.2.1 Streamwise flow development

The development of the mean flow was examined by studying the decay of U_m with streamwise distance, and the spread of y_m, $y_{0.5}$, and $z_{0.5}$ (Fig. 4.11). Figure 4.11a shows that when the offset heights are fixed at $h/d = 0.5$ or 2.0 and the Reynolds number is increased, the local maximum velocity (U_m) in the region $2 \leq x/d \leq 40$ decays faster at a lower Reynolds number than at a higher Reynolds number. At x/d = 10 and

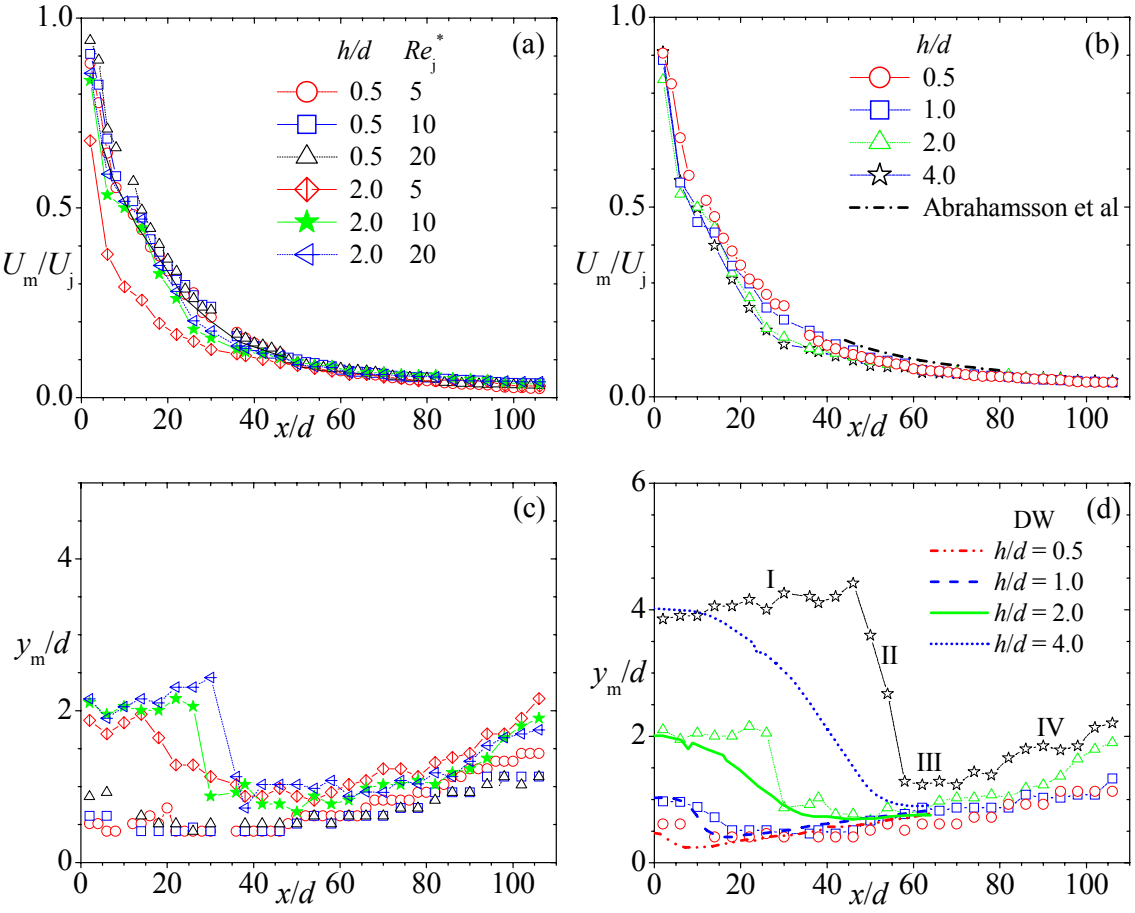

Figure 4.11: Variation of local maximum mean velocity, U_m in (a) and (b); and location of U_m, y_m in (c) and (d). Notation: DW – Davis & Winarto (1980).

h/d = 2.0, for example, $U_m/U_j \approx$ 30% and 50%, respectively, for Re_j = 5000 and 20000. This is partly explained by the more uniform velocity distribution and higher jet momentum flux at a higher Reynolds number than at a lower Reynolds number. However, at a fixed Reynolds number, U_m decays faster for h/d = 2.0 than 0.5. Further downstream ($60 \leq x/d \leq 100$), U_m values collapsed reasonably well for the three Reynolds numbers implying no significant Reynolds number effects. For a fixed Reynolds number at Re_j = 10000 in the region $2 \leq x/d \leq 40$, the decay is more rapid for a larger h/d (Fig. 4.11b). The U_m values for Re_j = 10000 also collapsed reasonably well for all offset heights.

Table 4.3: Decay and spread rates for a Reynolds number of 10000

Decay and spread rates			
h/d	n	$dy_{0.5}/dx$	$dz_{0.5}/dx$
0.5	1.15	0.054	0.255
1.0	1.16	0.054	0.254
2.0	1.17	0.056	0.250
4.0	1.20	-	0.245

The data in the region $x/d \geq 60$ are independent of Reynolds number. The decay of U_m is usually described by a power law of the form: $U_m \propto x^{-n}$, where n is the decay rate. The decay rates in this study were estimated by fitting the above power law to the U_m values in the region $60 \leq x/d \leq 100$. As can be seen in Table 4.2, the decay rates for the various test cases fall within the range $n = 1.17 \pm 0.03$. The R^2 values for the curve fit were at least 0.96 indicating the fit was good. The decay rates obtained in the present study also fall within the range of $1.00 \leq n \leq 1.29$ reported in the literature for generic

turbulent wall jets (Abrahamsson et al., 1997), and are comparable to $n = 1.15$ for offset jets (Davis & Winarto, 1980).

As mentioned earlier, the inner region ($y \leq y_m$) of the wall jet has characteristics similar to canonical wall bounded flows. Thus, the variation of y_m with x/d in Figs. 4.11c-d can be used to study the effects of Reynolds number and offset height on the growth of the inner shear layer. Figure 4.11c demonstrates that the y_m values increase with Reynolds close to the jet exit but become comparable from $x/d \approx 20$ and 40 for $h/d = 0.5$ and 2.0, respectively. In this range, the y_m values for $Re_j = 5000$ are slightly higher for both $h/d = 0.5$ and 2.0. With reference to Fig. 4.11d, the development of the inner shear layer can be divided into four regions (as indicated on the y_m profile for $h/d = 4.0$). Region I is adjacent to the exit section and is characterized by near constant values of y_m. This is followed by a sharp decrease in y_m (Region II) and another region, Region III, where y_m values remain nearly constant. In the final region (Region IV), y_m increases nearly linearly with x. The data for $h/d = 0.5$ and 1.0 are similar. For these two test cases, Region I is limited to $x/d \leq 10$. As the offset height increases, so does the streamwise extent of Region I ($x/d \leq 25$ for $h/d = 2$ and $x/d \leq 45$ for $h/d = 4$). Compared to the present results, Region I of the data reported by Davis & Winarto (1980) is much shorter, and the transition from Region I to Region III is more gradual, an indication that the flow field in this region is strongly dependent on initial conditions such as Reynolds number and nozzle type.

The jet half widths, $y_{0.5}$ and $z_{0.5}$, respectively, are a measure of the spread of the jet in the wall-normal and lateral directions. As shown in Figs. 4.12a, the $y_{0.5}$ values increase with Reynolds number close to the jet exit but collapsed from $x/d \approx 30$ and 70 for h/d

= 0.5 and 2.0, respectively. For a given Reynolds number (Re_j = 10000) the values of $y_{0.5}$ increase with h/d except for h/d = 0.5 and 1.0 where the data nearly collapsed onto each other. All the $y_{0.5}$ values are linear in the region $x/d \geq 72$ with the exception of h/d = 4.0 which needs an extended distance to become linear. It should be pointed out that the values of $y_{0.5}$ for the present generic wall jet (h/d = 0.5) are intermediate to the values reported in previous studies by Abrahamsson et al. (1997) and Davis & Winarto (1980).

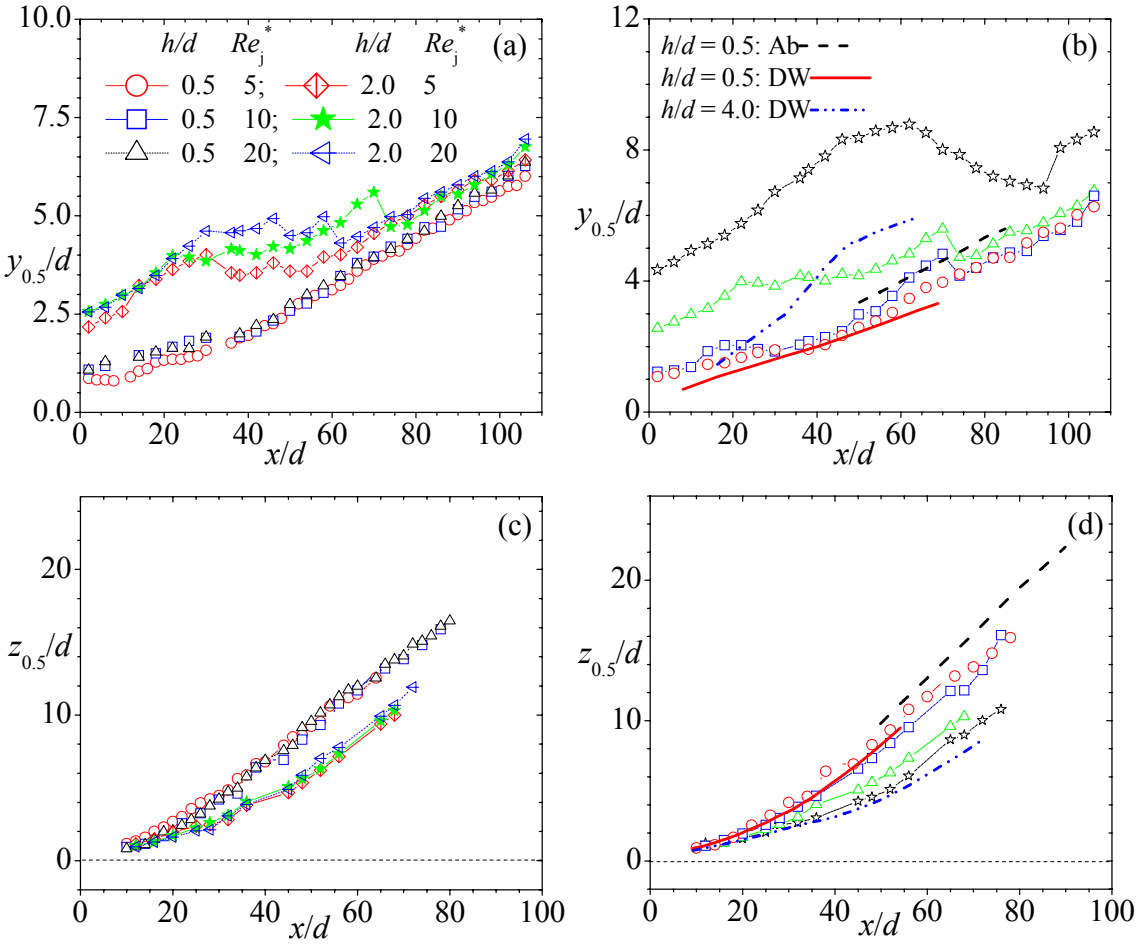

Figure 4.12: Variation of wall-normal jet half width, $y_{0.5}$ in (a) and (b); and lateral jet half width, $z_{0.5}$ in (c) and (d). Symbols in (c) are as in (a). Symbols of the previous data in (d) are as in (b). Symbols of the present data in (b) and (d) are as in Fig. 4.11b.

Unlike the wall-normal half width, the half width in the lateral direction ($z_{0.5}$) in Fig. 4.12c collapsed in the region $x/d \geq 10$.

The $z_{0.5}$ values consistently increased with x/d and became nearly linear in the region $x/d \geq 55$. The results for $h/d = 0.5$ and 2.0 clearly demonstrate that the spread in the lateral direction is not significantly dependent on Reynolds number. However, for a fixed Reynolds number (i.e., $Re_j = 10000$), the $z_{0.5}$ values decrease with increasing h/d. As shown in Fig. 4.13, the large differences observed in the $z_{0.5}$ values diminished dramatically when the half width ($z_{0.5}$) is offset by the corresponding offset height (h) such that $z^{**} = (z_{0.5} + h)/d$ is plotted rather than $z_{0.5}/d$.

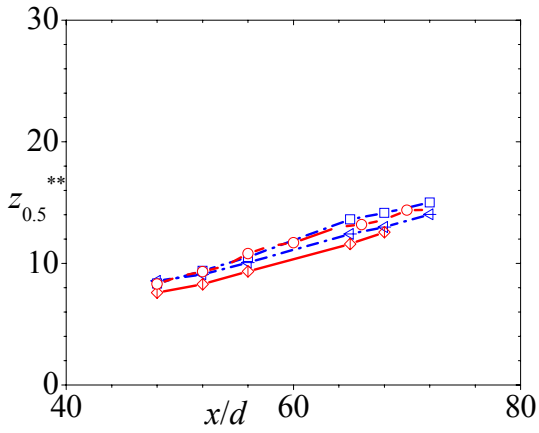

Figure 4.13: Variation of lateral jet half width, $z_{0.5}$ with the scaling $z_{0.5}^{**} = (z_{0.5} + h)/d$. Symbols are as in Fig. 4.12d.

Following previous studies, the spread rates were estimated as the gradient (i.e., $dy_{0.5}/dx$ or $dz_{0.5}/dx$) of the linear fit to the measured data. For the wall-normal direction, the spread rate could not be determined for the test case $h/d = 4$ due to lack of extended

linear region. The spread rates ($dy_{0.5}/dx$ and $dz_{0.5}/dx$) for the various test cases are reported in Table 4.2. The $dy_{0.5}/dx$ values for h/d = 0.5 and 1.0 are identical while the corresponding values for h/d = 2 is only 4% higher. The present values are consistent with 0.050 ± 0.015 reported in the literature for generic turbulent wall jets. However they are larger than $dy_{0.5}/dx$ = 0.041 ± 0.005 obtained by Davis & Winarto (1980) for h/d = 0.5 to 4.0. It is worth pointing out that the increase in $y_{0.5}$ with x is much more than that of y_m with the implication that the effect of the outer region on the inner layer increases with x/d (Abrahamsson et al., 1997). The spread rate in the lateral direction ($dz_{0.5}/dx$ = 0.250 ± 0.005) is also nearly independent of offset height. These values fall within the range of 0.25 ± 0.08 reported in the literature for generic turbulent wall jets. Davis & Winarto (1980) reported values of $dz_{0.5}/dx$ = 0.33, 0.29, and 0.23 for h/d = 1, 2, and 4, respectively. These values show decreasing trend with h/d similar to the present results although the decrease is more dramatic than in the present. The present results are consistent with anisotropic spread rate reported in previous studies. In the present study, the ratio $(dz_{0.5}/dx)/(dy_{0.5}/dx)$ varies from 4.5 to 4.7 compared to values in the range of 3.7 to 8.6 for generic jets (Davis & Winarto, 1980; Swamy & Bandyopadhyay, 1975) and 5.0 to 9.2 for offset jets reported by Davis & Winarto (1980).

4.2.2 Mean velocities

In this section, the present results in the similarity region are compared with previous results in the literature. Since it was shown in the previous section that there is no Reynolds number effect in the self-similar region a single Reynolds number is used. The Reynolds number, Re_j =10000 is employed because measurements were performed

for all the offset heights (Table 3.1). In addition, only the location at $x^*/d = 60$ in the self-similar region is considered.

4.2.2.1 Symmetry (*x*-*y*) plane

Figure 4.14 shows profiles of the mean velocities. The present profiles from the wall to $y/y_{0.5} = 1.5$ are in very good agreement with each other irrespectively of h/d and data from previous 3D turbulent wall jets. Even the 2D turbulent wall jet of Karlsson et al. (1992) collapsed in this region. In the outer region ($y/y_{0.5} > 1.5$), however, differences are found among the various profiles. The lack of collapse is usually attributed to the measurement technique employed. Venas et al. (1999) compared turbulent wall jet data from standard HWA, pulsed HWA and LDA, and found that the turbulence intensities in the outer edge of the jet are in good agreement for the pulsed HWA and LDA data which are higher than the data from the standard HWA. The profiles presented in Fig. 4.14 demonstrate that the discrepancy cannot be attributed to experimental techniques alone. This observation is based on the premise that data from the same techniques (e.g., hotwire data of Abrahamsson et al., 1997 and Padmanabham & Gowda, 1991a, b) do not collapse. In addition, profiles from the different h/d values of the present study do not collapse. It, therefore, appears that the outer edge of the flow is strongly dependent on the specific jet exit conditions.

The values of V in the present and previous 3D turbulent wall jet studies (Fig. 4.14b) are negative across the flow. The profiles in the present study are larger in magnitude than in the previous 3D turbulent wall jet studies. In contrast, the 2D turbulent wall jet (Karlsson et al., 1992) has positive V values in the region $y/y_{0.5} \leq 1.4$. The V

values are similar for h/d = 0.5 and 1.0 and are comparable with those of Abrahamsson et al. (1997). The V profiles for h/d = 2.0 and 4.0 are also similar from the wall to $y/y_{0.5} \approx$ 0.8. Beyond this the values for h/d = 2.0 decay slowly towards zero while that for h/d = 4.0 decayed quickly to zero at $y/y_{0.5} \approx 1.1$. With the exception of h/d = 4.0 in the region $y/y_{0.5} \geq 0.8$, $\partial V/\partial y$ is predominantly negative for the 3D jets but positive for the 2D wall jet. This is consistent with previous studies. The implication of this observation is that both the mechanism for the production of v^2 and wall-normal momentum transport for 3D jets are different from the 2D wall jets. For example, the negative $\partial V/\partial y$ values for the 3D jets would augment the production of v^2 and turbulence kinetic energy while the positive $\partial V/\partial y$ values for the 2D wall jets will decrease the production of v^2 and turbulence kinetic energy

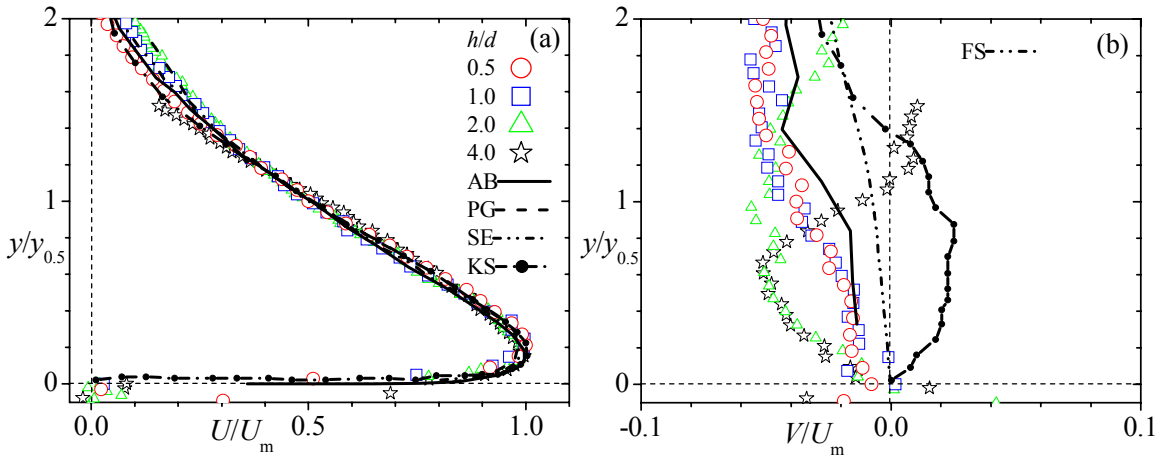

Figure 4.14: Profiles of mean velocities. Streamwise U in (a) and wall-normal V (b) in the x-y plane. Notation: AB – Abrahamsson et al. (1997); PG - Padmanabham & Gowda (1991a, b); SE - Sun & Ewing (2002a, b); KS - Karlsson et al. (1992); WF - Wygnanski & Fiedler (1969); FS - Fujisawa & Shirai (1989).

4.2.2.2 Lateral (*x*-*z*) plane

The streamwise (U) and lateral (W) mean velocity profiles in the lateral plane are shown in Fig. 4.15. Similar to the profiles of U in the *x*-*y* plane, the present U profiles in the lateral plane collapsed reasonably well with previous 3D wall jets results in the region $z/z_{0.5} < 1.4$ as well as the free round jet profile of Wygnanski & Fiedler (1969).

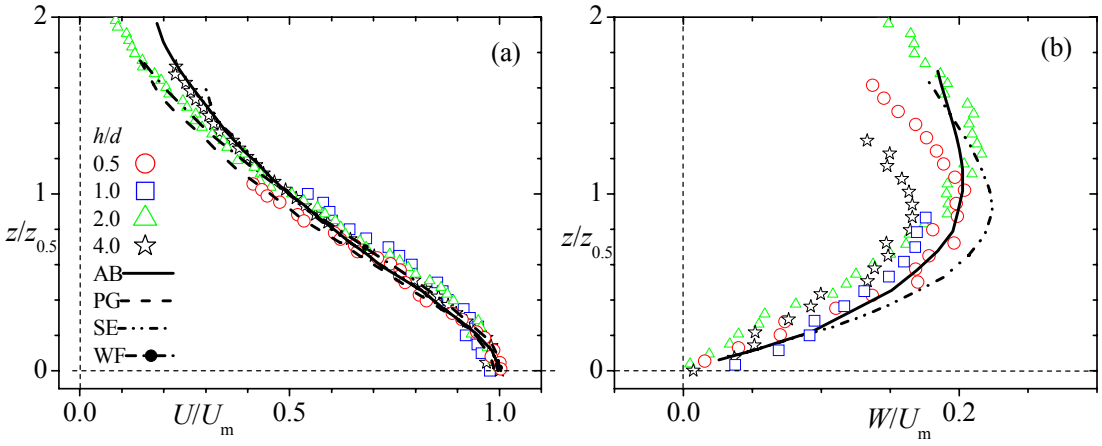

Figure 4.15: Profiles of mean velocities. Streamwise U in (a) and lateral W (b) velocities in the *x*-*z* plane. Reference notations are as in Fig. 4.14.

Similar to the *x*-*y* plane, differences are found among the various profiles in the outer most region ($z/z_{0.5} > 1.5$) of the flow. The W profiles for $h/d = 0.5$ increased from zero in the symmetry plane to about $0.2U_m$ at $z/z_{0.5} = 1.0$. The present W profile compare very well with that of Abrahammson et al. (1997) but are less than the W profile of Fujisawa & Shirai (1989) in the region $z/z_{0.5} < 1.0$. The W values for $h/d = 2.0$ and 4.0 are also similar in the region $z/z_{0.5} < 0.8$ but these are also less than the value for $h/d = 0.5$ and 1.0. It is evident from the figures that the lateral mean velocities are much higher than wall-normal

mean velocities. This is consistent with the observed larger lateral spread of the jets than their wall-normal spread.

4.2.3 Turbulence intensities and Reynolds shear stresses

4.2.3.1 Symmetry (*x*-*y*) plane

The profiles of *u*, *v*, and *uv* obtained in the present study are shown in Fig. 4.16. The profiles of some previous studies are also shown for comparison. The figure shows a reasonable collapse of the profiles of the present study but there are some discrepancies among the various studies. The present data compare favourably with those of Padmanabham & Gowda (1991a, b) up to $y/y_{0.5} \approx 1.3$. Beyond that location, their profile decayed rather faster. The profiles of the rest of the other previous studies are much lower than those obtained in the present study. The peak values of *u* and *v* of the present study are 38% higher than reported by Abrahammson et al. (1997). The differences can be partly attributed to the higher background turbulence levels. Because of the intense interaction between the inner and outer regions, the high turbulence levels observed in the outer region are evident in the inner region. Figure 4.16c shows that the shear stress profiles changed sign at $y/y_{0.5} \approx 0.1$ which is less than y_m and consistent with previous studies. Although *u* and *v* values of Padmanabham & Gowda (1991a, b) are comparable to the present study, their shear stress values are much lower. This would imply that the correlation coefficient between *u* and *v* is much smaller than that in the present study. The peaks of *uv* are up to 52% higher than reported by Sun & Ewing (2002a, b).

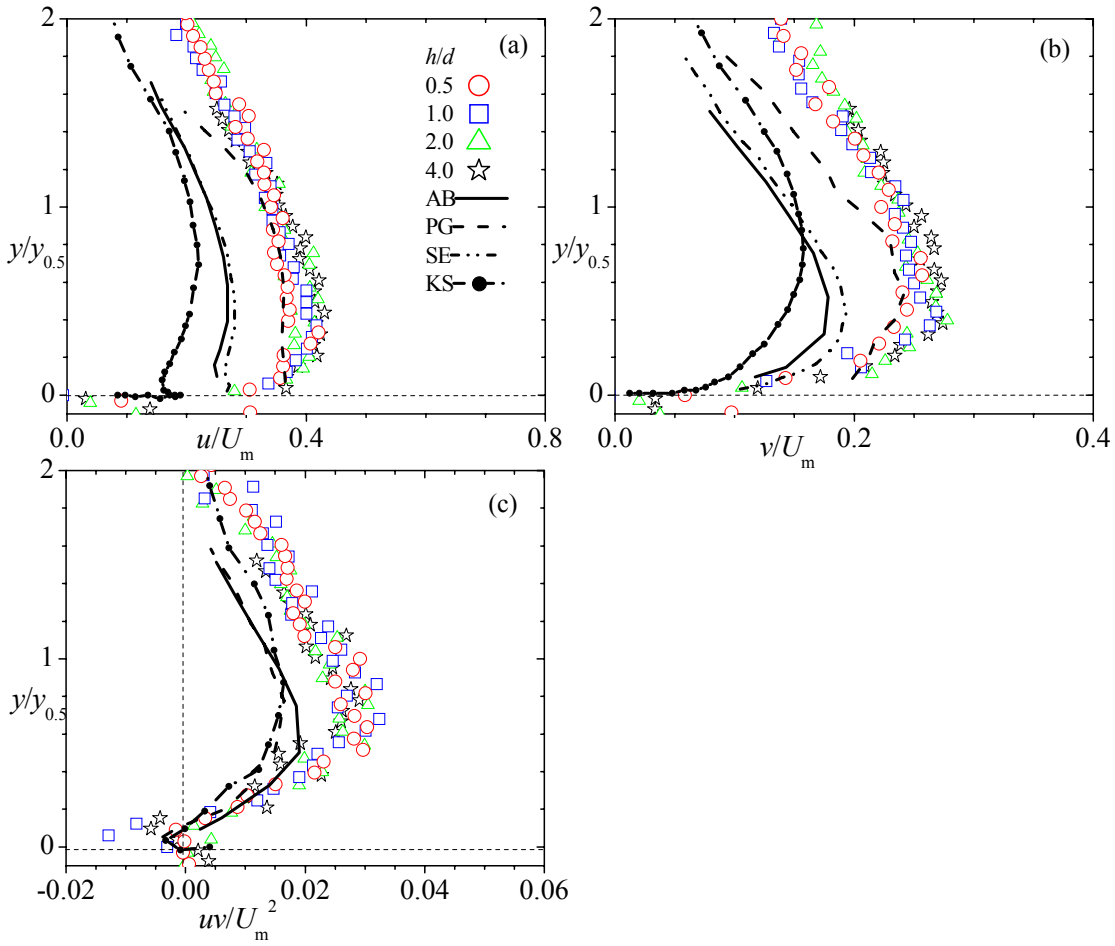

Figure 4.16: Profiles of turbulence intensities and Reynolds shear stresses in the *x*-*y* plane. Streamwise *u* (a), wall-normal *v* (b); and Reynolds shear stresses *uv* (c). Reference notations are shown in Fig. 4.14.

4.2.3.2 Lateral (*x*-*z*) plane

The profiles of *u*, *w*, and -*uw* are reported in Fig. 4.17. There is a reasonable agreement among the present *u* profiles which are up to 17% higher than Padmanabham & Gowda (1991a, b). The free round jet profile of Wygnanski & Fiedler (1969) has lower peaks but decays more slowly from $z = 0$. For example, from $z/z_{0.5} = 0$ to $z/z_{0.5} = 1.0$, the

peak value in the study of Wygnanski & Fiedler (1969) decayed by only about 10% compared to 48% in the present study. Since the spanwise profiles for the wall jet were extracted at y_m (which is only about 3 to 6 mm above the solid wall in the present study), the more rapid reduction observed for u in the 3D turbulent wall jet than the free round jet may be due to wall damping effects in the 3D turbulent wall jet. The present profiles

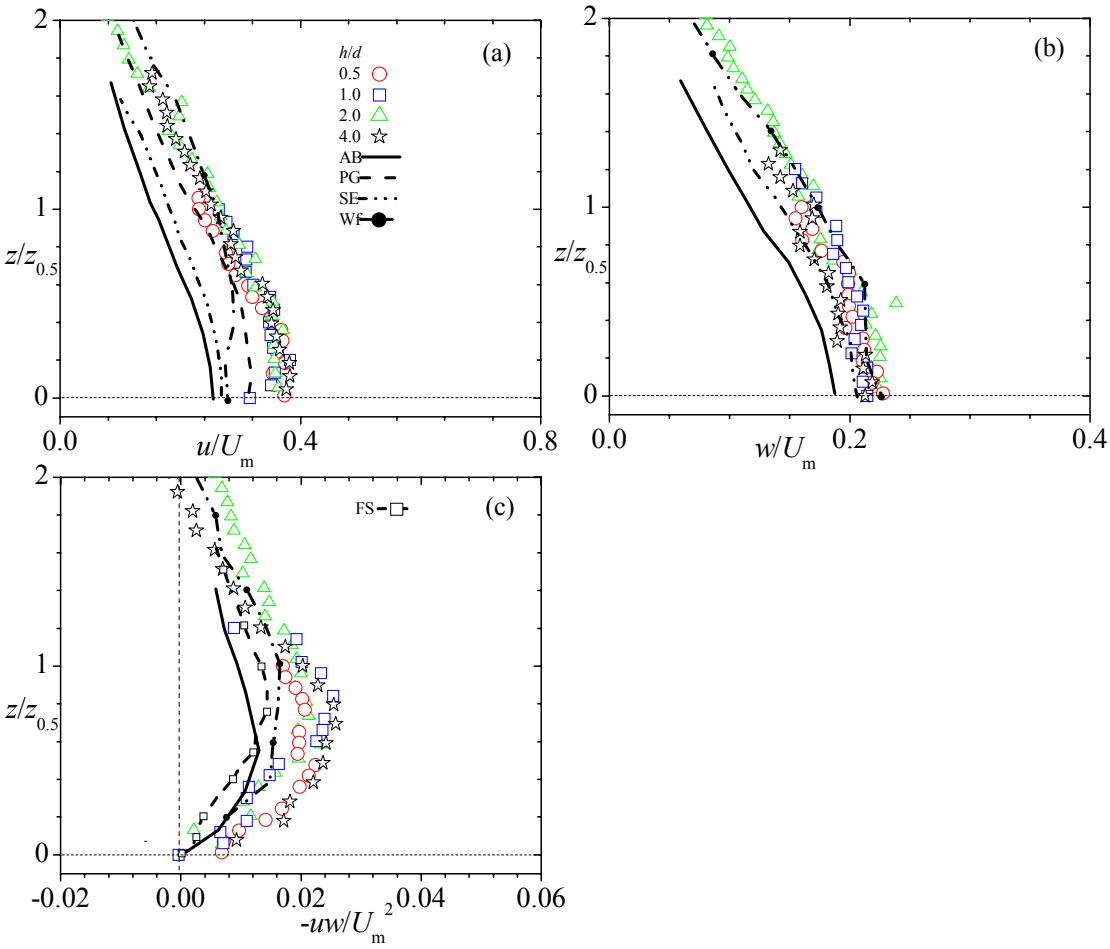

Figure 4.17: Profiles of turbulence intensities and Reynolds shear stresses in the x-z plane. Streamwise u (a), lateral w (b); and Reynolds shear stresses $-uw$ (c). Reference notations are shown in Fig. 4.14.

of w are comparable to the profiles of free jet reported by Wygnanski & Fiedler (1969). The values of Abrahammson et al. (1997) are about 14% lower than the present values. The $-uw$ profiles of the present study are higher than in previous studies. The peak values of the present study are about 65% higher than those of Abrahamsson et al. (1997). The free round jet profile of Wygnanski & Fiedler (1969) has a peak of about 30% lower. The peak values of the turbulence statistics in the lateral plane are generally lower than those in the symmetry plane. In fact, the maximum value of u is about 8% lower than the u value in the symmetry plane. Similarly, the maximum values of w and $-uw$ are about 18% and 30%, respectively, lower than the values of v and uv in the symmetry plane.

4.2.4 Stress ratios, triple velocity products and budget terms

In this section, the stress ratios, the triple velocity products, and some of the budget terms in the symmetry plane are reported and discussed. As mentioned in Chapter 2, there is considerable scatter in these quantities in the x-z plane and are therefore not reported.

4.2.4.1 Stress ratios

The two-equation turbulence models are still popular RANS models in the fluid engineering community. In these models, an isotropic assumption is implied. In many engineering shear flows, however, the turbulence fluid is anisotropic. It is therefore useful to evaluate the degree of isotropy in the present fluid flow. The distribution of the stress ratios such as v^2/u^2 and $uv/2k$ would provide insight into the large scale anisotropy and Townsend's structure parameter. The locations in Fig. 4.18 were selected to represent

Regions II, III, and IV as indicated in Fig. 4.11d. Figure 4.18a shows the ratio v^2/u^2 which is indicative of the degree of anisotropy. As indicated in the figure, the anisotropy decreased from $v^2/u^2 \leq 0.3$ in the inner region to values of up to 0.5 in the outer region. The v^2/u^2 for generic wall jet ($h/d = 0.5$) increased consistently with x/d (from Region II to IV) by about 20% in peak values. There is no consistent change in the values for h/d = 2.0 but the values for $h/d = 4.0$ collapsed fairly well. Interestingly, the v^2/u^2 values for h/d = 0.5 and 4.0 in the outer region are similar while the values for $h/d = 2.0$ are higher. In the inner region, the maximum value of the stress ratios are approximately 0.25, 0.33 and 0.37, respectively, for h/d = 0.5, 2.0 and 4.0. These values are all less than typical values of 0.46 and 0.73, respectively, for the inner and outer regions of a boundary layer reported by Townsend (1980). Furthermore, the stress ratios in the outer regions of these jets are $v^2/u^2 \approx 0.45$, 0.60, and 0.46 for h/d = 0.5, 2.0 and 4.0, respectively. The outer region can be compared to a plane jet. The stress ratios of a plane jet are $v^2/u^2 \approx 0.69$ (Townsend, 1980), which are much higher than the values for h/d = 0.5 and 4.0 of the present study.

Townsend's structure parameter $-uv/2k$ is important for calibrating turbulence models. In the present study, the lateral component of the normal stress w^2 was not measured and so the w^2 values in the symmetry plane were estimated from $k = 0.75(u^2 + v^2)$, where $w^2 \approx 0.5(u^2 + v^2)$. The structure parameter is typically taken as 0.15 in zero-pressure gradient flows. For example, a value of $-uv/2k$ = 0.15 or 0.12 have been specified in the turbulence models proposed by Harsha & Lee (1970) and Launder et al. (1975), respectively. Figure 4.18b shows that $uv/2k < 0.05$ in the inner region and increased to peak values of up to 0.13 in the outer region. The peaks of $uv/2k$ increased

with x/d from Region II to IV by 40% and 13% at $y^* \approx 0.9$ for h/d = 0.5 and 2.0, respectively, but decreased with increasing h/d from $uv/2k = 0.12 \pm 0.02$ at h/d = 0.5 to 0.07 ± 0.02 at h/d = 4.0; more than a 60% drop. Based on these results, the appropriate choice of Townsend's structure parameter should depend on h/d and x/d. The present results show that turbulence models based on isotropic assumptions cannot accurately predict the present flow. Furthermore, the commonly used value of the Townsend parameter ($-uv/2k = 0.15$) is not appropriate for the present flow.

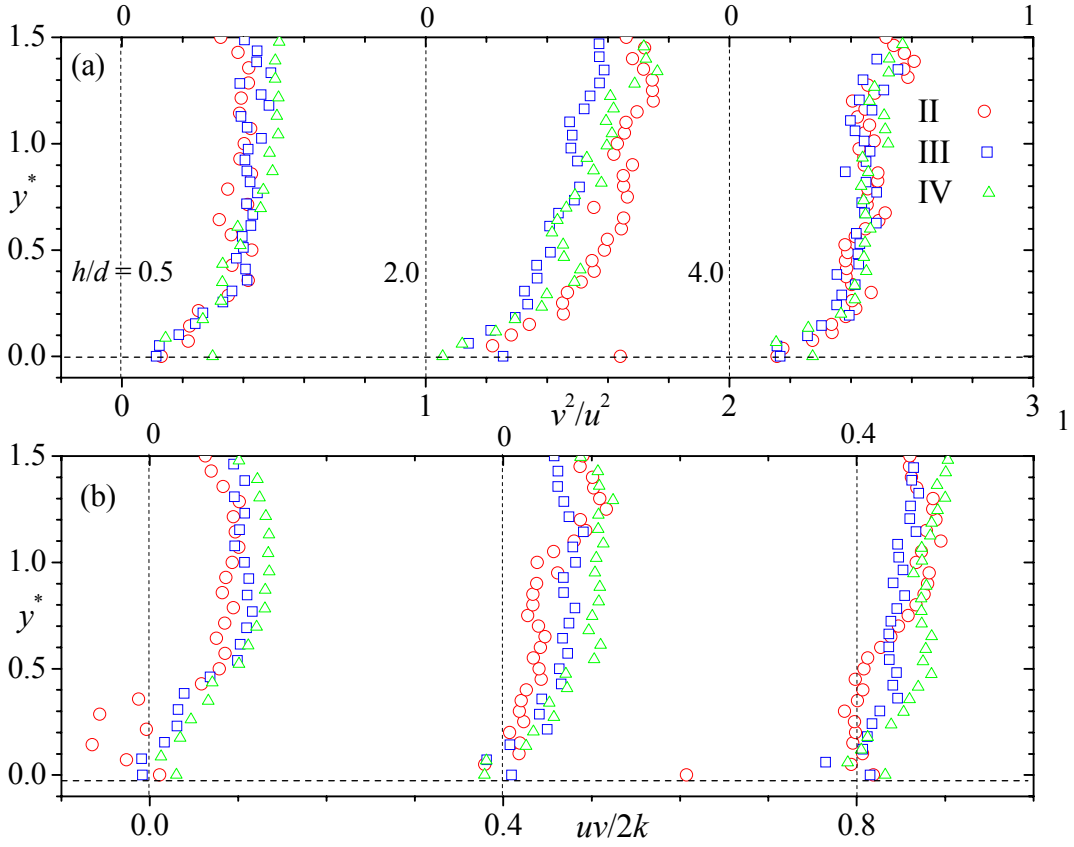

Figure 4.18: Profiles of the turbulence structural parameters (a) v^2/u^2, and (b) $uv/2k$ in the symmetry plane. $y^* = y/y_{0.5}$.

4.2.4.2 Triple velocity products

As stated in Chapter 2, the triple velocity products are also important because their gradients constitute the turbulent diffusion terms in the transport equations for the turbulent kinetic energy and Reynolds stresses. Thus, profiles of the triple velocity products would provide guidance for modeling the turbulent diffusion term in the turbulent kinetic energy and Reynolds stress transport equations. The following triple products, u^3, uv^2, u^2v, and v^3 at $x^*/d = 20$, 40 and 80 in the symmetry plane are reported in Fig. 4.19 with U_m and $y_{0.5}$ as the velocity and length scales, respectively. The figure shows that the triple products are predominantly positive. With the exception of $h/d = 4$, the triple products at $x^*/d = 20$ are negative close to the wall. The magnitudes of the negative values decrease with increasing x/d. The location of sign change in u^2v and uv^2 is much closer to the wall than the peak values of uv. For 2D wall jets, the sign change of u^2v and uv^2 occurs at $y^* \approx 0.75$ (Irwin, 1973) which are much farther from the wall than observed for the present 3D generic and offset jets. This can be attributed to the stronger effect of the outer region on the inner region in the 3D wall jet than the 2D wall jet (Abrahamsson et al., 1997). The profiles of uv^2, u^2v, and v^3 have comparable values with peaks values occurring at $y^* \approx 1.0$. However, the profiles of u^3 are up to two times larger than the other products. In addition the peaks for $h/d = 0.5$ and 2.0 at $x/d = 80$ as well as $h/d = 2$ at $x/d = 20$ occurred at $y^* \approx 0.6$. The triple products (u^2v and v^3) reported by Abrahamsson et al. (1996) at $x^*/d = 80$ have similar trends but their values are less than half of the values in the present study. In addition, the u^2v values are all positive even though uv was reported to sign close to the wall, while v^3 changed sign at $y^* \approx 0.25$ compared to $y^* \approx 0.5$ in the present. The present results (u^2v, uv^2, and v^3) imply that

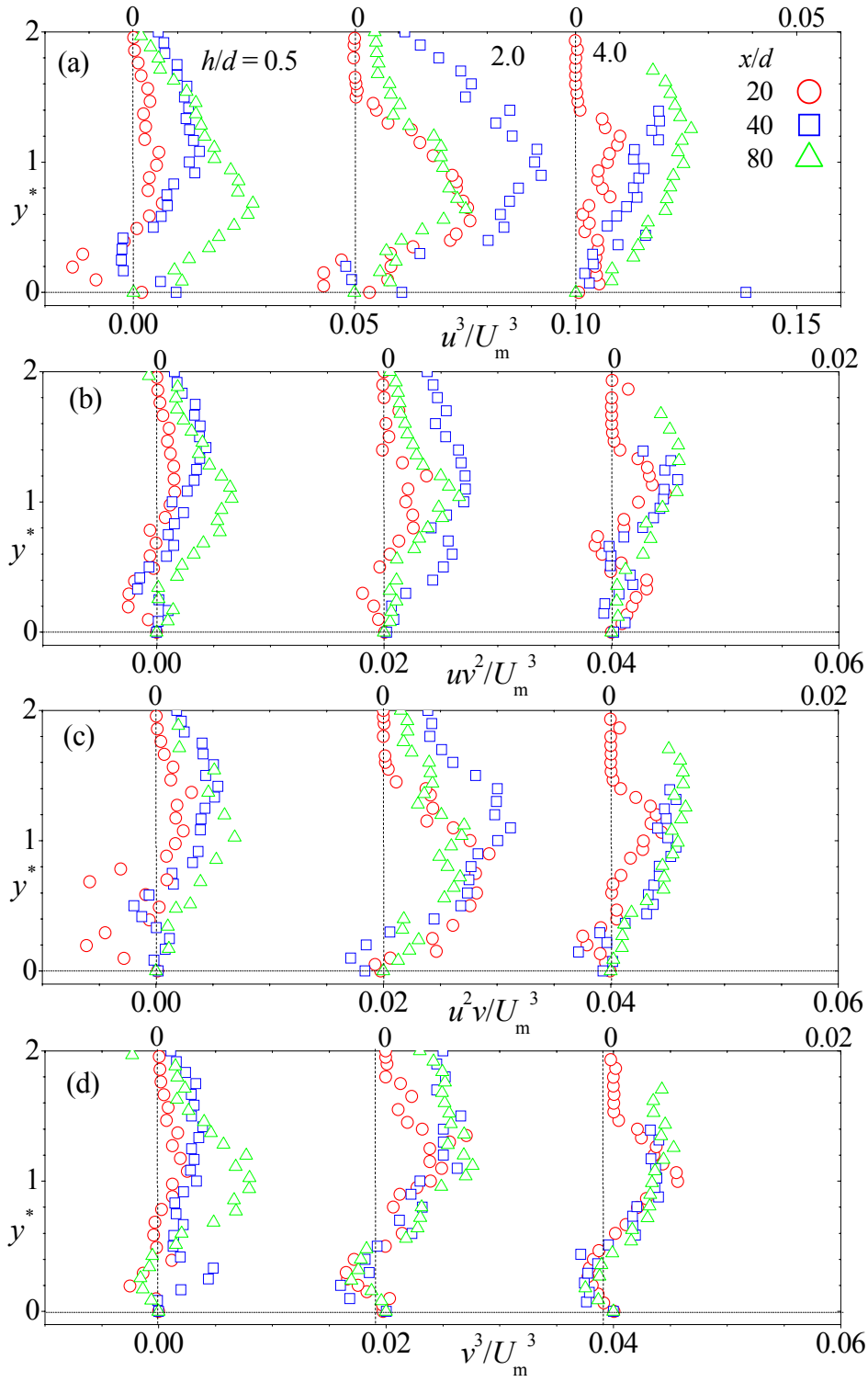

Figure 4.19: Profiles of the triple velocity products in the symmetry plane. (a) u^3, (b) u^2v, (c) uv^2, and (d) v^3. $y^* = y/y_{0.5}$.

turbulent kinetic energy and Reynolds shear stress are largely transported from the outer region (i.e., $y^* \approx 0.6$ to 1.0) to the wall region and outer edge of the jet.

4.2.4.3 Energy budget terms

The production (P_k), dissipation (ε_k), and advection (C_k) terms in the symmetry plane are reported at x^*/d = 20 and 60 representing the developing and self-similar regions, and Re_j = 10000. The goal is to study how these quantities change with h/d when U_m and $y_{0.5}$ are used as the velocity and length scales, respectively. Note that as in many of the earlier plots some of the points are skipped to reduce data congestion. The profiles of the individual components (not shown here) show that the net contribution from the normal stresses ($u^2\partial U/\partial x$ and $v^2\partial V/\partial y$) and the term $uv\partial V/\partial x$ are small making $-uv\partial U/\partial y$ the major contributor to P_k. Figure 4.20a,c,e compares the profiles of $-uv\partial U/\partial y$ and P_k for h/d = 0.5, 2.0 and 4.0, respectively. For h/d = 0.5 the profile of $-uv\partial U/\partial y$ is much closer to P_k at x^*/d = 20 than 60 (Fig. 4.20a). However, for h/d = 2.0 and 4.0, the reverse is true; i.e., the profiles $-uv\partial U/\partial y$ are much closer to P_k at x^*/d = 60 than 20 (Fig. 4.20c,e). This difference can be attributed to the contribution from the term $(u^2 - v^2)\partial V/\partial y$, which obviously depends strongly on the gradient $\partial V/\partial y$. From the mean velocities (Fig. 4.3), it is evident that the gradients are more significant at x^*/d = 60 than 20 for for h/d = 0.5. However, for the offset jets (Fig. 4.4b) the gradients appear to be more significant at x^*/d = 20 than 60. The sign of P_k is dependent on $\partial U/\partial y$ since uv is always positive except very close to the wall. The values of P_k in Fig.4.20b are negative very close to the wall ($y/y_{0.5} < 0.18$) but increased rapidly to positive values with peaks at $y/y_{0.5} \approx 0.8$ at x^*/d = 20 and $y/y_{0.5} \approx 0.6$ at x^*/d = 60 before decreasing to negligible values at $y/y_{0.5} \approx 1.8$. Note

that the negative values close to the wall especially for h/d = 0.5 and 2.0 are missing because of the skipping of some of the data. Figure 4.20b is replotted as Fig. D.3 in Appendix D for only h/d = 0.5 and 2.0 with less skipping to reveal the negative values close to the wall. The trend in P_k is similar to that of Abrahamsson et al. (1997), but the present profiles are much higher. The P_k profiles clearly increase with h/d values at x^*/d = 20 but at x^*/d = 60 the profiles are comparable. The resolution of the PIV system used in present study is not high enough to completely resolve the contributions of the fine scales to the dissipation rate. However, the trends in the data are valuable. The profiles shown in Fig. 4.20d revealed that the dissipation rate is negative (a sink) and fairly high across most of the jet. The dissipation profiles increase with both h/d and x/d. The profiles for h/d = 4.0 is similar to that reported by Abrahamsson et al. (1997). Notwithstanding the inability to resolve the contribution from the small scales to the dissipation rate, it is obvious from Figs. 4.20b and 4.20d that the magnitude of the dissipation rate is significantly lower than the production. Thus turbulence models that assume local equilibrium (i.e., production = dissipation) will not be able to accurately predict the flow. Figure 4.20f shows that the profiles of C_k have both positive and negative values similar to the values reported by Abrahamsson et al. (1997). However, the present values changed from negative to positive at earlier $y/y_{0.5}$ values ($y/y_{0.5} \approx 0.5$ compared to $y/y_{0.5} \approx 1.0$) and also has more negative values. The C_k profiles have no consistent trend with h/d but are more negative at x^*/d = 60 than at x^*/d = 20.

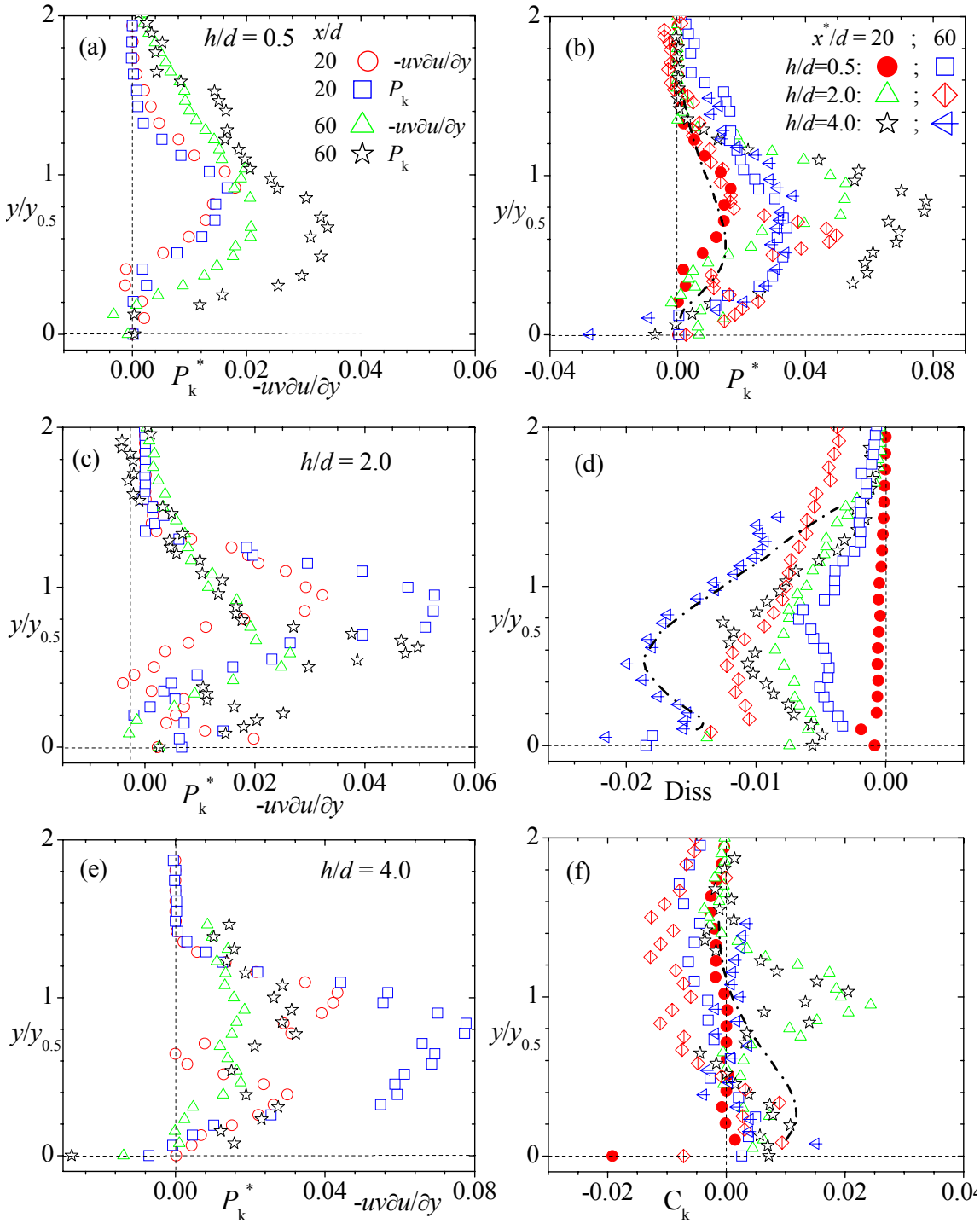

Figure 4.20: Energy budget terms. Comparison f production terms: P_k and $-uv\partial U/\partial y$ in (a), (c) and (e). (b) Production, P_k; (d) Dissipation, *Diss*; and (f) Convection, C_k.

4.3 Two-point correlation

The two-point correlations were used to examine how the turbulence structures are correlated at x/d = 15 and 75 representing the developing and self-similar regions, respectively. The procedure outlined in Chapter 2 was employed, where the auto-correlations in the streamwise and wall-normal directions are denoted by R_{uu} and R_{vv}, respectively. The average sizes of the iso-contours of R_{uu} and R_{vv} as well as the average inclinations of R_{uu} were estimated and discussed.

4.3.1 Two-point correlations in the symmetry plane

The iso-contours of R_{uu} and R_{vv} at y/y_m = 0.5 and 2.0 representing the inner and outer regions, respectively, are shown in Figs. 4.21-4.24. The iso-contour levels range from 0.6 (outermost iso-contour line) to 1.0 (centre of the iso-contours) at 0.1 intervals.

In the developing region, the iso-contours of R_{uu} (Fig. 4.21) in the inner region are relatively more rounded but smaller than in the outer region. The iso-contours appear to increase in size with the offset height (h/d). In addition, these iso-contours grow in size in the outer region. While the iso-contours of the generic wall jet (h/d = 0.5) become even more rounded in the outer region, those of the offset jets (h/d = 2.0 and 4.0) are elongated in the streamwise direction. This is indicative of the more correlated streamwise turbulence in the offset jets compared to the generic wall jet. In the self-similar region, the R_{uu} iso-contours are all elongated in the streamwise direction. In addition, the iso-contours in the inner region are inclined whereas those in the outer region are not. The shape of the iso-contours in the inner region

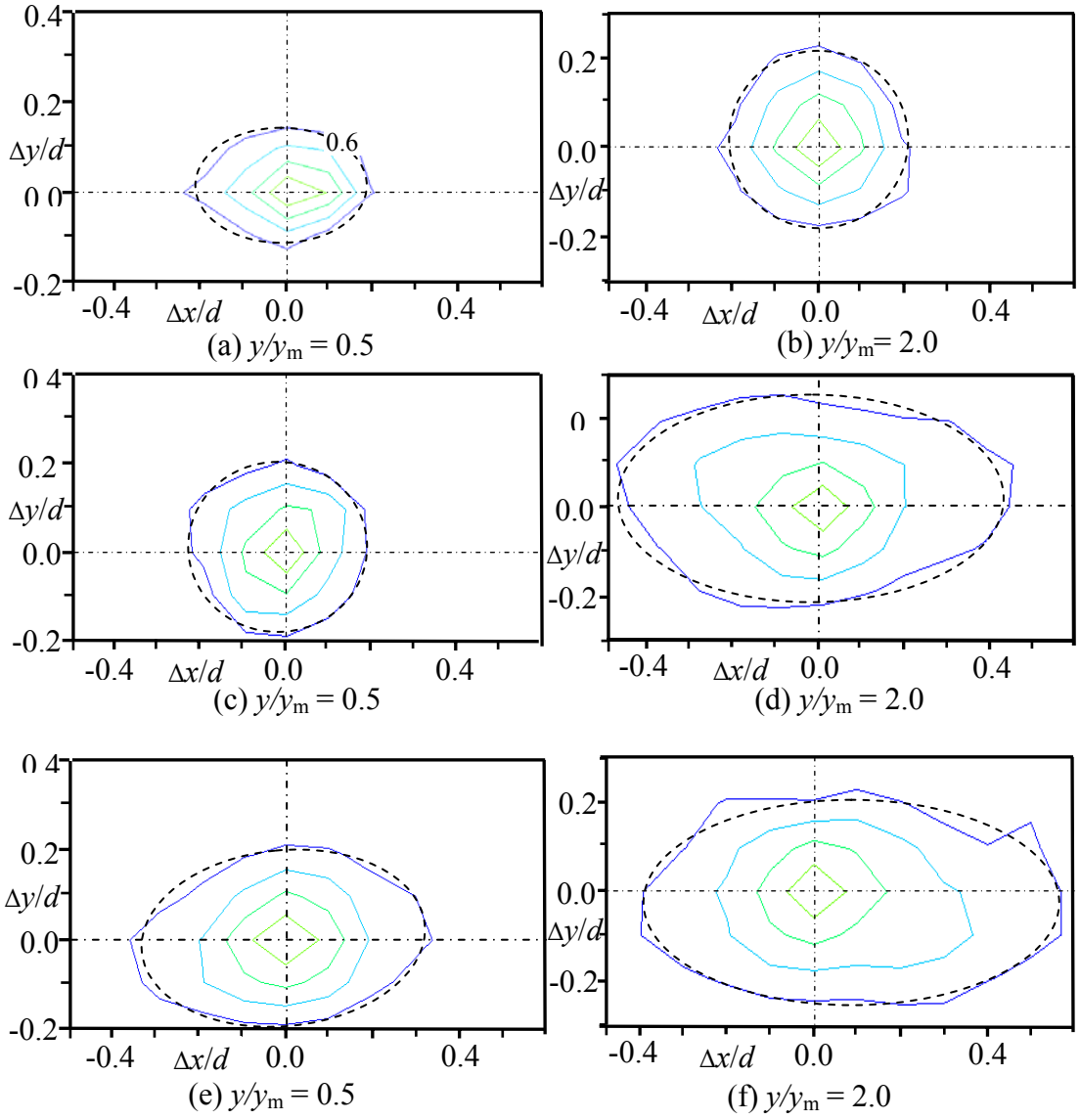

Figure 4.21: Iso-contours of two-point correlation for the streamwise (u') fluctuating velocities (i.e., R_{uu}) in the developing region, x/d = 15 in the x-y plane. The wall-normal locations (y/y_m) are indicated. Offset heights: h/d = 0.5 in (a) and (b); h/d = 2.0 in (c) and (d); and h/d = 4.0 in (e) and (f).

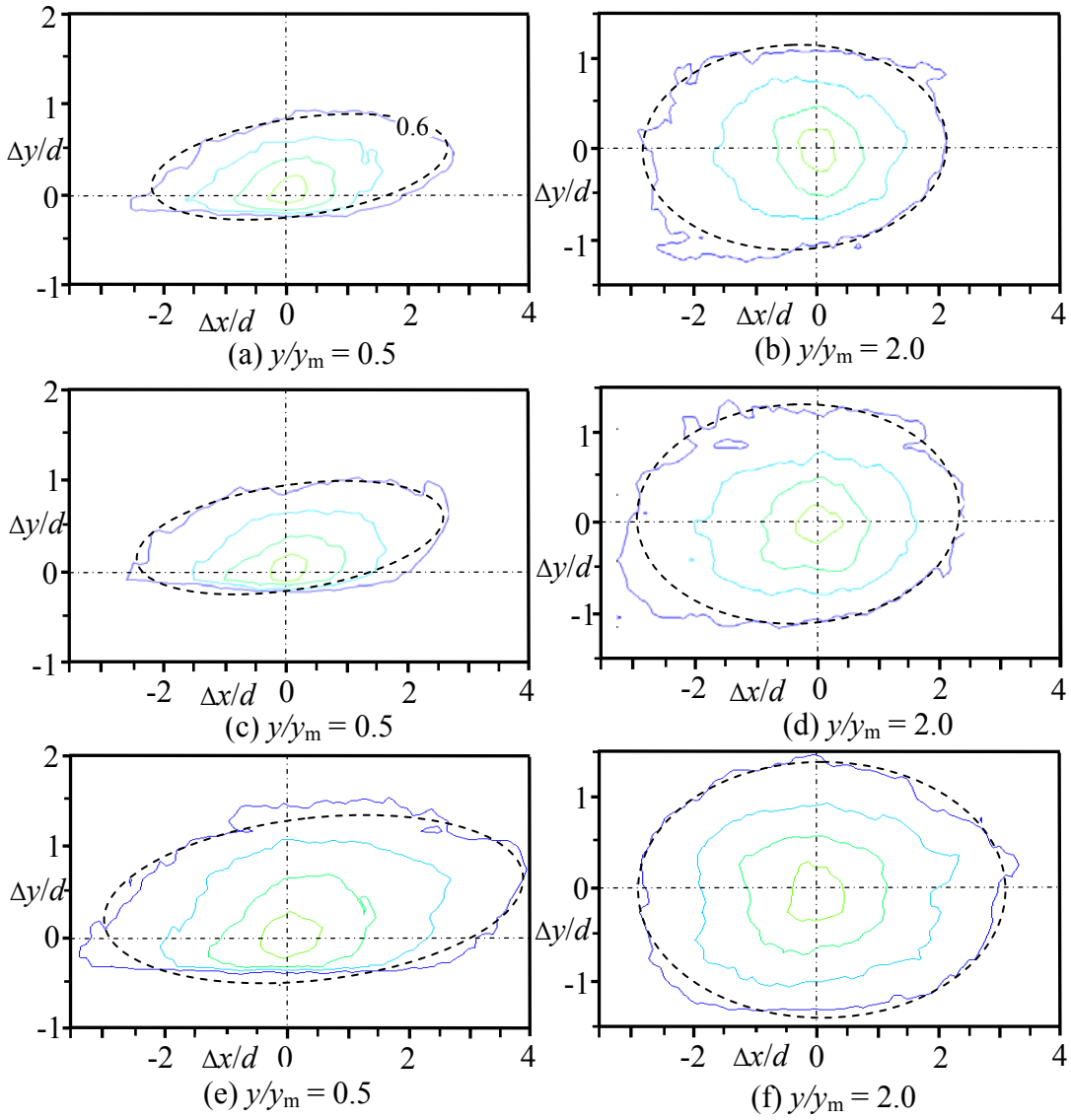

Figure 4.22: Iso-contours of two-point correlation for the streamwise (u') fluctuating velocities (i.e., R_{uu}) in the self-similar region, x/d = 75 in the x-y plane. The wall-normal locations (y/y_m) are indicated. Offset heights: h/d = 0.5 in (a) and (b); h/d = 2.0 in (c) and (d); and h/d = 4.0 in (e) and (f).

resembles those in a boundary layer (Volino et al., 2007). The sizes and inclinations of R_{uu} are estimated in the subsequent paragraphs. The iso-contours of R_{vv} (Figs. 4.23-4.24) in inner and outer regions are relatively more rounded than the iso-contours of R_{uu} but are smaller in size. The R_{vv} iso-contours in the outer region are larger in size than those in the inner region for the same reason explained in earlier. Similar to the R_{uu} iso-contours, the R_{vv} iso-contours at corresponding locations are much larger in the self-similar region than the developing region.

The iso-contours of R_{vv} are more correlated in the wall-normal direction than in the streamwise direction. In addition, the suppression of the R_{vv} iso-contours in the inner layer by the wall is also evident in the figure. The plots also reveal that the iso-contours increase in size with the offset heights. The sizes and inclinations of R_{uu} are also estimated in the subsequent paragraphs.

In summary, the iso-contours of both R_{uu} and R_{vv} are larger in the outer region than in the inner layer. In addition, the iso-contours in the self-similar regions (i.e., x/d = 75) are much larger in size than the corresponding iso-contours in the developing region. This indicates that the turbulence fluctuations are correlated over more extended distances in the outer and self-similar regions than in the inner and developing regions. This implies large scale structures exist in the outer region.

One-dimensional two-point correlation profiles extracted along the streamwise and wall-normal direction (dash lines in Figs. 4.21-4.24) in the inner region are shown in Fig. 4.25. These profiles are used to quantitatively study the decay of the auto-correlations in the streamwise and wall-normal directions. Note that R_{uu}(x) and

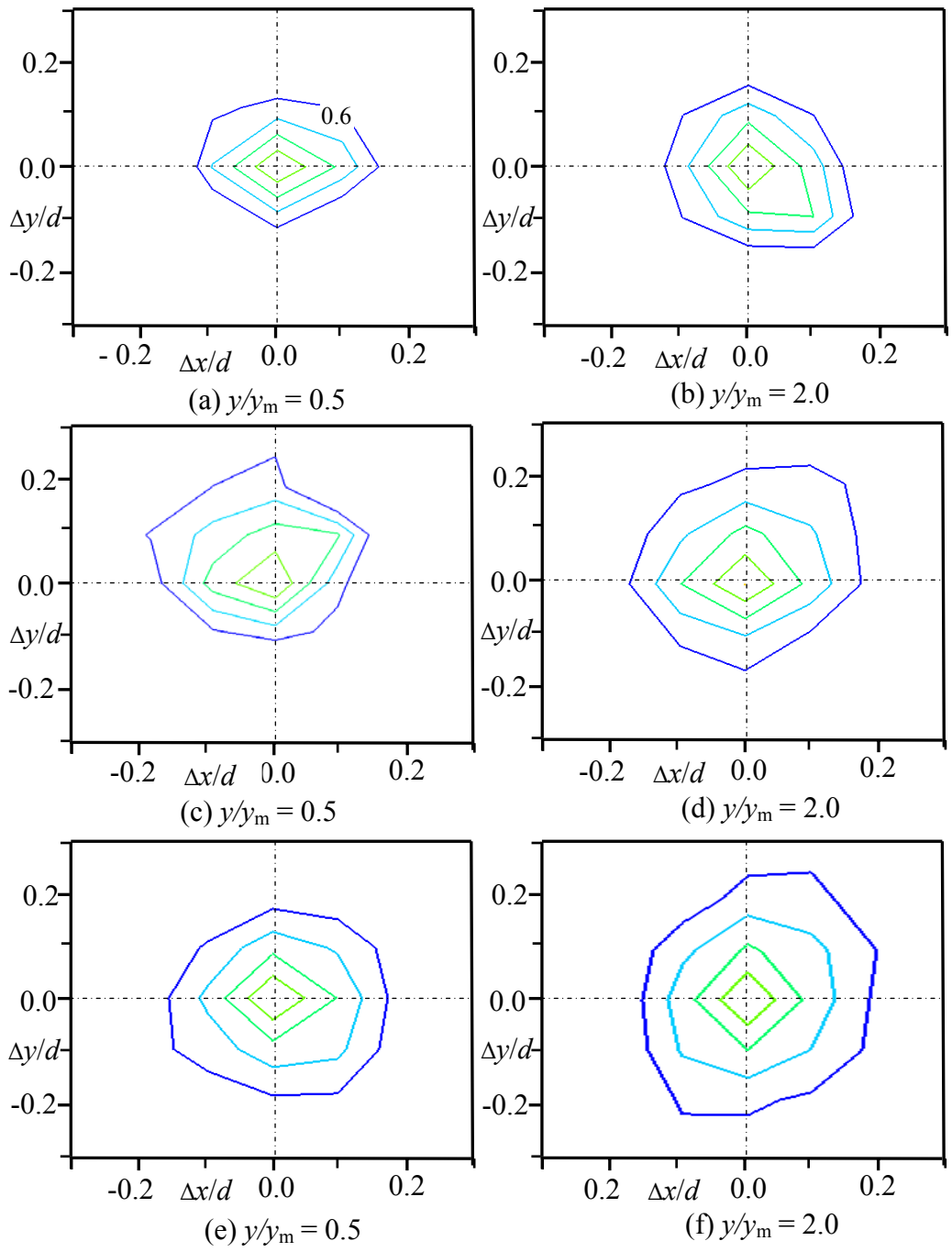

Figure 4.23: Iso-contours of two-point correlation for the wall-normal (v') fluctuating velocities (i.e., R_{vv}) in the developing region, x/d = 15 in the x-y plane. The wall-normal locations (y/y_m) are indicated. Offset heights: h/d = 0.5 in (a) and (b); h/d = 2.0 in (c) and (d); and h/d = 4.0 in (e) and (f).

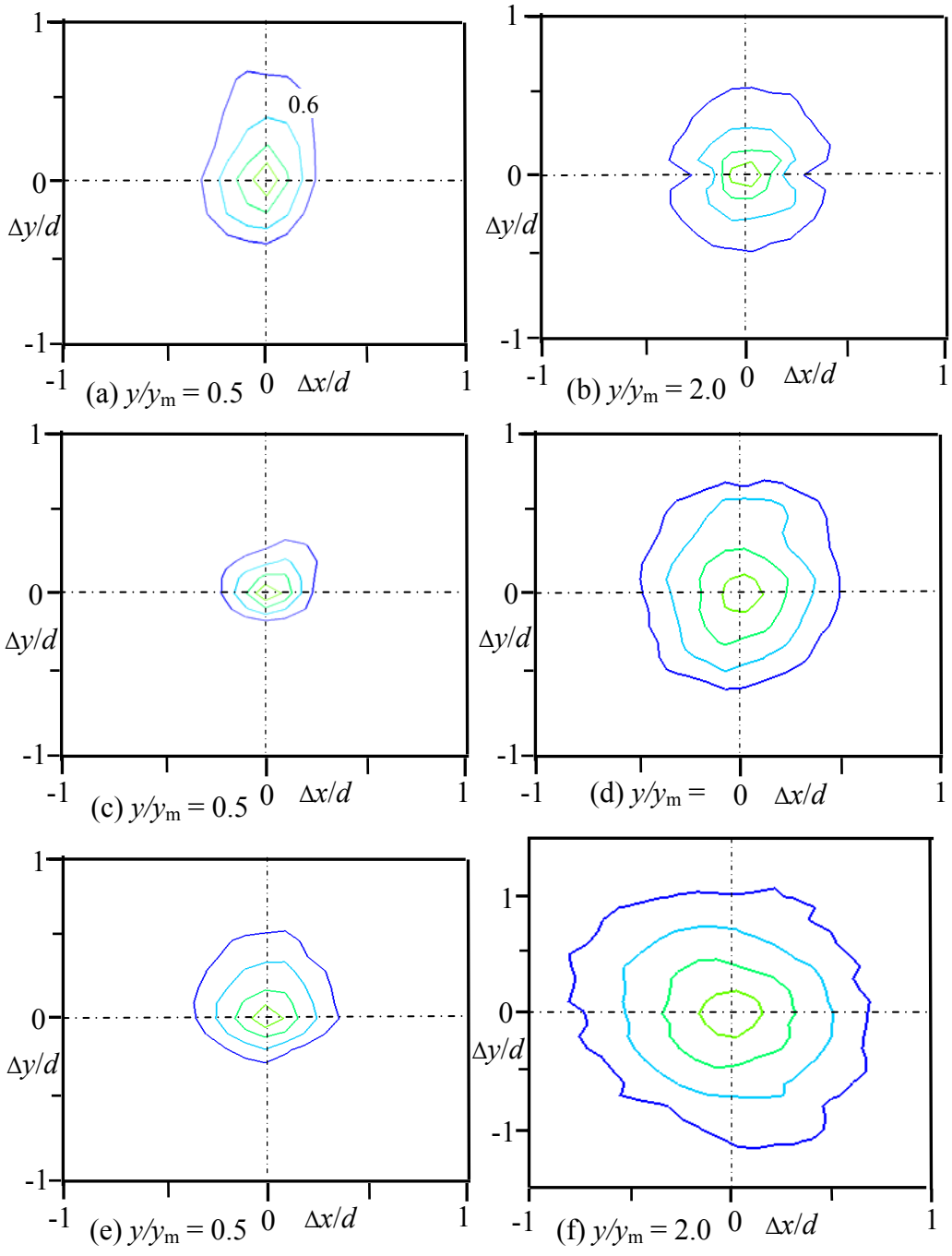

Figure 4.24: Iso-contours of two-point correlation for the wall-normal (v') fluctuating velocities (i.e., R_{vv}) in the self-similar region, x/d = 75 in the x-y plane. The wall-normal locations (y/y_m) are indicated. Offset heights: h/d = 0.5 in (a) and (b); h/d = 2.0 in (c) and (d); and h/d = 4.0 in (e) and (f).

R_{vv}(x) denote the auto-correlations along the streamwise direction while R_{uu}(y) and R_{vv}(y) denote the auto-correlations along the wall-normal direction. The figure confirms that the iso-contours decay faster in the developing region (x/d = 15) indicating less extended turbulence correlations than in the self-similar region (x/d = 75). In addition, the decay is less rapid with increasing offset heights (h/d). In Fig. 4.25b, for instance, the values of R_{uu}(x) in the developing region dropped dramatically from 100% at x/d = 0 to approximately 35%, 43%, and 67% at just x/d = 0.5, respectively, for h/d = 0.5, 2.0 and 4.0. At the same streamwise location (x/d = 0.5) in the self-similar region, the values of R_{uu}(x) decayed to approximately 83%, 86%, and 90%, respectively, for h/d = 0.5, 2.0 and 4.0. The figure also shows that the auto-correlations R_{uu} decays faster along the wall-normal direction than in the streamwise direction. For example, for h/d = 2.0 at $\Delta x/d$ = 2 in the self-similar region, R_{uu}(y) = 0.47 while R_{uu}(x) = 0.73. However, R_{vv} decays faster in the streamwise direction than in the wall-normal direction. For instance, for h/d = 2.0 at $\Delta x/d$ = 2 in the self-similar region, R_{vv}(x) = 0.09 while R_{vv}(y) = 0.26. It is also obvious from the figure that R_{vv} values decay more significantly with distance than their corresponding R_{uu} values. The results confirm the earlier observation that R_{uu} iso-contours are more extended in the streamwise direction than in the wall-normal direction whereas the extents of R_{vv} iso-contours are elongated more in the wall-normal direction. The slower decay of the turbulence correlations in the self-similar region indicates the presence of more organised large scale structures.

As mentioned in Chapter 2, the inclinations of R_{uu} (denoted β) in the inner layer represents the average inclination of the vortical structures having the form of a

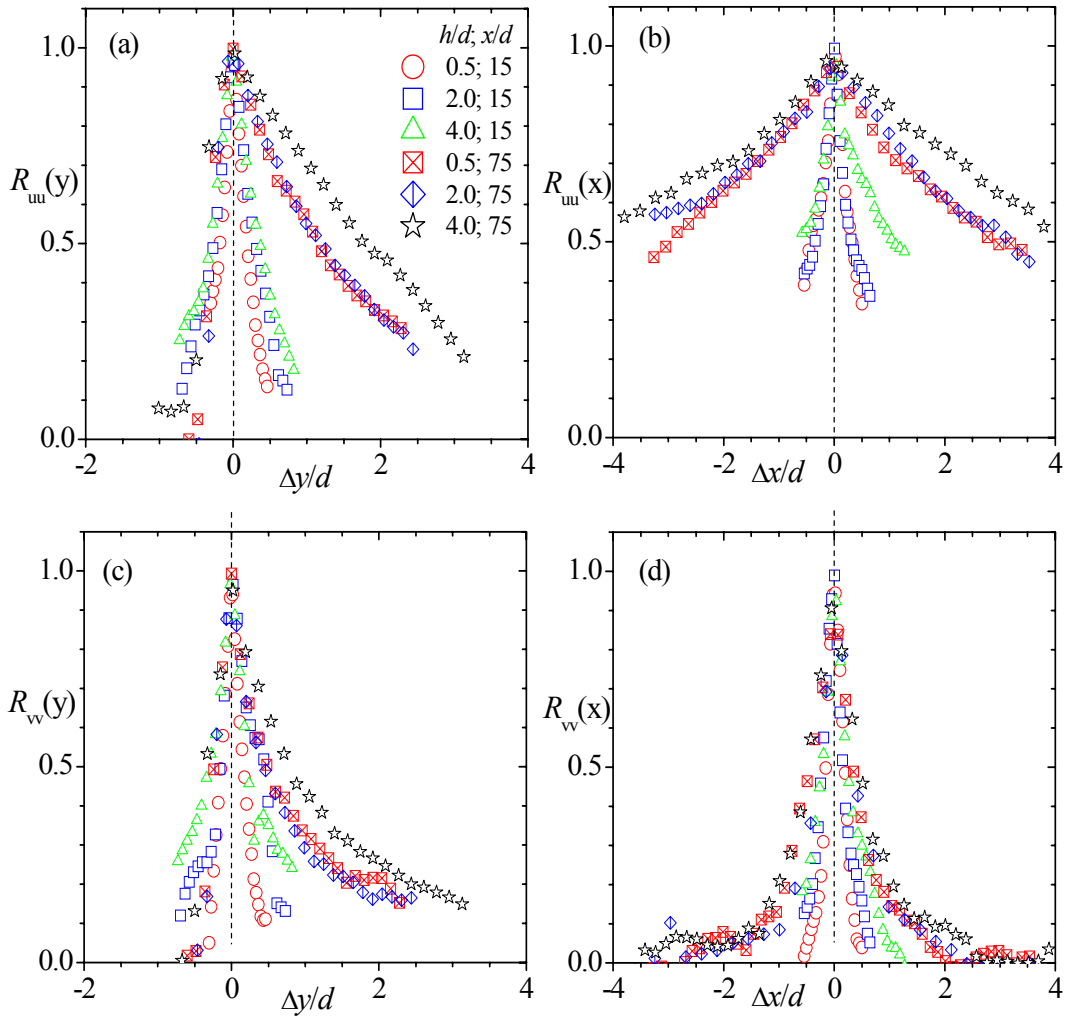

Figure 4.25: One-dimensional two-point correlation profiles extracted along the vertical and horizontal dash lines in Figs. 4.21-4.24. (a) $R_{uu}(y)$, (a) $R_{uu}(x)$, (a) $R_{vv}(y)$, and $R_{vv}(x)$.

hairpin (or hairpin vortices). Following previous studies (Volino et al, 2007), the values of β were obtained by fitting least-squares through points farthest away from the self-correlation peak at different iso-contour levels. In the present studies, R_{uu} iso-contour levels from 0.6 to 1.0 at 0.1 intervals were used to develop these least-squares fits. Due to uncertainty in using the iso-contours computed directly from the PIV data,

it was decided to fit ellipses of different sizes and inclinations to the measured iso-contours and then employ these ellipses to estimate the inclinations and extents of the iso-contours. Typical ellipses are shown in Figs. 4.21-4.22. The values of β estimated from the iso-contours of R_{uu} for selected y/y_m values in the self-similar region are reported in Table 4.3. The error in the estimation of β is approximately 10%. The inclinations are highest in the inner layer and decrease away from the wall. There is no consistent trend in the inclinations for h/d = 0.5 and 2.0. However, the values for h/d = 4.0 are relatively smaller than the others. In the inner layer the inclinations are $\beta = 11.2^o \pm 0.6^o$. These values are in good agreement with reported values in boundary layer studies. For example, Tomkins and Adrian (2003) reported $\beta = 10^o$ to 20^o while Krogstad and Antonia (1994), and Volino et al. (2007) reported $\beta = 10^o$, and $13.2^o \pm 2.5^o$, respectively.

Table 4.4: Inclinations of iso-contours at selected wall-normal distances

	Inclinations β^o		
y/y_m	h/d = 0.5	h/d = 2.0	h/d = 4.0
0.5	11.3	11.8	10.6
1.0	8.6	9.2	7.9
1.5	7.1	6.7	5.6
2.0	4.0	3.6	0.0

Following previous studies (Volino et al., 2007), the streamwise extent of R_{uu} (i.e., Lx_{uu}) was also estimated as twice the distance from the self-correlation peak to the most downstream location on R_{uu} = 0.6. On the other hand, the wall-normal extents of R_{uu} (i.e., Ly_{uu}) and R_{vv} (i.e., Ly_{vv}) were determined as the wall-normal distance between the closest and farthest points from the wall on the R_{uu} = 0.6 and

R_{vv} = 0.6 iso-contour levels. Similarly, the streamwise extent of R_{vv} (i.e., Lx_{vv}) was estimated as the distance between the most downstream and upstream points on the R_{vv} = 0.6 iso-contour level. The error in estimating these extents was also approximately 10%. The values of Lx_{uu}, Ly_{uu}, Lx_{vv} and Ly_{vv} are plotted in Fig. 4.26. The superscript (*) denoted normalization of the parameters by the jet exit diameter. The Lx_{uu}^{*} values vary with offset height as expected. In the inner region the variation

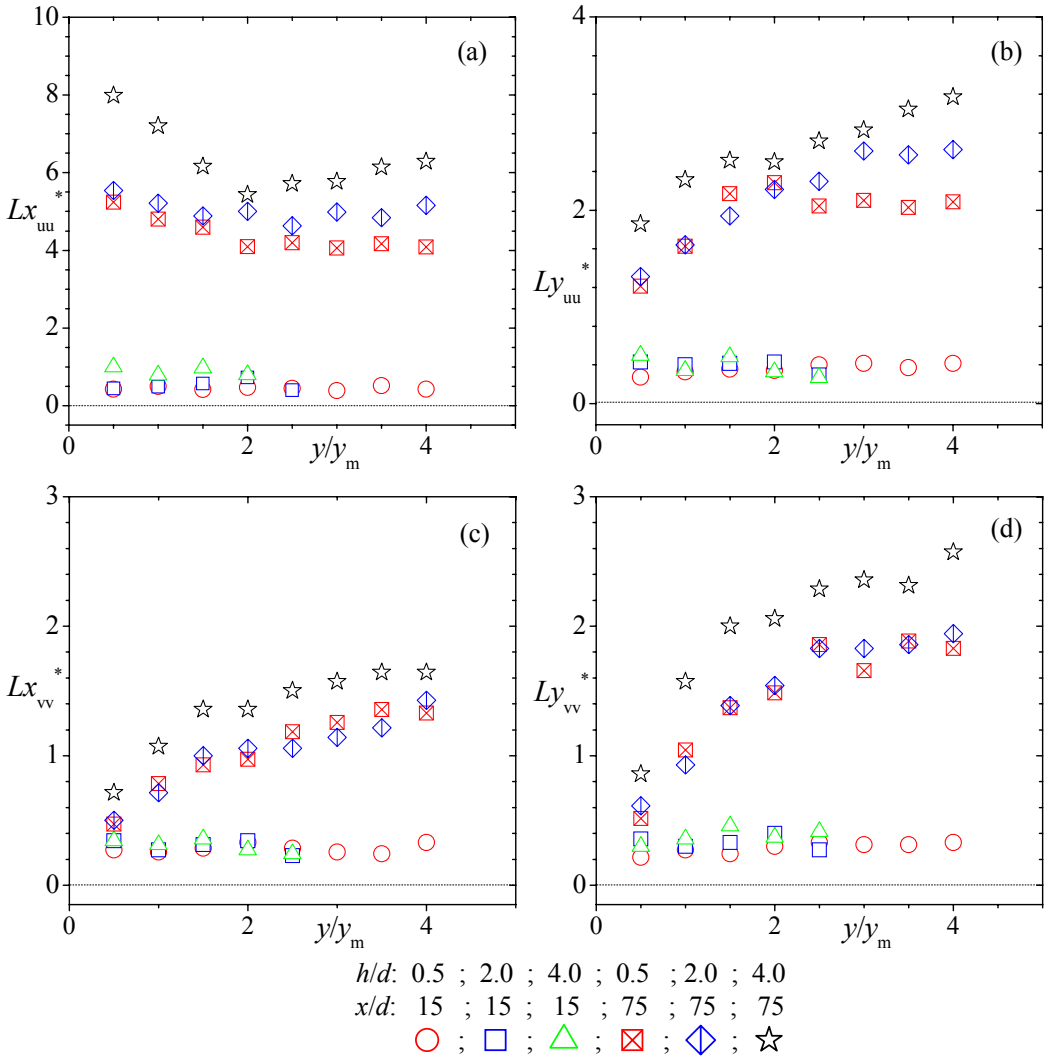

Figure 4.26: Streamwise extent of (a) R_{uu} (i.e., Lx_{uu}) and (c) R_{vv} (i.e., Lx_{vv}); and wall-normal extent of (b) R_{uu} (i.e., Ly_{uu}) and (d) R_{vv} (i.e., Ly_{vv}).

in the values is small. However, in the self-similar region, the Lx_{uu}^{*} values clearly increase with offset height. These values initially decrease with y/y_m before becoming approximately constant at 4.1, 4.9, and 5.8, respectively, for h/d = 0.5, 2.0, and 4.0. The values in the developing region are nearly constant at 0.6 ± 0.2. This clearly shows that the streamwise extent in the self-similar region is more than 4 times larger than the values in the developing region. The values of Ly_{uu}, Lx_{vv}, and Ly_{vv} all increase nonlinearly with y/y_m. The Ly_{uu} and Ly_{vv} values for h/d = 0.5, and 2.0 also appear to level out and become nearly constant beyond $y/y_m = 2.5$. The Ly_{uu} and Ly_{vv} values are comparable and more than 30% larger than the Lx_{vv} values.

The results of the inner layer (i.e., $y \leq y_m$) of the self-similar region can be compared with the boundary layers results of Volino et al. (2007). In this region, the ratio of $Lx_{uu}/Ly_{uu} = 4.2 \pm 0.2$ is nearly twice the value of $Lx_{uu}/Ly_{uu} = 2.5$ reported by Volino et al. (2007). However, the ratio of $Lx_{vv}/Ly_{vv} = 0.87 \pm 0.05$ in the present study is comparable with the value of $Lx_{vv}/Ly_{vv} = 0.80$ reported by Volino et al. (2007). This shows that the structures in the inner layer of the wall jets are more stretched in the streamwise direction than is the case of a boundary layer. Significantly larger values of Lx_{uu} than Lx_{vv} are also reported in turbulent boundary layer studies and it has been suggested that the larger values of Lx_{uu} are due to the notion that R_{uu} is tied to the common convective velocity of each hairpin pocket (Volino et al., 2007).

In the x-z plane, the iso-contours of R_{uu} and R_{ww} at $y = y_m$ and $z = 0$ are shown in Fig. D.4 in Appendix D for the developing (x/d = 15) and self-similar (x/d = 75) regions. Similar to the observations made for x- y planes, the figure shows that the R_{uu} and R_{ww} iso-contours in the self-similar region are much larger than in the developing

region. In addition, the iso-contours appear more rounded than those in the *x*- *y* planes. The one dimensional correlation profiles extracted in the *x* and *z* directions through the centre of the iso-contours are displayed in Fig. 4.27. This figure is used to quantify some of the qualitative features observed in the iso-contour plots. The figure shows that the sizes of the iso-contours in the developing region are similar with no significant differences in their decay. They all decayed to zero or close to zero over a distance of two diameters (i.e., 2*d*). In the self-similar region, however, there are

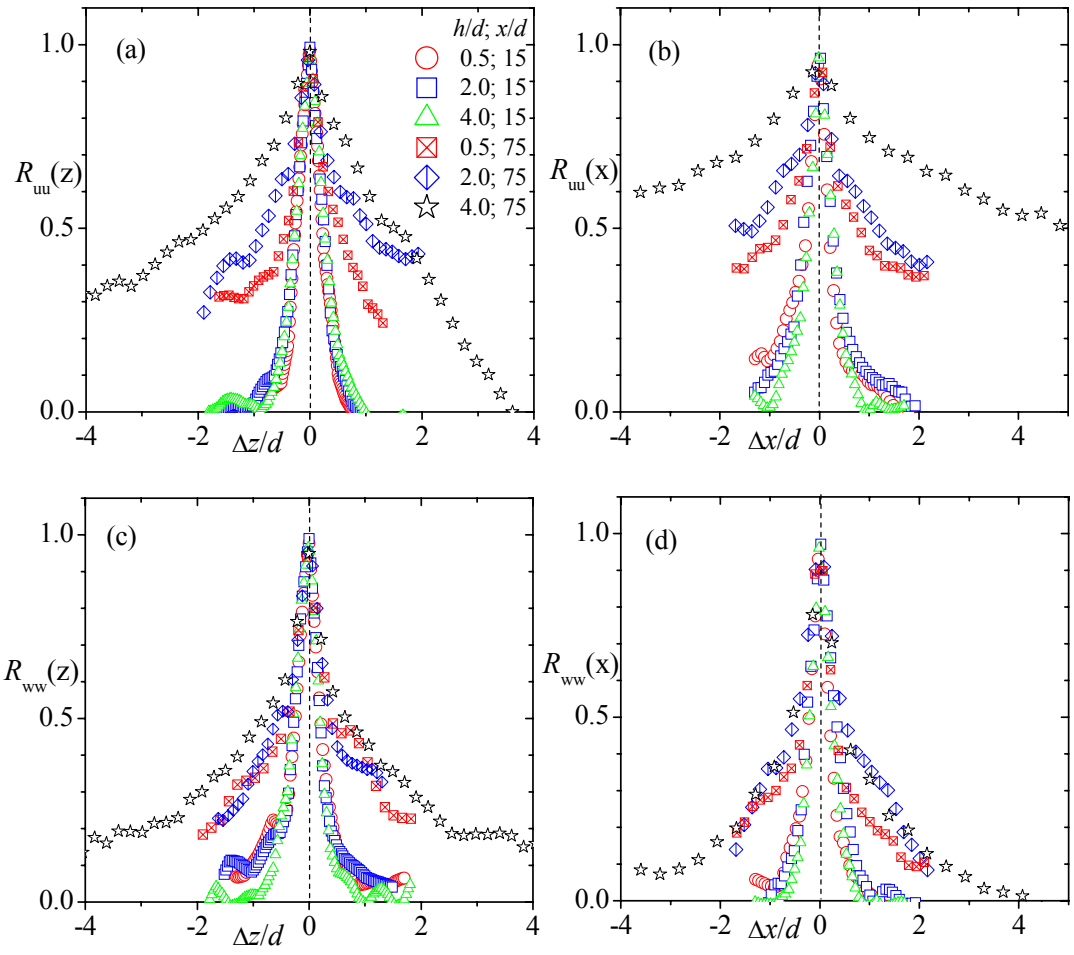

Figure 4.27: One-dimensional two-point correlation profiles extracted along the jet flow and across the jet flow as indicated by the dash lines in Fig. D.4. (a) $R_{uu}(z)$, (a) $R_{uu}(x)$, (a) $R_{ww}(z)$, and $R_{ww}(x)$.

significant differences in the decay in some of the test cases. The decay rate of the $R_{ww}(x)$ iso-contours is identical for the three offset heights. For example, at 1.5d from the centre, the iso-contours decayed from 100% to 22% for the three offset heights. The decay of the iso-contours of $R_{ww}(z)$ is also identical for h/d = 0.5 and 2.0 which dramatically decayed from 100% to 22% at 1.5d from the centre. The decay for h/d = 4.0 is slightly slower. It decayed from 100% to 36% at 1.5d from the centre. The turbulence correlations of the streamwise turbulence (R_{uu}) for the different offset heights are not identical as is the case for the lateral turbulence. For example, the iso-contours of $R_{uu}(x)$, also decayed from 100% to 40%, 48%, and 70% for h/d = 0.5, 2.0, and 4.0, respectively, in a distance of 1.5d. Similarly, the $R_{uu}(z)$ decayed to 30%, 40% and 55% for h/d = 0.5, 2.0, and 4.0, respectively. The figure and values also show that R_{ww} decays faster than R_{uu}.

4.4 Proper Orthogonal Decomposition

The snapshot approach of proper orthogonal decomposition (POD) introduced by Sirovich (1987) was employed in this study. The POD implementation was performed following the procedure outlined by Meyer et al. (2007) and is presented in Appendix A. In this section, the convergence of the turbulence kinetic energy and the spectra of the turbulence kinetic energy for the low-order POD modes are reported. In addition, iso-contours and profiles of the reconstructed turbulence intensities, and Reynolds shear stresses for the low-order modes are reported. The following three flow regions are analyzed: $12 \leq x/d \leq 18$; $36 \leq x/d \leq 42$; and $72 \leq x/d \leq 78$. These flow regions are denoted as I, II, and III, respectively. Regions I and III represent the developing and self-similar regions, respectively. The intermediate region, II, was determined in Section 4.1.2 to also be a self-similar region for the generic wall jet but developing regions for the offset jets. To ensure that equivalent flow regions are analyzed, the wall-normal and lateral distances were maintained at $0 \leq y/y_{0.5} \leq 2$ and $0 \leq z/z_{0.5} \leq 2$, respectively. For the *x*-*z* plane the field of view was not able to capture up to z = 2 for the far downstream locations without sacrificing too much resolution. This is because of the characteristically large lateral spread of the 3D wall jets. As a result the analysis for *x*-*z* plane was limited to $52 \leq x/d \leq 58$. Therefore III represents $52 \leq x/d \leq 58$ in the *x*-*z* plane. It should be pointed out that the results of Section 4.1.2 showed that $52 \leq x/d \leq 58$ is also in the self-similar region.

4.4.1 Convergence of POD modes

The number of snapshots (*N*) required to adequately capture the energy content for a given mode depends on the complexity of the flow. As mentioned in Chapter 2, it

has been observed that as the number of snapshots increases, the computed energy spectrum approaches the analytical spectrum and the fidelity of the snapshot procedure improves (Breuer & Sirovich, 1991). Following previous studies (Breuer & Sirovich, 1991), the number of snapshots necessary to perform POD analysis in the present study was evaluated by computing the fractional turbulence kinetic energy associated with the first few modes for increasing number of snapshots. The developing and self-similar regions (I and III) in both the *x*-*y* and *x*-*z* planes were selected for the convergence analysis.

In the symmetry (*x*-*y*) plane, the energy fractions (E_λ) are shown in Fig. 4.28 for the developing and self-similar regions. The figure shows that for each mode in the two regions, the energy fraction decreases with the number of snapshots to a threshold value where it is nearly independent of the number of snapshots (N). For example, for $N \geq 1000$, there are no significant changes in the energy fraction. For instance, at mode 50, increasing the number of snapshots from 1000 to 1600 changes the energy fraction by less than 1% irrespective of the offset height, h/d (Fig.4.28).

In the lateral (*x*-*z*) plane, the convergence exhibit trends akin to the observation made for the *x*-*y* plane (Fig. 4.29). Based on these observations, it was determined that $N = 1600$ is sufficient to perform the POD analysis. The number of snapshots used in the present study is more than the number of snapshots used in some previous POD studies. For example, Kostas et al. (2005) used 1024 snapshot for a backward facing step flow while Meyer et al. (2007) used 1000 snapshots for their analysis of a turbulent jet in cross flow. The figure also shows that the convergence in the self-similar region is faster than that in the developing region. This is demonstrated, for example, by the better collapse of

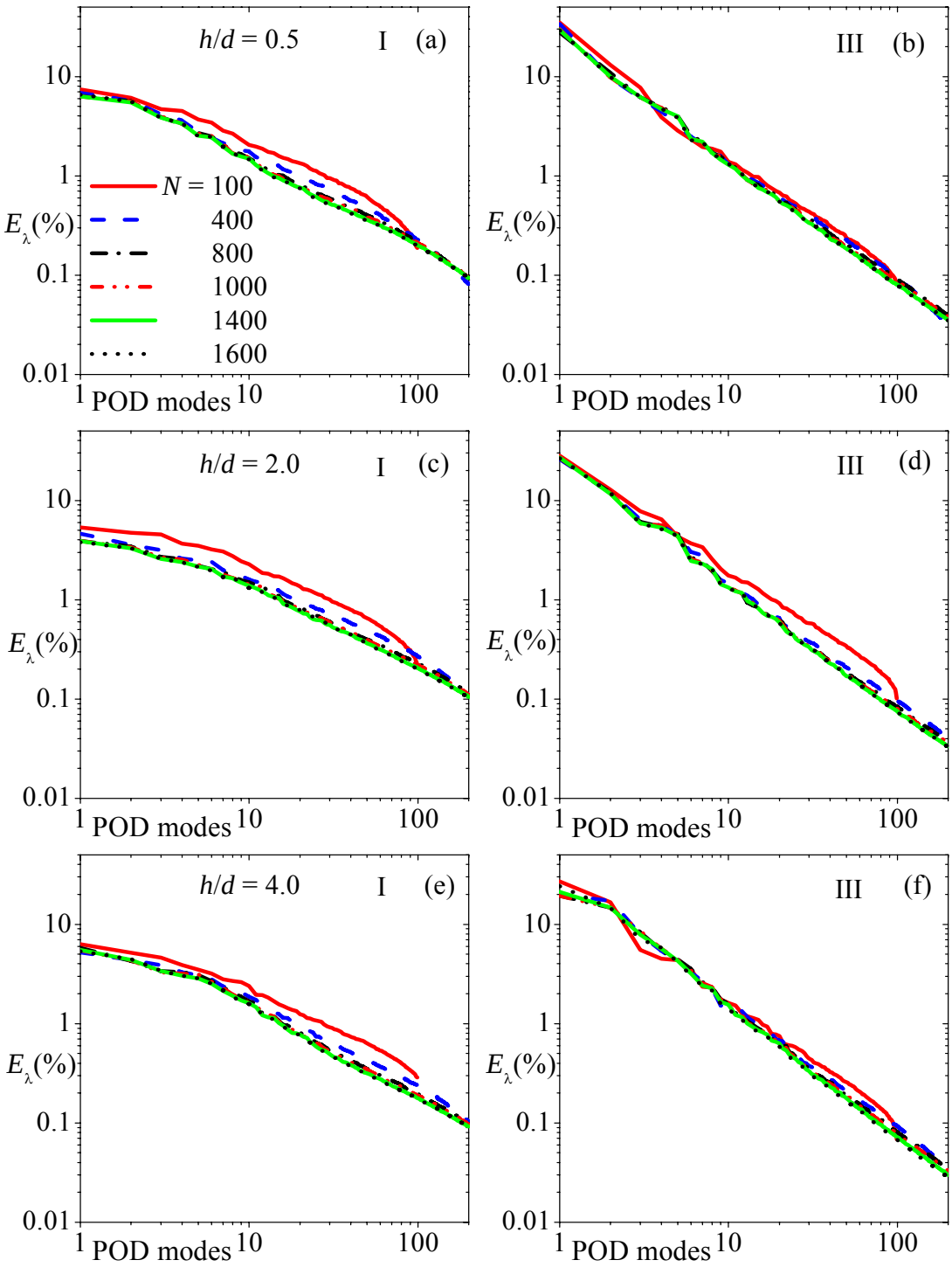

Fig. 4.28: Variation of fractional energy contribution E_λ with number of modes in x-y plane for varying number of snapshots in selected planes. Developing region, I: $12 \leq x/d \leq 18$; and self-similar region, III: $72 \leq x/d \leq 78$.

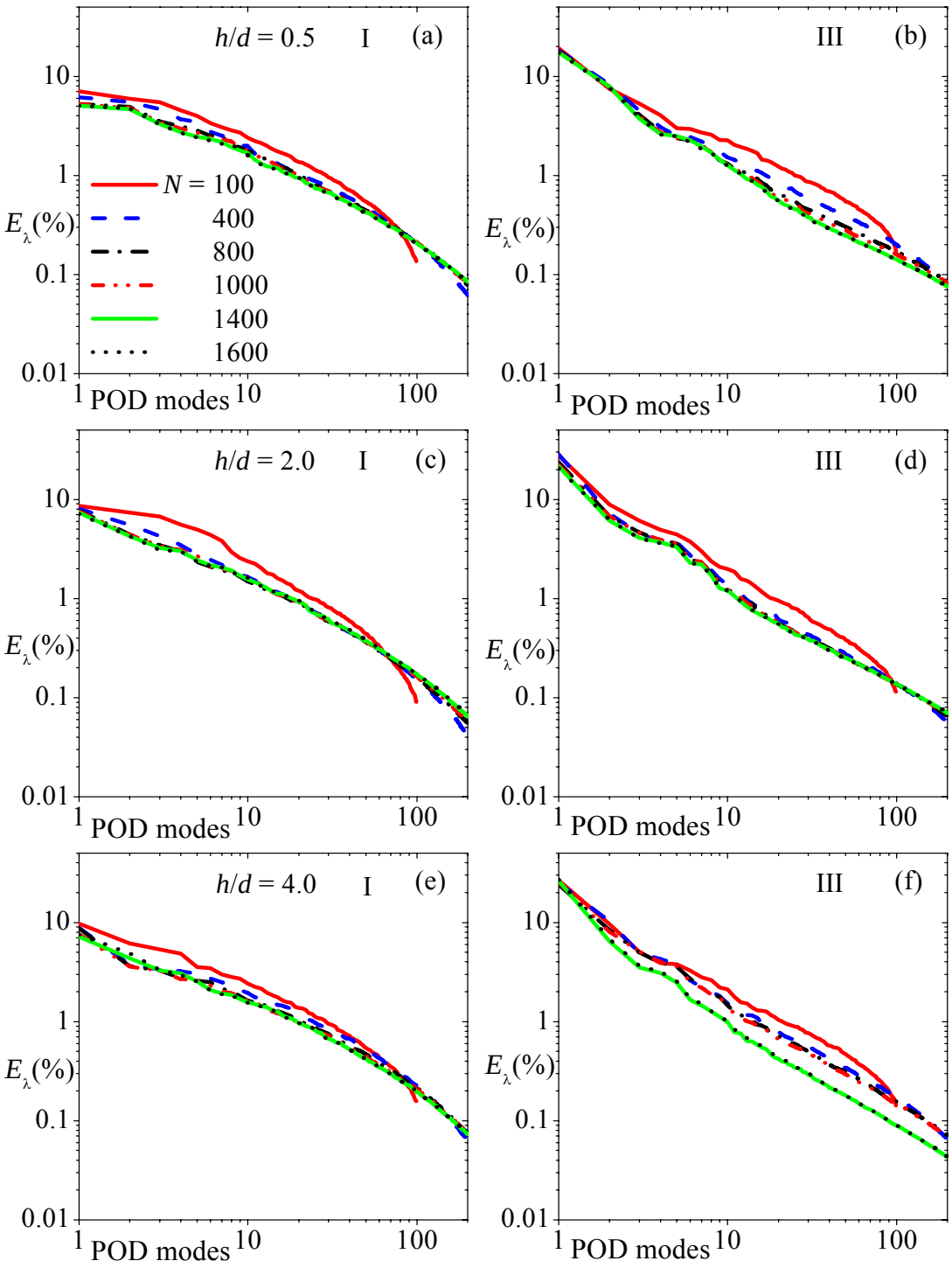

Figure 4.29: Variation of fractional energy contribution E_λ with number of modes in x-z plane for varying number of snapshots in selected planes. Developing region, I: $12 \leq x/d \leq 18$; and self-similar region, III: $52 \leq x/d \leq 58$.

the energy fraction from N = 400 for the self-similar region (III) than the developing region (I).

4.4.2 Spectral of turbulent kinetic energy

The fractional energy (E_λ) and the cumulative energy (ΣE_λ) contribution for each flow region for N = 1600 are reported here. The goal is to reveal the energy content for each POD mode in the three flow regions stated above: I, II, and III. In addition, the variation of the energy content with the jet offset is compared.

In the symmetry (x-y) plane, the fractional energy (E_λ) for the first mode accounts for less than 10% of the total energy in the developing region (Fig. 4.30). However, in the self-similar region, the energy content of the first mode is more than 20% of the total energy. More specifically, the fractional energies for h/d = 0.5 are 6.6%, 20.9% and 29.1%, respectively for Regions I, II, and III. Similarly, the energy fractions for the first mode are 3.8%, 20.2%, and 26.7% for h/d = 2.0 and 5.3%, 18.5%, and 24.1% for h/d = 4.0. It is evident from these values that the energy content of the first mode which represents the contribution from large scale structures increases downstream along the flow direction. The energy content of the first mode for the generic wall jet (h/d = 0.5) is slightly larger than those of the offset jets (h/d = 2.0 and 4.0). Furthermore, the energy fraction decays exponentially with increasing modes, however, the rate of decay is more drastic in the self-similar region (III). For example, for the first 50 modes the energy fraction dropped approximately one order of magnitude (i.e., from 6.6% to 0.35%) in the developing region (I) but approximately two orders of magnitude (i.e., from 29.1% to 0.18%) in the self-similar region (III). This means that most of the energy in the self-

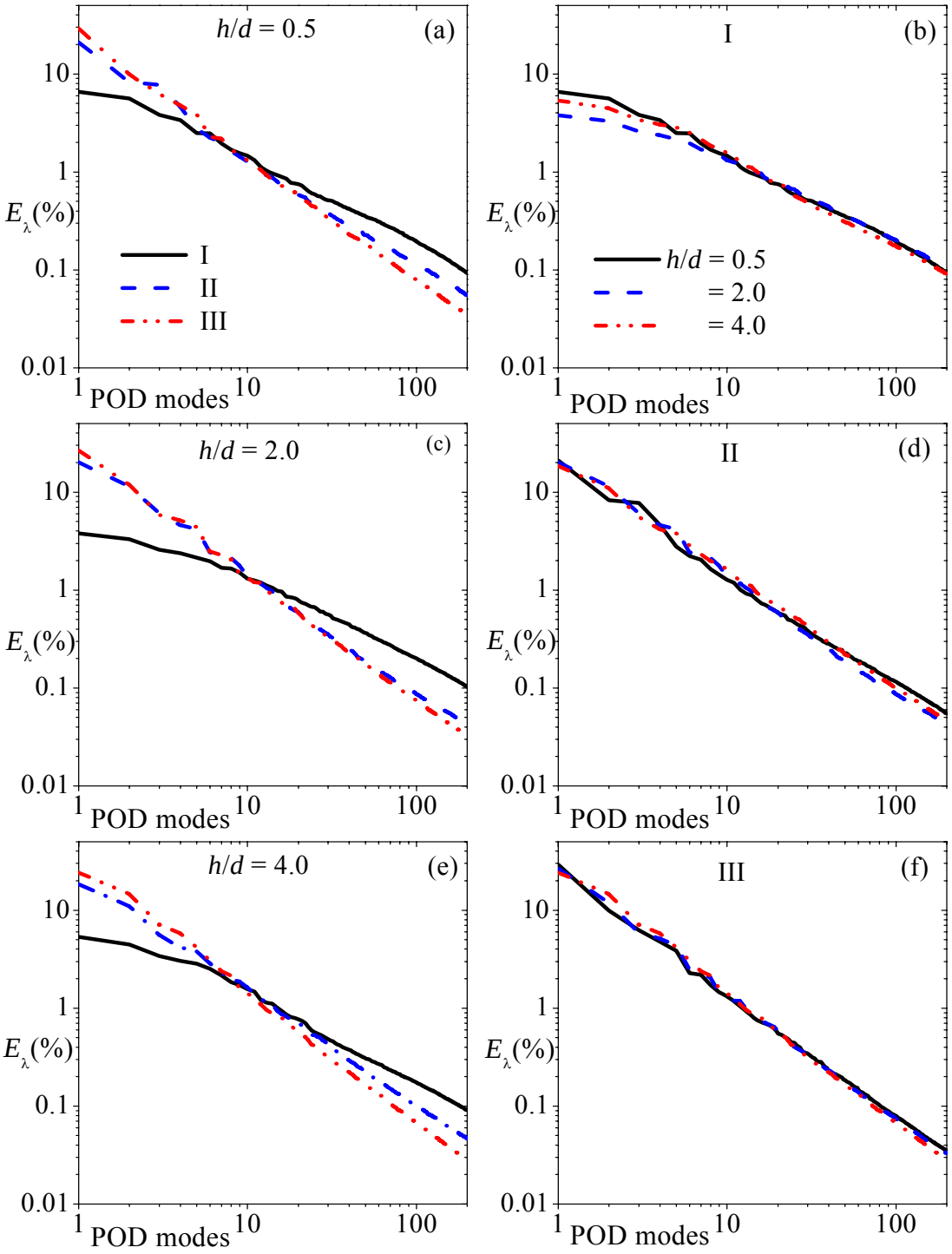

Figure 4.30: Variation of fractional energy contribution E_λ with number of modes in x-y plane for snapshots of $N = 1600$ in selected planes. Developing region, I: $12 \leq x/d \leq 18$; and self-similar region, III: $72 \leq x/d \leq 78$.

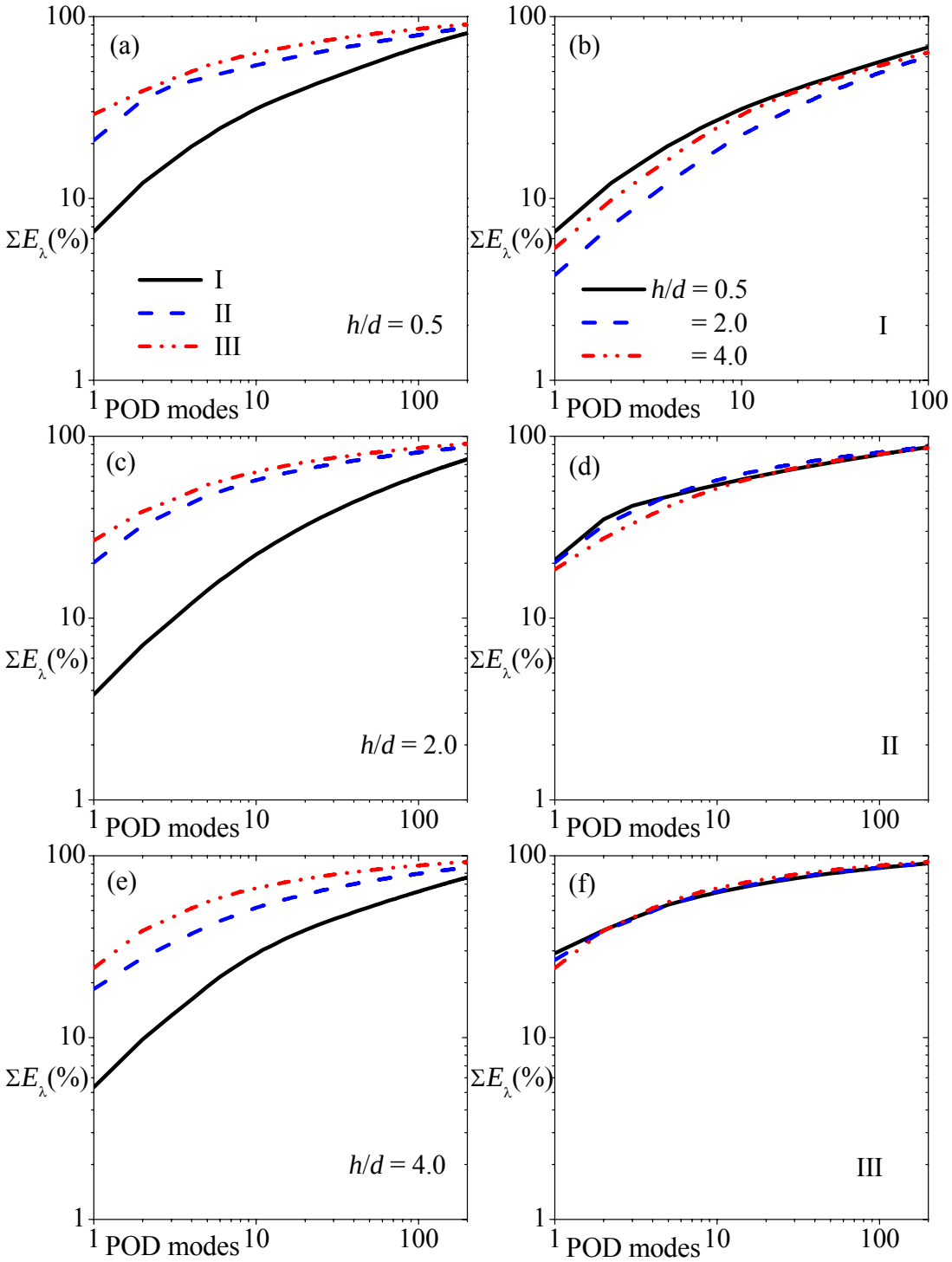

Figure 4.31: Variation of cumulative energy contribution ΣE_λ % with number of modes in x-y plane for snapshots of N = 1600 in selected planes. Developing region, I: $12 \leq x/d \leq 18$; intermediate region, II: $36 \leq x/d \leq 42$; and self-similar region, III: $72 \leq x/d \leq 78$.

similar region in stored in the low-order modes. It also implies that the self-similar region contains more large scale structures than developing region. Shah (2009) also reported the fractional energy of the first mode of 23% for a channel flow which is comparable to the present values.

Plots of the cumulative energy contribution (denoted by ΣE_λ) of the POD modes is shown in Fig. 4.31. For test h/d = 0.5, the first 50 modes contributes cumulative energies of ΣE_λ = 56%, 72%, and 81%, respectively, for Regions I, II, and III. The corresponding ΣE_λ values for h/d = 2.0 are 47%, 74%, and 81% for Regions I, II, and III, respectively. These values also demonstrates that the energy in the self-similar region (III) accumulates fastest while the energy in the developing region (I) accumulate slowest. This is a further confirmation that the large scale structures dominate the self-similar region.

In the *x*-*z* plane, the energy fractions of h/d = 0.5 for the first mode are 5.1%, 12.8% and 17.4%, respectively for Regions I, II, and III (Fig. 4.32). Similarly, the energy fractions for first mode are 7.1%, 13.6%, and 20.7% for h/d = 2.0 and 7.5%, 24.1%, and 27.0% for h/d = 4.0. Consistent with the observation made in the *x*-*y* plane, the energy fraction increases downstream along the flow direction for a specific POD mode. The decay of the energy fraction is also similar to the decay in the *x*-*y* plane. In the self-similar region (III), for instance, the spectra decayed approximately 99% for the first 50 modes in both *x*-*y* plane (i.e., from 29.1% to 0.18%) and approximately 98% in the *x*-*z* plane (i.e., from 17.4% to 0.25%).

The cumulative energy contribution shown in Fig. 4.33 is also similar to those in the *x*-*y* plane. For example, the first 20 modes accumulated 39% and 50% of the total

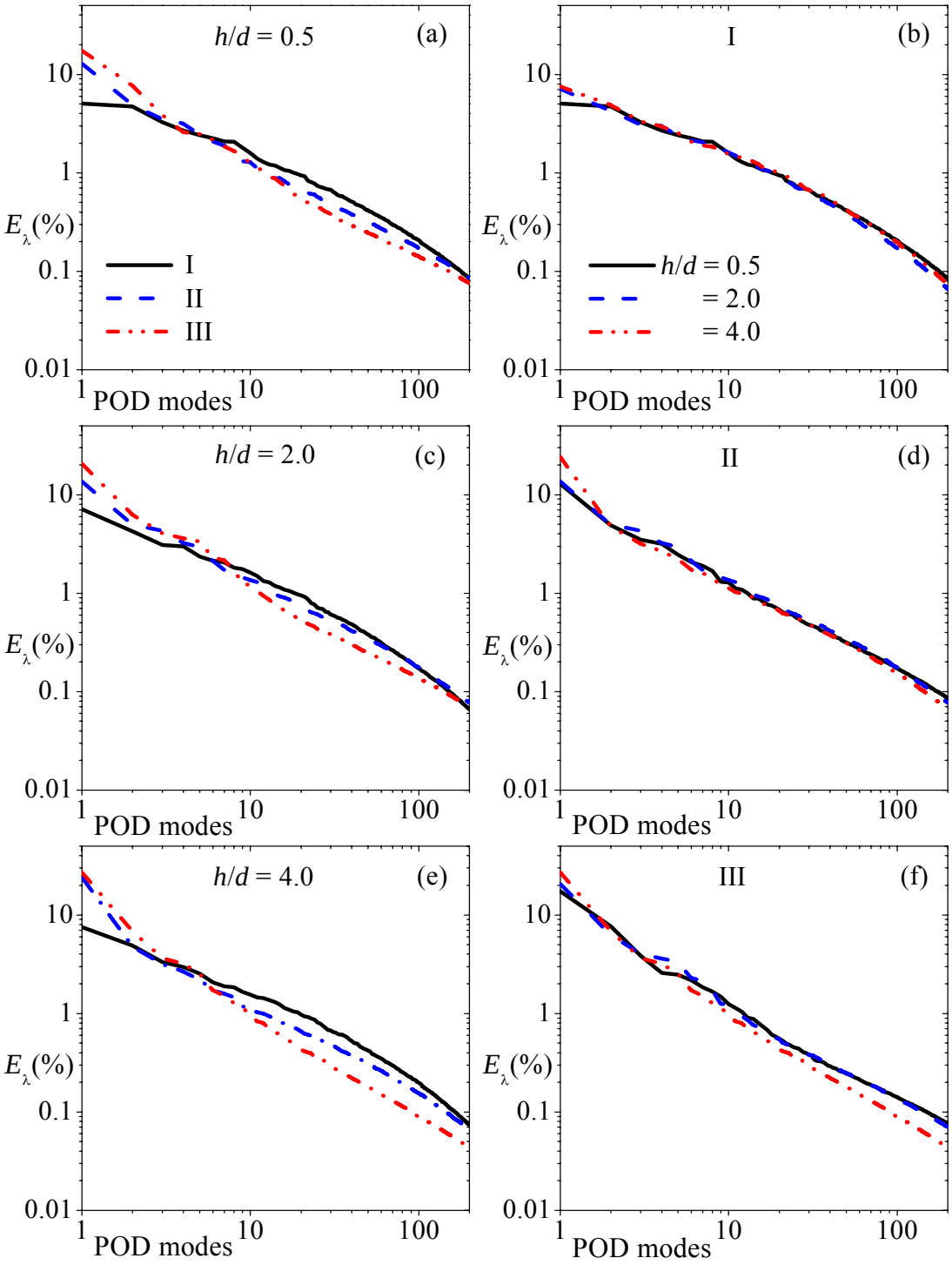

Figure 4.32: Variation of fractional energy contribution E_λ with number of modes in x-z plane for snapshots of N = 1600 in selected planes. Developing region, I: $12 \leq x/d \leq 18$; and self-similar region, III: $52 \leq x/d \leq 58$.

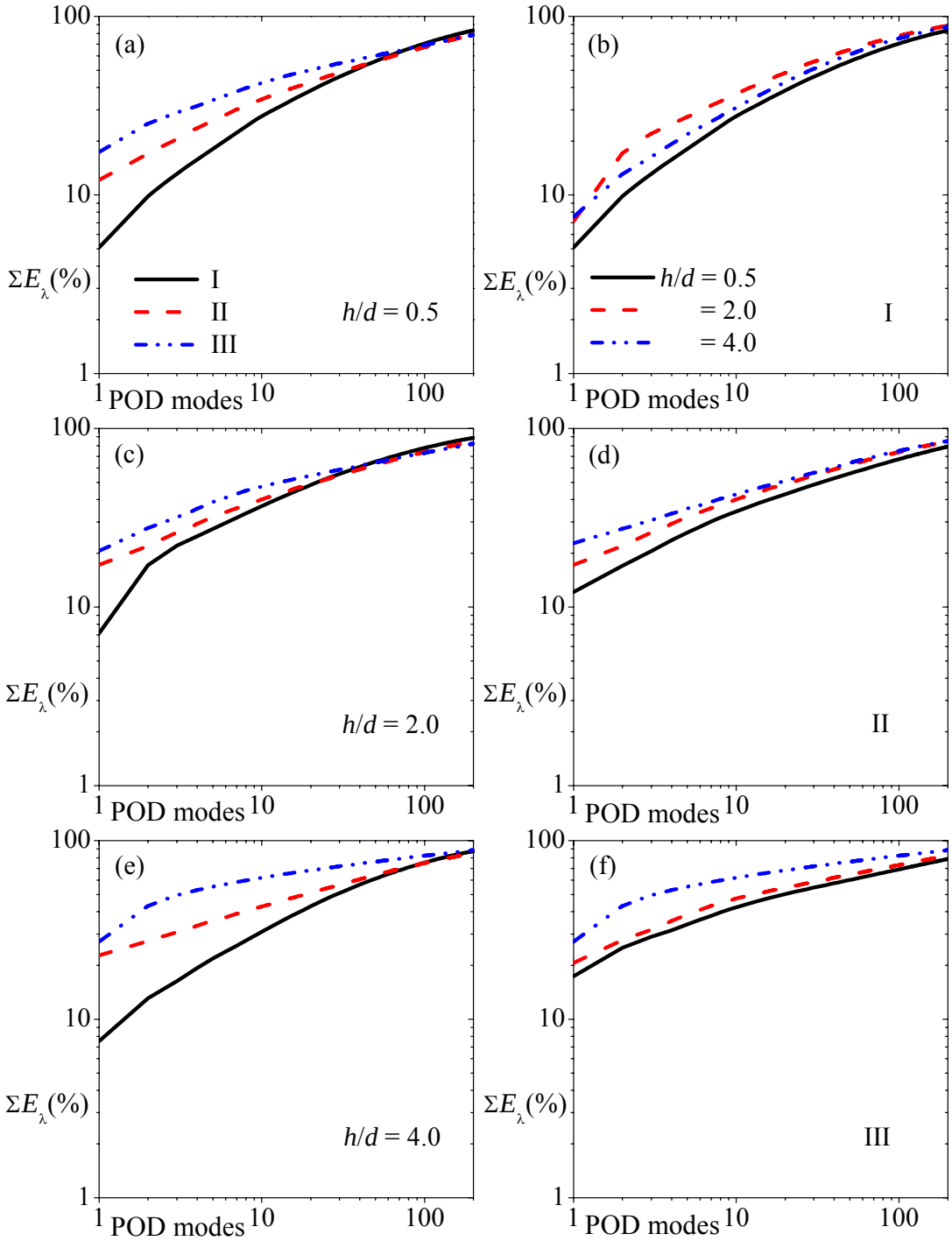

Figure 4.33: Variation of cumulative energy contribution ΣE_λ % with number of modes in x-z plane for snapshots of N = 1600 in selected planes. Developing region, I: $12 \leq x/d \leq 18$; intermediate region, II: $36 \leq x/d \leq 42$; and self-similar region, III: $52 \leq x/d \leq 58$.

energy content in the developing and self-similar regions, respectively, for the generic wall jet.

4.4.3 Reconstruction of turbulent quantities

In this section, the POD modes were used to reconstruct the turbulent quantities. This allows the contribution of some selected modes to the turbulence quantities to be evaluated. The reconstructed quantities are presented in the form of iso-contours and profiles. Low-order representations of the streamwise turbulence intensities, wall-normal turbulence intensities, and Reynolds shear stresses are reconstructed. For the reconstructed iso-contours the following individual POD modes are employed for the reconstruction: modes, m = 1, 5 and 10 modes using 1600 snapshots. Since the contribution to the low-order modes is dominated by large scale structures, the aim is to highlight the contribution of the large scale structures to the turbulence intensities and Reynolds shear stresses. For the reconstructed profiles, the cumulative contribution is examined. The sum of the first m = 1, 2, 3, 5 and 25 modes are used in the reconstruction.

4.4.3.1 Reconstructed iso-contours of turbulent quantities

In the symmetry (x-y) plane, the iso-contours of the turbulent quantities for h/d = 0.5 and 2.0 are shown in Figs. 4.34-4.39. The streamwise turbulence intensities, wall-normal turbulence intensities, and Reynolds shear stresses are denoted by u, v, and uv, respectively. As indicated in the figures, the iso-contours of the first mode (m = 1) have relatively larger values than modes m = 5 and 10. The modal contribution to the turbulent quantities decays as the order of the modes increases. The larger values from the first

mode indicate more contribution from the large scale structures. The contribution from the low-order modes are generally in the outer regions of the jets. This implies that the large scale structures populate the outer regions of the jets more than in the inner region. There is such a drastic decay in the energy contribution to *uv* that by the tenth mode the contribution of uv/U_m^2 is less than 0.4%. This means that large portion of the contribution to *uv* is limited to the first few POD modes. The implication is that the most energetic or large scale structure contributes to *uv* the most. The observation is consistent with previous POD studies in channel flows (Reichert et al., 1994; Moin & Moser, 1989). Blackwelder & Kovasznay (1972) found that large scale structures in a turbulent boundary layer contribute relatively more to Reynolds shear stresses. However, the decay in *v* is the slowest. The figures also show that more energy is captured in the self-similar region (III) than in the developing region (I). Furthermore, there is a more dramatic decrease in the contribution to the turbulence quantities in the self-similar region as the number of POD modes increases than in the developing region. For example, in Fig. 4.34, the peak of *u* is greater than 27.0% for first mode but less than 9.0% for the tenth mode ($m = 10$) in the self-similar region (a three fold decay). For the developing region, however, the peak of *u* is greater than 13.2% for the first mode but less than 8.8% for the tenth mode. This again confirms that large eddies contribute more to the self-similar region than the developing region. The implication of this is that the self-similar region is dominated by more large scale structures than the developing region.

For the effect of offset heights on POD modes, the figures show that as h/d increases, the effectiveness of the reconstruction decreases. For example, the peak of *u* is greater than 13.2% for $h/d = 0.5$ and the tenth mode but $11.0\% \leq (u)_{peak} \leq 13.2\%$ and

$8.8\% \leq (u)_{peak} \leq 11.0\%$ for $h/d = 2.0$ and 4.0, respectively and the tenth mode. In the self-similar region, however, peaks of u are greater than 27% for all h/d values. It is therefore evident that, in the developing region, the contribution to the generic wall jets ($h/d = 0.5$) is slightly more. This is expected since the offset jets require more downstream distance to develop into wall jets. The iso-contours of the turbulent quantities for $h/d = 4.0$ in the x-y plane are presented in Figs. D.5-D.7 of Appendix D.

In the x-z plane, the streamwise and lateral turbulence intensities, and Reynolds shear stresses are denoted by u, w, and $-uw$, respectively. Figures 4.40-4.45 are the iso-contours of these turbulent quantities. As indicated in the figures, the contribution to the reconstructed quantities decrease as the mode number increases. The trends in this plane are similar to those described in the x-y plane described above. As a result, the plots in the x-z plane will not be discussed again. The iso-contours of the turbulent quantities for $h/d = 4.0$ in the x-z plane are presented in Figs. D.8-D.10 of Appendix D.

4.4.3.2 Reconstructed profiles of turbulent quantities

Figures 4.46-4.48 show profiles of the reconstructed turbulence intensities and Reynolds shear stresses for the three offset heights, h/d = 0.5, 2.0, and 4.0 in the developing ($x/d = 15$) and self-similar ($x/d = 75$) regions. The ensemble PIV data are used as the basis for comparing the reconstructed data. The quantities are all normalized by the maximum mean velocity (U_m) of the ensemble PIV data. The convergence of the reconstructed data towards the PIV data is expressed as a percentage of U_m. In the developing region ($x/d = 15$) of the generic wall jet ($h/d = 0.5$), the profiles approach the ensemble PIV profiles progressively as the sum of the modes increases (Fig. 4.46).

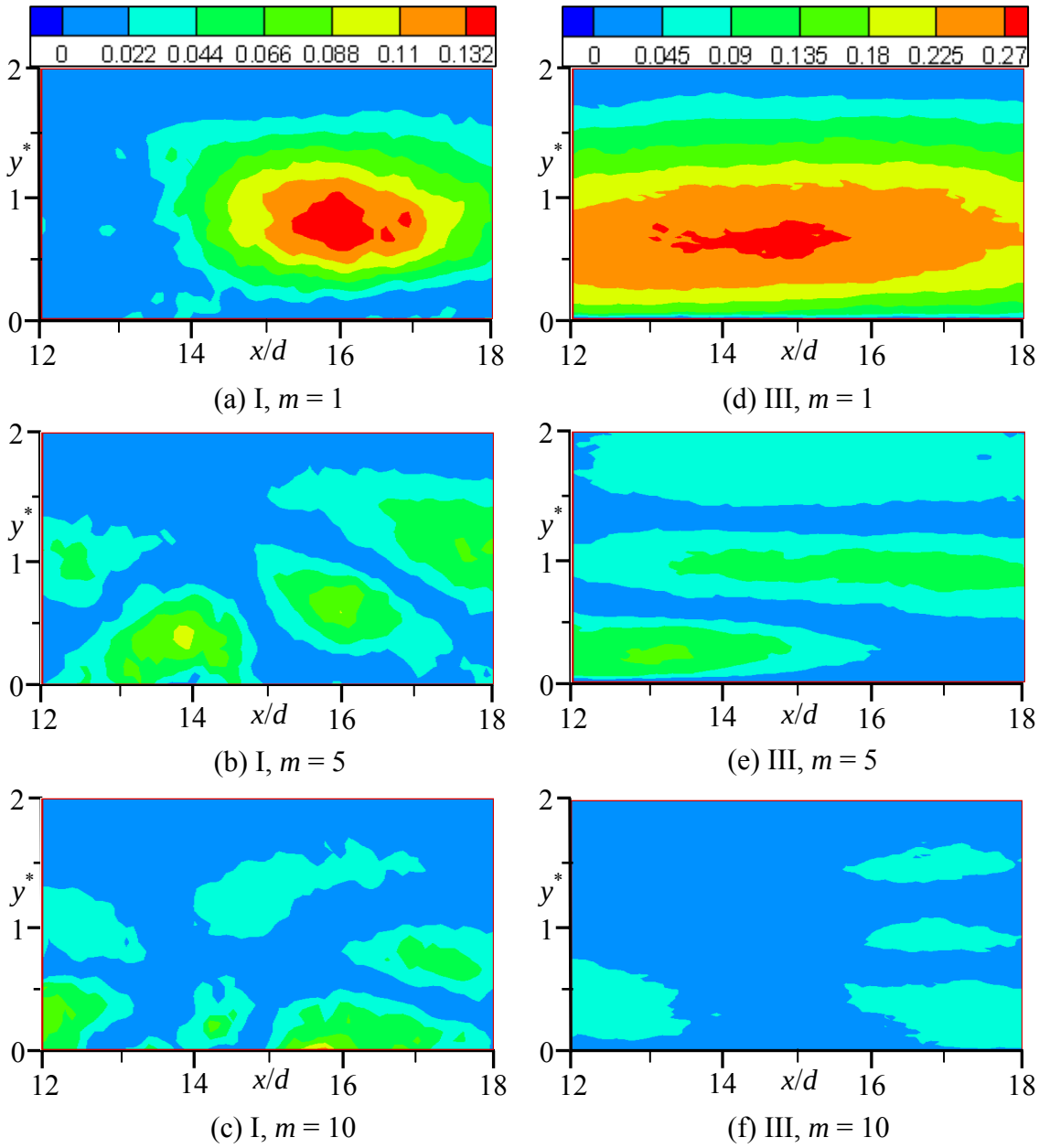

(a) I, $m = 1$ (d) III, $m = 1$

(b) I, $m = 5$ (e) III, $m = 5$

(c) I, $m = 10$ (f) III, $m = 10$

Figure 4.34: Iso-contours of streamwise turbulence intensities (u) for modes, $m = 1$, 5 and10 for $h/d = 0.5$ in x-y plane. The developing region (I): (a) to (c); and self-similar region (III): (d) to (e).

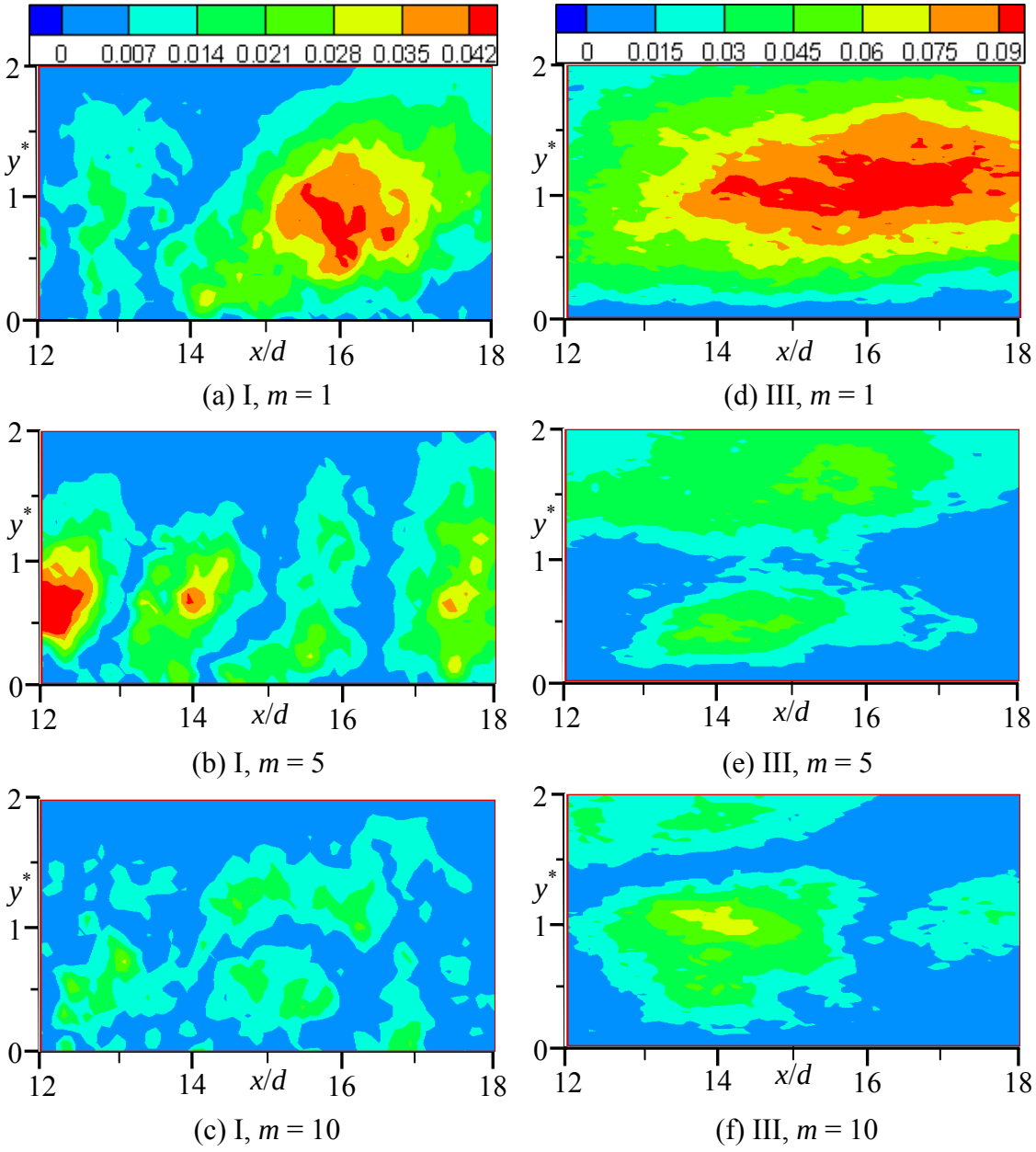

Figure 4.35: Iso-contours of wall-normal turbulence intensities (v) for modes, m = 1, 5 and 10 for h/d = 0.5 in x-y plane. The developing region (I): (a) to (c); and self-similar region (III): (d) to (e).

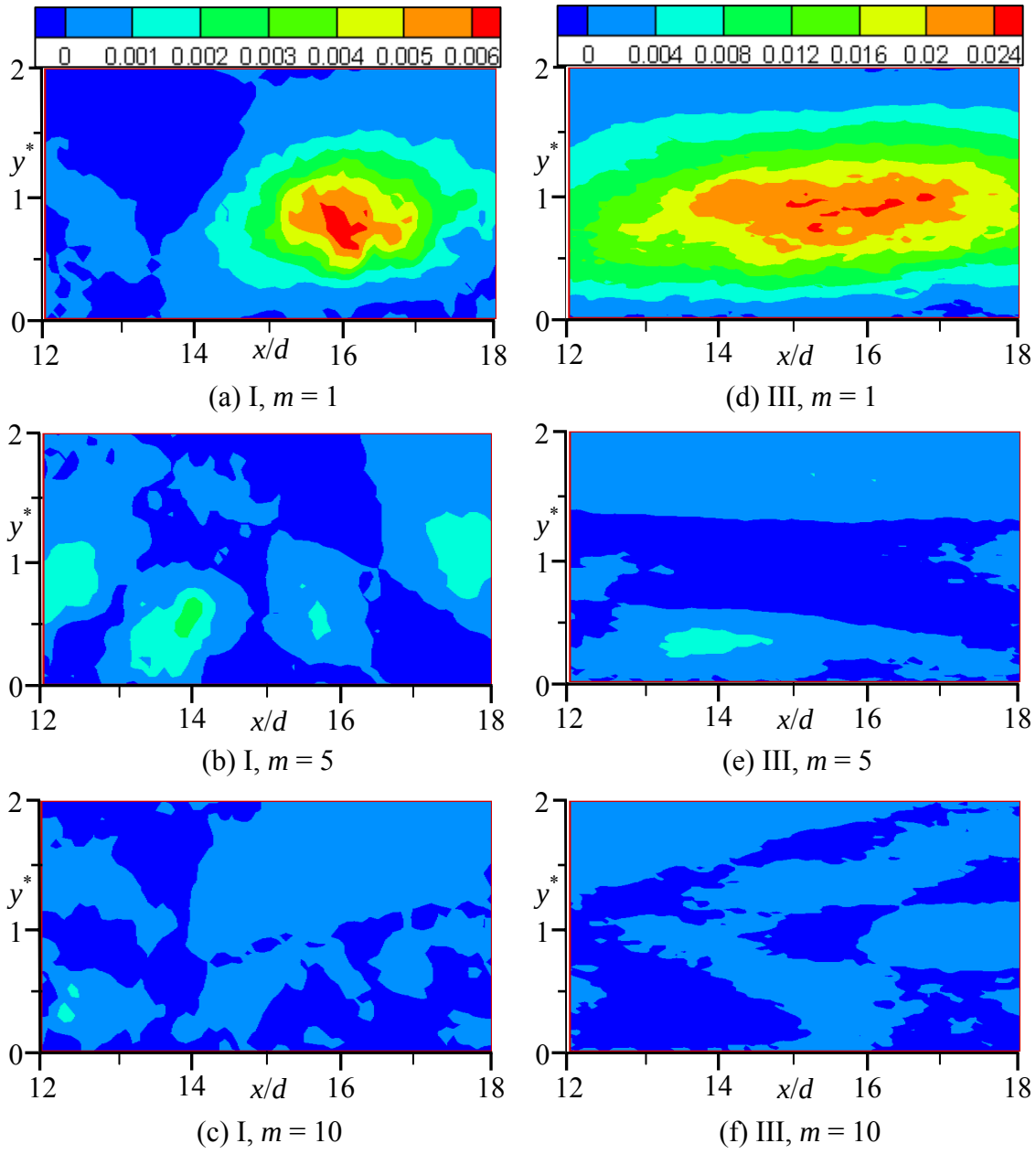

Figure 4.36: Iso-contours of Reynolds shear stresses (uv) for modes, m = 1, 5 and 10 for h/d = 0.5 in x-y plane. The developing region (I): (a) to (c); and self-similar region (III): (d) to (e).

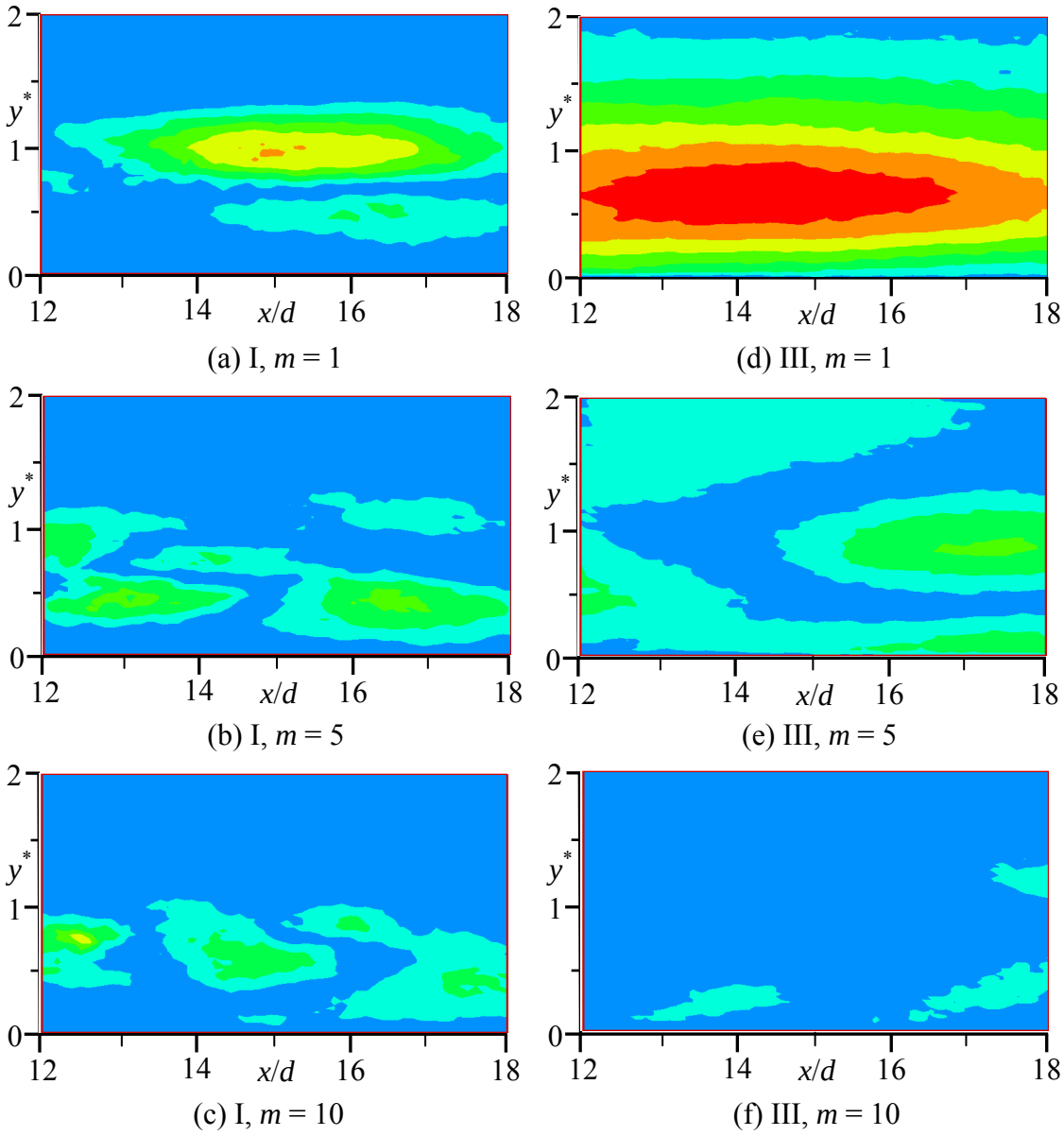

Figure 4.37: Iso-contours of streamwise turbulence intensities (u) for modes, m = 1, 5 and 10 for h/d = 2.0 in x-y plane. The developing region (I): (a) to (c); and self-similar region (III): (d) to (e). Legend is as in Fig. 4.34.

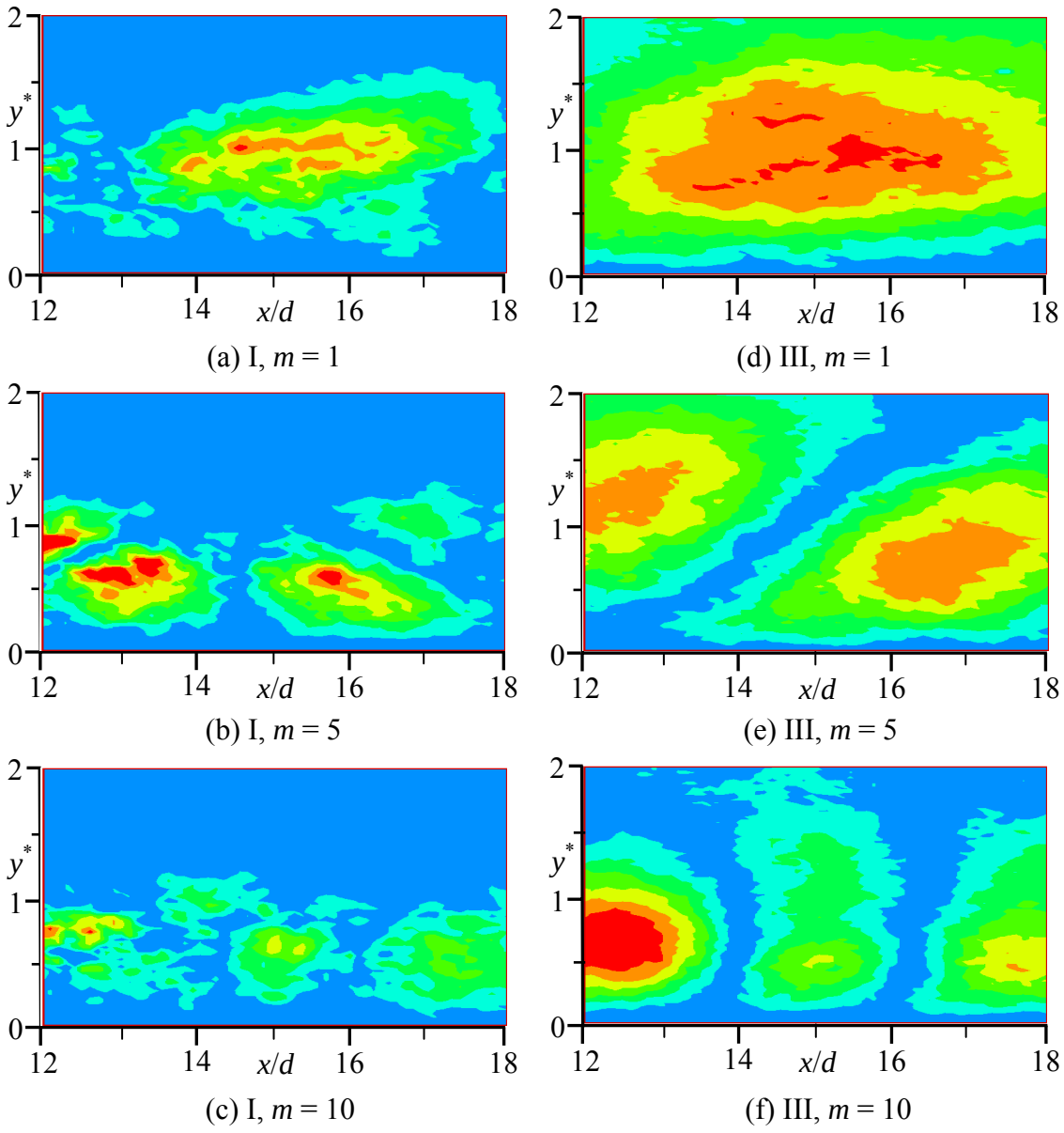

Figure 4.38: Iso-contours of wall-normal turbulence intensities (v) for modes, m = 1, 5 and 10 for h/d = 2.0 in x-y plane. The developing region (I): (a) to (c); and self-similar region (III): (d) to (e). Legend is as in Fig. 4.35.

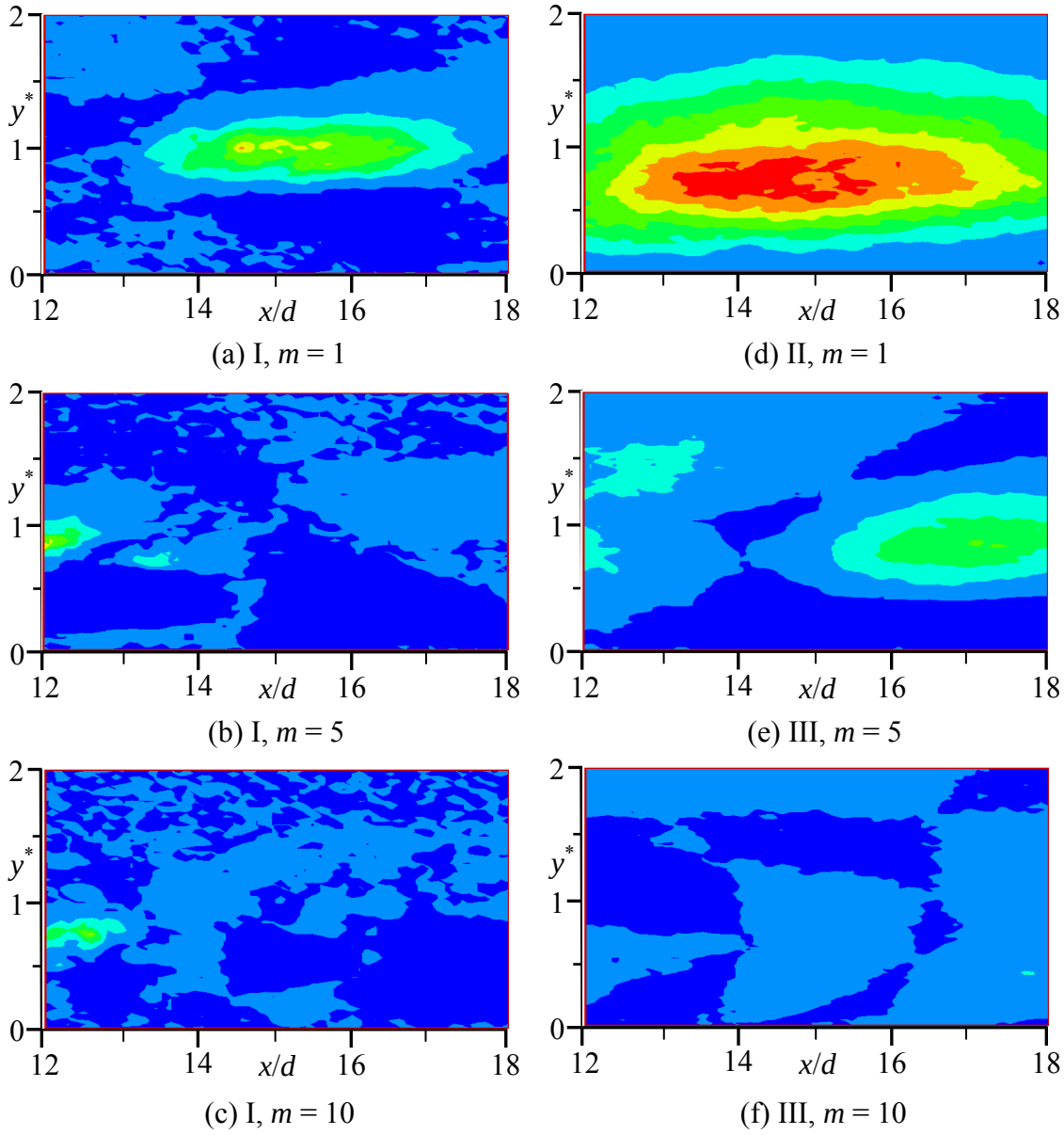

Figure 4.39: Iso-contours of Reynolds shear stresses (uv) for modes, m = 1, 5 and 10 for h/d = 2.0 in x-y plane. The developing region (I): (a) to (c); and self-similar region (III): (d) to (e). Legend is as in Fig. 4.36.

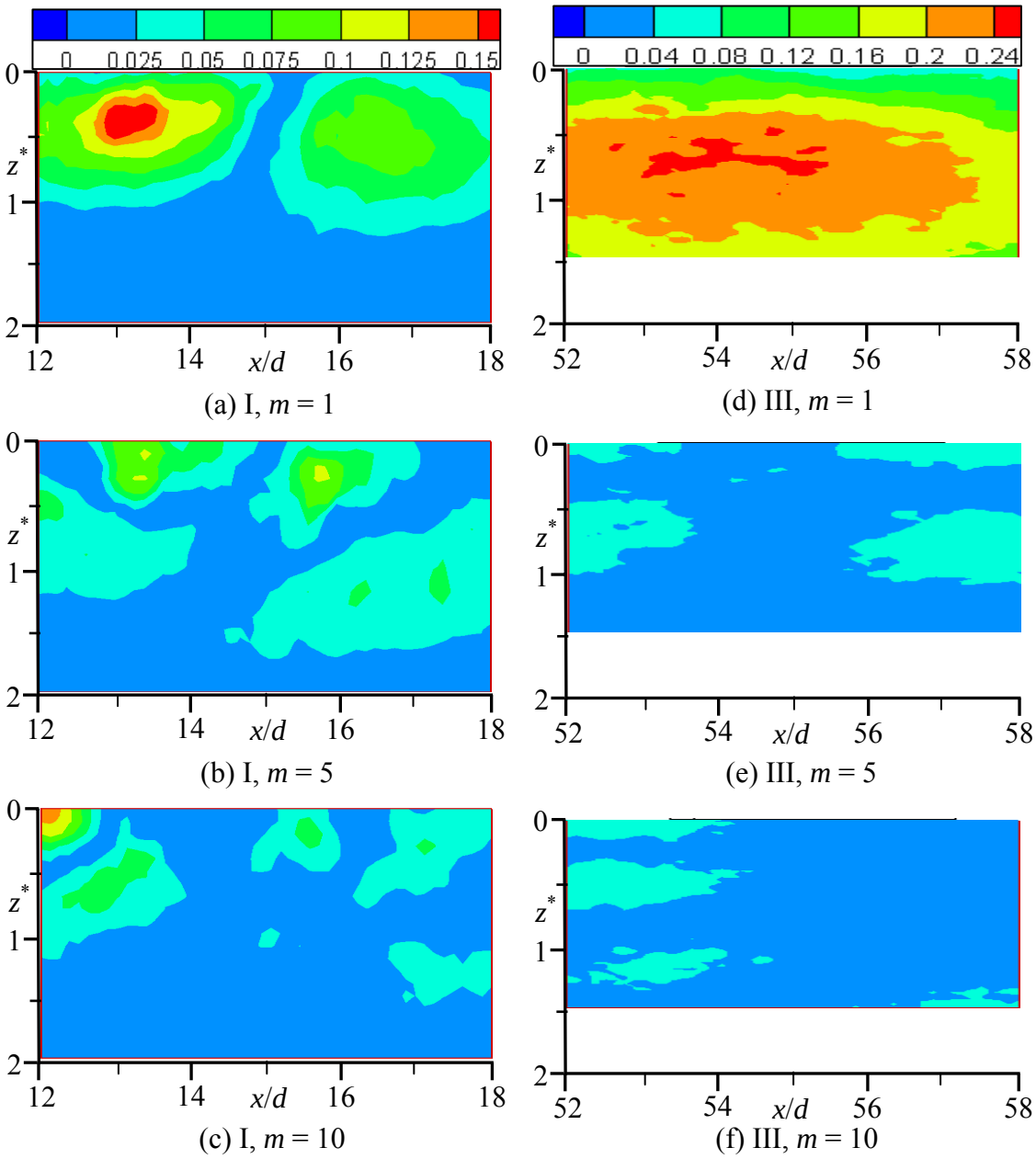

Figure 4.40: Iso-contours of streamwise turbulence intensities (u) for modes, m = 1, 5 and 10 for h/d = 0.5 in x-z plane. The developing region (I): (a) to (c); and self-similar region (III): (d) to (e).

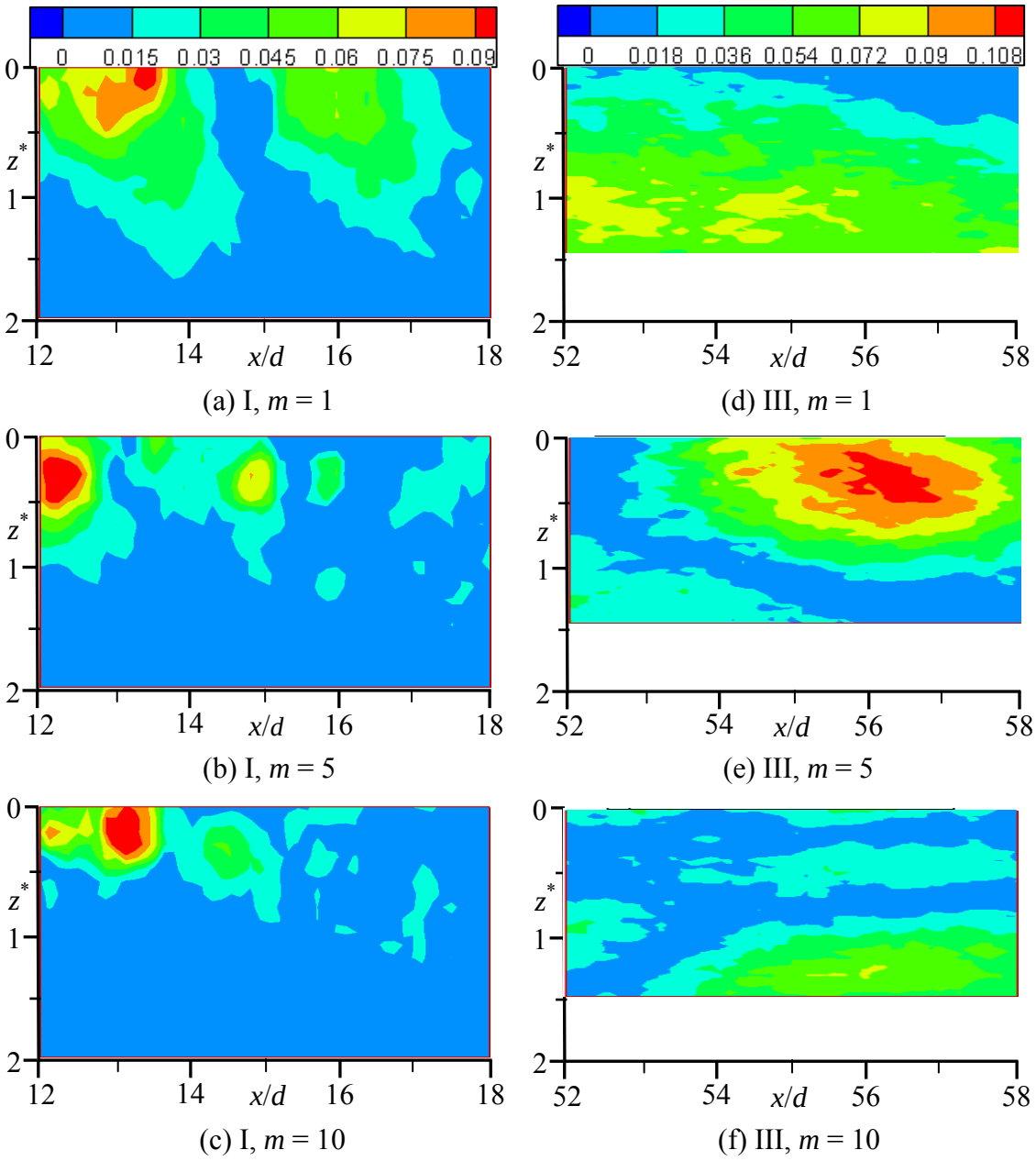

Figure 4.41: Iso-contours of lateral turbulence intensities (w) for modes, m = 1, 5 and 10 for h/d = 0.5 in x-z plane. The developing region (I): (a) to (c); and self-similar region (III): (d) to (e).

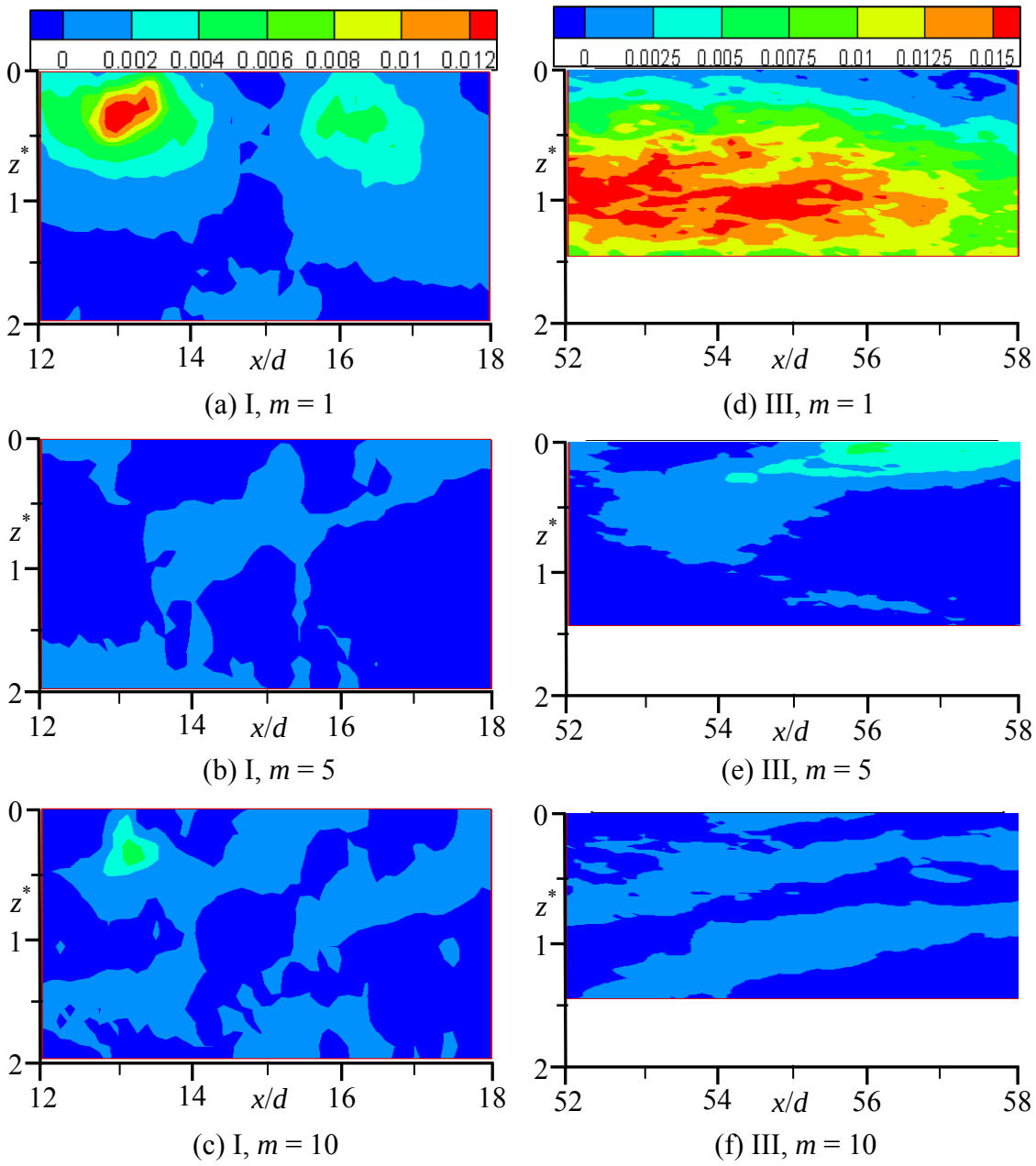

Figure 4.42: Iso-contours of Reynolds shear stresses (-*uw*) for modes, *m* = 1, 5 and 10 for *h*/*d* = 0.5 in *x*-*z* plane. The developing region (I): (a) to (c); and self-similar region (III): (d) to (e).

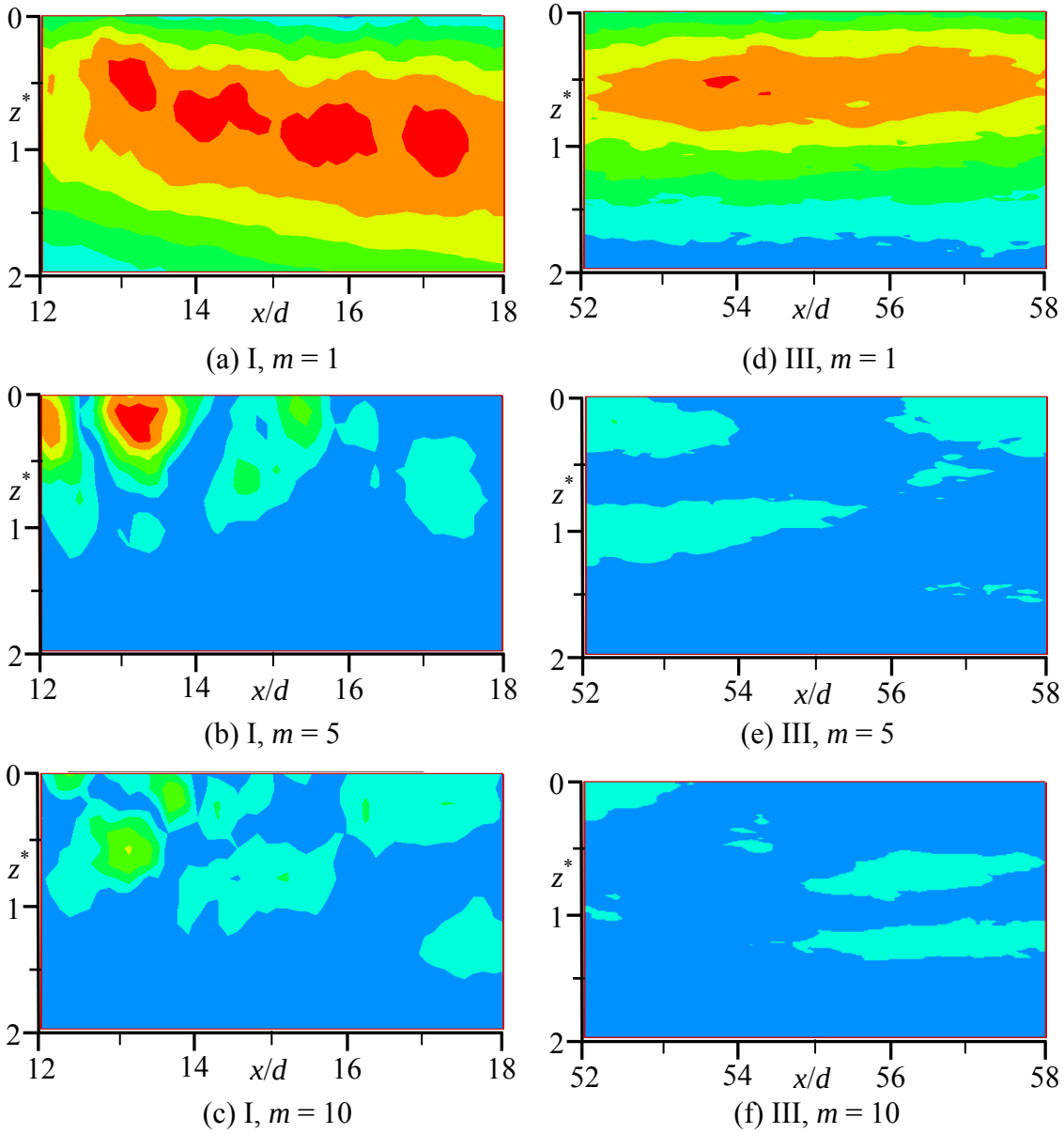

Figure 4.43: Iso-contours of streamwise turbulence intensities (u) for modes, m = 1, 5 and 10 for h/d = 2.0 in x-z plane. The developing region (I): (a) to (c); and self-similar region (III): (d) to (e). Legend is as in Fig. 4.40.

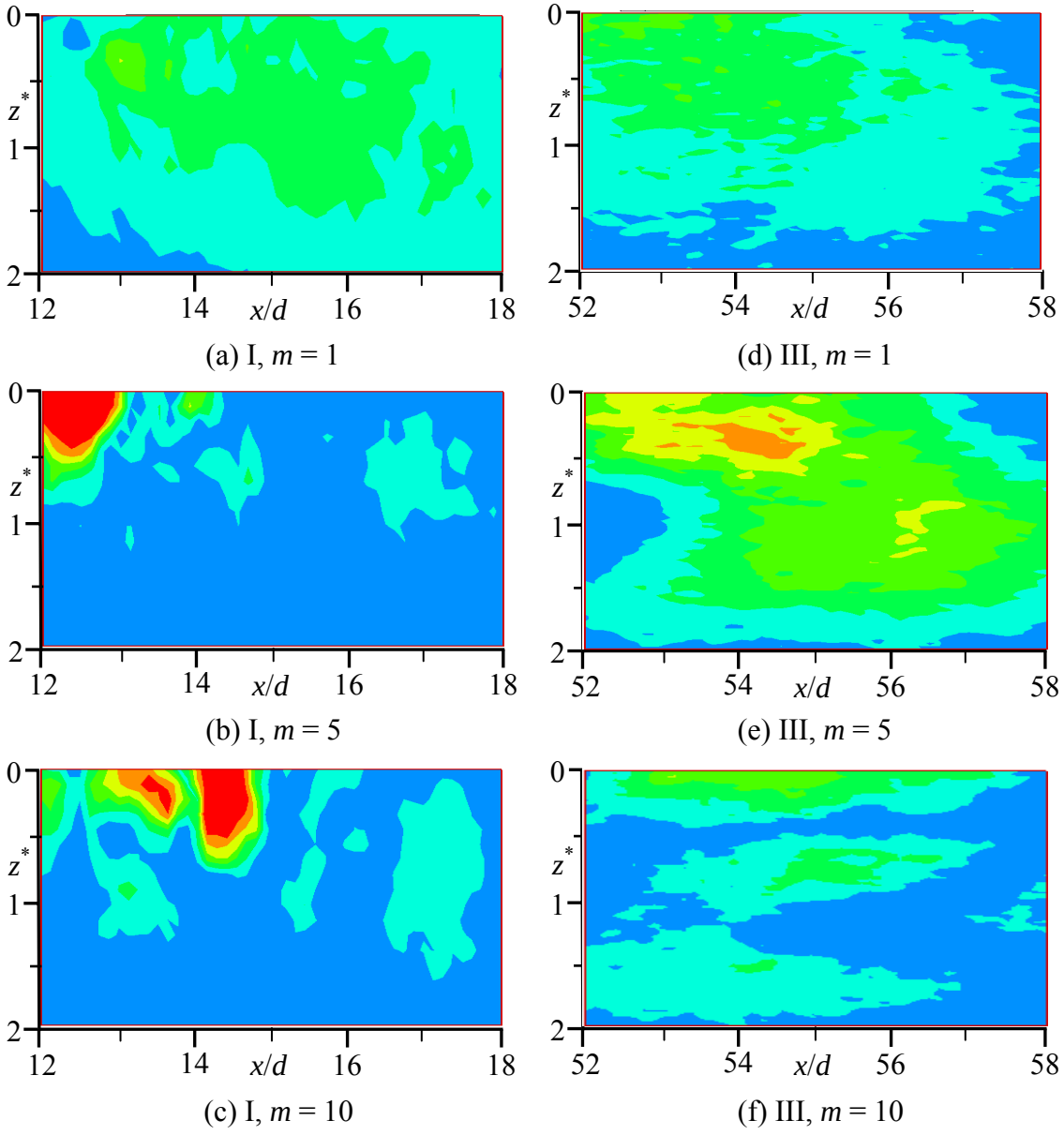

Figure 4.44: Iso-contours of lateral turbulence intensities (w) for modes, m = 1, 5 and 10 for h/d = 2.0 in x-z plane. The developing region (I): (a) to (c); and self-similar region (III): (d) to (e). Legend is as in Fig. 4.41.

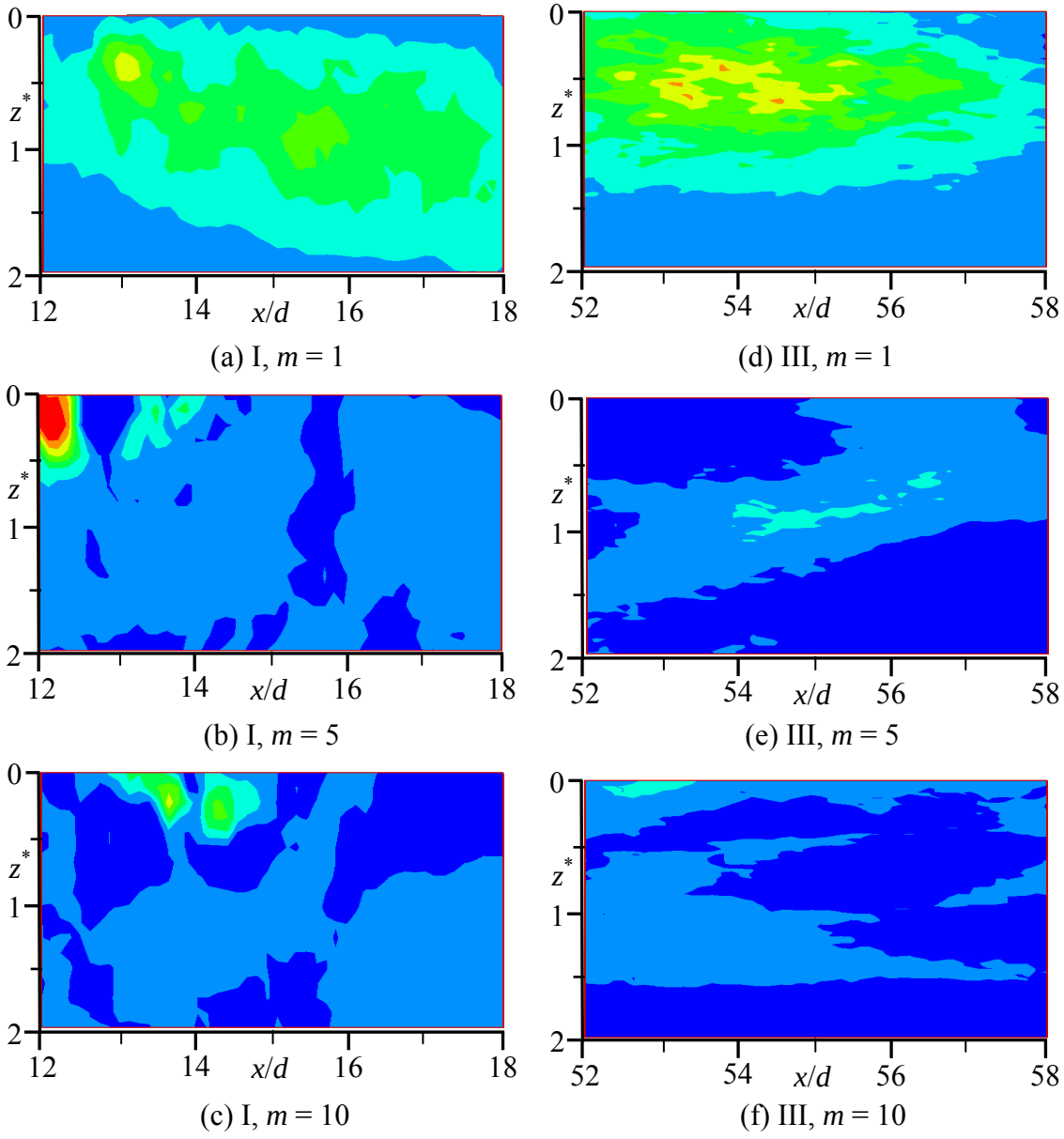

Figure 4.45: Iso-contours of Reynolds shear stresses (-*uw*) for modes, *m* = 1, 5 and 10 for *h*/*d* = 2.0 in *x*-*z* plane. The developing region (I): (a) to (c); and self-similar region (III): (d) to (e). Legend is as in Fig. 4.42.

For the streamwise turbulence intensities (u), the profiles for the various modes approach the ensemble PIV profiles significantly faster in the outer region ($y/y_{0.5} > 0.18$) than in the inner region ($y/y_{0.5} \leq 0.18$). For example, the peak values of the reconstructed data in the inner region are 6%, 7% and 47%, respectively, for the sum of the first 1, 3, and 25 modes. The corresponding peak values are 50%, 62% and 75% in the outer region. It is evident that there is no significant increase in the peak values from the first mode to the first 3 modes. The faster convergence towards the PIV data in the outer region confirms the earlier observation that energetic structures populate the outer region compared to the inner region. The convergence trends in the wall-normal turbulence intensities (v) are similar to the trends in u, although, the values for the first 5 modes are relatively smaller. For example, the peak values of v are 30% and 50% are reconstructed in the inner and outer regions, respectively, with the sum of the first 25 modes compared to peak values of 47% and 75% for u. These results show that the large scale structures contribute more to u than v. The convergence of the reconstructed Reynolds shear stresses (uv) towards the PIV data is quite fast but the negative and positive peak values were not captured in the first 3 modes. In the outer region of the developing region, 31%, 63% and 63% peak values, respectively, were reconstructed by the first 1, 3, and 25 modes.

In the self-similar region (i.e., $x/d = 75$), the general trends observed for the developing region above apply to the turbulence intensities, although, the convergence is faster. For instance, the peak values in the inner region are 52%, 80% and 91%, respectively, for the first 1, 3, and 25 modes. Similarly, 77%, 84% and 92% of peak values are reconstructed by the first 1, 3, and 25 modes, respectively, in the outer region. The corresponding peak values of the wall-normal turbulence intensities are 13%, 17%

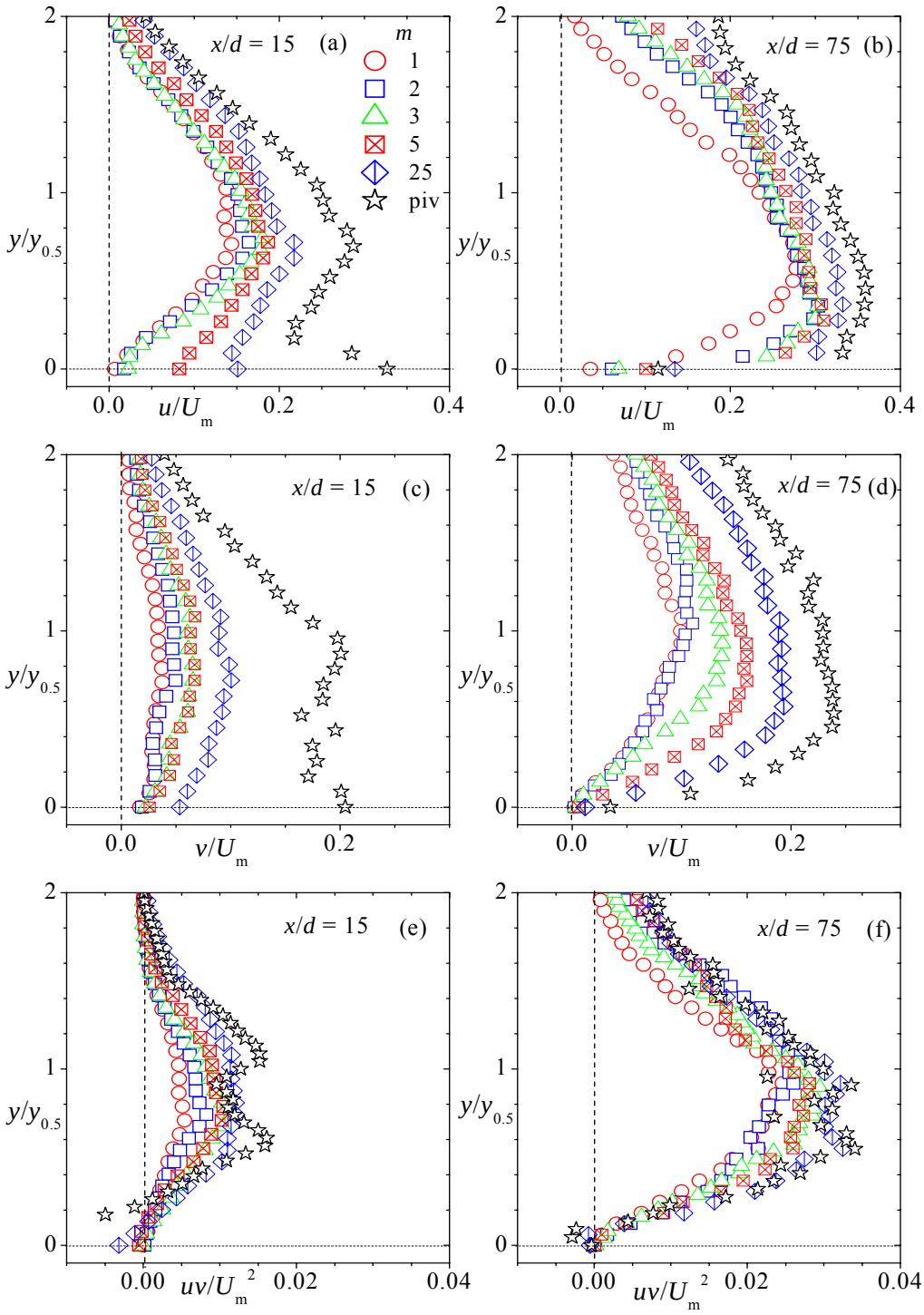

Figure 4.46: Profiles of reconstructed turbulent quantities in the developing (x/d = 15) and self-similar (x/d = 75) regions for h/d = 0.5. For the sum of the first m = 1, 2, 3, 5 and 25 modes: streamwise turbulence intensities (a) & (b); wall-normal turbulence intensities (c) & (d); and Reynolds shear stresses (e) & (f). piv is the ensemble PIV data.

and 64% in the inner region and 42%, 57% and 80% in the outer region. Similar to the developing region, it is evident from these values that the turbulence intensities are reconstructed more in the outer region than in the inner region. In addition, the streamwise turbulence intensities are reconstructed more than the wall-normal turbulence intensities. It is also evident that the percentage reconstructed is much higher in the self-similar region than in the developing region. Similar to the developing region, the Reynolds shear stresses are almost completely reconstructed in the self-similar region. Furthermore, 95% of Reynolds shear stresses are reconstructed with the first 25 modes.

Attention is now turned to the reconstructed profiles of the offset jets (h/d = 2.0 and 4.0). Figures 4.47-4.48 show that the energy distribution in the offset jets is similar to that in the generic wall jet. In both the developing and self-similar regions, the convergence of the Reynolds shear stresses towards the ensemble PIV profiles is the fastest. This is followed by the streamwise turbulence intensities and the finally the wall-normal turbulence intensities. The proportions of the reconstructed profiles are consistently higher in the self-similar regions than in the developing regions. For each sum of modes, the outer region convergences faster toward the ensemble PIV profiles than the inner region. The following are some peak values expressed as percentage of their corresponding ensemble PIV peak values to confirm the above statements. For h/d = 2.0, the peak values in the inner region are approximately 4%, 28% and 60% for u; 0%,16% and 32% for v; and 9%, 18% and 72% for uv for the first 1, 3, and 25 modes. Similarly, the peak values are approximately 52%, 55% and 74% for u; 23%, 29% and 55% for v; and 43%, 57% and 94% for uv in the outer region for the first 1, 3, and 25

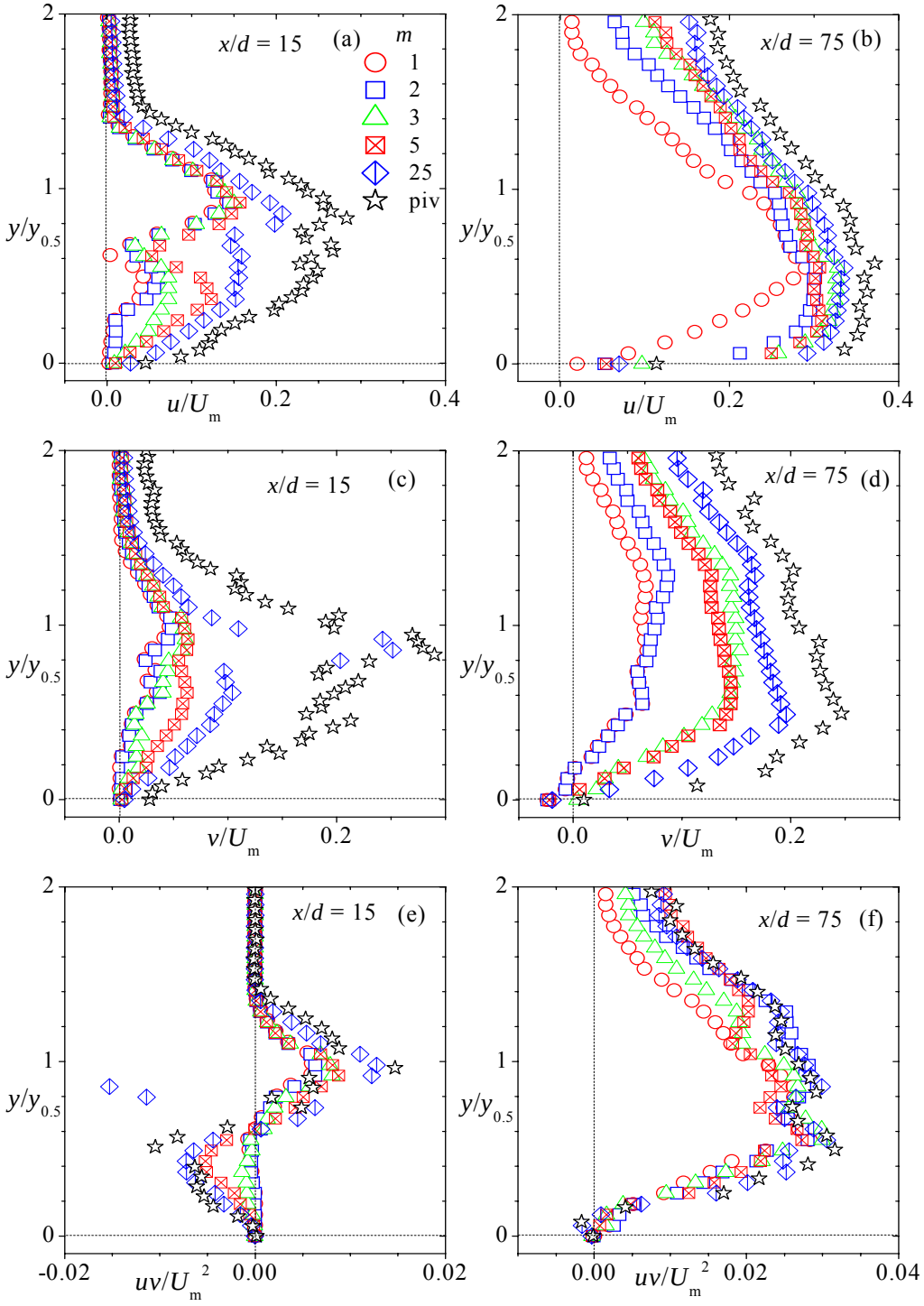

Figure 4.47: Profiles of reconstructed turbulent quantities in the developing (x/d = 15) and self-similar (x/d = 75) regions for h/d = 2.0. For the sum of the first m = 1, 2, 3, 5 and 25 modes: streamwise turbulence intensities (a) & (b); wall-normal turbulence intensities (c) & (d); and Reynolds shear stresses (e) & (f). piv is the ensemble PIV data.

modes. The peak values for $h/d = 4.0$ are not significantly different from the above stated values.

In the *x*-*z* (i.e., lateral) plane, the reconstructed profiles exhibit trends and characteristics similar to those described for the *x*-*y* plane and will not also be repeated here. It should be pointed out, however, that in this plane, the convergence towards the ensemble PIV profiles is faster away from the symmetry plane (i.e., $z = 0$) than close to it. The reconstructed profiles in the *x*-*z* plane are shown in Fig. D.11-D.13 of Appendix D.

Before closing this section, it is worthwhile summarizing the salient observations. The results indicate that irrespective of the test condition, the outer region consistently converges faster than the inner region because of the presence of large scale structures in the former. Similar trends were reported by Shah (2009) for a turbulent channel flow. However the present results have faster convergence than in that study. For example, it was reported that nearly 80%, 62% and 100% of the *u*, *v* and -*uv* were reconstructed closed to the channel centerline by the first 50 modes (Shah, 2009). Meanwhile, 92%, 80% and 95% of the *u*, *v* and -*uv* were reconstructed by only the first 25 modes in the present study. The reconstruction is more effective in the self-similar region than in the developing region. This also suggests that large scale structures grow as the flow evolves downstream. Even though the POD is optimized for energy, the reconstructed Reynolds shear stress profiles were observed to converge towards the ensemble PIV profiles faster than the profiles of the reconstructed turbulence intensities. The first 25 modes alone can reconstruct more than 90% of the Reynolds shear stresses in the outer region of the self-similar section. This means that the contribution of the large scale structures to the

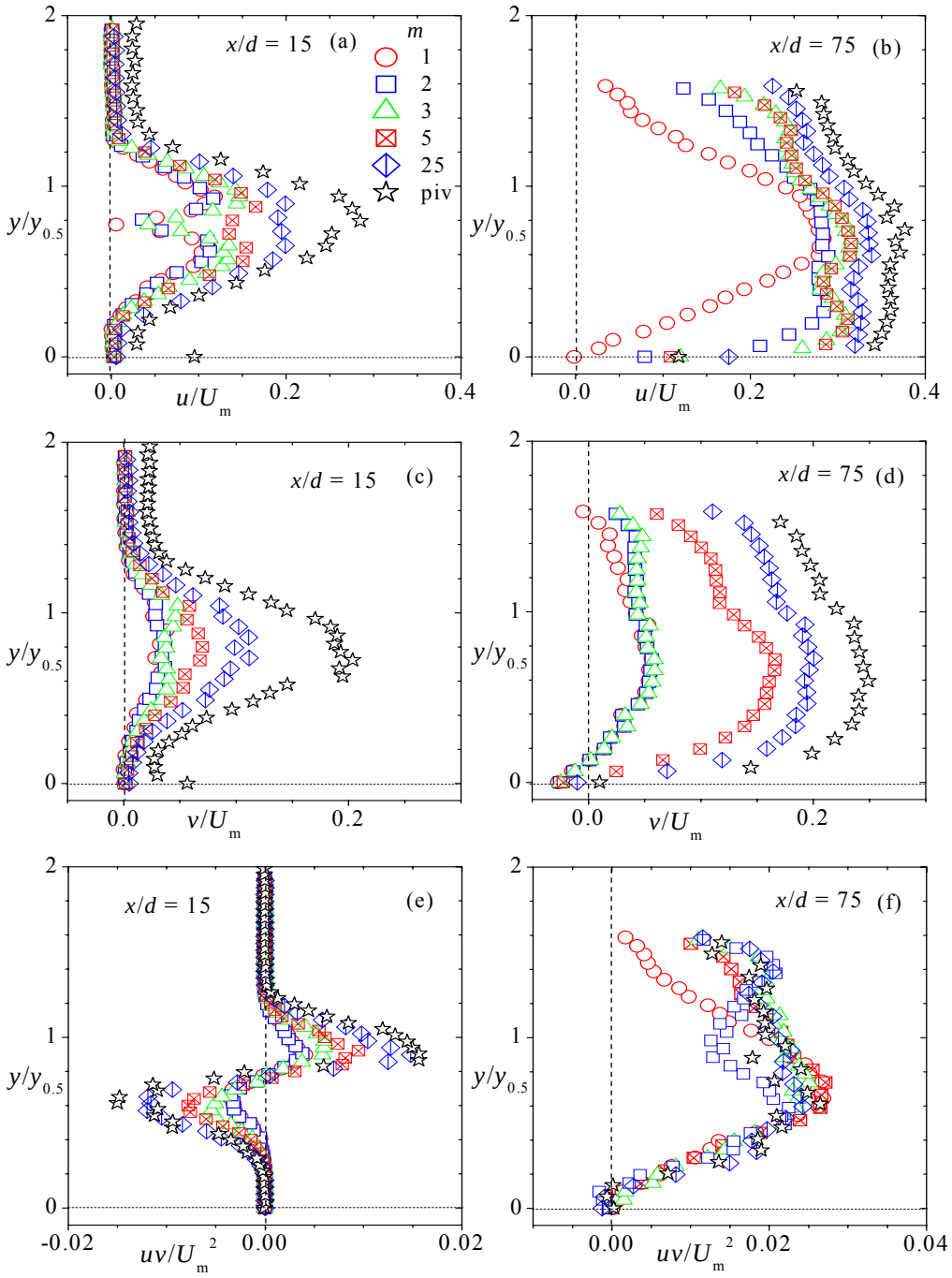

Figure 4.48: Profiles of reconstructed turbulent quantities in the developing (x/d = 15) and self-similar (x/d = 75) regions for h/d = 4.0. For the sum of the first m = 1, 2, 3, 5 and 25 modes: streamwise turbulence intensities (a) & (b); wall-normal turbulence intensities (c) & (d); and Reynolds shear stresses (e) & (f). piv is the ensemble PIV data.

Reynolds shear stresses is more than to the other quantities. As mentioned earlier, these results are consistent with previous POD studies in channel flows (Reichert et al., 1994; Moin & Moser, 1989). Blackwelder & Kovasznay (1972) concluded that large scale structures in a turbulent boundary layer contribute relatively more to Reynolds shear stresses. More importantly, how energy is redistributed to the various components of the Reynolds normal stresses in the generic wall jet and the offset jets was observed to be similar. In both cases the turbulence energy is transferred to the streamwise component of the Reynolds normal stress, and subsequently redistributed into the wall-normal and lateral components. For the lower modes (modes 1 to 25) presented here it means large scale structure contribute proportionally more to the streamwise turbulence intensities than the wall-normal turbulence intensities.

CHAPTER 5

SUMMARY OF RESULTS AND FUTURE WORK

In this chapter, a summary of the results and conclusions are reported. The implications of the results for turbulence modeling and recommendations for future work are also presented.

5.1 Summary of Results and Conclusions

A comprehensive experimental study was undertaken to examine and document the development and structures of turbulent 3D offset jets. The generic 3D wall jet at the same Reynolds numbers was used as the basis of comparison. The experiments were performed using a high resolution particle image velocimetry technique to perform velocity measurements at three Reynolds numbers based on the jet exit velocity and diameter of 5000, 10000 and 20000, and four jet offset heights of 0.5, 1.0, 2.0 and 4.0. The measurements were performed in the streamwise/wall-normal plane from 0 to 120 jet exit diameters and in the streamwise/lateral plane from 10 to 80 jet exit diameters.

The first part of the study considered the mean quantities and the turbulence statistics. The decay of the maximum mean velocities and spread of the jet half widths became independent of Reynolds number much earlier in the generic wall jet than the offset jets. The decay rate and wall-normal spread rate increased slightly with the offset height whereas the lateral spread rate decreased with offset heights. The reattachment lengths are also independent of Reynolds number but increase linearly with offset height. The values of the reattachment length obtained for the 3D offset jets are smaller than the corresponding values obtained for the 2D offset jets. This can be attributed to the effect

of entrainment in the near field. The streamwise mean velocities, turbulence intensities and Reynolds shear stresses attained self-similarity earlier in the generic wall jets than in the offset jets, when the jet half widths and local maximum velocities are used as the length and velocity scales, respectively. The turbulence statistics in the present study are generally higher than in previous 3D wall jet studies partly due the high exit turbulence levels. In addition, the spread rate in the wall-normal direction is larger than values reported in the literature. The results show that there is delayed development of the offset jets which increases with offset heights. The results also indicate that in the outer region of the streamwise/wall-normal plane, the mean streamwise velocities collapsed much earlier and better when a combination of the location of the maximum streamwise velocity (y_m) and jet half width are used as the length scale instead of only the jet half width. However, the collapse of the turbulence intensities and Reynolds shear stresses were not improved by this normalization.

It was observed that the stress ratios (v^2/u^2) in the inner are much smaller than reported for boundary layers and v^2/u^2 in the outer regions are also smaller than those of the plane jets. Similarly, the Townsend's structure parameter ($uv/2k$) in the inner layers is much smaller than the value traditionally used for boundary layers but the $uv/2k$ value in the outer regions is similar to those used for boundary layers. The triple velocity products of the present 3D wall jets have the trends similar to those of 2D wall jets; however, the present values are much larger than 2D wall jet values. As a result of the stronger effect of the outer region on the inner region in the 3D wall jets than the 2D wall jets, the triple velocity products in the 3D wall jets changed sign close to the wall than in 2D wall jets. Unlike canonical boundary layer flows and 2D wall jets, the wall-normal velocity

gradients ($\partial V/\partial y$) are predominantly negative. As a result, there are both significant transfer of momentum in the wall-normal direction and turbulence augmentation ($v^2\partial V/\partial y$) in the 3D wall jets. In addition, the wall-normal velocity gradients are more significant in the flow development region of the offset jets and thus contribute more to momentum transport and turbulence production than in generic wall jets.

In addition to the one-point statistics, the two-point velocity correlations were used to study how the fluctuating turbulence intensities are correlated in the developing and self-similar regions. The observations and conclusions made are as follows: the iso-contours of both the streamwise and wall-normal auto-correlations are larger in the outer region than in the inner layer. Furthermore, the iso-contours in the self-similar regions are much larger in size than the corresponding iso-contours in the developing region. This indicates that the turbulence fluctuations are correlated over more extended distances in the outer and self-similar regions than in the inner and developing regions, and therefore implies large scale structures exist in the outer region. The auto-correlations also increase in size with the offset heights indicating that the large scale structures grow with offset heights. The iso-contours of the streamwise auto-correlations in the inner region of the jets inclined at angles $\beta = 11.2^{o} \pm 0.6^{o}$. These values are in good agreement with reported values in boundary layer studies. However, the angles decrease with the wall-normal distance from the wall and become zero when the wall effect is nonexistent.

In the final part of the study, the proper orthogonal decomposition was employed to assess the energy content of the various POD modes along the downstream direction of the flow. The POD results indicate that, irrespective of the test condition, the energy content in the self-similar region is consistently more than in the developing region

because of the presence of large scale structures. As a result, the reconstruction of the turbulence intensities and Reynolds shear stresses from selected low-order POD modes is more effective in the self-similar region than the developing region. Furthermore, the reconstructed profiles indicated that the outer regions converged faster, which is a further confirmation that the outer region has more large scale structures than the inner region. Consistent with previous studies, the present results imply that large scale structures contributed more to the Reynolds shear stresses than to the Reynolds normal stresses and the energy is redistributed to the Reynolds normal stresses in the streamwise direction first before the Reynolds normal stresses in the wall-normal direction.

5.2 Implications for Turbulence Modeling

The comprehensive experimental data obtained for the 3D offset jets in this study are invaluable benchmark data for validating and calibrating advanced turbulence models for fluid engineering applications.

The results indicate that the convective and diffusion terms in turbulent kinetic energy transport equation are not negligible so that the production term is not exactly balanced by dissipation rate. Therefore, turbulence models based on the equilibrium assumption will not be able to reproduce the 3D offset jets.

The results also show that the offset jet flows are highly anisotropic and therefore turbulence models which cannot distinguish between the various Reynolds normal stresses would not be suitable for the type of flows in this present study.

The Townsend's structure parameter ($uv/2k$) in the inner layers is much smaller than the value traditionally used for boundary layers which implies the traditional value is not suitable for offset jets.

The results of the proper orthogonal decomposition indicate that the first 25 POD modes contain more than 90% of the Reynolds shear stresses and up to 90% of turbulence intensities in the outer regions in the self-similar regions. This result can provide a guide for effective optimization of LES.

Since the turbulence production by the wall-normal Reynolds normal stress ($v^2 \partial V/\partial y$) is not negligible, RANS models such as the Second Moment Closures that implicitly account for the normal stresses will be more ideal for predicting the flow features of 3D offset jets.

5.3 Recommendations for Future Work

Due to limitations of the test facilities, the present study performed measurements in the streamwise/wall-normal plane as well as the streamwise/lateral plane at the wall-normal location of the maximum mean streamwise velocities. Although this study is the most comprehensive 3D offset jet study to date, it was not possible to measure the complete Reynolds stresses of 3D wall jets and offset jets. Measurement techniques that can obtain volumetric velocity data such as the holographic particle image velocimetry technique could provide the complete Reynolds stresses and quantify the contribution of the gradients to the various vorticities. These will shed more light on the mechanisms responsible for the anisotropic spreading in the 3D wall jets and how it is sustained.

In addition, the standard PIV could not resolve the temporal evolution of the flow. The Time-Resolved PIV technique which is capable of providing the temporal evolution of the velocity field and the time-space correlations could be employed to study the time scales and other temporal characteristics of the coherent structures.

Furthermore, the present and previous 3D offsets were performed on smooth surfaces. It would be interesting to investigate how surface roughness affects the flow structures.

BIBLIOGRAPHY

Abrahamsson, H., Johansson, B. & Lofdahl, L. 1994 A turbulent plane two-dimensional wall-jet in a quiescent surrounding. *Euro. J. Mech., B/Fluids*. **13**, pp. 533-556.

Abrahamsson H, Johansson B. & Lofdahl, L. 1997 The turbulence field of a fully developed three-dimensional wall jet. Internal Report 97/1.

Adrian, R. J. 1991 Particle imaging techniques for experimental fluid mechanics, Ann. Rev. Fluid Mech., **23**, pp. 261-304

Adrian, R. J., Christensen, K. T. & Liu, Z.-C. 2000 Analysis and interpretation of instantaneous turbulent velocity fields. *Exp. Fluids*, **29**, pp. 275–290.

Alfonsi, G. & Primavera, L. 2007 Dynamics of POD Modes in Wall Bounded Turbulent Flow. *Proc. R. Soc. A.*, **463**, pp. 593-612.

Ashforth-Frost, S. & Jambunathan, K. 1996 Effect of nozzle geometry and semi-confinement on the potential core of a turbulent axisymmetric free jet. *Int. Comm. Heat and Mass Transfer*, **23**, No. 2, pp. 155-162.

Aung, W. 1983 Separated Forced Convection. ASME-JSME Thermal Engineering Joint Conference Proceedings, v2, Honolulu, Hawaii, March 20-24, pp. 499-515.

Bakewell, H. P. & Lumley, J. L. 1967 The viscous sublayer and adjacent wall region in turbulent pipe flows. *Phys. Fluids*, **10**, pp. 1880-1889.

Balachander, R. & Ramachandran, S. 1999 Turbulent Boundary Layers in Low Reynolds Number Shallow Open Channel Flows. *Trans. ASME J. Fluids Eng.*, **121**, pp. 684 - 689.

Bernard, P. S. & Wallace, J. M. 2002 Turbulent Flow: Analysis, Measurement,

Prediction. John Wiley & Sons, Inc. Hoboken, New Jersey.

Bi, W., Sugii, Y., Okamoto, K. & Madarame, H. 2003 Time-resolved proper orthogonal decomposition of the near-field flow of a round jet measured by dynamic particle image velocimetry. *Meas. Sci. Tech*., **14**, pp. L1–L5.

Blackwelder, R. F. & Kovasznay, L. S. G. 1972 Large-scale motion of a turbulent boundary layer during relaminarization. *J. Fluid Mech*., **53**, pp. 61.

Bourque, C. & Newman, B. G. 1960 Reattachment of a two-dimensional incompressible jet to an adjacent flat plate. *Aero. Quart*., **11**, pp. 201–232.

Breuer, K. S. & Sirovich, L. 1991 The Use of Karhunen-Loève Procedure for the Calculation of Linear Eigenfunctions. *J. Comp. Phys.*, **96**, pp. 277-296.

Christensen, K. T. & Adrian, R. J. 2001 Statistical evidence of hairpin vortex packets in wall turbulence. *J. Fluid Mech*., **431**, pp. 433-443.

Christensen, K. T. & Wu, Y. 2005 Visualization and Characterization of Small-Scale Spanwise Vortices in Turbulent Channel Flow. *J. Visualization*, **8**, No. 2, pp. 177-185.

Cizmas, P. G., Palacious, A., Brien, T. O. & Syamlal, M. 2003 Proper Orthogonal Decomposition of Spatio-Temporal Patterns in Fluidized Beds. *Chem. Eng. Sci*., **58**, pp. 4417–4427.

Codazzi, D., Teitgen, R. & Burnage, H. 1981 Jet turbulent paribtal axisymetrique. Similitude de l'bcoulement hors de la couche limite. C. R. *Acad. Sci. Ser. H*, **293**, pp. 103-6.

Coleman, H. W. & Steele, W. G. 1995 Engineering Application of Experimental Uncertainty Analysis. *AIAA J*., **33**, pp. 1888-1896.

Craft, T. J. & Launder, B. E. 2001 On the spreading mechanism of the three-dimensional turbulent wall jet. *J. Fluid Mech*., **435**, pp. 305-326.

Davis M. R. & Winarto, H. 1980 Jet diffusion from a circular nozzle above a solid plane. *J. Fluid Mech*., **101**, pp. 201-221.

Eaton, J. K. & Johnston, J. P. 1981 A Review of Research on Subsonic Turbulent Flow Reattachment. *AIAA J.*, **19**, pp. 1093 – 1100.

Eriksson, J. G., Karlsson, R. I. & Persson, J. 1998 An Experimental Study of a Two-Dimensional Plane Wall Jet. *Exp. Fluids*, **25**, pp. 50-60.

Etheridge, D. W. & Kemp, P. H. 1978 Measurements of turbulent flow downstream of a rearward-facing step. *J. Fluid Mech*., **86**, pp. 545-566.

Ewing, D. & Pollard, A. 1997 Evolution of the large-scale motions in a three-dimensional wall jet. In *28th AIAA Fluid Dynamics Conference/4th AIAA Shear Flow Control Conference*, Paper No. 97-1964.

Forliti, D. J., Strykowski, P. J. & Debatin, K. 2000 Bias and Precision Errors of Digital Particle Image Velocimetry. *Exp. Fluids*, **28**, pp. 436-447.

Forthmann, E. 1934 Uber turbulente Stranhlausbreitung. *lng.-Arch*., **5**, pp. 42, also *NACA TM789*, 1936.

Fujisawa, N. & Shirai, H. 1989 Mean flow and turbulence characteristics of Three-dimensional wall jet along plane surface. *Trans. Jpn. Soc. Aero. Sci.*, **32**, No. 95, pp. 35–46.

Gamard, S., Jung, D. & George, W. K. 2004 Downstream evolution of the most energetic modes in a turbulent axisymmetric jet at high Reynolds number. Part 2. The far-field region. *J. Fluid Mech*., **514**, pp. 205–230.

Gao, N. & Ewing, D. 2008 On the phase velocities of the motions in an offset attaching planar jet. *J. Turb.*, **9**, No. 27, pp. 1–21.

Gao, N. & Ewing, D. 2007 Experimental investigation of planar offset attaching jets with small offset distances. *Exp. Fluids*, **42**, pp. 941–954.

Gordeyev S.V. 1999 Investigation of Coherent Structure in the Self-Similarity Region of the Turbulent Planar Jet Using POD and Wavelet Analysis. Ph.D. Thesis, University of Notre Dame, Indiana, USA.

Gordeyev, S. V. & Thomas, F. O. 2002 Coherent structure in the turbulent planar jet. Part 2. Structural topology via POD eigenmode projection. *J. Fluid Mech.*, **460**, pp. 349-380.

Gordeyev, S. V. & Thomas, F. O. 2000 Coherent Structure in the Turbulent Planar Jet Part1. Extraction of Proper Orthogonal Decomposition Eigenmodes and Their Self- Similarity. *J. Fluid Mech.*, **414**, pp. 145 - 195.

Graftieaux, L., Michard, M. & Grosjean, N. 2001 Combining, PIV, POD, and vortex Identification Algorithms for the Study of Unsteady Turbulent Swirling Flows. *Meas. Sci. Tech.*, **12**, pp. 1422 – 1429.

Granville, P. S. 1977 Drag and Turbulent Boundary Layer of Flat Plates at Low Reynolds numbers. *J. Ship Res.*, **21**, pp. 30 – 39.

Gui, L., Longo, J. & Stern, F. 2001 Biases of PIV measurement of turbulent flow and the masked correlation-based interrogation algorithms. *Exp. Fluids*, **30**, pp. 27-35.

Guitton, D. E. & Newman, B. G. 1977. Self-preserving turbulent wall jets over convex surfaces. *J. Fluid Mech.*, **81**, pp. 155

Hall, J. W. 2005 The Role of the Large-Scale Structures in the Development of

Turbulent Wall Jets. PhD Thesis, McMaster University, Hamilton, Ontario, Canada.

Hall, J. W. & Ewing, D. 2007a The Asymmetry of the Large-Scale Structures in Turbulent Three-Dimensional Wall Jets Exiting Long Rectangular Channels. *J. Fluids Eng*., **129,** pp. 929-941.

Hall, J. W. & Ewing, D. 2007b Three-Dimensional Turbulent Wall Jets Issuing from Moderate-Aspect-Ratio Rectangular Channels. *AIAA J*., **45**, No. 6, pp. 1177-1186.

Hammad, K. J. & Milanovic, I. M. 2009 A POD Study of an Impinging Jet Flow Field. In proceedings of the ASME 2009 Fluids Engineering Division Summer Meeting, Paper No. FEDSM2009-78398.

Harsha, P. T. & Lee, S. C. 1970 Use of Turbulence Kinetic Energy in Free Mixing Studies. *AIAA J*., **8**, No. 6, pp. 1026 – 1032.

Head, M. R. & Bandyopadhyay, P. 1981 New aspects of turbulent boundary-layer structure. *J. Fluid Mech*., **107**, pp. 297-338.

Hoch, J. & Jiji, L. M. 1981 Two-dimensional turbulent offset jet-boundary interaction. *Trans. ASME J. Fluids Eng*., **103**, pp. 154–161.

Holmes, P. Lumley, J. L. & Berkooz. G. 1996 Turbulence, Coherent Structures, Dynamical Systems and Symmetry. Cambridge University Press, New York.

Iqbal, M. O. & Thomas, F. O. 2007 Coherent structure in a turbulent jet via a vector implementation of the proper orthogonal decomposition. *J. Fluid Mech*., **571**, pp. 281-326.

Irwin, H. P. A. 1973 Measurements in a self-preserving plane wall jet in a positive pressure gradient. *J. Fluid Mech*., **61**, pp. 33-83.

Jović, S. 1996 An Experimental Study of a Separated/Reattached Flow Behind a Backward Facing Step, Re_h = 37000. NASA Technical Memorandum 110384.

Karlsson, R. I., Eriksson, J. & Persson, J. 1992 LDV Measurement in a Plane Wall Jet in a Large Enclosure. 6th International Symposium on Applications of Laser Techniques to Fluid Mechanics. July 20th-23rd, Lisbon, Portugal.

Keane, R. D. & Adrian, R. J. 1990 Optimization of Particle Image Velocimetry, Part1: Doubled Pulsed System. *Meas. Sci. and Tech.*, **1**, No. 11, pp. 1202-1215.

Keane, R. D. & Adrian, R. J. 1992 Theory of Cross-Correlation Analysis of PIV images. *Appl. Sci. Res.*, **49**, pp. 191-215.

Kostas, J. 2002 An Experimental Investigation of the Structure of a Turbulent Backward Facing Step Flow. Ph.D. Thesis, Monash University, Melbourne, Australia.

Kostas, J., Soria, J. & Chong, M. 2005 A comparison Between Snapshot POD Analysis of PIV Velocity and Vorticity Data. *Exp. Fluids*, **38**, pp.146-160.

Krogstad, P. -Å. & Antonia, R. A. 1994 Structure of turbulent boundary layers on smooth and rough walls. *J. Fluid Mech.*, **277**, pp. 1-21.

Kumada, M., Mabuchi, I. & Oyakawa, K. 1973 Studies on Heat Transfer to Turbulent Jets with Adjacent Boundaries: 3rd Report, Mass Transfer to Plane Turbulent jet Reattached on an Offset Parallel Plate. *Bull JSME*, **16**, No. 101, pp. 1712–1720.

Launder, B. E. & Reece, G. J. 1975 Progress in the development of a Reynolds stress turbulence closure. *J. Fluid Mech.*, **68**, pp. 537 – 566.

Launder, B. E. & Rodi, W. 1981 The Turbulent Wall Jet. *Prog. Aero. Sci.*, **19**, pp. 81- 128.

Launder, B. E. & Rodi, W. 1983 The Turbulent Wall Jet-Measurement and Modeling.

Ann. Rev. Fluid Mech., **15**, pp. 429-459.

Law, A., W-K. & Herlina 2002 An Experimental Study on Turbulent Circular Wall Jets. *J. Hydr. Eng*., **128**, pp. 161-174.

Lida, S. & Matsuda, H. 1988 An experimental study of circular turbulent wall jet along a convex wall. *Transactions of the JSME*, **50**, pp. 354–360.

Lumley, J. L. 1967 The Structure of Inhomogeneous Turbulent Flow. In Atmospheric Turbulence and Radio Wave Propagation (*ed*. Yaglon, A. M. & Tatarski, V. I.), pp.167-178, Nauka, Moscow.

Lund, T. S. 1986 Augmented thrust and mass flow associated with two-dimensional jet reattachment. *AIAA J*., **24**, pp. 1964–1970.

Mathieu, J. & Scott, J. 2000 An Introduction to Turbulent Flow. Cambridge University Press, Cambridge, UK.

Matsuda, H., Lida, S. & Hayakawa, M. 1990 Coherent Structures in a Three-Dimensional Wall Jet. *J. Fluids Eng*., **112**, pp. 462-467.

McRee, D. I. & Moses, H. L. 1967 The Effect of Aspect Ratio and Offset on Nozzle Flow and Jet Reattachment. *Advances in Fluidic*, ed by F. T. Brown, ASME, New York, pp. 142 – 161.

Mei, M. Adrian, R. J. & Hanratty, T. J. 1991 Particle disperson in isotropic turbulence under stokes drag and Basset force with gravitational settling. *J. Fluid Mech*., **225**, pp. 481-495.

Meyer, E. K., Pedersen, J. M. & Özcan, O. 2007 A Turbulent Jet in Crossflow Analysed with Proper Orthogonal Decomposition. *J. Fluid Mech*., **583**, pp. 199-227.

Moin, P. & Kim, J. 1985 The structure of the vorticity field in turbulent channel flow.

Part 1. Analysis of instantaneous and statistical correlation. *J. Fluid Mech*., **155**, pp. 441–464.

Moin, P. & Moser, R. 1989 Characteristic-eddy Decomposition of Turbulence in a Channel. *J. Fluid Mech*., **200**, pp. 479 – 509.

Nasr, A. & Lai, J. 1997 Comparison of flow characteristics in the near field of two parallel plane jets and an offset plane jet. *Phys. Fluids*, **9**, pp. 2919–2931.

Nasr, A. & Lai, J. 1998 A turbulent plane offset jet with small offset ratio. *Exp. Fluids*, **24**, pp. 47–57.

Neuendorf, R. & Wygnanski, I. 1999 On a turbulent wall jet flowing over a circular cylinder. *J. Fluid Mech*., **381**, pp. 1-25.

Newman, B. G., Pate, R. P., Savage, S. B. & Tjio, H. K. 1972 Three-dimensional, Incompressible Turbulent Wall Jets. *Aero. Quart*., **23**, pp. 188-200.

Nozaki, T., Hatta, K., Nakashima, M. & Matsumura, H. 1979 Reattachment flow issuing from a finite width nozzle. *Bull JSME*, **22**, No. 165, pp. 340–347.

Nozaki, T., Hatta, K., Nakashima, M. & Matsumura, H. 1981 Reattachment flow issuing from a finite width nozzle (Report 2. Effects of Initial Turbulence Intensity). *Bull JSME*, **24**, No. 188, pp. 363–369.

Nozaki, T., Hatta, K., & Matsumura, H. 1982 Reattachment flow issuing from a finite width nozzle (Report 3. Effects of Inclinations of Reattachment Wall). *Bull JSME*, **25**, No. 200, pp. 196-203.

Nozaki, T. 1983 Reattachment flow issuing from a finite width nozzle (Report 4. Effects of Aspect Ratio of the Nozzle). *Bull JSME*, **26**, No. 221, pp. 1884–1890.

Orrelano, A. & Wengle, H. 2001 POD Analysis of Coherent Structures in Forced

Turbulent Flow over a Fence. *J. Turb*., **2**, pp. 1-35.

Padmanabham, G. & Gowda L. B. H. 1991a Mean and Turbulence Characteristics of a Class of Three-Dimensional Wall Jets – Part 1: Mean Flow Characteristics. *J. Fluids Eng*., **113**, pp. 620-628.

Padmanabham, G. & Gowda, L. B. H. 1991b Mean and Turbulence Characteristics of a Class of Three-Dimensional Wall Jets – Part 2: Turbulence Characteristics. *J. Fluids Eng*., **113**, pp. 629-634.

Pelfrey, J. R. R. 1984 Characteristics of a Turbulent Plane Offset Jet. PhD Thesis. Clemson University, New York, USA.

Pelfrey, J. R. R. & Liburdy, J. A. 1986a Mean Flow Characteristics of a Turbulent Offset Jet. *Trans. ASME J. Fluids Eng*., **108**, 82 – 88.

Pelfrey, J. R. R. & Liburdy, J. A. 1986b Effect of curvature on the turbulence of a two-dimensional jet. *Exp Fluids,* **4**, 143 – 149.

Perry, C. C.1967 Two-Dimensional Jet Attachment. *Advances in Fluidic*, ed by F. T. Brown, ASME, New York, pp. 205 – 217.

Prasad, A.K. 2000 Particle Image Velocimetry. *Current Sci*., **79**, pp. 51-57.

Prasad, A. K., Adrian, R. J., Landreth, C. C., and Offutt, P. W. 1992 Effect of Resolution on the Speed and Accuracy of Particle Image Velocimetry Interrogation. Exp. Fluids, **13**, pp. 105–116.

Raffel, M., Willert, C.E. & Kompenhaus, J. 1998 Particle Image Velocimetry: A Practical Guide. Springer Verlag.

Rajaratnam, N. & Pani, B. S. 1974 Three-Dimensional Turbulent Wall Jets. *J. Hydr. Div*., **100**, pp. 69-83.

Rajaratnam, N. & Subramanya, K. 1968 Plane Turbulent Reattached Wall Jets. *J. Hydr. Div*., **94**, pp. 95-112.

Reichert, R. S, Hatay, F. F., Birigen, S. & Huser, A. 1994 Proper Orthogonal Decomposition Applied to Turbulent Flow in a Square Duct. *Phys. Fluids*, **6**, pp. 3086-3092.

Sakai, Y. Tanaka, N. & Kushida, T. 2006a On the Development of Coherent Structure in a Plane Jet (Part 1, Characteristics of Two-Point Velocity Correlation and Analysis of Eigenmodes by the KL Expansion). *JSME Int. J.*, Ser B, **49**, No. 1, pp. 115-124.

Sakai, Y. Tanaka, N., Yamamoto, M. & Kushida, T. 2006b On the Development of Coherent Structure in a Plane Jet (Part 3, Multi-Point Simultaneous Measurement of Main Streamwise Velocity and the Reconstruction of Velocity Field by the KL Expansion). *JSME Int. J.*, Ser B, **49**, No. 3, pp. 722-730.

Sawyer, R. A. 1960 The flow due to a two dimensional jet issuing parallel to a flat plate. *J. Fluid Mech*., **9**, pp. 543–561.

Sawyer, R. A. 1963 Two dimensional reattaching jet flows including the effect of curvature on entrainment. *J. Flud Mech*., **17**, pp. 481–498.

Scarano, F. & Riethmuller, M. 1999 Iterative multigrid approach in PIV image processing with discrete window offset. *Exp. Fluids*, **26**, 513-523.

Sen, M., Bhaganagar, K. & Juttijudata, V. 2007 Application of Proper Orthogonal Decomposition (POD) to Investigate a Turbulent Boundary Layer in a Channel with Rough Walls. *J. Turb*., **8**, pp. 1-21.

Sforza, P. M. & Herbst. G. 1970 Study of Three-Dimensinal, Incompressible Turbulent

Wall Jets. *AIAA J*., **8**, pp. 276-283.

Shah, M. K. 2009 Effects of Pressure Gradient on Separated and Reattached Turbulent Flows. Ph.D. Thesis, University of Manitoba, Winnipeg, Canada.

Shinneeb, A.-M. 2006 Confinement Effects in Shallow Water Jets. University of Sasketchewan, Saskatoon, Ph.D. Thesis.

Skåre, P. E. & Krogstad, P.-Å. 1994 A Turbulent Equilibrium Boundary Layer Near Separation. *J. Fluid Mech*., **272**, pp. 319-348.

Simpson, R. L. 1976 Interpreting Laser and Hot-film Anemometer Signals in a Separating Boundary Layer. *AIAA J*., **14**, No. 1, pp. 124 – 126.

Sirovich, L. 1987 Turbulence and the Dynamics of Coherent Structures, Part 1: Coherent Structures. *Quart. J. Appl. Math*., **45**, No. 3, pp. 561 – 571.

Sun, H. & Ewing, D. 2002a Effect of initial and boundary conditions on the development of three-dimensional wall jet. In Proceedings of the AIAA winter meeting, Tahoe. AIAA. AIAA 2002-0733.

Sun, H. & Ewing, D. 2002b Development of the large-scale structures in the intermediate region of the three-dimensional wall jet. In Proceedings of the Fluids Engineering Division Summer Meeting, Montreal, New York, July 2002. ASME. Paper Number FEDSM2002-31414.

Sreenivasan, K. R. 1999 Fluid Turbulence. *Rev. Mod. Phys*., **71**, s383-s395; reprinted in More Things in Heaven and Earth: A Celebration of Physics at the Millennium, B., Bederson, ed. (Springer, New York, 1999), pp. 644-664.

Stern, F. Muste, M., Berninati, L. M. and Eichinnger, W. E. 1999 Summary of Experimental Uncertainty Assessment Methodology with Example. IIHR

Technical Report No. 406. The University of Iowa, Iowa City.

Swamy, N. V. C. & Bandyopadhyay, P. 1975 Mean and turbulent characteristics of three-dimensional wall jets. *J. Fluid Mech*., **71**, 541-562.

Swamy, N.V.C. & Bandyopadhayay, P. 1981 The Structure of Three-Dimensional Wall Jets. *Indian J. Tech*., **19**, pp. 390-394.

Tachie, M. F. 2000 Open Channel Turbulent Boundary Layers and Wall Jets on Rough Surfaces. PhD Thesis. University of Saskatchewan, Canada.

Tomkins, D. D. & Adrian R. J. 2003 Spanwise structure and scale growth in turbulent boundary layers. *J. Fluid Mech*., **490**, pp. 37-74.

Townsend, A. A. 1980 The Structure of Turbulent Shear Flow. Cambridge University Press.

Tsunoda, H., Yoshihito, S., Takeshi, K. 2006 Plane Offset Jet Discharged into Water of Finite Depth. *JSME International Journal*, Series B: **47**, No 4, pp. 1111-1117.

Venas, B., Abrahamsson, H., Krogstad, P.-A. & Lofdahl L. 1999 Pulsed hot-wire measurement in two- and three-dimensional wall jets. *Exp. Fluids*, **27**, pp. 210-218.

Volino, R. J. Schultz, M. P. Flack, K. A. 2007 Turbulence structure in rough- and smooth-wall boundary layers. *J. Fluid Mech*., **592**, pp. 263-293.

Westerweel, J., Draad, A. A., Th. Van der Hoeven, J. G. & Oord van, J. 1996 Measurement of Fully Developed Turbulent Pipe Flow with Digital Particle Image Velocimetry. *Exp. Fluids*, **20**, pp. 165 – 177.

Willert, C. E. & Gharib, M. 1991 Digital Particle Image Velocimetry. *Exp. Fluids*, **10**, pp. 181-193.

Wygnanski, I. & Fiedler, H. 1969 Some measurements in the self-preserving jet. *J. Fluid Mech.*, **38**, pp. 577-612.

Zhou, X. & Hitt, D. L. 2004 Proper orthogonal decomposition analysis of coherent structures in a transient buoyant jet. *J. Turb.*, **5**, No. N28, pp. 1-2.

APPENDIX A

IMPLEMENTATION OF POD

In this section, the implementation of the POD is outlined. As mentioned earlier, the snapshot POD method proposed by Sirovich (1987) is employed in the present study. In this case, each instantaneous PIV image is considered a snapshot of the flow field and the total number of snapshots is denoted by N. The total number of velocity vectors in each snapshot is denoted by M. For the two-dimensional flow domain measurements considered in this study, the snapshot POD analysis concerns the fluctuating parts of the velocity components (u_j^n, v_j^n) where u and v denote the fluctuating part of the velocity components in the streamwise and transverse directions, respectively. The index n runs through the N snapshots (i.e., n = 1, …, N) while j runs through the M positions of velocity vectors in a given snapshot (i.e., j = 1, …, M).

The present snapshot analysis follows the procedure outlined by Meyer *et al.* (2007), and is described below. The ensemble-average velocity ($\overline{u}$) for a sequence of snapshots $\hat{\boldsymbol{u}}^n$ is given by:

$$\overline{u} = \frac{1}{N}\sum_{i=1}^{N} \hat{u}^n \tag{A.1}$$

The fluctuating part of the velocities is then obtained by subtracting $\overline{u}$ from the vectors in each snapshot as follows

$$u = \hat{u} - \overline{u} \tag{A.2}$$

All fluctuating velocity components from the N snapshots are arranged in a matrix $\boldsymbol{U}$ as follows:

$$\boldsymbol{U} = [\boldsymbol{u}^1 \quad \boldsymbol{u}^2 \quad \cdots \quad \boldsymbol{u}^N] = \begin{bmatrix} u_1^1 & u_1^2 & \cdots & u_1^N \\ \vdots & \vdots & \vdots & \vdots \\ u_M^1 & u_M^2 & \cdots & u_M^N \\ v_1^1 & v_1^2 & \cdots & v_1^N \\ \vdots & \vdots & \vdots & \vdots \\ v_M^1 & v_M^2 & \cdots & v_M^N \end{bmatrix} \tag{A.3}$$

The $N \times N$ auto-covariance matrix is obtained from

$$C = U^T U \tag{A.4}$$

A set of N eigenvalues, λ^i, and a corresponding set of orthonormal eigenvectors, $\boldsymbol{A}^i$ which satisfy the relation,

$$CA^{\mathrm{i}} = \lambda^{\mathrm{i}} A^{\mathrm{i}} \tag{A.5}$$

can be evaluated from the auto-covariance matrix, where i = 1, …, N. Here the eigenvalues are ordered by decreasing value:

$$\lambda^1 > \lambda^2 > \cdots \lambda^{\mathrm{N}} > 0 \tag{A.6}$$

The normalized POD modes ($\boldsymbol{\phi}^i$) are constructed from the projection of the eigenvectors ($\boldsymbol{A}^i$) of Equation A.5 on the original fields as follows:

$$\phi^i = \frac{\sum_{n=1}^{N} A_n^i u^n}{\left\| \sum_{n=1}^{N} A_n^i u^n \right\|}, \qquad i = 1,\ldots,N \tag{A.7}$$

where A_n^i is the nth component of the eigenvector corresponding to λ^i from Equation (A.5). Here || . || is the L_2-norm defined as,

$$\|y\| = \sqrt{y_1^2 + y_1^2 + \cdots + y_M^2} \tag{A.8}$$

The functions ϕ^i are called empirical eigenfunctions, coherent structures, or POD modes. Note that the eigenvalues, λ^i, represent the kinetic energy associated with each POD mode. The total energy for N POD modes is given by the sum of all the eigenvalues as,

$$E = \sum_{i=1}^{N} \lambda^i \tag{A.9}$$

Meanwhile the energy fraction associated with i^{th} mode is given by

$$E_\lambda = \lambda^i / E \tag{A.10}$$

The expansion or POD coefficients, a_i, of each mode were calculated by projecting the data set corresponding to the fluctuating part of the velocity onto the calculated eigenfunctions:

$$a^n = \Psi^T u^n \tag{A.11}$$

where, $\Psi = \left[\phi^1 \ \phi^2 \ldots \phi^N\right]$.

The fluctuating velocities can be reconstructed using:

$$u^n = \sum_{i=1}^{n} a_i^n \phi^i = \psi a^n \tag{A.12}$$

The average least-squares truncation error is given by (Cizmas et al., 2003).

$$\varepsilon_m = \overline{\left\| u^n - \sum_{i=1}^{m} a_i^n \phi^i \right\|^2} \tag{A.13}$$

Where *m* specifies the number of modes used in the reconstruction.

APPENDIX B

PRINCIPLES OF PARTICLE IMAGE VELOCIMETRY

This section describes the principles of the particle image velocimetry (PIV). A detailed analysis of the PIV techniques could take volumes of notes. The goal of this section, however, is to provide only the relevant information to the understanding of this technique. It should be pointed out that the PIV manual supplied by Dantec Dynamics Inc. is the key reference for this section and readers are encouraged to consult that manual for more in-depth analysis if the need arises.

B.1 Principles of Particle Image Velocimetry

The PIV is a non-intrusive optical measurement technique that provides simultaneous whole-field instantaneous velocity measurements. The PIV is well suited for estimating velocity gradients and derived quantities such as vorticity and the various terms in the transport equations for turbulent kinetic energy and Reynolds stresses. Due to these attractive features, the PIV has been applied in many areas of fluid mechanics and aerodynamics research in recent past. There two types of PIV: the standard PIV and the stereo PIV. The standard PIV can measure only two velocity components whereas the stereo PIV can measure all the three velocity components. In this chapter, the basic principle of the standard PIV is outlined and its various components are described.

B.1.1 Planar PIV

A typical experimental setup using a planar PIV is shown in Figure B.1. The

setup consists of an optically transparent test section, flow seeded with light scattering particles, a pulsed light source (laser) to illuminate the area of interest, a film or CCD camera to record the illuminated particles, a synchronizer to control the camera and laser, and a computer with suitable software to record, store and process the recorded images.

The basic principle of the PIV involves the following. A flow field is seeded with small light scattering particles that are presumed to faithfully follow the fluid motion. The flow field is then illuminated by two pulses of laser sheet separated by a time delay, Δt. The light scattered by the seeding particles and two successive images are recorded. The images are divided into grids called interrogation areas. For each interrogation area, a numerical correlation algorithm (auto-correlation or cross-correlation) is applied to statistically determine the local displacement vector (Δs) of particles between the first and the second illuminations. The velocity, V, for a particular interrogation area is then obtained from the expression $V = \Delta s/\Delta t$. A velocity vector map over the whole target area is obtained by repeating the correlation for each interrogation area over the two image frames captured. Since the entire flow field can be analyzed at once, the PIV provides simultaneous whole field measurement. The description of the basic components of a PIV is presented in detail in the following sections.

B.1.2 Light source

For PIV measurements, a high intensity pulse laser is required to freeze the motion of the particles during image capturing. The fact that the whole field is illuminated and the camera captures the side-wards scattered light by the particles makes a high power laser necessary. Frequency doubled neodymium-yttrium-aluminum-garnet

(Nd:YAG) lasers are commonly used for PIV measurements because these lasers provide monochromatic light with high intensity illumination. Laser-emitted light is passed through a lens system to create a plane sheet of light to illuminate the region of interest. The length and width of the light sheet can be adjusted to the field of view required.

B.1.3 Seeding particles

The seeding particles should be small enough to follow the flow faithfully but large enough to scatter sufficient light for them to be detected by the camera. Also, the seeding particles should be distributed homogeneously (Westerweel *et al.*, 1996). Since, PIV measures the velocity of the particle but not the fluid velocity, it is essential that the particles have certain hydrodynamic properties to ensure that they faithfully follow the flow. Particles that have negligible settling velocity are desirable. The settling velocity can be estimated from Stokes drag law for flow around a sphere under gravity and is given by (Mei *et al.*, 1991),

$$v_s = \frac{(\rho_p - \rho_f) g d_p^2}{18 \mu_f}, \tag{B.1}$$

where ρ_p is the particle density, ρ_f is the fluid density, g is the acceleration due to gravity, d_p is the diameter of the particle and μ_f is the viscosity of the fluid. Hence, the settling velocity can be minimized by using small particles and/or particles whose density is similar to that of the working fluid. The ability of a particle to follow the flow is characterized by its response time. The response time is a measure of the tendency of the particles to attain velocity equilibrium with the fluid. The response time, τ_r, for the particle (for Stokes' flow) is (Raffel *et al.*, 1998):

$$\tau_r = \rho_p \frac{d_p^2}{18\mu_f} \quad \text{(B.2)}$$

The particles must also be good at scattering light to ensure that they are visible to the CCD sensor (Willert & Gharib, 1991). The particle size and shape, the refractive index and the wavelength of radiation are the factors that affect the light scatter by a particle. A variety of seeding particles are commercially available ranging from few microns to hundreds of microns. Some of the widely used particles for liquids are polyamide seeding particles, silver-coated hollow glass spheres, hollow glass spheres, polystyrene latex and fluorescent polymer particles, to mention a few.

B.1.4 Recording medium

The CCD camera is the most widely employed recording device for PIV. The CCD cameras have several advantages over the photographic film cameras. These advantages include higher frame rates and possibility of on-line image analysis. However, photographic film cameras do offer higher resolution. The major component of a CCD camera is the CCD sensor which consists of an array of detectors called pixels. The CCD camera employed in the PIV studies generally uses high-performance progressive scan interline CCD chips. The chip consists of an array of photosensitive cells and an equal number of storage cells. After the first laser pulse is triggered, the first image is acquired and immediately transferred from the photosensitive cells to the storage cells. Later, when the second laser pulse is triggered, the photosensitive cells are available to store the second image. In this case, the storage cells contain the first image and the photosensitive cells contain the second image. Then both images are transferred

sequentially from the camera to the computer for storage. This allows the exposure interval Δt to be reduced to less than 1 microsecond.

B.1.5 Methods of correlation in PIV

The images recorded by the CCD camera are sub-divided into smaller regions called interrogation areas. For each interrogation area, the images at the first and second frames are correlated to obtain an average displacement vector. The end result is a vector map of average displacements for all the interrogation areas. Auto-correlation and cross-correlation correlation are the most commonly used correlation methods.

In auto-correlation, the particles in an interrogation area are correlated with themselves. This results in a large central peak (the self-correlation peak) in the correlation plane along with two displacement peaks, one on each side of the central peak. The distance from the central peak to either of the displacement peaks corresponds to the average particle displacement in the interrogation area. Because of the presence of the self-correlation peak, particle displacements less than 2-3 pixels cannot be detected. This reduces the dynamic range of the auto-correlation technique. Furthermore, 180-degree directional ambiguity of the correlation method is a major drawback.

In cross-correlation, on the other hand, particles in two different interrogation areas belonging to two different images at the first and second frames are correlated. Since the order of the image recording is known, directional ambiguity is no longer a concern. With the cross-correlation method, two sequential images of flow field with a specific time between them are considered as two spatial signals. The spatial shift can be represented by using a linear digital signal image process as shown in Fig. B.1. The

function f(m, n) describes the light intensity within the interrogation area at time t and the function g(m, n) describes the intensity recorded at time Δt later. The function f(m, n) is considered as the input signal and g(m, n) is the output of the transfer function s(m, n) in the presence of noise function d(m, n). The capitalized function shown in Fig. B.1 represents the Fourier transforms of the respective functions, and u, v are the coordinates of the spatial frequency domain. The challenge of this technique is to estimate the spatial shift function s(m, n) on the basis of known functional values of f(m, n) and g(m, n) in the presence of noise function d(m, n). A commonly used method in finding spatial shift function s(m, n) is the statistical technique of spatial cross-correlation. The detail of this method and the computational implementation are given in Willert & Gharib (1991) and Raffel *et al.* (1998).

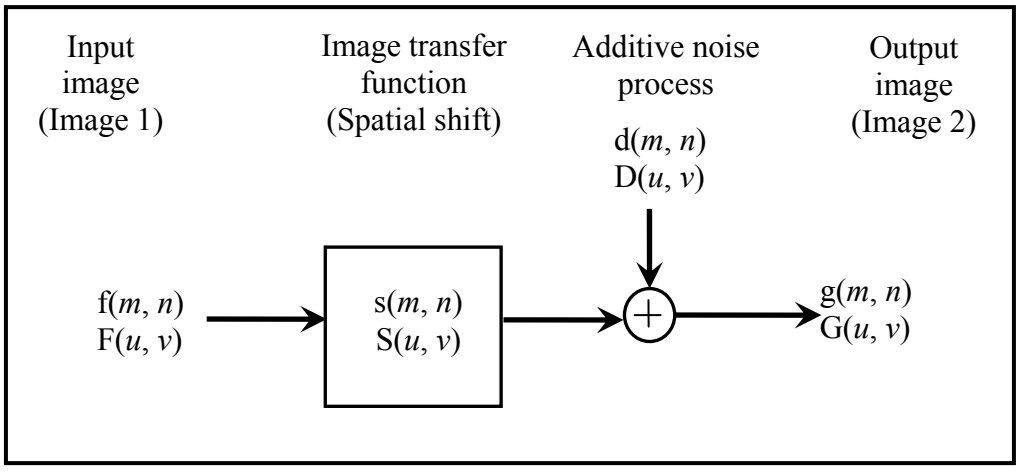

Figure B.1: Image displacement function (Dantec inc. PIV manual).

The adaptive-correlation algorithm is an advanced type of cross-correlation. It is an iterative method which relies on the knowledge of the actual velocity spatial

distribution (which is not known *a priori*) and is the objective of the measurement procedure itself. Therefore, an initial guessed offset value is used to introduce an offset from the first window (the interrogation area in the image frame from laser pulse one) to the second window. The result of each single interrogation is used as an input to evaluate the interrogation parameters for the subsequent iteration. The process terminates when a convergence criterion is fulfilled or after a prescribed number of iterations. The use of adaptive correlation helps in two major ways. First, the signal strength is raised due to the capture of the in-plane dropout. In-plane dropout occurs when during the time between the two light pulses some of the particle images leave the interrogation area and are lost. This loss of particles reduces signal strength and the number of successful vectors that can be obtained. Secondly, a refinement of the interrogation area is possible because an adaptive window offset may be applied, again producing a successful signal.

B.1.6 Optimizing PIV measurements

The combination of laser energy, camera magnification and light sheet dimension needs to be optimized in order to obtain results from a PIV system with high accuracy. Even under ideal experimental conditions, a PIV vector map may contain spurious vectors. These spurious vectors emanate from interrogation spots where signal-to-noise ratio is less than unity. That is, a noise peak is higher than the signal peak. To improve the signal-to-noise ratio, Keane and Adrian (1990) recommended the interrogation areas be large enough to accommodate a sufficient number of particles, but small enough so that one vector describes the field. The particle size should be selected such that the particle image size is approximately two pixels when imaged by the digital camera

(Raffel *et al.*, 1998). The particle image diameter, d_{image}, is given by:

$$d_{image} \approx [d_p^2 M_f^2 + (2.44(1+M_f)f_\#)\lambda] \quad \text{(B.3)}$$

where d_p is particle diameter, $f_\#$ is the *f*-number of the lens, λ is the wavelength of the laser light, and M_f is the magnification factor of the camera. Raffel *et al.* (1998) suggested that when the image diameter becomes too small there is insufficient information to make effective use of sub pixel interpolation because there is a likelihood of biasing data towards integer pixel values. Sub pixel interpolation is used to increase the resolution or accuracy when detecting the position of the correlation peak which makes it possible to determine displacements with the accuracy of fractions of a pixel.

The seeding density is dependent on the type of PIV method used. For the two-frame cross-correlation method, Willert & Gharib (1991) showed that to obtain a high valid detection probability the particle image density should be larger than 6. Using very high particle image densities, large particle image diameters, and small interrogation cell sizes will reduce the error due to gradients. The movement of the particles can only be tracked as long as they remain within the same interrogation area during both exposures. Also, the particles should not traverse more than a quarter of the side length of the interrogation areas between exposures to keep the number of particles that leave the interrogation area down.

The thickness of a laser sheet, Δz, is usually chosen to be smaller than the depth-of-field of the recording system, δ_z. Consequently, all particles illuminated by the light sheet produce in-focus images, reducing background noise in the image field (Adrian, 1991). The depth-of-field of the lens is given by,

$$\delta_z = 4(1+M_f^{-1})^2 f_\#^2 \lambda. \quad \text{(B.4)}$$

It should be noted that for a given magnification, a large depth-of-field can only be obtained at the cost of increasing the $f_\#$ implying that a smaller fraction of the light scattered by the particles will reach the sensor.

APPENDIX C

ERRORS AND ERROR ANALYSIS IN PIV

In this section errors present in PIV measurements are discussed. The techniques for error analysis are reported. The complete uncertainty analysis for this study is also presented.

C.1 Measurement Error

Measurement is the act of assigning a value to some physical variable. The relative closeness of agreement between an experimentally determined value of a quantity and its true value indicates the accuracy of a measurement. The difference between the experimentally determined value and the true value is the measurement error. Most often, the true values of measured quantities are unknown. Therefore, estimation of the error must be made and that estimate is called an uncertainty. Coleman & Steele (1995) have presented a detailed uncertainty assessment methodology. Stern *et al.* (1999) provided comprehensive guidelines for the application of uncertainty assessment methodology into the test process and documentation of results. In general, the total error is composed of two components: a precision component, P, and a bias component, B. Coleman & Steele (1995) classified an error as precision if it contributes to the scatter of the data and systematic error is a bias error. Gui *et al.* (2001) quantified the evaluation of bias uncertainty in PIV measurements and its contribution to the total measurement uncertainty. Forliti *et al.* (2000) reported that the evaluation bias and gradient of the evaluation bias can both be minimized effectively by using Gaussian

digital masks on the interrogation window, so that the measurement uncertainty can be reduced. The sources of error include: bad selection of time between image pairs, sub-pixel displacement bias, insufficient sample size, effect of velocity gradients, spatial resolution, These uncertainties include particle response to fluid motion, light sheet positioning, light pulse timing, and the error arising from the peak-finding algorithm to determine the average particle displacement.

C.1.1 Minimizing measurement error

Through careful selection of experimental conditions such as time between image pairs certain errors can be minimized. Peak locking, which is an artifact of sub-pixel particle displacement being biased toward integer values, is a major contributor to the bias error. In the present study, a number of steps were taken during image acquisition and image processing to reduce peak locking. The particle image diameter was estimated to be $d_p = 15.6\ \mu$m, which is approximately 2.1 px. This value is close to the value of 2.0 px recommended by Raffel *et al.* (1998) to minimize peak locking. The histograms of typical instantaneous images in the developing and self-similar regions are shown in Fig. C.1. The figure does not reveal any discernible peak locking effects which imply that the contribution to the bias error is minimal. The large sample size (1800 instantaneous images) also reduces the precision error.

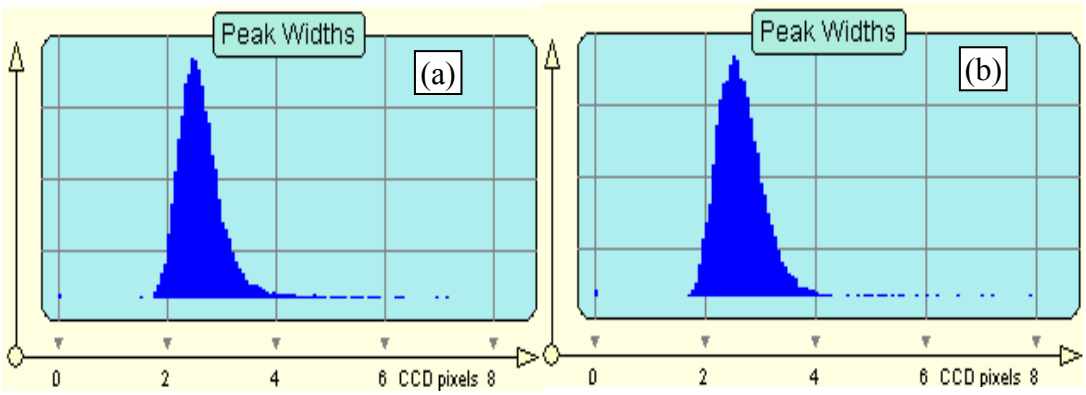

Figure C.1: Histograms of typical instantenous images in the developing and self-similar regions. (a) developing region, (b) self-similar region.

The effect of velocity gradient bias errors that occurs in flows with large mean velocity gradients is also a concern. The velocity gradients tend to broaden the displacement peak and reduce the amplitude. The error associated with the velocity gradient is typical of all boundary layer flows. Keane & Adrian (1992) suggested that for the cross-correlation technique, to achieve an acceptable valid detection probability of 95%, the acceptable gradients should follow the expression:

$$\frac{M_f \Delta U_y \Delta t}{d} < 0.03, \qquad \text{(C.1)}$$

where, $\Delta U_y = (\partial U/\partial y)(d/2)$, Δt is the time between the two laser pulses and d is the length of the interrogation area size. In the inner region of the the generic wall jet ($h/d = 0.5$) at $Re_j = 10000$, for instance, $M_f = 6.07^{-1}$, $\Delta t = 250\times10^{-6}$ s. and $\partial U/\partial y \approx 21.06$ s^{-1} in the self-similar region. These yield a value of approximately 4×10^{-4} for the left hand side of Eqn. C.1, which satisfies the relationship. For the offset jets, the condition expressed in the

above equation (not shown) was easily satisfied.

In PIV, it is necessary to keep the interrogation area size as small as possible in order to improve spatial resolution so as to resolve the smallest spatial scales in the flow. On the other hand, the dynamic range of the measured velocity increases with larger interrogation area sizes which implies that larger interrogation area sizes are desirable to achieving large velocity dynamic range. The above conflicting interests require a compromise between spatial resolution and velocity dynamic range. The dynamic range in a PIV measurement based on a pixel displacement level is the displacement divided by the sub-pixel accuracy. The sub-pixel accuracy is a function of many parameters, for which most are beyond the PIV system itself and therefore often unknown. As a rule-of-thumb 0.1 pixel accuracy is a realistic value (Scarano & Riethmuller, 1999). In the present measurements, it was ensured that particle displacement was less than ¼ of the size of the interrogation area as recommended by many researchers (Willert & Gharib, 1991). For a typical PIV recording of 32×16 pixels, the maximum displacement is approximately 8 pixels so that the velocity dynamic range is of the order of 8/0.1 = 80.

C.1.2 Error estimation

Adrian (1991) proved that random influences can be summed into a single error, and it can be found by repeating the measurement. Prasad (2000) reported that random influences in PIV usually scale with the particle image diameter as:

$$\sigma_{random} = cd_e , \qquad \text{(C.2)}$$

where, d_e is the effective particle diameter and c is a constant whose value is between

0.05 and 0.10, depending upon experimental conditions. The uncertainty analysis of the present measurement follows the AIAA standard derived and explained by Coleman & Steele (1995). A complete uncertainty analysis of the PIV measurement involves identifying and quantifying both the bias and the precision errors in each part of the measurement chain.

C.1.2.1 Biased error

In PIV measurements, the instantaneous velocity at any point is the average fluid velocity for an interrogation region and is described by the following equation in Gui *et al.* (2001).

$$u_i = \frac{\Delta s L_0}{\Delta t L_I}, \tag{C.3}$$

where i equals 1 and 2 for the x and y coordinates, respectively, Δt is the time interval between laser pulses, Δs is the particle displacement from the correlation algorithm, L_0 is the width of the camera view in the object plane, and L_I is the width of the digital image. The bias limit of the measured velocity is determined with a root-sum-square (RSS) of the elementary bias limits based on the sensitivity coefficients given as:

$$B_{u_i}^{\ 2} = \theta_{L_0}^2 B_{L_0}^2 + \theta_{L_I}^2 B_{L_I}^2 + \theta_{\Delta s}^2 B_{\Delta s}^2 + \theta_{\Delta t}^2 B_{\Delta t}^2, \tag{C.4}$$

where the sensitivity coefficients, θ_x, are defined as

$$\theta_X = \frac{\partial u_i}{\partial X}, \quad X = (L_0,\ L_I, \Delta t, \Delta s) \tag{C.5}$$

The classification of bias error sources and contribution to the bias limits for U and V were performed for the various test conditions. As a case in point, this classification has

been provided in Table C.1 and Table C.2, respectively, for the inner region of the generic wall jet at Re_j = 10000. Also shown in Tables C.1 and C.2 are the manufacturer's specifications of the elementary bias limits for Δt and Δs. The bias limit for L_0 is obtained from a calibration procedure. Note that percentage bias errors (%Bias error) in U and V are both expressed as a percentage of U.

Table C.1: Bias limits of the local streamwise mean velocity (U) in the inner region of the generic wall jet (h/d = 0.5) at Re_j = 10000.

Variable	Magnitude	B_x	θ_x	$B_x\theta_x$	$(B_x\theta_x)^2$
L_o (m)	9.20E-02	5.00E-04	1.14E+00	5.71E-04	3.26E-07
L_I (pix)	2.05E+03	5.00E-01	-5.13E-05	2.56E-05	6.57E-10
Δt (s)	2.50E-04	1.00E-07	-4.20E+02	4.20E-05	1.76E-09
Δs (pix)	5.84E-01	1.27E-02	1.80E-01	2.28E-03	5.21E-06
U (m/s)	1.05E-01				
				$\Sigma(B_x\theta_x)^2$ =	5.54E-06
				Bias error =	2.35E-03
				%Bias error =	2.24%

Table C.2: Bias limits of the local wall-normal mean velocity (V) in the inner region for h/d = 0.5.

Variable	Magnitude	B_x	θ_x	$B_x\theta_x$	$(B_x\theta_x)^2$
L_o (m)	9.20E-02	5.00E-04	1.68E-01	8.41E-05	7.07E-09
L_I (pix)	2.05E+03	5.00E-01	-7.55E-06	3.77E-06	1.42E-11
Δt (s)	2.50E-04	1.00E-07	-6.19E+01	6.19E-06	3.83E-11
Δs (pix)	8.62E-02	1.27E-02	1.80E-01	2.28E-03	5.20E-06
V (m/s)	-1.55E-02				
				$\Sigma(B_x\theta_x)^2$ =	5.21E-06
				Bias error =	2.28E-03
				%Bias error =	2.17%

C.1.2.2 Precision error

The precision error, P, of a measured variable, X is given by

$$P_x = \frac{K \cdot \sigma}{\sqrt{N}}, \tag{C.6}$$

where K is the confidence coefficient and has a value of 2 for a 95% confidence level for sample size of N images (N = 1800). The symbol σ is the standard deviation of the sample of n readings of the variable X, and is defined as:

$$\sigma = \sqrt{\frac{1}{n-1}\sum_{k=1}^{n}\left(X_k - \overline{X}\right)^2}, \tag{C.7}$$

where $\overline{X}$ is the mean given by the equation ;

$$\overline{X} = \frac{1}{n}\sum_{k=1}^{n} X_n \quad . \tag{C.8}$$

Due to enormous data storage capacity required for the PIV images, 10 thousand images were acquired and divided into 10 sub-data sets of one thousand per set, in order to compute the standard deviation in Eqn. C.7. This means the number of readings in this case is n = 10. From each of the 10 data sets the standard deviations of U and V were obtained at the same locations in the inner and outer regions to compute the final σ from Eqn. C.7. In the inner region, for example, the standard deviation for U and V of approximately 34% and 18%, respectively, were obtained. From Eqn. C.6, the precision errors of approximately 1.6% and 0.9% were estimated, respectively.

C.1.2.3 Total error

The total uncertainty, E, in the result u_i is the RSS of the bias and precision limits,

given by

$$E_X = \sqrt{B_X^2 + P_X^2} \tag{C.9}$$

The total uncertainty was obtained from the values of the bias and precision errors obtained earlier and Eqn. C.9 to be ±2.8% and ±2.4% for U and V, respectively, in the inner region. The measurement uncertainty in turbulence intensities and Reynolds stresses was estimated to be ±8% and ±12%, respectively. The uncertainty in the triple velocity products and energy budget terms is on the order of ±14%.

APPENDIX D

ADDITIONAL FIGURES

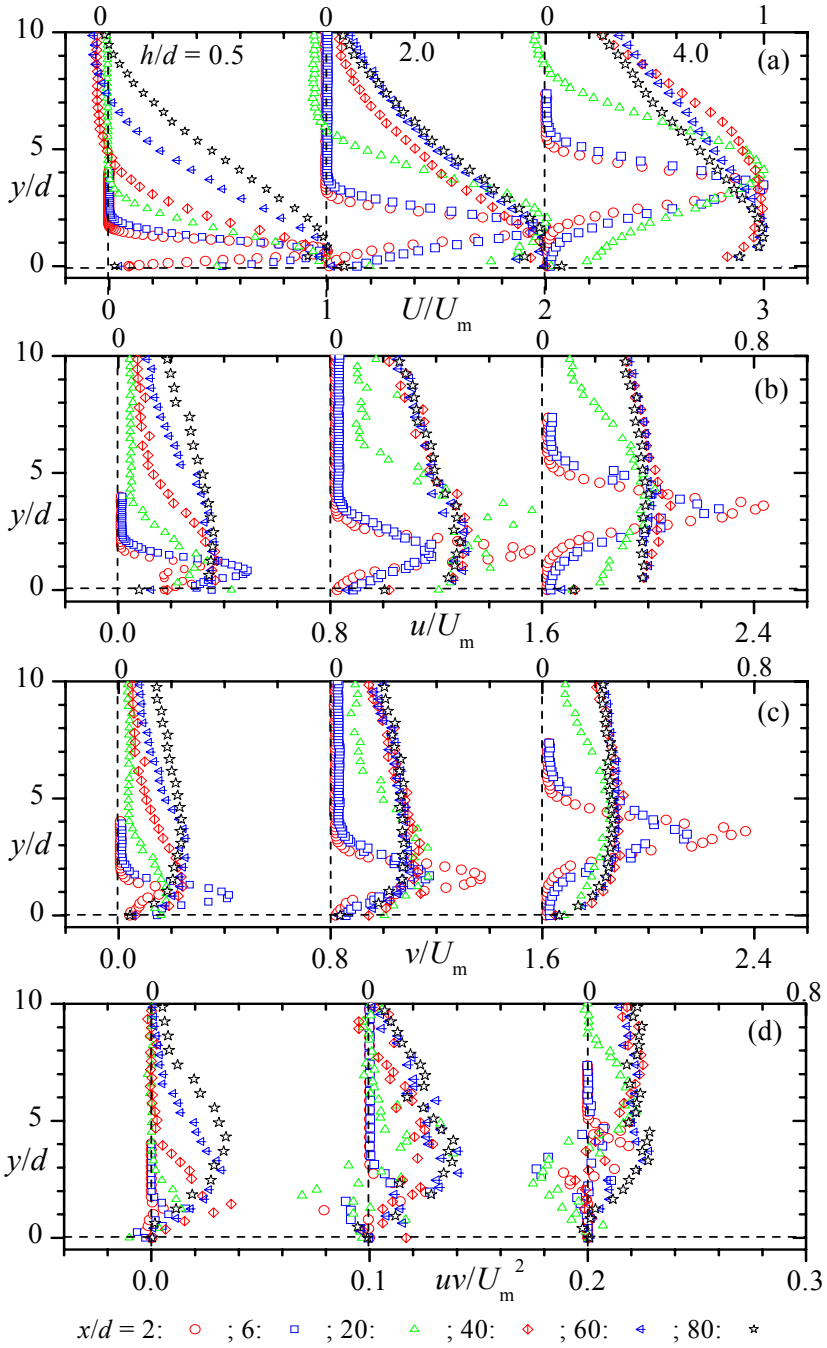

Figure D.1: Mean streamwise velocities (a); streamwise (b) and wall-normal (c) turbulence intensities; and Reynolds shear stresses (d). The maximum local velocities, U_m, and jet exit diameter, d, are the velocity and length scales, respectively.

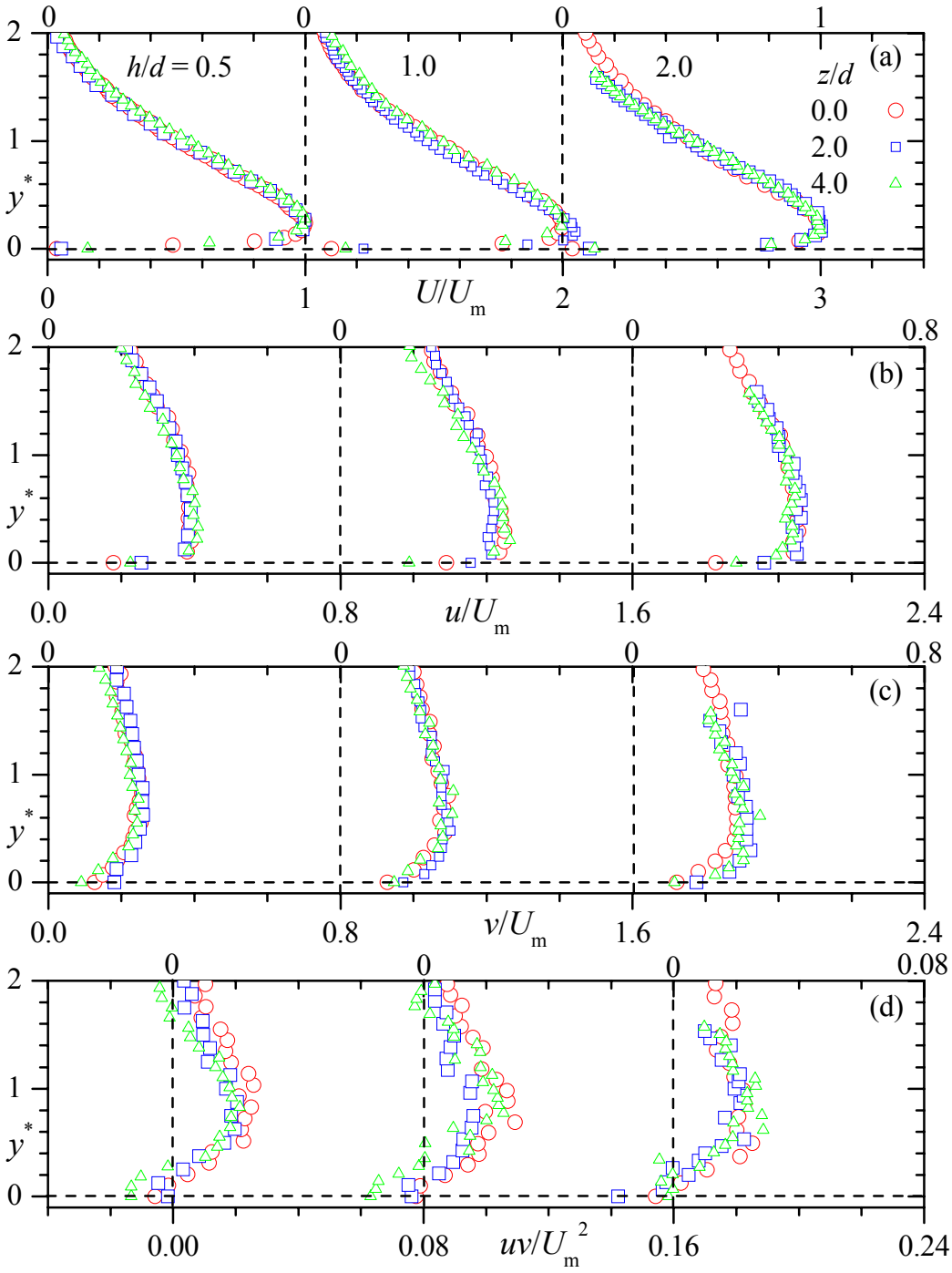

Figure D.2: Profiles of (a) streamwise mean velocities, U, (b) streamwise turbulence intensities, u (c) wall-normal turbulence intensities, v, and (d) Reynolds shear stresses, uv, in planes offset planes at $z/d = 0$, 1, 2, and 4. $z^* = z/\ z_{0.5}$.

Table D.1: Maximum velocities and jet half widths at offset planes, z/d

h/d	U_m (m/s)			$y_{0.5}$ (mm)		
	$z = 0$	$z = 2$	$z = 4$	$z = 0$	$z = 2$	$z = 4$
0.5	0.137	0.126	0.104	17.5	15.2	14.8
1.0	0.129	0.122	0.101	18.4	16.6	15.4
2.0	0.121	0.117	0.106	29.9	28.0	24.4

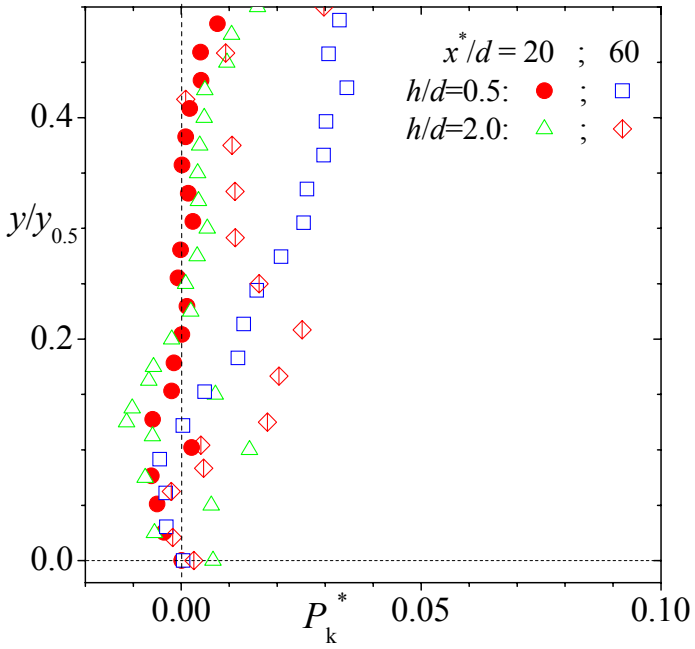

Figure D.3: Production of turbulence kinetic energy, P_k, in the developing, $x/d = 20$, and self-similar, $x/d = 60$, regions. Note: $h/d = 0.5$ is generic jet and $h/d = 2.0$ is offset jet. $P_k = -u^2\partial U/\partial x - uv\partial V/\partial x - uv\partial U/\partial y - v^2\partial V/\partial y$ and $P_k^* = P_k$ normalized by the U_m and $y_{0.5}$.

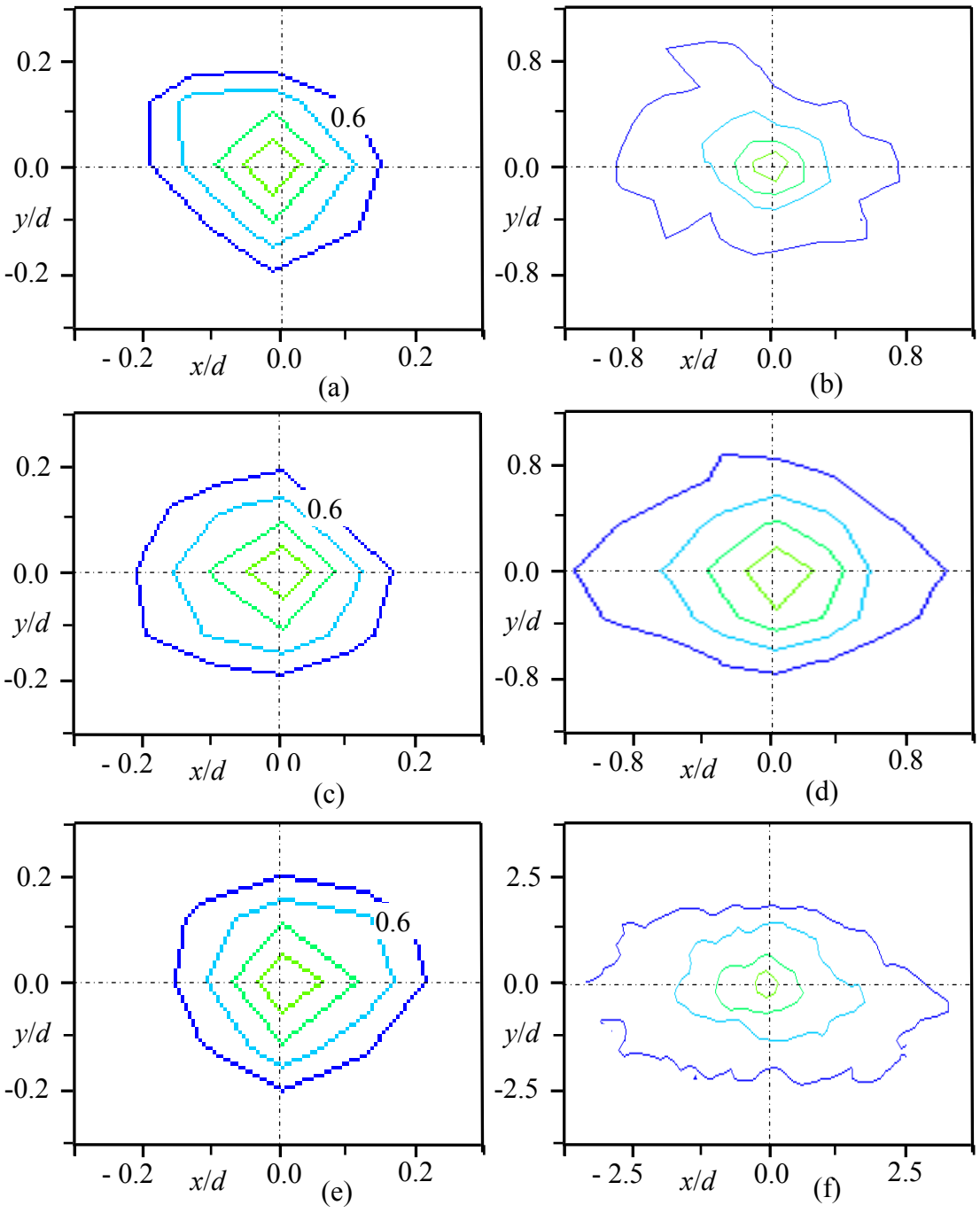

Figure D.4: Iso-contours of the auto-correlations in streamwise, R_{uu}, directions at the developing (x/d = 15) and self-similar (x/d = 75) regions in the x-z plane. The wall-normal locations (y/y_m) are indicated. Offset heights: h/d = 0.5 in (a) and (b); h/d = 2.0 in (c) and (d); and h/d = 4.0 in (e) and (f).

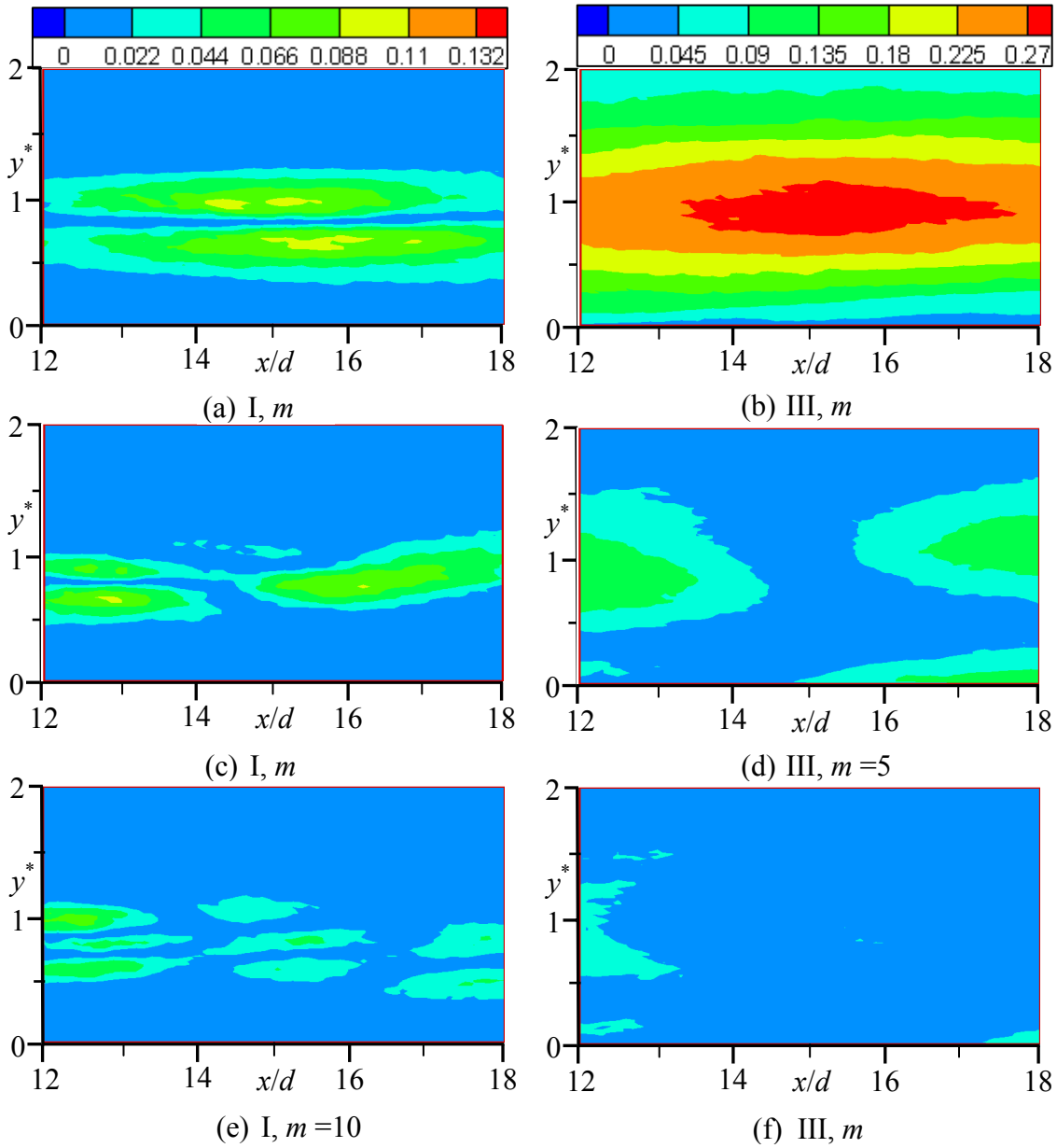

Figure D.5: Iso-contours of the reconstructed streamwise turbulence intensities, u, for modes, m = 1, 5 and10 for h/d = 4.0 in x-y plane. The developing region (I): (a) to (c); and self-similar region (III): (d) to (e).

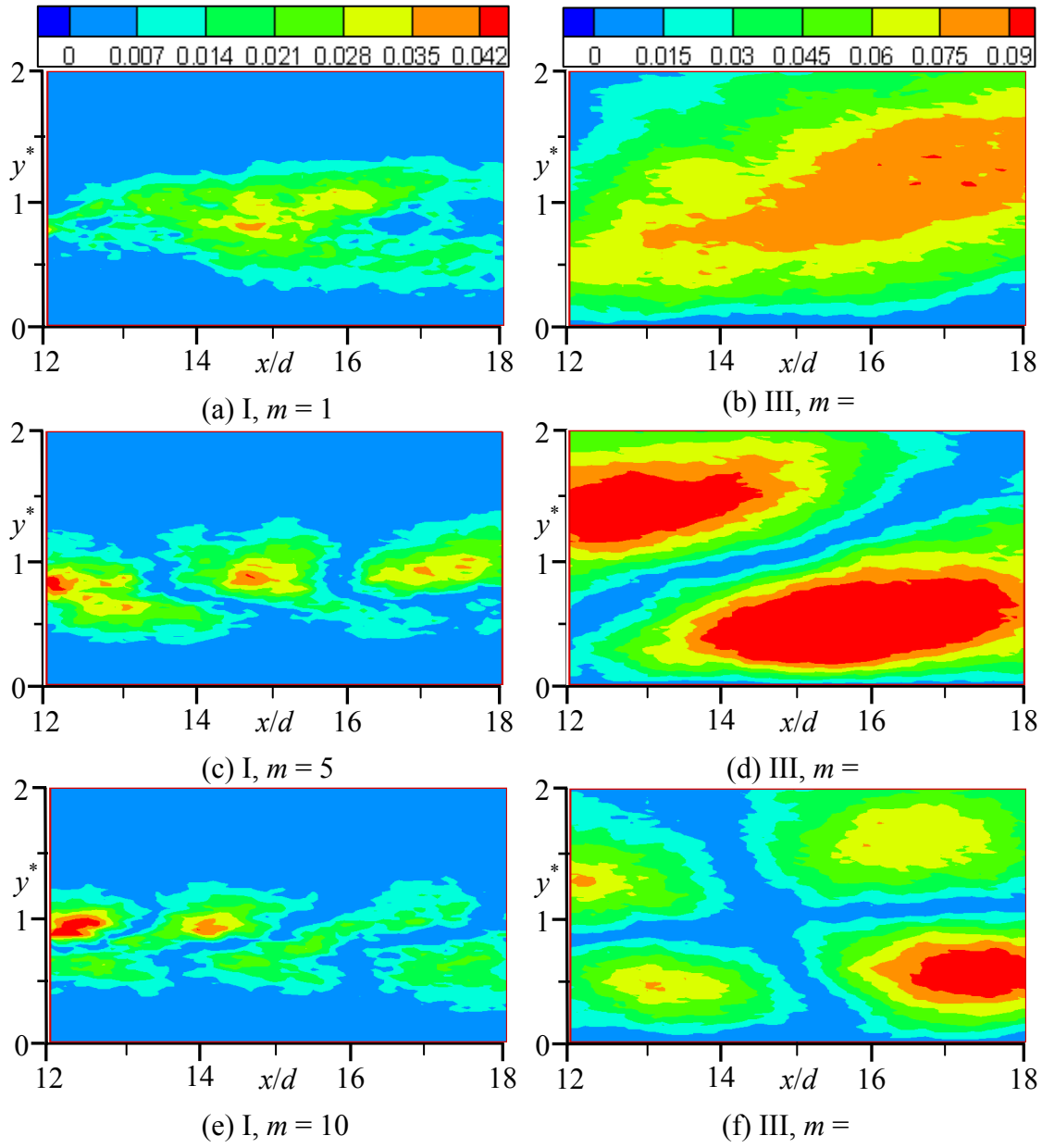

Figure D.6: Iso-contours of the reconstructed wall-normal turbulence intensities, v, for modes, m = 1, 5 and10 for h/d = 4.0 in x-y plane. The developing region (I): (a) to (c); and self-similar region (III): (d) to (e).

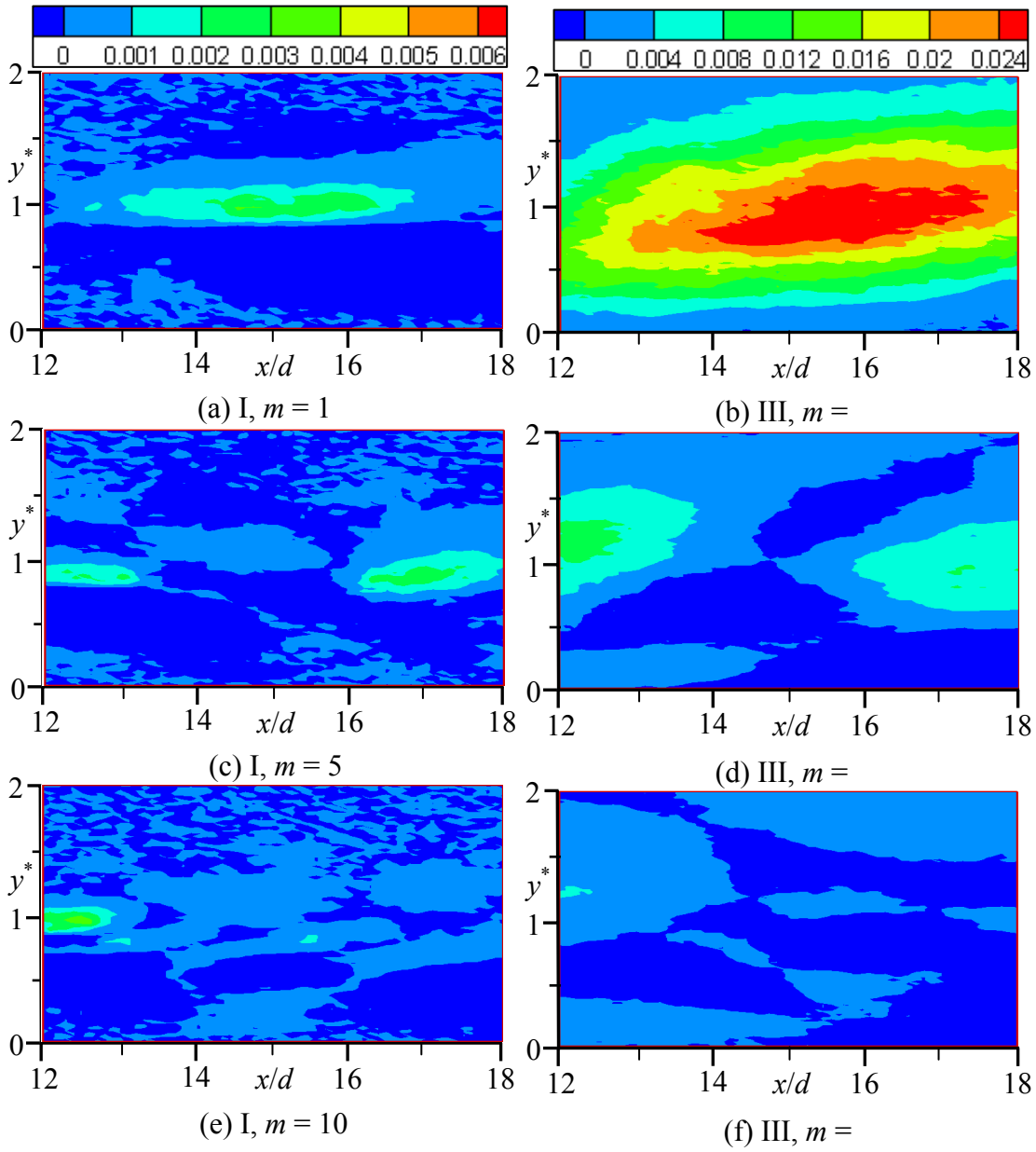

Figure D.7: Iso-contours of the reconstructed Reynolds shear stresses, uv, for modes, m = 1, 5 and10 for h/d = 4.0 in x-y plane. The developing region (I): (a) to (c); and self-similar region (III): (d) to (e).

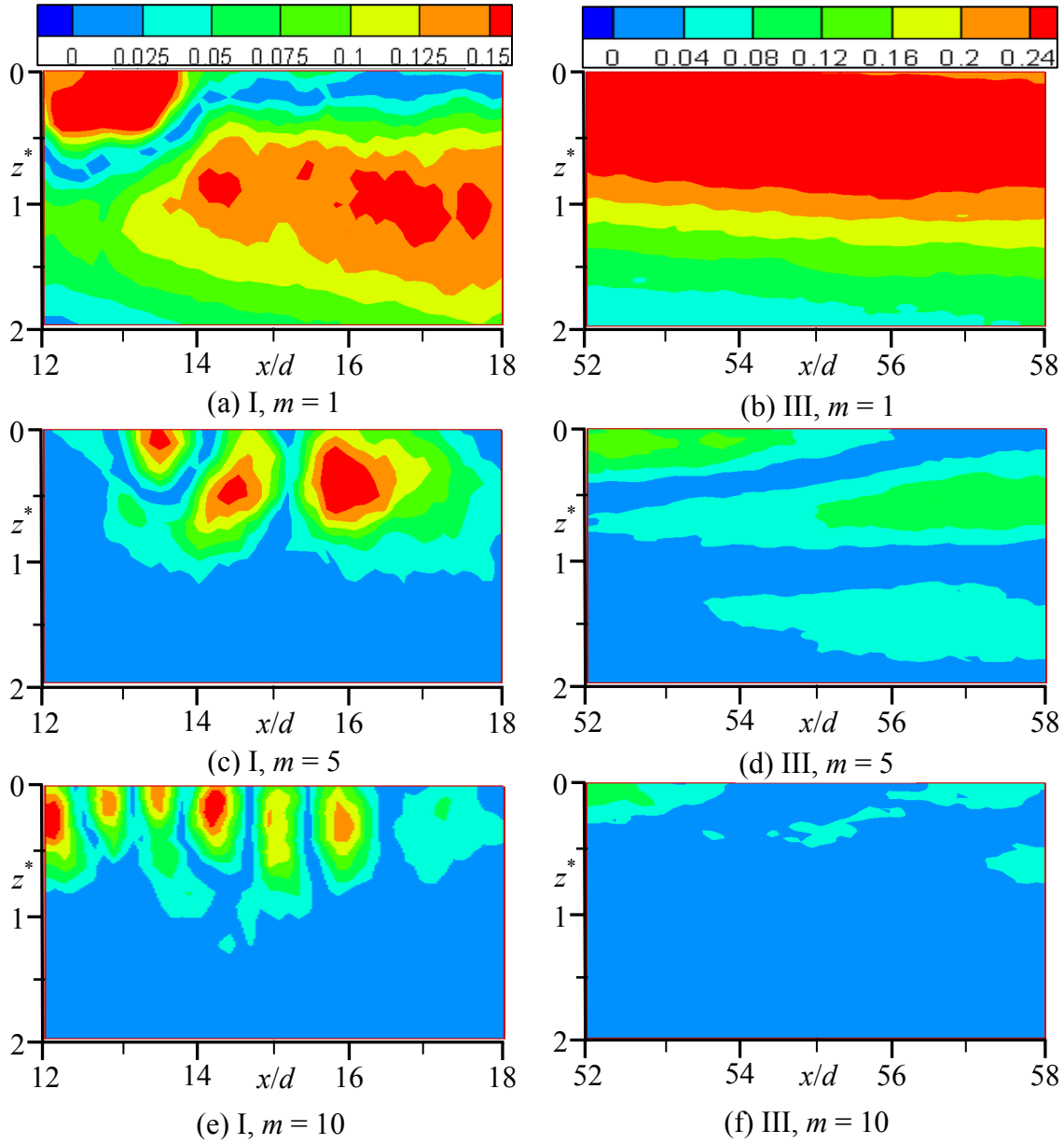

Figure D.8: Iso-contours of the reconstructed streamwise turbulence intensities, u, for modes, m = 1, 5 and10 for h/d = 4.0 in x-z plane. The developing region (I): (a) to (c); and self-similar region (III): (d) to (e).

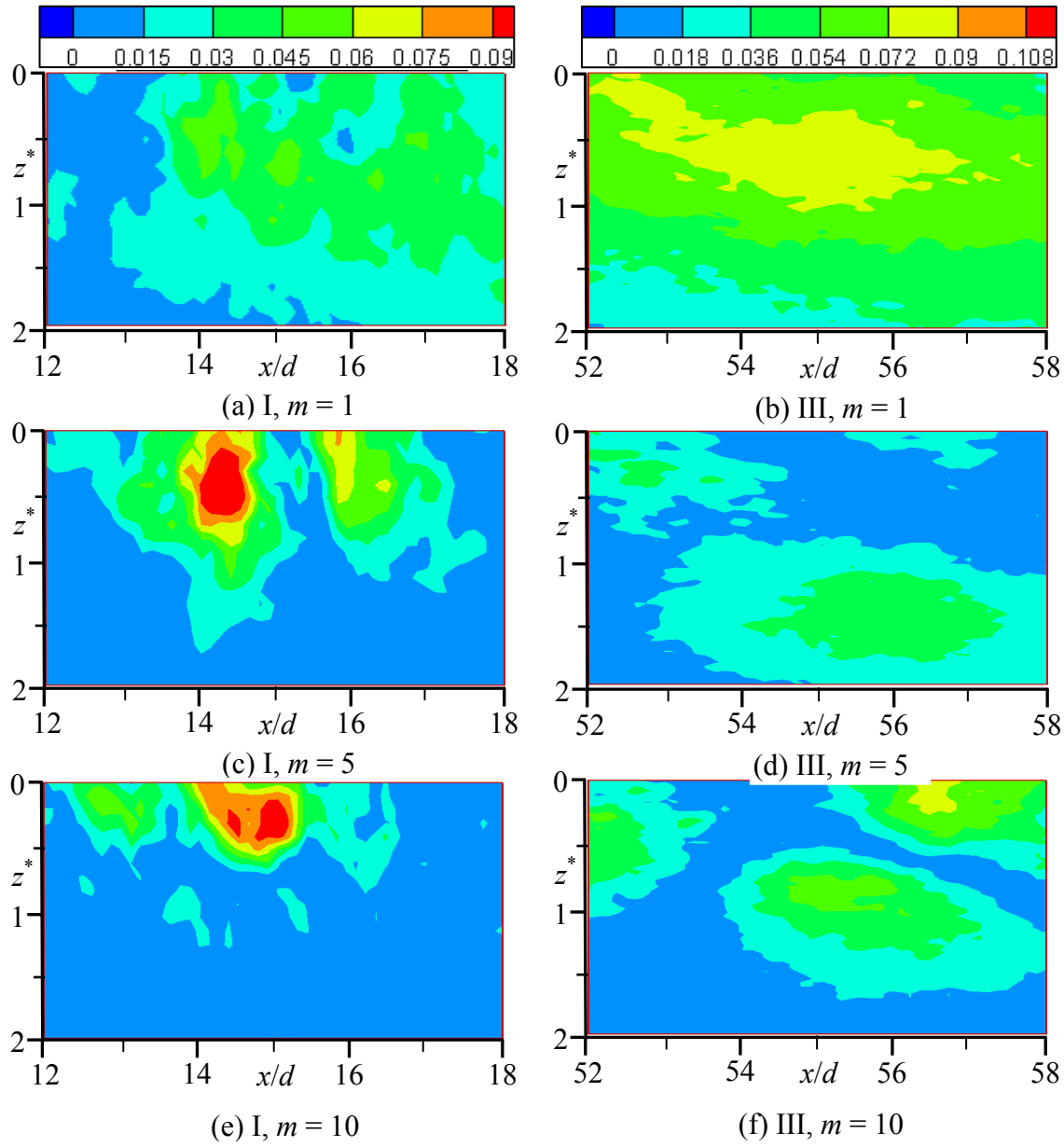

Figure D.9: Iso-contours of the reconstructed wall-normal turbulence intensities, w, for modes, m = 1, 5 and10 for h/d = 4.0 in x-z plane. The developing region (I): (a) to (c); and self-similar region (III): (d) to (e).

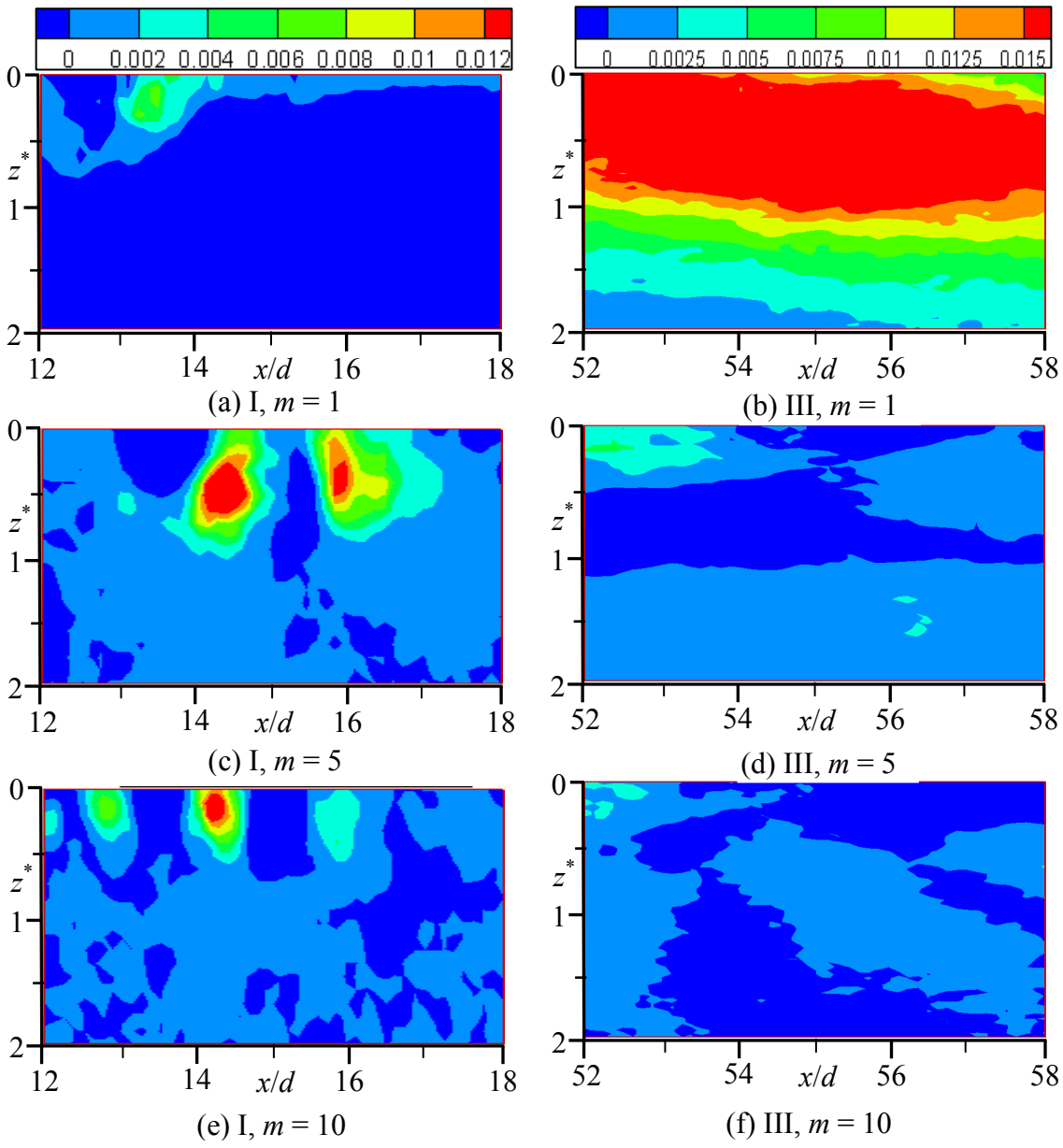

Figure D.10: Iso-contours of the reconstructed Reynolds shear stresses, -*uw*, for modes, *m* = 1, 5 and10 for *h*/*d* = 4.0 in *x*-*z* plane. The developing region (I): (a) to (c); and self-similar region (III): (d) to (e).

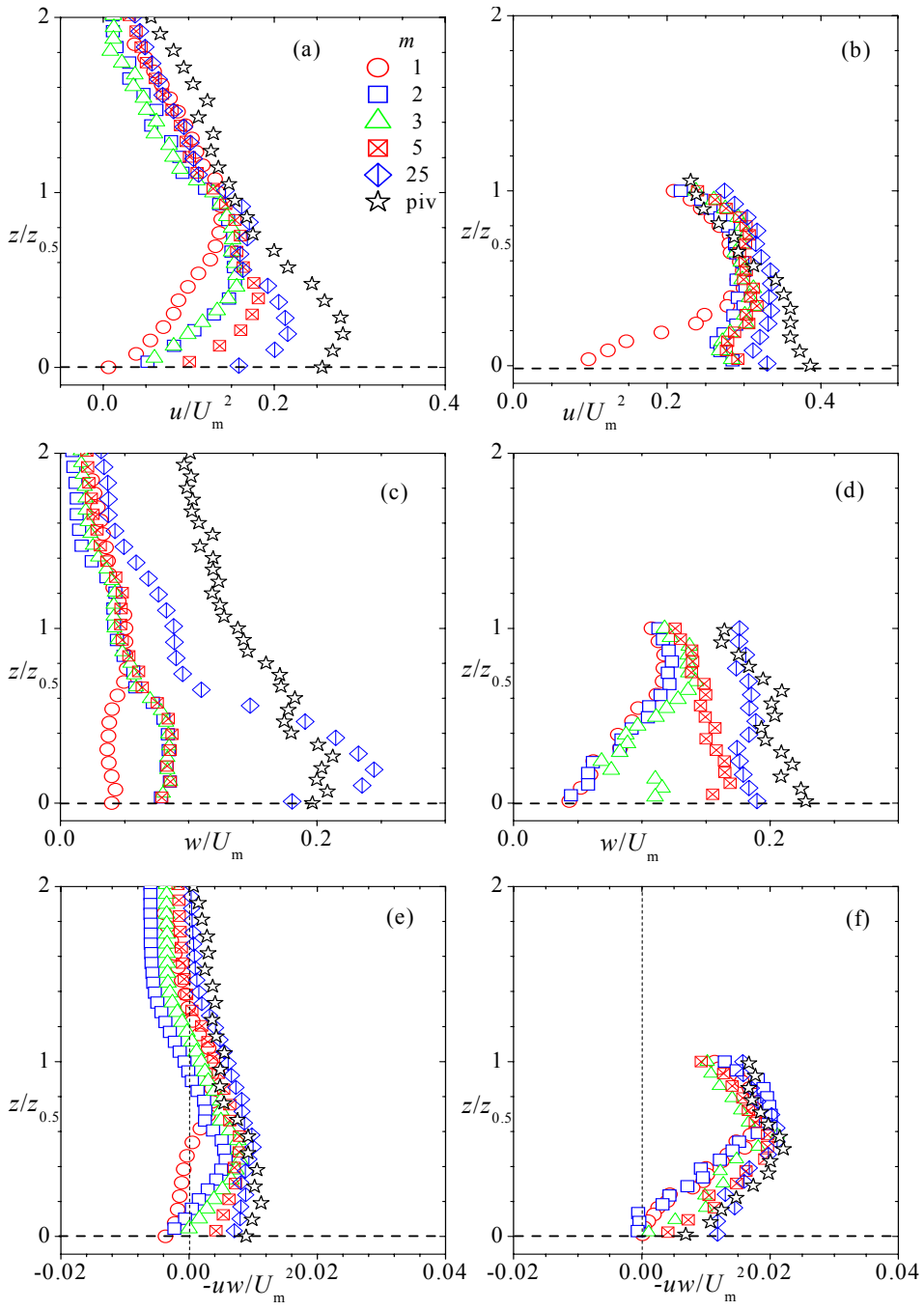

Figure D.11: Profiles of reconstructed turbulent quantities in the developing (x/d = 15) and self-similar (x/d = 52) regions for h/d = 0.5 in the x-z plane. For the sum of the first m = 1, 2, 3, 5 and 25 modes: streamwise turbulence intensities (a) & (b); wall-normal turbulence intensities (c) & (d); and Reynolds shear stresses (e) & (f). piv is the ensemble PIV data.

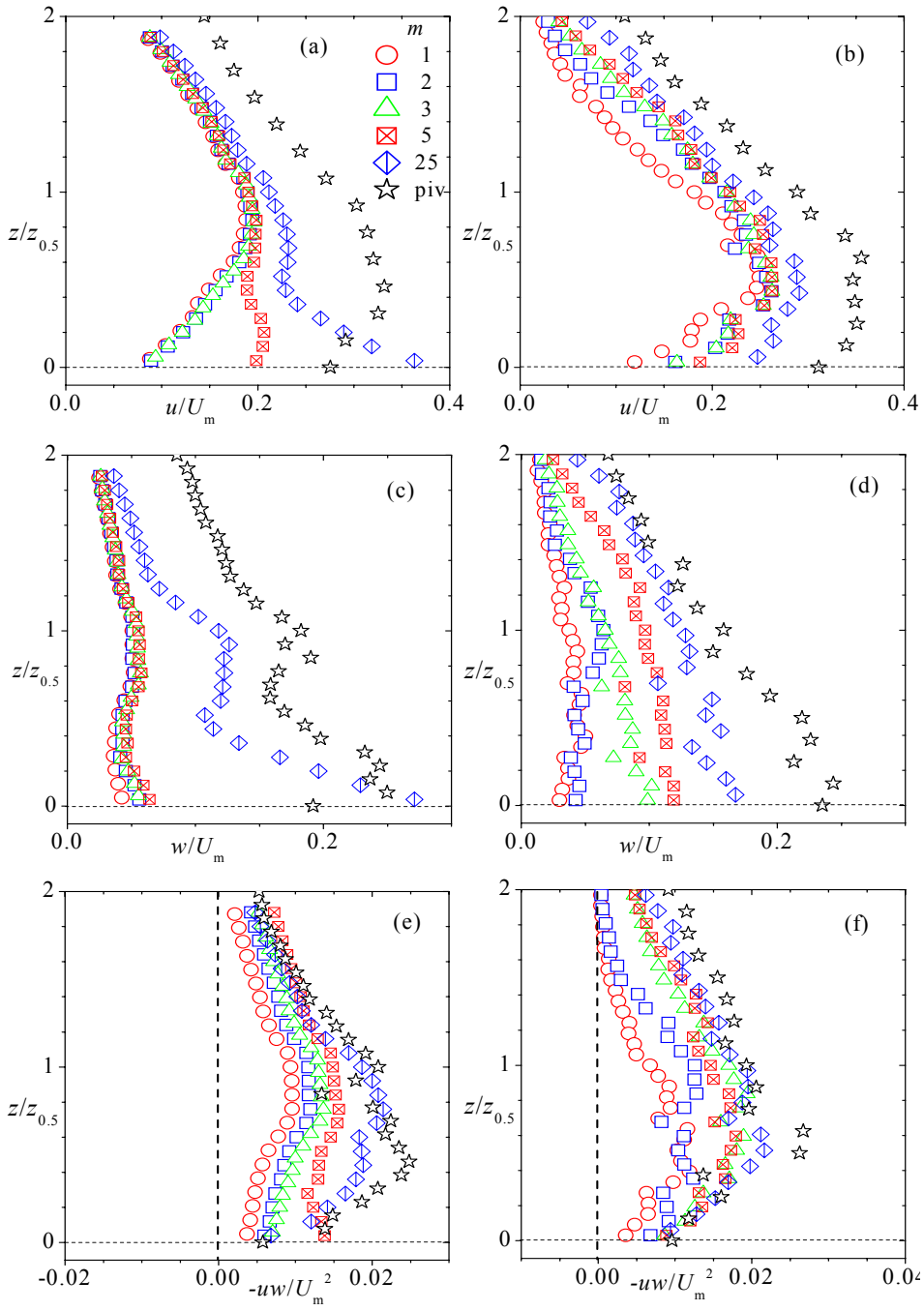

Figure D.12: Profiles of reconstructed turbulent quantities in the developing (x/d = 15) and self-similar (x/d = 52) regions for h/d = 2.0 in the x-z plane. For the sum of the first m = 1, 2, 3, 5 and 25 modes: streamwise turbulence intensities (a) & (b); wall-normal turbulence intensities (c) & (d); and Reynolds shear stresses (e) & (f). piv is the ensemble PIV data.

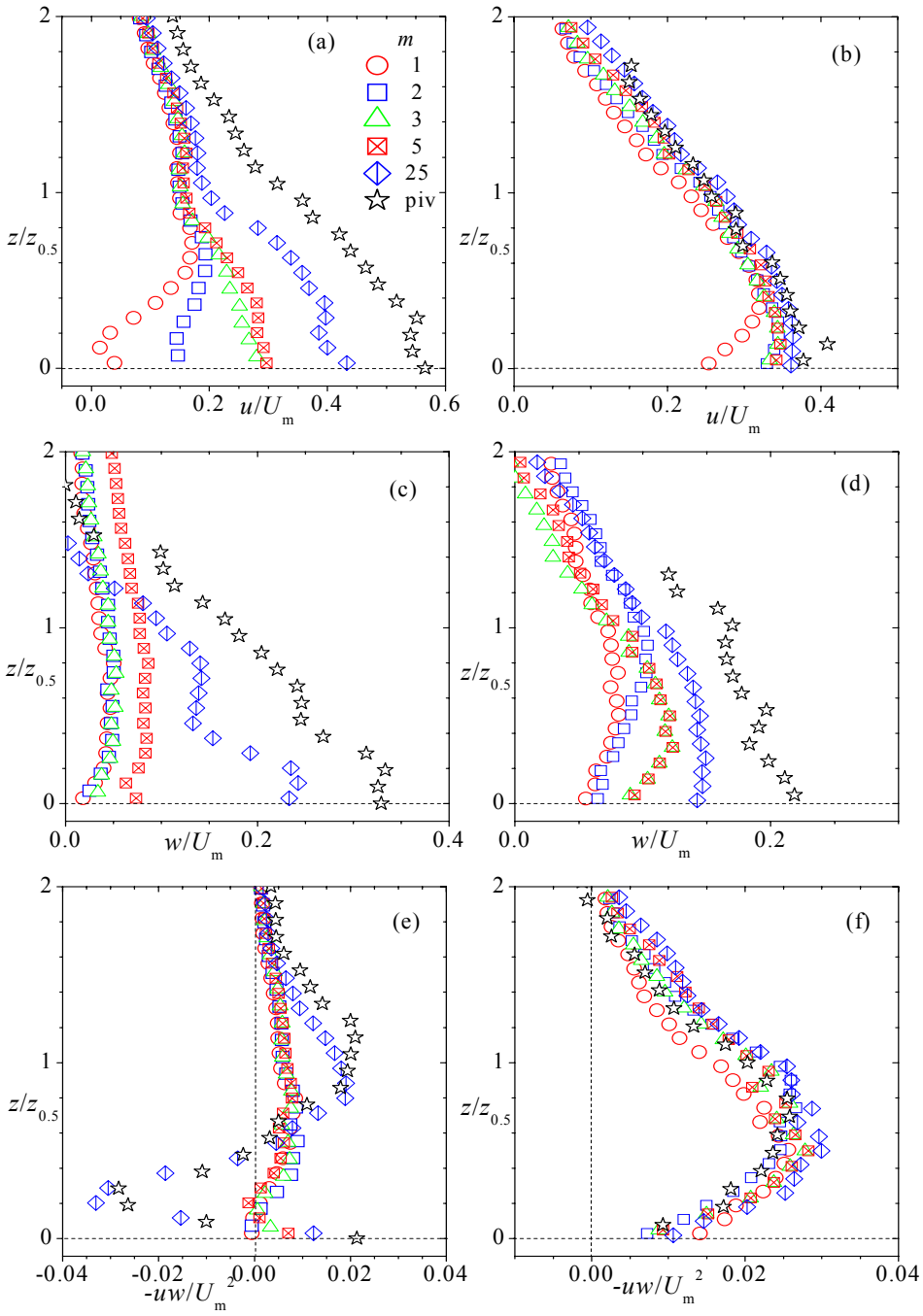

Figure D.13: Profiles of reconstructed turbulent quantities in the developing (x/d = 15) and self-similar (x/d = 52) regions for h/d = 4.0 in the x-z plane. For the sum of the first m = 1, 2, 3, 5 and 25 modes: streamwise turbulence intensities (a) & (b); wall-normal turbulence intensities (c) & (d); and Reynolds shear stresses (e) & (f). piv is the ensemble PIV data.